Development of Theranostic Probes Using Conjugated Polymer Nanoparticles for Application in Cancer Treatment

Zhao, Miao

Awarding institution:
King's College London

King's College London

Development of Theranostic Probes Using Conjugated Polymer Nanoparticles for Application in Cancer Treatment

A thesis submitted to the King's College London in applications for the degree of

Doctor of Philosophy

by

Miao Zhao

Department of Physics

September 30, 2022

ACKNOWLEDGEMENTS

First of all, I would like to thank my family for the love and support they have given me over the past four years, allowing me to concentrate on my studies in a foreign country. In particular, I would like to thank my mother for her patience and encouragement when I was depressed.

I wish to express my gratitude to my supervisor Dr. Aliaksandra Rakovich for accepting me into her group and for her support and guidance along the way. She is extremely patient and conscientious in helping me from applying for a scholarship to working on the project and writing the thesis. I would also like to thank my second supervisor Prof. Mark Green for his assistance with my research and the various resources he provided to me.

I would also like to acknowledge our many collaborators, without whom this project would not have been the same. In particular, a special thanks to Dr Philip Manning for your kind help with the measurement of superoxide radicals. Dr. Laura Urbano and Prof. Sean G. Ryan are acknowledged for the NIR imaging and cell viability assays of PTB7 CPNs. Dr. Katelyn Spillane and her student Maria Liopoulou for confocal imaging of PTB7@F127-FA CPNs and also allowed me to use her lab and provided cells for my experiments. I would like to thank Professor Sergi Garcia-Manyes for providing some cell lines and allowing me to store my cells in his ultra-cold freezer. Finally, a special thanks to Prof. Klaus Suhling for letting me use his tissue culture lab to culture my cells there.

I would like to thank my colleagues Steve Po, Marciano Palma Do Carmo and Ancin Maria Devis for sharing experience in all aspects of work and life. Your friendly company made my four years in the United Kingdom enjoyable and enriching.

I would like to thank the China Scholarship Council and King's College London for funding my PhD.

Finally, I would like to give special thanks to all my friends for making this experience an enjoyable one.

Miao Zhao

Contents

Abstract

Photodynamic therapy (PDT) is a form of treatment based on the interactions of light, photosensitizer, and oxygen. PDT offers considerable potential in oncotherapy due to its several advantages, including reduced invasiveness, low drug resistance, and minimum injury to essential organs. Optically active probes that combine a PDT modality with fluorescence properties can enable simultaneous diagnostic and therapeutic functions – a domain of a recently established research field called theranostics.

Conjugated polymer nanoparticles (CPNs) have attracted much attention for nanomedical applications because of their inherent photostability, high fluorescence brightness, visible or near-infrared (NIR) emission, excellent biocompatibility, and compositions that are free from heavy metal ions. PTB7, a low-bandgap conjugate polymer with near NIR absorption and emission, has been previously reported to possess photosensitizing properties, upon which the PDT modality of the probe can be based. It was therefore identified as a promising material for the development of a theranostic probe.

In this work, NIR-active theranostic CPNs probes based on PTB7 were developed, capable of photosensitizing reactive oxygen species (ROS) upon excitation in the first biological window (NIR-I). The main absorption and emission bands of the produced CPNs fell in the range of 650−950 nm, allowing facile and efficient implementation of our PTB7 CPNs as bioimaging agents. PTB7 stabilized by amphiphilic copolymer PSMA, referred to as PTB7@PSMA CPNs demonstrated superior NIR imaging in A549 cells, but PTB7@F127 CPNs exhibited a poor affinity for A549 cells. Meanwhile, the prepared PTB7@F127 CPNs were shown to produce increased amount of singlet oxygen ($^1O_2$) upon photoexcitation in the NIR region compared to bare PTB7. The photodynamic properties of CPNs were evaluated both in aqueous dispersions and in HaCaT cells, which revealed that the $^1O_2$ production was completely quenched in PTB7@PSMA CPNs. The results demonstrate that the photosensitizing ability of PTB7 CPNs was largely determined by the nature of the stabilizing shell, and that it is crucial to choose an appropriate stabilising material when designing theranostic CPNs.

The synthetic process of PTB7@F127 CPNs was then optimized to improve overall CPNs performance by investigating the effects of different core material PTB7 to shell material F127 ratios as well as the effects of pH during CPN synthesis. The 1:300 mass ratio was found to be optimal, for which particles with a hydrodynamic size of approximately 180-190 nm were obtained – this was deemed to be suitable for biological applications. Alterations in pH were equally found to have a substantial effect on the structure and characteristics of water-

dispersible CPNs, when changes in pH were implemented prior to CPN synthesis. Comparing the addition of 0-30 µL of acetic acid to a 2.5 mL (100 µg/mL) aqueous suspension system, it was determined that 10 µL of acid added produced the greatest results, resulting in a three-fold increase in the yield of $^1O_2$ production.

In order to apply the PTB7@F127 CPNs for PDT of tumour cells, folic acid (FA) was attached to the surface of CPNs. FA modification is a common strategy of increasing the tumour targeting ability of nanomaterials, as folate receptors are overexpressed by most tumour cells, thus ensuring the modified nanoparticles can be applied in a wide range of tumour targeting applications. In this study, PTB7@F127 CPNs were modified with FA in a facile way that ensured a clarified CPN suspension with good water dispersibility. After FA-modification, the $^1O_2$ generation of the probes decreased by more than half, and the PLQY decreased by ~30%. However, these decreases were found to be offset by the much-improved adhesion of PTB7 CPNs to folate-receptor-positive HeLa cells, confirming the specific tumour targeting ability of the developed probes.

In addition to above, a review of the effect of copolymer selection on the characteristics of the prepared CPNs was performed, focusing on the four amphiphilic copolymers (PSMA, F127, PLAG, and polymers with PEG) that are most commonly used to make CPNs for biological applications. This review embodies a valuable guide for the selection of stabilising copolymers aimed towards the rational design of CPNs for biological applications.

Keywords: conjugated polymer nanoparticles, theranostic probe, NIR-I, reactive oxygen species, photodynamic therapy, tumour cell targeting modification

ABBREVIATIONS & ANNOTATIONS

Units

°C	Celsius
a.u.	Arbitrary units
Ev	Electron volt
G	Standard gravity or gram
Da	Dalton
L	Litre
m	Metre
M	Molar
min	Minute
mol	Mole
V	Volt
rpm	Revolutions per minute
s or sec	Second
W	Watt

Mathematical symbols

A (ABS)	Absorbance
C	Concentration
d or D	Diameter
D_i	Diffusion coefficient of species
E_g or ΔE	Bandgap energy
t	Time
λ	Wavelength
ε	Extinction coefficient

Chemical groups and compounds

$^1O_2$	Singlet oxygen
CO_2	Carbon Dioxide
-COOH	Carboxylic acid group

D_2O	Heavy water
DI	De-Ionized
DMSO	Dimethyl sulfoxide
H^+	Proton
H_2O	Water
MB	Methylene Blue
N_2	Nitrogen (gas)
Na	Sodium
NaOH	Sodium Hydroxide
$-NH_2$	Amino group
-OH	Hydroxyl group
PEG	Polyethylene glycol
PO_3^-	Phosphite
Tris	tris(hydroxymethyl)aminomethane

Other abbreviations

ACQ	Aggregation-Caused Quenching
AFM	Atomic Force Microscopy
AIE	Aggregation-Induced Enhanced
BF	Bright Field
CP(s)	Conjugated Polymer(s)
CPNs	Conjugated Polymer Nanoparticles
DAPI	4′,6-diamidino-2-phenylindole
DCFDA	2',7'-dichlorofluorescin diacetate
DLS	Dynamic Light Scattering
DMEM	Dulbecco's Modified Eagle Medium
EPR	Enhanced Permeability and Retention
FA	Folic Acid
FBS	Fetal Bovine Serum
FDA	Food and Drug Administration
FR	Folate Receptor

FRET	Förster Resonance Energy Transfer
FWHM	Full-Width Half-Maximum
LED	Light-Emitting Diode
MRI	Magnetic Resonance Imaging
NP(s)	Nanoparticle(s)
NIR	Near Infra-Red (spectral region)
PA	Photoacoustic
PB	Presto Blue
PC	Protein Corona
Pdots	Polymer Dots
PDT	Photodynamic therapy
PEO	Poly(ethylene oxide)
PET	Photoinduced Electron Transfer
PFA	Paraformaldehyde
PL	Photoluminescence
PLQY	Photoluminescence Quantum Yield
PPO	Poly(propylene oxide)
PS	Photosensitiser
PTT	Photothermal therapy
QD(s)	Quantum Dot(s)
ROS	Reactive Oxygen Species
SDS	Sodium Dodecyl Sulfate
SEM	Scanning Electron Microscope
SOD	Superoxide Dismutase
SOG	Singlet Oxygen Generation
SOSG	Singlet Oxygen Senser Green
TPA	Two-Photon Absorption
UV-vis	Ultraviolet–visible
WGA	Wheat Germ Agglutinin
Zeta Potential	ζ-potential

Chapter 1 – Introduction

Every year about 13 million cancer cases are newly diagnosed and deaths are estimated to reach 13.1 million by 2030.[1] Early diagnosis of cancer greatly increases the chances for successful treatment. In general, the early diagnosis is the single most important factor in determining the patient's survival and quality of life post-treatment, especially for cancers of breast, cervix, mouth, larynx, colon and rectum, and skin.[2] In many cases, however, cancer tissues produce an extremely small amount of indicators in these early stages, making them unlikely to be detected. This in turn makes the development of probes for early diagnosis of cancer one of the greatest challenges of today.

During the last decade, the search for improvements in early diagnosis has further led to an emergence of a new direction – theranostics, which explores the use of various kinds of nanoparticles (NPs) for simultaneous cancer imaging and therapy. Furthermore, theranostic applications, in combining diagnostics and therapeutics, can achieve real-time monitoring of the therapeutic process.[3]

When designing theranostic probes, both the diagnostic and the therapeutic functionalities can be achieved in different ways. The diagnostic modality is typically based on an imaging technique, for example an addition of a molecule that is acoustically active to enable ultrasound imaging, or an addition of magnetically-active atoms to enable MRI imaging. Therapeutic modalities, on the other hand, can be achieved via an addition of an activatable drug, or one that is released upon triggering. Optically-activatable probes, in which both the modalities are addressed via photoexcitation, have several advantages in this regard, the main of which being that their translation into clinical environments is facilitated by the existence and wide use of endoscopic technologies as well as the wide availability of high-powered and affordable sources. In this way, the fluorescence of the optically-activated probes can be utilized for simultaneous diagnosis and delineation of cancerous tissues, while the therapeutic modality can be based on one of the available phototherapies, such as the photodynamic therapy of cancer.[4]

PDT relies on the photosensitization capability of the probe, i.e. a photo-induced production of reactive oxygen and nitrogen species that attack cell membranes and eventually cause cell death via apoptotic or necrotic pathways.[5]

Reactive oxygen species (ROS) are chemically reactive chemical species containing oxygen. Examples include singlet oxygen, superoxide, peroxides, hydroxyl radical.[6] ROSs are considered to be the essential part of cell functions like apoptosis and cell signaling, but are

also found to play a major role in promoting carcinogenesis.[7] In order to promote uncontrolled proliferation, the protection from the Akt pathway, which ensures resistance to senescence and ROSs for normal cells, is removed in human cancers. Thus, ROS-induced apoptosis is facilitated in cancer cells compared to normal cells.[8,9]

PDT is a clinically approved therapeutic technique for cancer and other diseases.[10] Compared with conventional treatment such as chemotherapy, surgery, radiation, PDT has many advantages such as reduced invasiveness and drug resistance, as well as appropriateness to a broad spectrum of cancer species.[11,12] It has become one of the new types of cancer treatments and has attracted attention recently.

In PDT, photosensitizers are excited with a light of specific wavelength, generate excessive cytotoxic ROSs and ultimately induce targeted lesions regression. The host immune system may be stimulated by PDT, which can lead to acute inflammation, expression of heat-shock proteins, invasion and infiltration of the tumour by leukocytes, and possibly increase the presentation of tumour-derived antigens to T cells.[13] Recently, smart nanomedicine-based techniques could delicately adjust the pharmacokinetics of therapeutic drugs and the tumor microenvironment to optimize both PDT and immunotherapy, resulting in an increased anticancer effect.[14]

According to a review article discussing the immune response induced by PDT, using immunotherapy to treat tumors is a new therapeutic strategy that alters the immune microenvironment and triggers the immune system to eliminate cancer cells and tumor tissues. This approach provides the advantage of inducing long-lasting immune memory responses without harming normal cells or tissues. However, not all patients respond positively to immune drugs, and some may even develop drug resistance or experience immune-related side effects. It has been revealed that combining PDT with antitumor immunotherapy can not only enhance the PDT-induced antitumor immune response but also stimulate the proliferation and activation of immune memory cells, suppress tumor metastasis, and prevent tumor recurrence.[15]

For these reasons, the development of photosensitizers is of essential importance. It is urgently required to develop photosensitizers with good biocompatibility, excellent ROSs generation, and strong near infrared absorption which can lead to larger penetration depth.

Nanomaterials are promising photosensitizers because of their unique sizes and the associated unique behaviors and related effects. One example of such effects is the enhanced permeability and retention effect (EPR), which enables the accumulation of nanomaterials in the pathological areas. Tumor tissues have irregular angiogenesis which leads to impaired vessel

structure and widespread fenestration of blood vessels. Compared to healthy tissues, NPs can easily extravasate into the tumor's interstitium because of the leaky vasculature.[16] This extravasation of NPs is also considered to be a kind of passive targeting.

However, nanomaterials have intrinsic problems as photosensitizers. QDs, for example, have excellent optical properties, but a wide variety of QDs are made from toxic heavy metal elements.[17] Gold NPs have better biocompatibility than QDs, but most absorb in UV- vis region,[18] where the absorption of the tissues is quite high, limiting the applicability of these particles in PDT applications. In contrast, conjugated polymer nanoparticles (CPNs), that comprise large πconjugated backbones and delocalized electronic structure, have attracted much attention because of their excellent properties such as good photostability, high fluorescence brightness, NIR emission, excellent biocompatibility, and compositions which are free from heavy metal ions.[19–23] In addition, a small number of CPNs have been reported to generate ROSs,[24] and as such, they are emerging as a promising class of materials for PDT.

The main aim of this work was to develop CPN-based theranostic probes and establish this class of materials as a promising platform for the development of next-generation of photosensitizers (Figure 1.1). Specifically, CPNs as theranostic near infrared-active photosensitizers were studied, and further optimization of the CPNs structure was performed in order to improve its performance as a theranostic probe. Tumor cell-targetting modification was further implemented, as means of increasing the affinity of the developed CPNs probes to specific tumor cells.

The introductions to each of these aspects are given in later chapters, in conjunction with the corresponding experiments. The remainder of this introductory chapter presents a detailed review of existing literature on the development of CPNs-based probes, with a specific interest in the effect the stabilizing copolymer has on the properties of CPNs. This is an important and an undervalued issue that has not received a lot of attention in research to date, characterized by a distinct lack of papers where comparison of CPNs probes with different copolymer shells are compared. A focus review of the topic is therefore warranted here, both as an attempt to fill in the gaps in existing knowledge and to provide guidance to own research on CPNs-based probes.

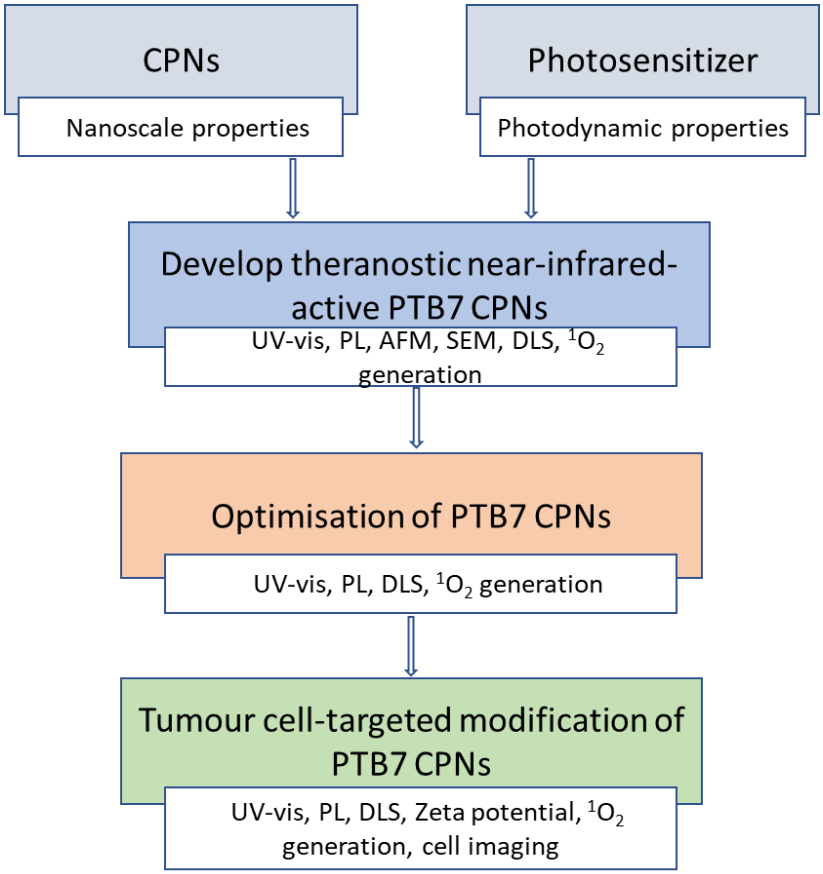

Figure 1.1 Flow-chart of the project. Nanomaterials with promising physicochemical and optical properties have emerged as promising photosensitizers, which are alternatives to standard PSs in overcoming these shortcomings. CPNs were characterized and optimized using a well-established spectroscopic platform with the aim of developing ideal NIR-active theranostic CPNs and making an in-depth study of the relationship between CPN structures and their properties that affect biological applications. For definitions of abbreviations used in this figure, please refer to the ABBREVIATIONS & ANNOTATIONS list above.

1.1 Introduction to the influence of copolymers on CPNs' properties

Conjugated polymers (CPs) are organic macromolecules characterized by a backbone chain consisting of alternating single- and double-bonds. The overlapping *p*-orbitals of this bond arrangement allow a delocalization of π-electrons across all the adjacently-aligned *p*-orbitals, giving rise to most of the useful optoelectronic properties of CPs. That delocalized π-electron system can absorb light and create and transport those photogenerated charge carriers. The light energy absorbed can be effectively converted to fluorescence, heat, and other energies, making CPs optically and electronically active materials.[25]

Due to this primarily organic composition, however, CPs are intrinsically hydrophobic, whilst in most cases, biological application of imaging and therapeutic agents requires them to have good water dispersibility.[26]

When it comes to fabrication of water-dispersible polymeric CPNs, the most popular method

is the nanoprecipitation method. In this method, CPs, together with an amphiphilic polymeric encapsulation matrix, are dissolved in an organic solvent prior to addition into a water phase under stirring or sonication.[27,28] The amphiphilic polymers are molecules that simultaneously contain hydrophobic and hydrophilic components. In aqueous environments, and driven by hydrophobic interactions, the amphiphilic polymer matrix forms micelle-like structures characterized by hydrophobic cores and hydrophilic shells. When used in the nanoprecipitation-driven fabrication of CPNs, it encapsulated the hydrophobic CPs in its core part, yielding a clear nanoparticle dispersion.[29] Further surface functionalization of CPNs with specific targeting ligands can then be performed to achieve targeted bio-imaging. It must be emphasized that most of the optoelectronic properties of the NPs of the CPNs originate from the conjugated polymer core, and these include the properties such as optical absorption and fluorescence spectra, fluorescence quantum yield, efficiency/existence of the donor to acceptor charge/energy transfer, which are discussed in detail later.

Many CPNs have been prepared using the nanoprecipitation method, consisting of different core conjugated polymers and/or different solubilizing shell materials. Several review papers have been previously published on this topic, summarizing the various types of CPNs that can be produced and their ensuing physicochemical properties.[30,31]

The purpose of this review is to focus on those properties of the CPNs which are affected by the choice of the amphiphilic polymer used within the solubilizing shell of the CPNs. I hope that in doing so, I can provide a deeper insight into the reciprocities of the system that is the CPNs and offer more holistic CPNs design strategies. For accessibility, however, the discussions are limited to the most common amphiphilic polymers used for CPNs stabilization: PSMA, F127, PLGA and PEG-containing polymers.[32–35] As the CPNs discussed here are used primarily for bio-applications, good biocompatibility is the essential requirement. All the above amphiphilic polymers are approved for pharmaceutical usage by the Food and Drug Administration (FDA).

PSMA, or Poly (styrene-co-maleic anhydride), is a copolymer typically composed of alternating styrene and maleic anhydride monomeric units. Styrene is hydrophobic while maleic anhydride is hydrophilic, and due to the opposing chemical nature of the two units, PSMA is dissolvable both in organic and aqueous solvents. This amphiphilic character can be exploited to encapsulate the inherently hydrophobic CPs and thus facilitate the dispersibility of CPs in aqueous environments.[36] The popularity of this copolymer in the CPNs literature is at least partially due to its ready commercial availability in a broad range of molecular weights and maleic anhydride content.[37] Another great advantage is that when forming

CPs@PSMA CPNs, PSMA can be a source of carboxyl functionalities while acting as a coating polymer.

Pluronics are commonly-used synthetic block copolymers that are composed of blocks of hydrophilic PEO (poly(oxyethylene)) and hydrophobic PPO (poly(oxypropylene)) polymers, arranged in a PEO_x-PPO_y-PEO_z triblock structure.[38,39] This triblock structure self-assembles into micelles in an aqueous environment in which PPO forms a hydrophobic core, and PEO forms a hydrophilic outer shell. Pluronics have different properties, depending on the relative values of x, y and z. One of the most widely used Pluronics is the biocompatible Pluronic F127 (PEO_{100}-PPO_{65}-PEO_{100}), which is also the main copolymer used for the purposes described above. Pluronic F127 has been used to prepare nanomicelles for drug and gene delivery. These applications have facilitated particle–cell interaction and enhanced cellular uptake efficiency.[40,41]

PEG, or polyethylene glycol, is a hydrophilic, often straight-chain polymer of ethylene oxide, whose general structure is $HO–(CH_2–CH_2–O)_n–H$.[42] Generally, PEG is considered to be an amphipathic molecule that possesses greater amphipathic character at greater chain lengths, or equivalently higher molecular weights.[43] The PEG polymer has excellent biocompatibility, which makes it a popular choice for biological applications of PEG-coated CPNs.[44] PEG is the most popular polymer for drug delivery applications as it can inhibit the fast recognition by the immune system and lead to a reduced blood clearance of nanocarriers, increasing blood circulation time.[45] Many different PEG-derived polymers are available, offering different end groups that could be used to functionalize the CPNs, *e.g.* further enhancing their cellular internalization or achieving specific targeting. For instance, N_3-PEG-NH_2 was modified with folic acid (FA) to develop a cellular probe.[46] Or modified -COOH end group of PS-PEG-COOH with streptavidin to achieve targeted imaging.[47]

Due to its excellent biocompatibility and biodegradable properties, PLGA or Poly (D, L-lactide-co-glycolide) is also one of the most frequently used biomaterials.[48] However, when used to prepare surface-modified polymeric nanoparticulate systems, it is most commonly combined with PLGA into a hydrophilic polymer PEG(PLGA-PEG),[49] PLGA-PEG combines many of the beneficial qualities of PLGA and PEG, and so it has arose as one of the most promising systems for nanoparticle formation and drug delivery applications in the last decade.[45,50–55] Polymeric nanomicelles using this PLGA-PEG copolymer form a core-shell architecture and have a relatively narrow size distribution of 10-100 nm. The PEG-PLGA-coated CPNs are one of the only systems where the influence of different PEG-PLGA matrices on optical imaging performance and biodistribution of CPNs has been investigated.

Specifically, NIR-emitting conjugated polymer PCPDTBT encapsulated with different PEG and PLGA molecular weights (PEG_{2K}–$PLGA_{4K}$, PEG_{2K}–$PLGA_{15K}$ and PEG_{5K}–$PLGA_{55K}$) were investigated, leading to a conclusions that encapsulation with the smallest of PEG and PLGA MWs (PEG_{2K}–$PLGA_{4K}$) result in threefold lower cytotoxicity (IC50 value) and higher photoacoustic amplitude compared to the other two systems, despite the smallest size of the resulting CPNs.[56] In yet another study, comparing the effect of the encapsulation model that included PEG-PLGA, PCPDTBT CPs encapsulated with the liquid midchain triglyceride (MCT) core of lipid nanocapsules (LNCs) exhibited a higher signal-to-background ratio in an optical imaging platform but a slightly lower photoacoustic amplitude compared to PCPDTBT@PEG-PLGA.[53] The above studies demonstrate that formulations for a conjugated polymer with different copolymers can have a significant impact on both imaging performance and biodistribution.

In this review, the use of each of these amphiphilic polymers for CPNs preparation was critically assessed. The review is broadly divided into three sections, each dedicated to a different property of the CPNs that can be controlled via modification of the solubilizing shells. Unsurprisingly, the review starts with a discussion of CPNs dispersibility in aqueous suspension before moving on to various properties affecting the possible applications of the CPNs and finally culminating in considering any biocompatibility implications. A summary of some general trends, observations, and omissions from the reviewed literature is provided at the end.

1.2 Colloidal dispersibility of CPNs

In the context of CPNs, solubility in aqueous solutions equates to colloidal dispersibility of CPNs. The applications of CPs are restricted due to the lack of water dispersity and the main obstacle to CPs in bio-applications is that CPs are mostly inherently hydrophobic and need further modification to ensure good water dispersity. One of the most important reasons to introduce copolymer is to form water-dispersible CPNs, and the water-dispersible CPNs have been successfully used in biological applications. [26,57]

The water dispersibility mainly depends on the size of particles, pH, and ionic strength.[58] The size of the particles is normally provided by measuring the dynamic light scattering (DLS) and some articles have also provided the surface zeta potential (ζ-potential) after using the above amphiphilic polymer to stabilize the CPs. What follows below is a review of the literature where the development of CPNs has been reported for applications requiring CPNs to possess aqueous stability and dispersibility, addressing each of the encapsulation matrices in turn.

To overcome the limited spatial resolution of conventional fluorescence microscopy by classic optical diffraction, super-resolution optical microscopy techniques have been developed. To achieve high-quality super-resolution fluorescence images, different types of photo blinking semiconducting Polymer dots (Pdots) featuring ultrahigh brightness and photostability have been used in super-resolution optical microscopy.[59] Pdots are viewed as a subset of CPNs that possess the properties of small particle size that should be less than 20-30 nm in diameter and high brightness.[60] As the fluorescence brightness is determined mainly by semiconducting polymers' weight or volume fraction, Pdots should comprise more than 50% semiconducting polymer.[23] Blue PFO and carmine PFTBT5 are two types of small photo blinking polymers with different colors. They have been prepared to be water-dispersible Pdots with PSMA using the nanoprecipitation procedure and applied in super-resolution microscopy.[59]

PSMA has also been used to increase the water dispersibility of CPs based on aggregation-induced emission (AIE) activities and fluorescence resonance energy transfer (FRET).[61,62] In contrast to the CPs showing limited fluorescence quantum yields in the solid or aggregate states due to the aggregation-caused quenching (ACQ) effect, CPs with AIE activities have significant advantages because their fluorescence is brighter in the aggregate states. So it is of great significate to develop AIE-active water-dispersible CPNs that offer huge potential in bioimaging applications. Liu and co-workers synthesized conjugated polymers EBKCP encapsulated with PSMA. The resulting CPNs show AIE characteristics which emit bright yellow fluorescence in aqueous media with a PLQY of 15%, and the Hela cell imaging results demonstrate that the CPNs are good contrast agents for biological florescence imaging.[61]

Another application of using PSMA is to increase the fluorescence QY by FRET between the donor-acceptor pairs inside the NPs while increasing the water dispersibility. Cao and co-workers used PSMA as the encapsulation matrix to fabricate water-dispersible CPNs based on CPs incorporated with two-photon absorption (TPA) units, electron-rich units and electron-deficient units. They found that although the introduction of PSMA slightly reduced the FRET efficiencies because the hydrophobic parts of PSMA interpenetrate with the polymer chain and reduce the contact between the donor and acceptor segments, the absolute intensities of the acceptor emission peaks were significantly larger compared to bare CPs without PSMA due to the separation effect of PSMA against aggregation induced quenching. So higher fluorescence QY and improving the optical performance in cell membrane imaging were achieved by introducing PSMA in FRET-based CPNs.[63]

CPs solubilized by F127 can have long-term stability that has a significant value for practical applications, and can have excellent stability in a large range of pH values. Huang and co-

workers use F127 encapsulated CPs (PFO) to improve their water dispersibility and use the CPNs to detect Sudan dye in an aqueous solution.[29] They found that the CPNs in water are very stable, as they observed no precipitate and aggregation several weeks after preparation. MEH-PPV blended with PCBM solubilized by F127 formed stable aqueous micelles. The colloidal stability was studied by measuring the DLS of the micelles over the pH range 2.0-12.0 in water as well as in PBS buffer solution (pH 7.4) over one week. Both of these two measurements showed a stable number-average hydrodynamic diameter of around 21 nm,[64]confirming F127's excellent resistance to pH changes.

Levi-Polyachenko and co-workers synthesized donor-acceptor CPNs based on PCPDTBSe using F127 as a stabilizer, showing excellent dispersibility in aqueous media.[65] The result shows that PCPDTBSe NPs without F127 coating are stable for one week in aqueous media, while PCPDTBSe NPs with F127 coating show more than two months in aqueous media. The authors also find that the shape of the CPNs has a considerable influence on the stability, and if PCPDTBSe coated with F127 is in the shape of nanofibers, the water stability is inferior that it falls out of the solution after 24 h.[65]

PEG is qualitatively different from other copolymers considered in this review in that its amphiphilicity is depended upon its molecular weight: the lower molecular PEGs are hydrophilic while the amphiphilicity increases with increased molecular weights or equivalently, the chain length of the conjugated polymers.[42]

For example, Liu and co-workers synthesized conjugated precursor polymer PFBD-N_3 which they conjugated with N_3-PEG_{600}-COOH and N_3-PEG_{2000}-COOH via click reactions, respectively. They found that the conjugated polyelectrolytes show better dispersibility in water with increasing PEG molecular weight.[66] This might be because the hydrophilicity of copolymer increased as the ratio of PEG chain increased.

In addition to PEG itself, various derivatives of PEG are also widely used as copolymers because of the versatile modifiable terminal groups. For example, PEG containing amphiphilic polymer 1,2-distearoyl-sn-glycero-3-phosphoethanolamine-N-[methoxy(polyethylene glycol)] (DSPE-PEG) is widely used to enhance water dispersibility. On the other hand, poly (ethylene $glycol)_{114}$-b-$poly(caprolactone)_{60}$ (PEG-PCL) is used as a copolymer of hydrophobic CPs, in which PCL is the hydrophobic end and PEG is the hydrophilic end.[67] N_3-PEG-NH_2 also be used to form water-dispersible conjugated NPs without further modification of the NH_2 end.[68] Four-arm amphiphilic block copolymers consisting of a hydrophilic chain of PEG and a hydrophobic segment of polycaprolactam were used to encapsulate the hydrophobic oxygen probe of PtTFPP to form a water-dispersible oxygen sensor, and the authors choose multi-arm block

polymers because they exhibit various morphologies and higher terminal group's concentrations than conventional linear polymers.[69]

Liu and co-workers prepared four CPs (PF/PFV/PFBT/MEH-PPV) encapsulated separately with PLGA to obtain stable aqueous solutions. The ζ-potential of these four CPs@PLGA were all reported to be smaller than -30 mV, reflecting effective electrostatic repulsion among particles and the observed good colloidal stability for the CPNs suspensions.[70] Another indicator of aqueous stability is the degree of leakage of CP molecules into the aqueous phase after encapsulation with copolymer matrix. The same work investigated PLGA-encapsulated CPNs composed from 4 different CPs, as summarized in Table 1.1. They find that, compared to small-molecule dye (coumarin-6) -loaded PLGA, which showed about 0.32% leakage in 24 h, the CPs@PLGA exhibit excellent stability with the shallow release of CP molecules into the aqueous phase. The hypothesized that the entanglement among the polymer chain of PLGA and CPs blocks the diffusion of CPs molecules into the aqueous phase, ultimately leading to their increased stability.[70]

Table 1.1 Characteristics of the CP-loaded PLGA NPs

Loaded CP	PF	PFV [b]	PFBT	MEH-PPV
Particle size [nm] [a]	261.2 ± 4.5	257.5 ± 4.2	242.9 ± 3.8	271.4 ± 5.2
Polydispersity [a]	0.129 ± 0.034	0.124 ± 0.031	0.120 ± 0.028	0.158 ± 0.037
Zeta potential [mV]	-36.61	-37.15	-33.42	-35.28
Encapsulation efficiency [%]	≈41.3	≈43.9	≈44.2	≈47.6
Leakage of CP in 5 days [%]	0.095	0.098	0.087	0.062

[a] The particle size and polydispersity of NPs are determined by laser light scattering. [b] For pure PFV NPs prepared without PLGA, the particle size is 221 ± 7.3 nm, and the polydispersity is 0.186 ± 0.049.

Based on its merit of good stability in biological systems, the PLGA-PEG matrix is also a popular choice when selecting a stabilizer copolymer. One disadvantage of core-shell CPNs is that many types of amphiphilic stabilizing agents can be displaced from the particle surface in biological fluids.[71] So choosing a suitable stabilizing copolymer that can ensure good stability in biofluids is very important. Dailey and co-workers incorporated CPs of PCPDTBT within PLGA-PEG systems, the PLGA-PEG CPNs have good colloidal stability and show excellent stability in biofluids.[56] The same group also indicate that the PLGA-PEG matrix is biodegradable and can improve the product yield of the hydrophobic CPs by increasing its water dispersibility. Two kinds of CPs (CN-PPV and F8BT) were investigated, and the structure of CN-PPV was shown to allow the formation of CPNs without the amphiphilic stabilizing copolymers. On the other hand, the hydrophobic nature of F8BT required the presence of a stabilizing copolymer in order to form CPNs. After incorporating the F8BT within

a matrix of the $PLGA_{55K}$-PEG_{5K}, the authors indicate that the product yield of the F8BT@ $PLGA_{55K}$-PEG_{5K} system improved, proving that encapsulation can be a highly successful strategy.[54]

ζ-potential

ζ-potential is an important physical property that provides valuable information about charged interfaces' electrical state. During the measurement, an electric charge is applied across the sample in a folded capillary flow cell. As a result, particles with a high ζ-potential are drawn to the electrode with the opposite charge. Doppler anemometry, which is a technique that assesses speed and direction of particle motion, is used to then calculate velocity of the particles, which is itself proportional to the magnitude of their ζ-potential.[72] The value of ζ-potential has been used as a quantitative measure of charge-induced colloidal stability. In general, ζ-potential values between ±30 and ±40 mV are considered indicators of the electrostatic stability of NPs.[73] Despite ζ-potential being an extremely valuable indicator of CPNs stability, it is still rarely reported in the literature. Nonetheless, some general observations can be made based on the few pieces of research that do mention it.

Among the works investigated, use of PSMA and PEG-based copolymers generally results in CPNs with increased charge density, when compared to F127- or PLGA-PEG-stabilized CPNs. For example, the ζ-potential of PBMC@PSMA CPNs was reported as −57.7 mV[74], and PFPtTFPP@PSMA CPNs as -33.4mV[75]. For the F127-stabilized CPNs, the ζ-potential typically falls around -12 mV mark, as exemplified by PBTB@F127 CPNs[76] and CN-PPV@F127+TMOS CPNs[77], although in the latter case, one should note that the CPs is stabilized with TMOS-dopped F127. The difference in the ζ-potential of the CPNs formed with different copolymers was specifically investigated in Mark Green's group, where both PSMA and F127 were used to encapsulate MEH-PPV, concluding that that the ζ-potential of PSMA-stabilized CPNs was larger in amplitude compared to F127-equivalent (-30 mV for MEH-PPV@PSMA CPNs and -10.0 mV for MEH-PPV@F127 CPNs).[78] CPs stabilized by PLGA-PEG copolymer also tend to have moderate charge density, as illustrated by relatively neutral surface charges of F8BT@ PEG_{5K}–$PLGA_{55K}$ CPNs (−4 to −10 mV) and CN-PPV@ PEG_{5K}–$PLGA_{55K}$ CPNs (−8 to −11 mV).[54]

An interesting alternative approach to influencing the surface charge of the CPNs can be followed when the CP is itself amphiphilic and has an inherent surface charge; in such cases, the copolymer can be deposited onto the CPNs via an electrostatic interaction. For example, Kissel and co-workers used a folate-conjugated cationic triblock copolymer to coat inherently

negatively-charged PF-NPs through electrostatic interaction. By increasing the weight ratio of copolymer to PF-NPs, a continuously increased ζ-potential from -40 mV to +30 mV could be achieved.[79]

With regards to investigations of ζ-potentials, CPNs stabilized by PEG-based amphiphilic copolymers has received better attention than other copolymers, with studies extending to investigations of ζ-potential changes upon further functionalization of CPNs. For example, Wang and co-workers found that upon modification of their PDPP-DBT@ DSPE-PEG-MAL CPNs with Tat, the ζ-potential of the CPNs changed drastically from −34.4 ± 1.8 mV to 23.1 ± 1.7 mV.[80] In addition, and using the same stabilizing copolymer, Liu and co-workers found a similarly drastic change in the ζ-potential of the CPNs is also obtained when CPs are modified with Tat prior to forming the CPNs: a value of -46.6 mV was reported for the ζ-potential of PTPEDC@ DSPE-PEG-Mal CPNs, whilst the ζ-potential of the pre-modified PTPEDC-Tat@ DSPE-PEG-Mal CPNs was 6.6 mV.[81]

The ζ-potential value not only influences the aqueous stability of CPNs, but it also plays an essential role in cellular uptake, cytotoxicity, and intracellular localization. These themes are discussed in more detail in the later sections; Here, I only emphasis that it should form part of a comprehensive consideration when selecting a suitable copolymer for a specific application.

Long-term stability

The long-term stability of CPNs post-fabrication is a topic that has so far been omitted from most publications. This is a significant oversight, since long-term stability of formulations plays a critical role in determining their suitability for clinical applications. As such, this is an area of CPNs-related research where reporting of results should be encouraged, to enable trends to be elucidated and conclusions to be made about the suitability of CPNs as therapeutic agents.

1.3 Optical properties

As stated previously, the CPNs' optical properties originate mainly from the core CPs material. Surprisingly, however, some changes in the optical properties of CPNs has been observed when they were coated with amphiphilic shells. Here, a review of these reports, together with some key observations are presented.

Shifts in optical spectra

The optical spectra (absorbance and photoluminescence) of CPs does often shift after being encapsulated in copolymers, when compared to CPs in the organic solvent; the direction and degree to which this happens, however varies case-by-case. This is reflective of the origin of

the optical properties of conjugated polymers and their dependency on the chain packing and/or disorder in the nanoparticulate system.

Interestingly, for F127-stabilized CPs, more often than not, the resulting CPs show redshift in their optical spectra. As shown in Figure 1.2, the absorbance peak of MEH-PPV is 498 nm in a chloroform solution, but redshift to 512 nm in the presence of F127, when co-precipitated into water to form CPNs. The emission spectrum measured for MEH-PPV in organic solvent solution compared to an aqueous solution with F127 is consistent with those for the absorption spectrum, which also shows a redshift. The authors speculate that, after being encapsulated in a hydrophobic F127 micelle core, the interchain interactions of the conjugated polymers increase, the polarizability of the environment around each polymer segment changes as well, and a fraction of the red-shifted aggregates with an energy disorder is formed.[64]

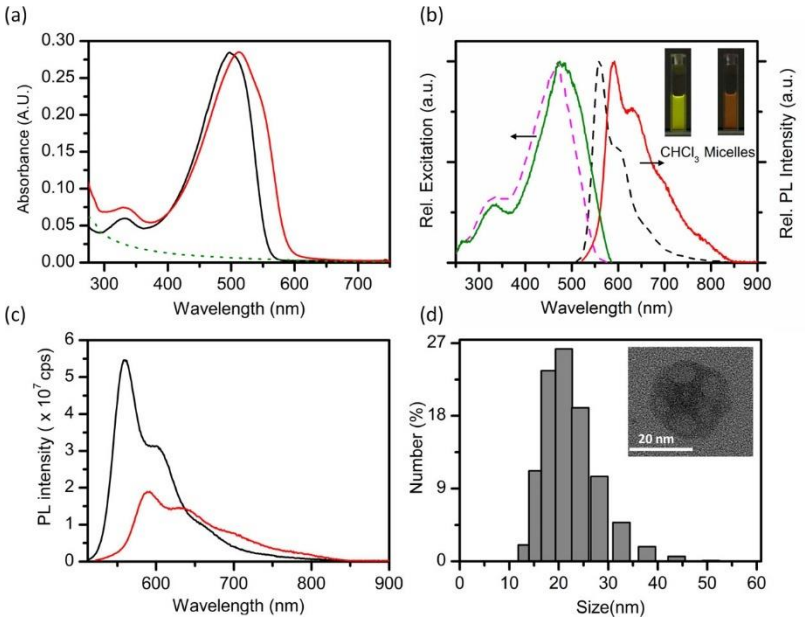

Figure 1.2 (a) Absorption spectra of a MEH-PPV solution in chloroform (black line) and the corresponding conjugated polymer nanomicelles prepared in water (red line). The dashed green line is an absorption spectrum of empty F-127 micelles. (b) Intensity-normalised excitation and emission spectra of a MEH-PPV solution (dashed lines) and MEH-PPV micelles (solid lines). Insets: photographs of MEH-PPV emission from a chloroform solution and a micellar suspension under black light illumination. (c) Emission spectra of MEH-PPV in chloroform solution (black line) and aqueous nanomicellar suspension (red line). (d) Number-average hydrodynamic size distribution of MEH-PPV micelles. Inset: transmission electron micrographs of a typical MEH-PPV micelle. (Copyright 2016 American Chemical Society)

Despite the common occurrence of redshifts in the optical spectra of CPs stabilized with F127, there are a few instances in which blue shifts or no shifts have been observed. For instance,

Huang and colleagues observed a slight blueshift in the absorbance of PFO@F127 aqueous solution compared to PFO in Tetrahydrofuran (THF).[29] Similarly, M. Green and the co-workers reported a blue shift in both absorption and emission spectra of MEH-PPV CPs upon encapsulation with F127 compared to those encapsulated by PSMA.[78] However, when PFPE was encapsulated with F127, no significant changes in absorbance were observed when compared to PFPE in THF.[29]

An interesting alternative observation of spectral changes upon formation of the CPNs is the opposing shift of the absorption and emission peaks, typically characterized by a blue-shifted absorption features and a red-shift of the emission peaks. This was, for example, observed by Dailey and co-workers, as shown in Figure 1.3, when PCPDTBT was encapsulated in PLGA-PEG. Compared to PCPDTBT in THF, PCPDTBT@ PLGA-PEG nanoparticle shows a ≈20–50 nm blue shift of absorption peak, which the authors attribute to the reduction in the length of π −conjugated domains through bending, torsion and kinking of the PCPDTBT polymer chains. The CPN formulations also show about an 80 nm red shift in the emission peak compared to the THF solution, which is also caused by the spatial changes in the polymer structure, causing an increased interchain interactions and the aggregate formation.[50]

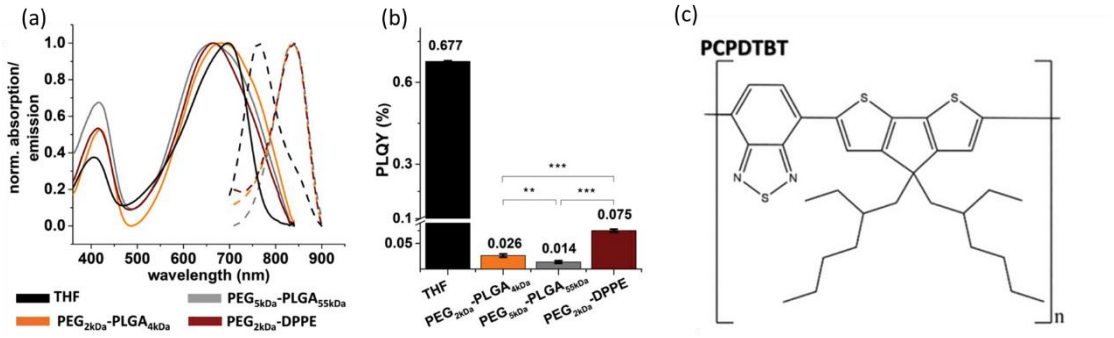

Figure 1.3 (a) Normalized absorption (solid lines) and emission spectra (dashed lines) of PCPDTBT in THF and 5% PCPDTBT CPNs. (b) PLQY of PCPDTBT in THF and different 5% PCPDTBT CPNs. PLQY values were directly measured in an integrating sphere at a fluorophore concentration of 1.7 µg mL^{-1}. All values represent the mean ± standard deviation of (n = 3) independently produced batches per formulation. p-Values were calculated using one-way ANOVA with Tukey's post hoc test, *p < 0.05, ** p < 0.01, *** p < 0.001. (c) Chemical structure of PCPDTBT. (With permission from John Wiley and Sons)

PLQY changes

When CPs are precipitated into nanoparticulate form, the photoluminescence quantum yield (PLQY) typically decreases strongly when compared to emission from fully solvated polymer chains in organic solvents. For example, Dailey and co-workers reported a 10-50 folds decrease

of the PLQY of PCPDTBT@PLGA-PEG CPNs when compared to PCPDTBT dissolved in THF. The same authors, also report that the choice of stabilizing copolymer can influence the degree to which this happens. For example, a three- to five- fold improvement in the PLQY of their CPNs could be achieved by replacing the PLGA-PEG copolymer with PEG_{2K}-DPPE during the nanoprecipitation process.[50] That being said, the choice of the solubilizing copolymer is not the only factor to determine the optical performance of the CPNs - variations in the fabrication procedure have also shown to be a factor. To this fact, Dailey and co-workers found that even the same CPs encapsulated within the same copolymer matrix exhibit different optical properties, when prepared through different manufacturing procedures.[54] Specifically, they compared the use of a microfluidic technique and a conventional solvent displacement method to manufacture CN-PPV and F8BT CPNs stabilized by the PEG_{5K}–$PLGA_{55K}$ copolymers. Their key observations were that the solvent displacement method produced smaller NPs (75–200 nm) than the microfluidic method (140–260 nm), with a corresponding trend in the PLQY of the prepared CPNs (the microfluidic technique produces CPNs of consistently higher PLQYs).[54] Most likely, this is a direct relation, with the smaller PLQYs of smaller NPs being a result of increased contortion of the polymer chains, leading to increased interchain interactions and/or aggregate formation due to tighter packing of chains.

When it comes to optimization of fluorescence properties via an appropriate selection of stabilizing copolymer, PSMA deserves a particular mention. In general, its addition to the nanoparticle composition at the right copolymer: conjugated polymer ratio will result in an improvement of the PLQY of the CPNs, when compared to bare CPNs, prepared in the absence of any stabilizing molecule.[63] However, use of other copolymers, such as F127, has been shown to result in better improvements of the emission properties, as was shown for MEH-PPV and PTB7 CPNs.[78] In their work, Peng Liu *et al.* stipulated that the hydrophobic ends of PSMA are able to interpenetrate the CPs chains, reducing the contact between individual chains and, in their case, reducing the energy transfer between the donor and acceptor units.[63] It is likely that similar effect is responsible for reduced fluorescence from CPNs characterized by H-aggregate emissions (which partially rely on interchain interactions). It is possible that a similar phenomenon is causing a decrease in fluorescence in CPNs that exhibit H-aggregate emissions, which are dependent on interchain interactions. In H-aggregates, the nearest-neighbor chromophores are oriented in a more face-to-face manner, resulting in the characteristic signature of increased exciton formation arising from interchain chromophore coupling in conjugated polymer systems.[82]

Photostability after encapsulated with copolymer

Excellent photostability of CPN suspensions in an aqueous medium is crucial clinical applications involving continuous irradiation of probes over extended periods of time, which include imaging of tissues and phototherapy. Yet, few reports can be found of any investigations of the photostability of CPN suspensions in the literature. The few examples that do exist, however, are promising in that most report excellent photostability of CPNs when stabilized by any copolymers. For example, upon a continuous laser excitation at 458 nm (5mW) over 10 minute period, the fluorescence intensity of PSMA-encapsulated EBKCP CPNs decreased by only 10%.[61] Liu and co-workers investigated the *in vitro* photostability of PFV@PLGA CPNs by continuous laser excitation at 405 nm for 20 mins during cell imaging, and detected no observable changes in the levels of the bright green fluorescence from the CPNs.[70] A similar observation was also made by Neumann *et al.* for PEG-PLGA-stabilized PCPDTBT CPNs when used for imaging of a phantom mouse, who report a less than 20% decrease in the signal-to-noise ratio after total irradiation time of approximately 100 hours.[50] The limited number of detailed investigations of the photostability of CPNs stabilized by different copolymers make it difficult to draw any conclusions as to any dependencies that may exist between the two. Table 1.2 provides a summary of physicochemical properties of bare and shelled CPNs, including the absorption and PL peaks position, PLQY, DLS size and ζ-potential information.

Table 1.2 comparison of physicochemical properties of bare and shelled CPNs

Core material	Shell	ABS peaks positions (nm)	PL peaks positions (nm)	QY if states (%)	Size (nm)	ζ-potential (mV)	Reference
F8BT	Bare	460 in THF	535 in THF	52-54	/	/	54
	PEG	494	539	31	207	/	71
	PEG_{5K}–$PLGA_{55K}$	470	538	37 ± 1	105	−4 to −10	54
Poly[9,9-bis(2-ethylhexyl)fluorene]	Bare	375	420	19	/	/	79
	PEI-PCL-PEG-FA	375	420	33	100	30	79
PFPtTFPP	PSMA	375	651	3.3/9	21	-33.4	75
PFP	PS-PEG-COOH	375	425	/	/	/	83
PFQ	PS-PEG-COOH	400	500	/	/	/	83
PFBT	PS-PEG-COOH	470	560	/	/	/	83
	PLGA	/	560	/	242.9	-33.4	70
PFBO	PS-PEG-COOH	550	603	/	/	/	83
DPP-TT	$DSPE\text{-}mPEG_{5K}$	720	1100	/	90	/	84
PTPEDC	DSPE-PEG-Mal	310	650	PTPEDC1: 11.9 ± 0.9 ; PTPEDC2: 3.1 ± 0.4	30	PTPEDC 1:-44.2; PTPEDC 2:-46.6; PTPEDC 1-Tat:-2.5; PTPEDC 2-Tat:-6.6	81
PDPP-DBT	DSPE-PEG-Mal	750	822	<0.1	100	CPNs:−34.4 ± 1.8 ; CPNs-Tat:23.1 ± 1.7	80

Table 1.2 (continued).

Core material	Shell	ABS peaks positions (nm)	PL peaks positions (nm)	QY if states (%)	Size (nm)	ζ-potential (mV)	Reference
PFBT	Bare	460	540	22	29	−22 ± 6	85
	PS-PEG-COOH	460	540	30	15	/	47
	PSMA	455	540	28	15	/	37
PFODBT	Bare	535	705	2.8	31	−25 ± 5	85
	DPPC	535	695	2.5	35	−36 ± 7	85
CP1-4	Bare	816/810/790/750	/	/	/	/	86
	PSMA	/	/	/	49	/	86
pDA	DSPE-mPEG	654	1047	2	<6	/	87
SP2	DSPE-mPEG$_{2K}$	660/635/712/748	835	10/0.5/1/0.1	46	/	88
PBIBDF-BT	Bare	811	/	/	/	/	89
	mPEG-b-PHEP	811	/	/	50	/	89
	PEG-PCL	782	/	/	156.2	/	67
PCPDTBT+PC70BM	PEG-b-PPG-b-PEG	650	840	/	54.33	/	90
PFVBT	Bare	365/502	612	/	/	/	91
	PEG(N_3 -PEG-NH_2)	502	598	/	120±11	/	92
PIDTTTQ	Bare	620 – 1100	/	/	/	/	91
PFVBT+PIDTTTQ	DSPE-PEG$_{2K}$-Mal	500	612	23 ± 1	34 ± 0.9	/	91
PBTB	Bare	635	/	/	/	/	76
	F127	330 and 500	420 and 653	/	192	-12.0	76
PFTBT5	PSMA	365	650	/	13	/	59
PFO	Bare	385	419	/	/	/	93
	F127	380	439	63	105-142	/	93
	PSMA	375	430	/	10	/	59
PtTFPP	Bare	390	650	/	/	/	69
	PEG	390	650	M_1:15.9 , M_2:11.4 , M_3: 6	M_1:203.8, M_2:89.3, M_3:400	/	69
PtTFPP + PFO	Poly-L-lysine	440	650	/	110	53 for Pt-NPs, 45 for ICG-Pt-NPs with ICG	94
Polyelectrolyte	PEG(N_3 -PEG-NH_2)	375 and 505	640	P2: 1 P3: 12 P4: 11	130	/	46
HCPE	PEG(N_3 -PEG-NH_2)	P1: 355 P2: 361	P1: 409 P2: 415	P1:40 P2:30	P1: 10.8 P2: 13	/	68
PFBD-N_3	Bare	315 and 463	530 in toluene, to 537 in THF, 549 in chloroform and 557 in dichloromethane	/	/	/	66
	PEG(N_3-PEG-COOH)	320 and 468	585	shelled with PFBD-PEG600-COOH:11 and shelled with PFBD-PEG2000-COOH:17	/	/	66
PFPE	Bare	340	375 and 393 400 and 419	/	/	/	93
	F127	345		76	99.6-137.4	/	93

Table 1.2 (continued).

Core material	Shell	ABS peaks positions (nm)	PL peaks positions (nm)	QY if states (%)	Size (nm)	ζ-potential (mV)	Reference
MEH-PPV	Bare	480 in THF	510 in THF 560 in	70 in THF	/	/	[78]
	Bare	498 in chloroform	chloroform 540 495	27 in chloroform	/	/	[64]
	PSMA	/	590	25	60-140	-30	[78]
	F127	/	590	35	40-80	-10	[78]
	F127	512		15	61	0	[64]
	PLGA	/		/	271.4	-35.3	[70]
PCPDTBSe	F127	PCPDTBSe @F127 nanoparticles abs=764nm ; PCPDTBSe @F127 nanofibers: 800nm	/	/	92	/	[65]
CN-PPV	Bare	450 in THF	550 in THF	52 in THF	/	/	[77]
	Bare	430 in THF	547 in THF	52 in toluene	/	/	[54]
	F127+TMOS	470	623	30	54.53 ± 3.4	-12	[77]
	PEG_{5K}–$PLGA_{55K}$	430	635	35	75	−8 to −11	[54]
PBMC	PSMA	417	558	2	43.96	−57.7	[32]
EBKCP	Bare	447 in THF	547 in THF	6 in THF	/	/	[61]
	PSMA	442	563	15	65	/	[61]
PCPDTBT	Bare	690 in THF	760 in THF	67.7 in THF	/	/	[56]
	PEG_{2K}–$PLGA_{4K}$	670	850	2.3	/	/	[56]
	PEG_{5K}–$PLGA_{55K}$	640	850	1.1	/	/	[56]
	PEG_{2K}-DPPE	650	850	7.5	/	/	[50]
	PEG_{2K}–$PLGA_{15K}$	650	850	0.6	/	/	[56]

1.4 Cell targeting and uptake

NPs are known to undergo increased cellular uptake and accumulation in tumour tissues as compared to normal tissues due to the EPR effect.[95] However, the EPR effect is heterogeneous amongst tumour types, and such tumour-dependent characteristics limit the usefulness of the EPR effects in bioapplication.[96] In the past, the use of CPNs functionalized with targeting entities resulted in better imaging contrast than relying on passive CPNs accumulation in the tumor *via* the EPR effect.[97] The reason for this is that cell adhesion and uptake of the NPs is strongly dependent on cell type, copolymer on the CPNs surface and the interaction of the two. A CPNs stabilized by a specific copolymer may have a strong affinity to some cells, have poor affinity to others or non-specifically adhere to almost any type of cells. In cases where CPNs naturally have poor affinity to specific cell types, additional functionalization can improve cell targeting and uptake; however, this can only be achieved if functional groups on the surface of the CPNs are available for further functionalization. Lack thereof would severely restrict the application of the developed CPNs in targeted imaging.[98] Incorporating different polymeric matrixes during CPNs preparation is an efficient method to introduce surface functional groups to facilitate their bioapplications[70], and this property is common amongst all four types of

copolymers under review here.

According to the articles reviewed, PSMA and PEG-based copolymers appear to be most suitable for general bioimaging applications, adhering naturally to most cell types and/or providing easy chemical routes for more specific targeting via click chemistry or carbodiimide reactions. On the other hand, CPs@F127 CPNs tend to have a much more selective cellular affinity, with strongly inhibited non-specific cellular uptake. As such, and as mentioned above, further modification of CPs@F127 CPNs has the potential to produce highly specific cellular probes for targeting cancerous tissues. In fact, the only reports of cell adhesion or internalization for F127-solubilized CPNs without any further modification have been for Hela cell line. For example, Lee and co-workers used PBTB@F127 CPNs for imaging of Hela cells, and concluded that their CPNs diffused into the cytoplasm of the cells.[76] Green and co-workers utilized MEH-PPV CPNs, encapsulated in silica-shell cross-linked F127 micelles, and observed bright fluorescence of these CPNs within Hela cells.[78] When considering cell targeting and uptake for CPNs, the use of copolymer PSMA as solubilizing shells presents an excellent opportunity since, during the formation of CPNs in water, the maleic anhydride units of the PSMA are hydrolyzed, generating carboxyl groups. Using standard carbodiimide chemistry, these readily available carboxyl groups can then be reacted with the amine groups on antibodies, affording desired CPNs-antibody conjugates. For example, this strategy was successfully implemented by Wang *et al.* to achieve targeting of specific cell lines, depending on the antibodies they have attached (anti-EpCAM or anti-ErbB2) and the level of expression of corresponding antigens by the tested cell lines (SK-BR3, MCF-7 and HeLa).[57] Via the same route, Sun and co-workers functionalized PSMA-solubilized CPNs of PFO and PFTBT5 CPs with streptavidin, for use in super-resolution fluorescence imaging. They found that the resulting CPNs could specially target specific subcellular structures with high labelling density in BS-C-1 cells, including mitochondrial outer membranes, cytoskeleton microtubule filaments, and clathrin-coated vesicles.[59]

Chanfeng Wu *et al.* took an alternative approach to exploiting the natural hydrolyzation of the PSMA in water – they employed the carbodiimide chemistry to first functionalize their CPNs with azido and alkyne groups *via* a reaction with corresponding variants of amino-terminated PEG. They then proceeded to use the copper (I)-catalyzed click chemistry reaction to attach a small amount of fluorophores to the CPNs, whose fluorescence could then be used for bioimaging. The functionalization of CPNs with azido and alkyne functional groups is significant, since they are considered to be biorthogonal, *i.e.* they have no inherent interactions with any native biological groups, providing enhanced selectivity in cell labeling

applications.[37]

In stark contrast to these works, lack of any modification of the carboxyl group of the PSMA has been associated with generally un-specific binding to cell membranes [63], or endocytosis-driven accumulation of CPNs in lysosomes[61].

The PEG-derived copolymers also offer several routes to achieve enhanced cellular internalization or specific targeting. A common approach is to employ common variants with easily reactable functional groups, and impose the specificity following a further conjugation step with a targeting element. For instance, Wang and co-workers developed CPNs of PDPP-DBT encapsulated with DSPE-PEG-Mal copolymer, and the maleimide groups terminated at the DSPE-PEG-Mal chain ends were then used to conjugate with a cell-penetrating peptide (Tat). The resulting CPNs were NIR-active, and possessed photothermal properties, which meant that they could effectively coat the surface of Hela cells and generate localized heat to trigger target gene expression.[80] Liu and co-workers also used the same copolymer DSPE-PEG-Mal modified with Tat to encapsulate PTPEDC to achieve two-photon excited photodynamic therapy in Hela cell.[81] The maleimide groups terminated at the DSPE-PEG-Mal chain ends have also been decorated with anti-HER2 affibody by Liu and co-workers, who synthesized CPNs based on PFVBT and PIDTTQ, and DSPE-PEG_{2K}-Mal and achieved superior selectivity towards tumour cells with HER2 overexpression.[91]

Other common PEG derivatives employed for the purposes of CPNs solubilization include PS-PEG-COOH. Similarly, to DSPE-PEG-Mal, PS-PEG-COOH can also be modified with Tat through a covalent link. Feng and co-workers developed multiple wavelength emission CPNs with different fluorene derivatives as a core and PS-PEG-COOH as an encapsulation matrix. To perform the biological applications, CPNs were further modified with Tat and successfully employed in fluorescence imaging of A549 cells.[83] Chiu and co-workers demonstrated bioconjugation of ultrabright Pdots for specific cellular targeting. They encapsulated PFBT in the PS-PEG-COOH matrix, and then further functionalized their Pdots with streptavidin *via* the EDC coupling reaction. The developed Pdots and the anti-EpCAM primary antibody were then sequentially incubated in MCF-7 cultures, to achieve effective and specific cell targeting.[47]

An interesting observation regarding the use of the PEG-derived copolymers is that the length of the PEG chain sems to be a factor that can influence the cell uptake efficiency.

Liu and co-workers compared the uptake of PFBD-PEG_{600}-COOH NPs and PFBD-PEG_{2K}-COOH NPs in MCF-7 cell cultures. They determined that PFBD-PEG_{2K}-COOH NPs (the larger of the two) were less efficiently taken up by cells, which significantly inhibited non-specific cellular uptake. Further modification of the surface to PFBD-PEG_{2K}-RGD endowed

the CPNs with specificity required for targeted cancer cell imaging.[66]

PLGA is widely used for preparing polymeric NPs and is reported to benefit the NPs–cell interaction and enhance cellular uptake efficiency.[99] PCPDTBT@PEG-PLGA CPNs and PCPDTBT@PEG-DPPE CPNs exhibited higher uptake by J774A.1 cell when the suspensions were incubated in advance with mouse serum which emphasized the important role of the protein corona (PC) formation on the NPs' surface during interactions with J774A.1 cell.[50] Among these CPNs, PCPDTBT@PEG-PLGA CPNs have a higher take-up degree than PCPDTBT@PEG-DPPE CPNs. Comparing the PCPDTBT@PEG_{2K}-$PLGA_{4K}$ CPNs and PCPDTBT@PEG_{5k}-$PLGA_{55k}$ CPNs, the uptake degrees are more or less the same.[50] The results suggest that, the choice of the copolymer type dictates the cell-particle interactions more than the molecular weight of the copolymer. The authors also reported that PCPDTBT@ PEG_{2K}–$PLGA_{4k}$ accumulated more rapidly in the liver, whilst PCPDTBT@PEG_{2k}-DPPE demonstrated a higher level of accumulation in tumour tissues and a longer plasma circulation half-life.[50] Few reports can be found detailing the biodistribution of CPNs in vivo, however, highlighting the need for further investigation in this field.

Protein corona

Once the CPNs are applied to the biological system and encounter the biological environment of the systemic circulation, the circulating proteins that bind to the CPNs surface are referred to as the PC.[100] PC plays an essential role in making the NPs easily recognized by the innate immune system and causing quick clearance by phagocytic cells.[100] But there is very limited research on the interaction of PC formed on CPNs surface with phagocytic cells.

Dailey and co-workers used CPNs of F8BT stabilized with ionic surfactants sodium dodecyl sulfate (SDS) or nonionic surfactants PEG and compared them with polystyrene NPs of a similar size (PS200).[71] They investigated the differences in PC formation after incubation with a serum-containing medium among the three samples and studied the biological performance of phagocytic J774A.1 macrophage cells. They found that all three NPs did not aggregate in DMEM/FBS over a 24 h incubation period, while F8BT@SDS and PS200 NPs aggregated after about four hours in serum-free DMEM and F8BT@PEG NPs remained stable over 24 h. As shown in Figure 1.4, they also noticed that unlike PS200 enrichment of several serum proteins onto the particle surface, F8BT CPNs did not enrich specific proteins onto the nanoparticle surface. F8BT@PEG CPNs showed the minimal (<5%) cell uptaken while that of F8BT@SDS CPNs is 20% and PS200 is 60%.[71] This phenomenon is consistent with the research that PEG reduces nanoparticle recognition by phagocytic cells through steric repulsion

effects and thus has a longer circulation time.[101]

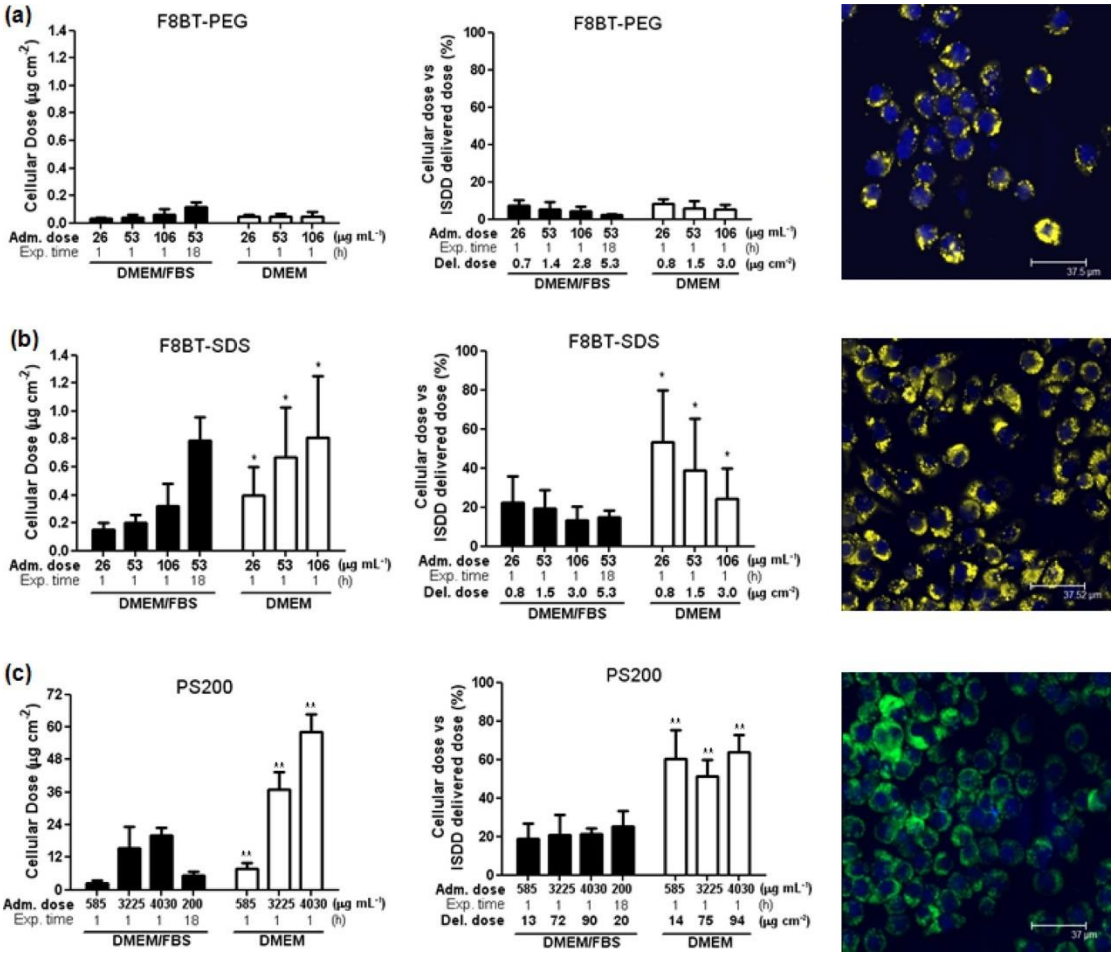

Figure 1.4 Cellular dose (left) and the cellular dose as a percentage of the ISDD delivered dose (center) are reported for seven different exposure scenarios: (a) F8BT-PEG, (b) F8BT-SDS, and (c) PS200. Exposure conditions are described on the abscissa and include administered dose (μg mL^{-1}), exposure time (h) and the corresponding ISDD delivered dose value (μg cm^{-2}). Data represent the mean ± SD of n = 4 independent experiments. (* $p < 0.05$, **<0.01, ***<0.001. The right panel depicts fluorescence micrographs of J774A.1 cells exposed to F8BT-PEG, F8BT-SDS and PS200 in DMEM/FBS (administered dose: 53, 53, and 200 μg mL^{-1}; incubation time: 18 h; ISDD delivered dose: 5.3, 5.3, and 20 μg cm^{-2}, respectively (Copyright 2015 American Chemical Society)

ζ-potential and size

ζ-potential and size of the CPNs play an essential role in influencing the interaction with cells. For example, charged polystyrene and iron oxide particles are taken up better than their uncharged counterparts by nonphagocytic cells.[102] Other studies have also indicated that the cellular uptake of NPs of 20-100 nm in diameter occurs mainly through caveolin-mediated endocytosis, while the cellular uptake of NPs of 100-350 nm size is primarily through clathrin-

mediated endocytosis.[103] Generally speaking, NPs in the size range of 15-260 nm can be taken up efficiently or stain the cellular membrane of different cell lines, whilst sizes smaller than 150 nm was preferable for live imaging in mice.[30]

One advantage of the CPNs as imaging probes is that their hydrodynamic sizes are tunable *via* the molecular weight of the copolymer chains. Hong and co-workers investigated tuning of the hydrodynamic size by coating pDA conjugated polymer with different DSPE-mPEG molecular weights (2 kDa and 5 kDa). The result shows that a shorter PEG chains favors the formation of smaller conjugated NPs in an aqueous solution.[87] As we mentioned previously, the most popular method to tune the size of micelles is changing the molar ratios of the hydrophobic and hydrophilic segments in the block copolymers.[69] The shorter PEG chains reduced hydrophilic ratio of the block copolymers.

Table 1.3 provides a summary of CPNs that have been utilized in cell experiments, in each case detailing the core material of the CPNs, the corresponding shell polymer, the cell lines in which they were tested and the class of applications for which they were used.

Table 1.3 CPNs used in cell lines

Cell Line	CPNs core material	Shell Polymer	Application	Reference
MCF-7	PFPtTFPP	PSMA	IMG	75
	P1-P4	PSMA	IMG	57
	PFVBT+PIDTTTQ	DSPE-PEG_{2K}-Mal	IMG	91
	PFVBT	N_3-PEG-NH_2	CT	92
	Polyelectrolyte	N_3-PEG-NH_2	IMG	46
	HCPE	N_3-PEG-NH_2	IMG	68
	PFBD-N_3	NH_2-PEG-COOH	IMG	66
	PFBT	PS-PEG-COOH	IMG	47
	PFBT	PSMA	IMG	37
	PF/PFV/PFBT/MEH-PPV	PLGA	IMG	70
U87 Glioma	P1 (BDT+BBT)	DSPE-PEG_{2K}	PA	104
	pDA	DSPE-mPEG	IMG	87
J774A.1	F8BT	PEG	CT	71
	PCPDTBT	PEG-PLGA	CT	56
KB	Poly[9,9-bis(2-ethylhexyl)fluorene]	PEI-PCL-PEG-FA	IMG/CT	79
A549	PFP/PFQ/PFBT/PFBO	PS-PEG-COOH	CT	83
HeLa	PTPEDC	DSPE-PEG-Mal	IMG	81
	PDPP-DBT	DSPE-PEG-Mal	CT	80
	P1-P4	PSMA	IMG	57
	PCPDTBT+PC70BM	PEG-b-PPG-b-PEG	CT	90
	PBTB	F127	CT	76
	MEH-PPV	F127	IMG	78
	MEH-PPV	PSMA	IMG	78
	CN-PPV	F127 + TMOS	IMG	77
	CN-PPV	PEG-PLGA	IMG	55
	PBMC	PSMA	CT	74
	DPSB unit (S2 and M2)	PSMA	IMG	63
	Sol.(incorporating π-extended boron ketoiminate units) EBKCP	PSMA	IMG/CT	61
	DPP-TT	DSPE-$mPEG_{5K}$	IMG	84
	PFTBT5+PFO	PSMA	CT	59
SK-BR-3	P1-P4	PSMA	IMG	57
	PFVBT+PIDTTTQ	DSPE-PEG_{2K}-Mal	IMG	91
	PFBT	PS-PEG-COOH	IMG	47

Table 1.3 (continued).

Cell Line	CPNs core material	Shell Polymer	Application	Reference
NIH 3T3	SP2	PEG-b-PPG-b-PEG	CT	105
	PFVBT+PIDTTTQ	DSPE-PEG_{2K}-Mal	IMG	91
	Polyelectrolyte	N_3-PEG-NH_2	IMG	46
	HCPE	N_3-PEG-NH_2	CT	68
	DPP-TT	DSPE-$mPEG_{5K}$	CT	84
	PF/PFV/PFBT/MEH-PPV	PLGA	IMG	70
	DPSB unit (S2 and M2)	PSMA	IMG	63
4T1	CP	PSMA	CT	86
	Donor (BT)-Acceptor (BIBDF)	PEG-PCL	CT	67
	CP1-CP4	DSPE-$mPEG_{2K}$	CT	106
MDA-MB-468	pDA	DSPE-$mPEG_{5K}$	IMG	87
MDA-MB-231	PBIBDF-BT	mPEG-b-PHEP	IMG	89
	PFVBT	N_3-PEG-NH_2	IMG	92
BS-C-1	PFTBT5+PFO	PSMA	IMG	59
Ramos	PtTFPP	PEG	CT	69
HepG-2	PtTFPP + PFO	Poly-L-lysine	IMG/CT	94
	DPSB unit (S2 and M2)	PSMA	IMG/CT	63
HT 29	PFBD-N_3	NH_2-PEG-COOH	IMG/CT	66
HCE	MEH-PPV	PSMA	IMG	78
	MEH-PPV	F127	CT	78
HEK 293	MEH-PPV	PSMA	CT	78
	CN-PPV	F127 + TMOS	IMG/CT	77
FHs 74 Int.	PCPDTBSe	F127	CT	65
CT-26	PCPDTBSe	F127	IMG/CT	65
WPE1-NB26	CN-PPV	F127+TMOS	IMG	77
WPE1-NA22	CN-PPV	F127+TMOS	IMG	77
RWPE-1	CN-PPV	F127+TMOS	IMG	77

* IMG = confocal imaging; CT = cytotoxicity; PA= photoacoustic imaging

1.5 Multimodal capacity

Several CPNs-based systems, stabilized by various copolymers, have been investigated for multimodal applications, including those that incorporated photo-activated therapeutic modalities. Here, some of these reports are reviewed, with a specific emphasis on the modification of PTT and PDT properties of CPNs upon the addition of copolymer as a solubilizing shell.

Improvement of PTT properties upon addition of shells

A single report exists, comparing the PTT properties of bare and copolymer-solubilized CPNs, making it impossible to draw any conclusions as to any possible dependencies. Interestingly, however, the same study suggests that the PTT properties of CPs materials might depend on their shape. As shown in Figure 1.5, Levi-Polyachenko and co-workers compared the photothermal performance of PCPDTBSe NPs shelled with F127 and PCPDTBSe nanofibers shelled with F127 to that of PCPDTBSe NPs without F127. The results showed that at lower concentration (10 μg/ml), PCPDTBSe nanofibers with F127 showed the most remarkable increment in temperature. At a higher concentration (100 μg/ml), PCPDTBSe NPs with F127

showed a much higher temperature (47°C), while the other two NPs showed a similar change in temperature (35°C). They conclude that PCPDTBSe NPs and PCPDTBSe nanofibers coated with F127 outperform bare PCPDTBSe NPs in generating more significant heat to destroy colorectal cancer cells, but that the shape of NPs, as well as the concentration, can also influence the photothermal capacity of the CPNs.[65] The influencing factor of shape on PTT performance does not only exist in CPNs; other kinds of NPs such as gold NPs also observed the same shape dependency, although likely owing to different photophysical phenomena.[107]

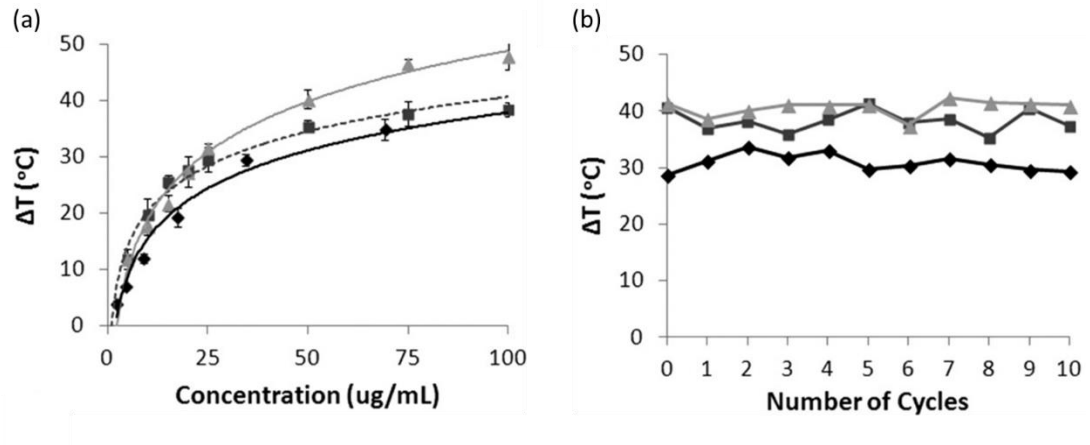

Figure 1.5 (a) A comparison of the heating efficiency and (b) heating reproducibility curves for bare PCPDTBSe NPs (black diamond), PW-PCPDTBSe NPs (grey triangles) and PW-PCPDTBSe nanofibers (dark grey squares). The concentration for heating reproducibility curves was 50 µg/mL of each different nanomaterial. Laser parameters were 3 W and 1 min for both. Error bars are shown as standard deviation of the mean. (with permission from John Wiley and Sons)

Improvement of PDT properties upon addition of copolymers

According to the reports reviewed as part of this literature review, there is no consistent usage of PSMA-solubilized CPNs for multimodal applications involving PDT. In view of the relatively small number of reports employing CPNs for PDT applications, and the majority of these focusing on PDT *via* generation of singlet oxygen, PSMA might still be a suitable solubilization candidate for development of PDT probes. Most likely, such implementation would have to rely on generation of other ROS instead of singlet oxygen.

The ability of F127-shelled CPNs to successfully produce singlet oxygen has also been reported by Choongho Kim *et al*.[108] for PBTB-based CPNs. Since singlet oxygen is produced via a triplet-triplet energy transfer between the photosensitizer and ground state molecular oxygen, it follows that F127 promotes such photophysical processes. Further reports also show that

F127 can boost photoinduced electron transfer (PET) processes, leading to improved sensitivity of PET-based chemical sensors (see Section 1.7).

PEG-based amphiphilic copolymers are the most widely used class of stabilizing copolymers for biological applications, which include bioimaging, photothermal and photodynamic therapy. Liu and co-workers fabricated multifunctional lipid-micelles which comprised of PCPDTBT and Ce6 molecules inside as core and a lipid–PEG out layer conjugated with gadolinium-1,4,7,10-tetraacetic acid. The prepared CPNs had excellent MR- and PA-imaging contrast-enhancement ability and simultaneous combined photothermal and photodynamic therapy.[109] DSPE-PEG is widely used to achieve imaging-guided photothermal therapy while exhibiting excellent biocompatibility,[84] and encapsulated with conjugated polymers for in vivo photoacoustic imaging.[88,104]

Developing multifunctional cellular probes with high selectivity has great significance in biological applications. PEG-based amphiphilic copolymers with different end groups that can be modified have been widely used to achieve targeted applications. For example, Liu and co-workers utilized copolymer N_3-PEG-NH_2, in which the -N_3 end is conjugated to conjugated polymer PFVBT while the -NH_2 end is modified with FA to develop cellular probe.[46] And the same, the group also utilized the -NH_2 end connected to doxorubicin to achieve photodynamic and chemo-therapies at the same time.[92] PEG copolymers have also been used in Donor-Acceptor-type CPNs, resulting in CPNs with excellent resistance to photobleaching when applied to PDT and PTT simultaneously.[67] (Table 1.4)

Unfortunately, the number of reports on the use of CPNs for PDT or PTT applications are still very few. As such, no conclusive evidence exists for the advantageous use of a specific copolymer when designing multi-modal probes.

Table 1.4 provides an overview of different reports investigating CPNs potential as PDT agents *via* characterization of their photosensitizing ability. Included in the table are core and shell materials of the CPNs tested, the methods using which photosensitization was investigated, the wavelength of irradiation used in the tests and the ROS species detected.

Table 1.4 CPNs used in PDT

CPN Core Material	Shell Polymer	Study	Irradiation Wavelength	ROS Detected	Reference
PTPEDC	DSPE-PEG-Mal	ABDA	400−700 nm, 50 mW/cm^2	singlet oxygen	81
		DCFDA (in solution)	400-700 nm, 50 mW/cm^2	singlet oxygen	81
PFVBT	DSPE-PEG$_{2K}$-Mal	DCFH/ABDA	white light irradiation (0.25W/cm^2) for minutes	singlet oxygen	91
		DCFDA	30 s white light irradiation, 0.25 W/cm^2	singlet oxygen	91
Donor (BT)-Acceptor (BIBDF)	PEG-PCL	DPBF+ESR	785 nm, 1.5 W/cm^2	singlet oxygen	67
		DHE	785 nm, 1.5 W/cm^2	singlet oxygen	67
PBTB	F127	RNO	254 nm,2 W/cm^2	singlet oxygen	76
		DCFDA	254 nm,100 mJ/cm^2	singlet oxygen	76
PtTFPP	Poly-L-lysine	ADMA+DPBF	540 nm and 405 nm, 0.03 and 0.06 W/cm^2	singlet oxygen	94
		MTT	740 nm, 3.0 W/cm^2	singlet oxygen	94
CP1-CP4	DSPE-mPEG$_{2K}$	ABDA	400-700 nm, 60 mW/cm^2	singlet oxygen	106
		DCFDA/PI/MTT	400-700 nm, 60 mW/cm^2	singlet oxygen	106

*** SOSG= singlet oxygen sensor green; ABDA= 9,10-anthracenediyl-bis(methylene) dimalonic acid； DHE= dihydroethidium**

1.6 Biocompatibility and cytotoxicity

Cellular uptake, body distribution, and clearance are affected by CPNs' size and surface properties.[110] Previous works show that the type of surfactants used for CPNs preparation plays an essential role in biocompatibility and PC formation.[56] After administration, the surface of NPs can interact with biomacromolecules in the physiological environment and form PC due to adsorption.[111] More specifically, the protein adsorption is dependent on the size, composition and charge of the NPs surface. Compared to the cationic and anionic systems, NPs with a neutral surface charge tend to show more negligible protein adsorption and lower non-specific cellular uptake and an increased circulation time.[112,113]

Although positively charged particles were generally taken up better than negatively charged ones, cationic NPs tend to have more significant cytotoxicity as cationic NPs appear to cause plasma-membrane disruption to a greater extent.[102] Although the ζ-potential of CPNs is primarily determined by CPs itself, the choice of stabilizing copolymer is an important variable in this aspect (see Table 1.2 in section of photostability after encapsulated with copolymer. This provides a viable route to optimize the ζ-potential of CPNs for a specific application through

an appropriate choice of stabilizing copolymers. For instance, Li Liu *et al*. continuously varied the ζ-potential of Poly[9,9-bis(2-ethylhexyl)fluorene]@PEI-PCL-PEG CPNs from -40 mV to 30 mV via coating of their CPNs with a cationic folate-conjugate. They observed that cytotoxicity of the CPNs increased in line with ζ-potential increases, which they ascribed to increased disruption within cells.[79] This report highlights the careful interplay between many different parameters that determine the suitability of the probe for a specific application, which can be influenced by the choice of the copolymer and its subsequent functionalization: the functionalization of the probe with a targeting element endows it with a specificity that is required for bioimaging applications; however the same process results in increased cytotoxicity of the probe.

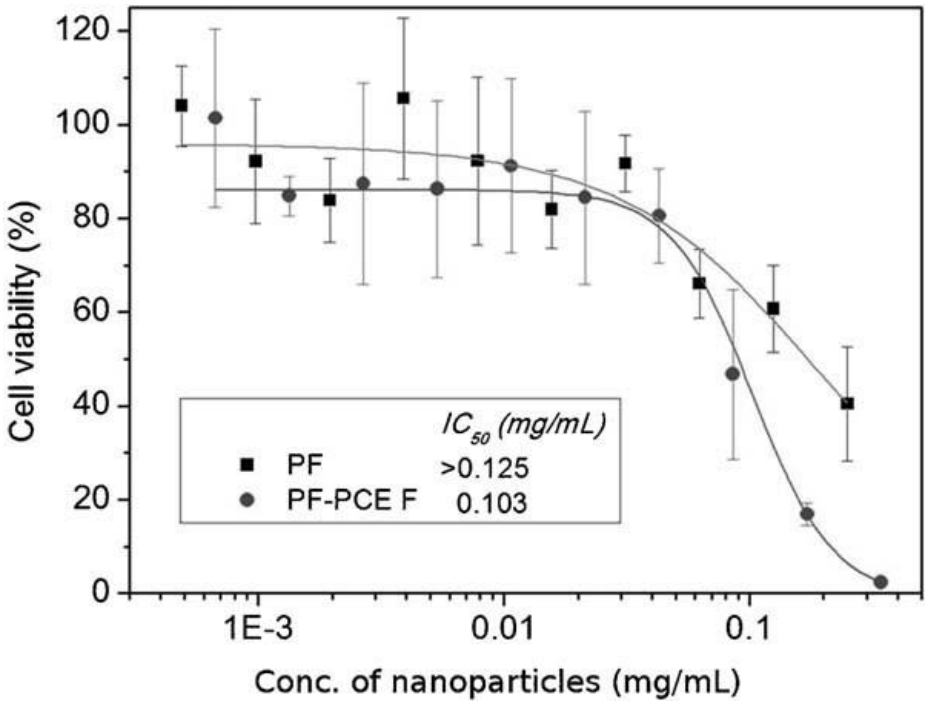

Figure 1.7 Cell viability of PCE-F coated PF-NPs on KB cells compared with unmodified PF-NPs. (with permission from John Wiley and Sons)

Dailey and co-workers found that, coating CN-PPV or F8BT CPs with a PEG_{5K}–$PLGA_{55K}$ copolymer did not cause any changes in the size and optical properties of the CPs, however the addition of the copolymer did provide a neutral net electrical charge to the nanoparticle surface, which is beneficial for biomedical applications.[54]

In a related work, and as shown in Figure 1.8, CN-PPV encapsulated with PLGA-PEG with different ratios (system abbreviation) and encapsulated small amounts (0.5–0.8% w/w) of small molecule NIR dyes, NIR680 and NIR720, showed excellent biocompatibility when used on

Hela cell cultures. On the other hand, the use of PLGA-PEG copolymer seemed to increase the percentage of cell population with impaired mitochondrial activity.[55]

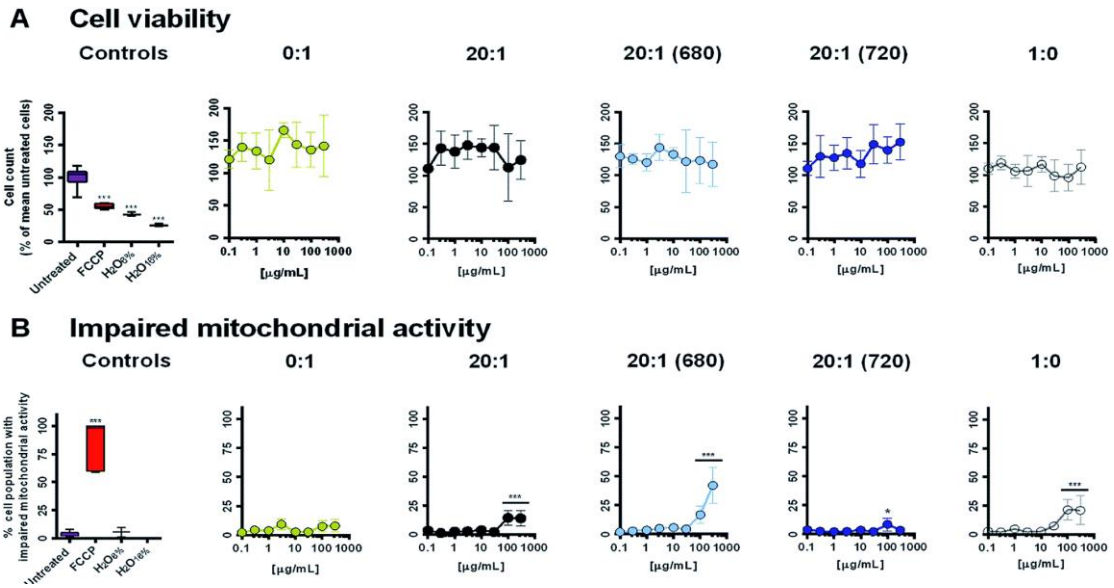

Figure 1.8 (A) THP-1 cell count per well after incubation for 24 h with various treatments. (B) Percentage THP-1 cell population with impaired mitochondrial activity (defined as a MitoTracker Red fluorescence intensity <2000 a.u.). Values represent the mean ± standard deviation from n = 3 experiments with different THP-1 passage numbers. (with permission from the Royal Society of Chemistry)

In search for a copolymer that minimizes cytotoxicity, F127 seems to have a unique advantage in providing CPNs with good biocompatibility. Green and co-workers synthesized MEH-PPV encapsulated by F127 and PSMA, and found that F127 had lower cytotoxicity compared to those encapsulated by PSMA.[78] Different shapes of CPNs that both PCPDTBSe NPs and PCPDTBSe nanofibers coated with F127 showed different physicochemical properties, but all appeared to not have any significant dark toxicity towards either CT26 cancer cells or FHs 74 noncancerous cells, confirming their good biocompatibility.[65] In line with previous discussions of further modification being an important factor in determining CPNs biocompatibility, further doping of F127 can equally affect the biocompatibility of the CPNs. For example, in their work Green and co-workers observe tolerated cytotoxicity in HEK cells caused by low concentrations of CN-PPV CPNs encapsulated with silica-shell cross-linked F127, with the toxicity increasing to lethal at high probe concentration.[77]

1.7 Conclusions and outlook

In summary, CPNs solubilized with copolymers present a promising and an exciting class of materials for development of theranostic probes. This chapter considered the effects of different

solubilizing copolymers on the physical and chemical properties and biological applications of CPNs. In general, the literature confirms that CPNs show minimal toxicities that can be tuned via appropriate selection of solubilizing copolymer and their further functionalization; as such, they present prominent advantages over other NPs in biological applications. However, it is also clear that copolymer selection is also crucial in determining many of the physicochemical properties of CPNs, including their water dispersibility, size, surface potential, photo- and colloidal stability, optical properties, cellular endocytosis, cell targeting and cell imaging, PC formation and blood circulation time, changes in photodynamic and photothermal properties and the above mentioned biocompatibility.[26,47,54,56,62,77,78] The interrelations between these parameters are complex and sometimes coupled in opposing or complementary trends. When combined with the limited literature exploring these exact interrelations and how they are affected by a range of different copolymers, it becomes difficult to draw concrete conclusions. Some general themes do emerge, however.

For drug delivery and *in vivo* biological applications, PEG is the most suitable copolymer because it can inhibit the fast recognition of foreign bodies by the immune system, leading to a longer blood circulation time. The use of F127 copolymer offers generally excellent biocompatibility and an ability to enhance charge and energy transfer processes, such as those that may be required for PDT applications. PSMA, on the other hand, has (unspecific) affinity to many different cell types and easily accessible carboxyl groups available for further functionalization if specificity needs to be achieved. However, there are no studies regarding the use of PSMA for single oxygen-based PDT, which leads to a hypothesis that PSMA may inhibit the photoinduced generation of $^1O_2$ from CPs or, more broadly, that many of the properties of CPNs that are critical to their biological applications are determined by the stabilizing copolymer shell if not its interaction with the conjugated polymer core. This hypothesis forms one of the main themes of this thesis, investigated using a model, theranostic NIR-active CPNs system, shelled with either F127 or PSMA as amphiphilic copolymers. One of the main goals of this approach was to develop an understanding of how each copolymer affected the performance of the fabricated CPNs and the underlying effects that are responsible for any differences in the performance.

In addition to these investigations, methods for optimization of CPNs synthesis were developed, which were based on the understanding of interactions between the copolymers and conjugated polymers. The developed methods allowed the fabrication of CPNs with enhanced optical and photosensitizing performance.

Finally, investigations into the unspecific binding of developed CPNs and their cell affinity to

different cell cultures were also performed, leading to the conclusion that the two properties are strongly influenced by the selection of the copolymer material, typically either enhancing or suppressing both processes. In the case of F127-shelled CPNs, which offered low degree of unspecific binding yet extremely low affinity to many cell lines, a tumor-targeting modification of the CPNs surface was successfully performed enduing them with a high specificity to FA-expressing cell lines.

1.8 References

1. Lucky, S. S. *et al.* Nanoparticles in photodynamic therapy. *Chem. Rev.* **115**, 1990–2042 (2015).

2. Early detection of cancer. *https://www.who.int/cancer/detection/en/*.

3. Xing, J. *et al.* Research advances in integrated theranostic probes for tumor fluorescence visualization and treatment. *Nanoscale* **12**, 24311–24330 (2020).

4. Dougherty, T. J. *et al.* Photodynamic therapy. *J. Natl. Cancer Inst.* **90**, 889–905 (1998).

5. Correia, J. H. *et al.* Photodynamic therapy review: principles, photosensitizers, applications, and future directions. *Pharmaceutics* **13**, (2021).

6. Hayyan, M. *et al.* Superoxide Ion: Generation and chemical implications. *Chem. Rev.* **116**, 3029–3085 (2017).

7. Liou, G. Y. & Storz, P. Reactive oxygen species in cancer. *Free Radic. Res.* **44**, 479–496 (2010).

8. Trachootham, D. *et al.* Targeting cancer cells by ROS-mediated mechanisms: a radical therapeutic approach? *Nat. Rev. Drug Discov.* **8**, 579–591 (2009).

9. Nogueira, V. *et al.* Akt determines replicative senescence and oxidative or oncogenic premature senescence and sensitizes cells to oxidative apoptosis. *Cancer Cell* (2008).

10. Dolmans, D. E. J. G. J. *et al.* Photodynamic therapy for cancer. *Nat. Rev. Cancer* **3**, 380–387 (2003).

11. Anand *et al.* Biomodulatory approaches to photodynamic therapy for solid tumors. *Cancer Lett.* **326**, 8–16 (2012).

12. Agostinis, P. *et al.* Photodynamic therapy of cancer. *CA A Cancer J. Clin.* **61**, 250–281 (2011).

13. Castano, A. P. *et al.* Photodynamic therapy and anti-tumour immunity. *Nat. Rev. Cancer* **6**, 535–545 (2006).

14. Ji, B., Wei, M. & Yang, B. Recent advances in nanomedicines for photodynamic therapy (PDT)-driven cancer immunotherapy. *Theranostics* **12**, 434–458 (2022).

15. Hua, J. *et al.* Current strategies for tumor photodynamic therapy combined with immunotherapy. *Front. Oncol.* **11**, 738323 (2021).

16. Hashizume, H. *et al.* Openings between defective endothelial cells explain tumor vessel leakiness. *Am. J. Pathol.* **156**, 1363–1380 (2000).

17. Hu, L. *et al.* Metal-based quantum dots: synthesis, surface modification, transport and fate in aquatic environments and toxicity to microorganisms. *RSC Adv.* **6**, 78595–78610 (2016).

18. Kim, H. S. & Lee, D. Y. Near-infrared-responsive cancer photothermal and photodynamic therapy using gold nanoparticles. *Polymers (Basel).* **10**, 1–14 (2018).

19. Pu, K. Y. & Liu, B. Optimizing the cationic conjugated polymer-sensitized fluorescent signal of dye labeled oligonucleotide for biosensor applications. *Biosens. Bioelectron.* **24**, 1067–1073 (2009).

20. Kilin, V. N. *et al.* Counterion-enhanced cyanine dye loading into lipid nano-droplets for single-particle tracking in zebrafish. *Biomaterials* (2014).

21. Zhu, C. *et al.* Water-soluble conjugated polymers for imaging, diagnosis, and therapy. *Chem. Rev.* **112**, 4687–4735 (2012).

22. Duan, X. *et al.* Cationic conjugated polymers for optical detection of DNA methylation, lesions, and single nucleotide polymorphisms. *Acc. Chem. Res.* **43**, 260–270 (2010).

23. Wu, C. & Chiu, D. T. Highly fluorescent semiconducting polymer dots for biology and medicine. *Angew. Chemie - Int. Ed.* **52**, 3086–3109 (2013).

24. Gesquiere, A. J. *et al.* Conjugated polymer nanotherapeutics for next generation photodynamic t herapy. *Med. Res. Arch.* **6**, 1–23 (2018).

25. Qian, C. G. *et al.* Conjugated polymer nanomaterials for theranostics. *Acta Pharmacol. Sin.* **38**, 764–781 (2017).

26. Li, K. & Liu, B. Polymer encapsulated conjugated polymer nanoparticles for fluorescence bioimaging. *J. Mater. Chem.* **22**, 1257–1264 (2012).

27. Mora-Huertas, C. E. *et al.* Influence of process and formulation parameters on the formation of submicron particles by solvent displacement and emulsification-diffusion methods: Critical comparison. *Adv. Colloid Interface Sci.* **163**, 90–122 (2011).

28. Nagavarma, B. V. N. *et al.* Different techniques for preparation of polymeric nanoparticles- A review. *Asian J. Pharm. Clin. Res.* **5**, 16–23 (2012).

29. Ye, X. *et al.* Fluorescent nanomicelles for selective detection of Sudan dye in pluronic F127 aqueous media. *ACS Appl. Mater. Interfaces* **6**, 5113–5121 (2014).

30. Abelha, T. F. *et al.* Conjugated polymers as nanoparticle probes for fluorescence and photoacoustic imaging. *J. Mater. Chem. B* **8**, 592–606 (2020).

31. Tuncel, D. & Demir, H. V. Conjugated polymer nanoparticles. *Nanoscale* **2**, 484–494 (2010).

32. Gao, Z. yan *et al.* Conjugated polymer nanoparticles based on carbazole for detecting ferric ion (III) with a large Stokes shift and high sensitivity and the application in cell imaging. *Dye. Pigment.* **168**, 68–76 (2019).

33. Pitto-Barry, A. & Barry, N. P. E. Pluronic® block-copolymers in medicine: From chemical and biological versatility to rationalisation and clinical advances. *Polym. Chem.* **5**, 3291–3297 (2014).

34. Acharya, S. & Sahoo, S. K. PLGA nanoparticles containing various anticancer agents and tumour delivery by EPR effect. *Adv. Drug Deliv. Rev.* **63**, 170–183 (2011).

35. Kamaly, N. *et al.* Targeted polymeric therapeutic nanoparticles: design, development and clinical translation. *Chem. Soc. Rev.* **41**, 2971–3010 (2012).

36. Jung, Y. *et al.* Encapsulating light-emitting polymers in block copolymer micelles. *Langmuir* **26**, 7540–7543 (2010).

37. Wu, C. *et al.* Ultrabright and bioorthogonal labeling of cellular targets using semiconducting polymer dots and click chemistry. *Angew. Chemie - Int. Ed.* **49**, 9436–9440 (2010).

38. Alexander, S. *et al.* Growth and shrinkage of pluronic micelles by uptake and release of flurbiprofen: Variation of pH. *Langmuir* **28**, 6539–6545 (2012).

39. Nguyen, P. M. *et al.* Extended release antibacterial layer-by-layer films incorporating linear-dendritic block copolymer micelles. *Chem. Mater.* **19**, 5524–5530 (2007).

40. Bae, K. H. *et al.* Oil-encapsulating PEO-PPO-PEO/PEG shell cross-linked nanocapsules for target-specific delivery of paclitaxel. *Biomacromolecules* **8**, 650–656 (2007).

41. Hartono, S. B. *et al.* Poly-L-lysine functionalized large pore cubic mesostructured silica nanoparticles as biocompatible carriers for gene delivery. *ACS Nano* **6**, 2104–2117 (2012).

42. Parray, Z. A. *et al.* Amphiphilic nature of polyethylene glycols and their role in medical research. *Polym. Test.* **82**, 106316 (2020).

43. Wu, J. *et al.* Binding characteristics between polyethylene glycol (PEG) and proteins in aqueous solution. *J. Mater. Chem. B* **2**, 2983–2992 (2014).

44. Zalipsky, S. & Menon-Rudolph, S. Hydrazide derivatives of poly(ethylene glycol) and their bioconjugates. in *Poly(ethylene glycol)* vol. 680 21–318 (American Chemical Society, 1997).

45. Locatelli, E. & Comes Franchini, M. Biodegradable PLGA-b-PEG polymeric nanoparticles: synthesis, properties, and nanomedical applications as drug delivery system. *J. Nanoparticle Res.* **14**, 1316 (2012).

46. Pu, K. Y. *et al.* A molecular brush approach to enhance quantum yield and suppress nonspecific interactions of conjugated polyelectrolyte for targeted far-red/near-infrared fluorescence cell imaging. *Adv. Funct. Mater.* **20**, 2770–2777 (2010).

47. Wu, C. *et al.* Bioconjugation of ultrabright semiconducting polymer dots for specific cellular targeting. *J. Am. Chem. Soc.* **132**, 15410–15417 (2010).

48. Makadia, H. K. & Siegel, S. J. Poly lactic-co-glycolic acid (PLGA) as biodegradable controlled drug delivery carrier. *Polymers (Basel).* **3**, 1377–1397 (2011).

49. Muthu, M. S. Nanoparticles based on PLGA and its co-polymer: An overview. *Asian J. Pharm.* **3**, 266–273 (2009).

50. Neumann, P. R. *et al.* Different PEG-PLGA matrices influence in vivo optical/ photoacoustic imaging performance and biodistribution of NIR-emitting π-conjugated polymer contrast agents. *Adv. Healthc. Mater.* **10**, (2021).

51. Abelha, T. F. *et al.* Low molecular weight PEG-PLGA polymers provide a superior matrix for conjugated polymer nanoparticles in terms of physicochemical properties, biocompatibility and optical/photoacoustic performance. *J. Mater. Chem. B* **7**, 5115–

5124 (2019).

52. Geng, J. *et al.* Conjugated polymer and gold nanoparticle Co-loaded PLGA nanocomposites with eccentric internal nanostructure for dual-modal targeted cellular imaging. *Small* **8**, 2421–2429 (2012).

53. Modicano, P. *et al.* Enhanced optical imaging properties of lipid nanocapsules as vehicles for fluorescent conjugated polymers. *Eur. J. Pharm. Biopharm.* **154**, 297–308 (2020).

54. Abelha, T. F. *et al.* Bright conjugated polymer nanoparticles containing a biodegradable shell produced at high yields and with tuneable optical properties by a scalable microfluidic device. *Nanoscale* **9**, 2009–2019 (2017).

55. Kemal, E. *et al.* Bright, near infrared emitting PLGA-PEG dye-doped CN-PPV nanoparticles for imaging applications. *RSC Adv.* **7**, 15255–15264 (2017).

56. Abelha, T. F. *et al.* Low molecular weight PEG-PLGA polymers provide a superior matrix for conjugated polymer nanoparticles in terms of physicochemical properties, biocompatibility and optical/photoacoustic performance. *J. Mater. Chem. B* **7**, 5115–5124 (2019).

57. Feng, L. *et al.* Preparation and biofunctionalization of multicolor conjugated polymer nanoparticles for imaging and detection of tumor cells. *Adv. Mater.* **26**, 3926–3930 (2014).

58. Jana, N. R. *et al.* Synthesis of water-soluble and functionalized nanoparticles by silica coating. *Chem. Mater.* **19**, 5074–5082 (2007).

59. Chen, X. *et al.* Multicolor super-resolution fluorescence microscopy with blue and carmine small photoblinking polymer sots. *ACS Nano* **11**, 8084–8091 (2017).

60. Yu, J. *et al.* Recent advances in the development of highly luminescent semiconducting polymer dots and nanoparticles for biological imaging and medicine. *Anal. Chem.* **89**, 42–56 (2017).

61. Dai, C. *et al.* A novel boron ketoiminate-based conjugated polymer with large Stokes shift: AIEE feature and cell imaging application. *New J. Chem.* **45**, 4071–4076 (2021).

62. Feng, L. *et al.* Preparation and biofunctionalization of multicolor conjugated polymer nanoparticles for imaging and detection of tumor cells. *Adv. Mater.* **26**, 3926–3930 (2014).

63. Liu, P. *et al.* Red-emitting DPSB-based conjugated polymer nanoparticles with high two-photon brightness for cell membrane imaging. *ACS Appl. Mater. Interfaces* **7**, 6754–6763 (2015).

64. Wang, S. *et al.* Encapsulation of MEH-PPV:PCBM hybrids in the cores of block copolymer micellar assemblies: photoinduced electron transfer in a nanoscale donor-acceptor system. *Langmuir* **32**, 329–337 (2016).

65. Macneill, C. M. *et al.* Soft template synthesis of donor-acceptor conjugated polymer nanoparticles: Structural effects, stability, and photothermal studies. *J. Polym. Sci. Part A Polym. Chem.* **52**, 1622–1632 (2014).

66. Liu, J. *et al.* PEGylated conjugated polyelectrolytes containing 2,1,3-benzoxadiazole units for targeted cell imaging. *Polym. Chem.* **3**, 1567–1575 (2012).

67. Yang, T. *et al.* Ultrastable near-infrared conjugated-polymer nanoparticles for dually photoactive tumor inhibition. *Adv. Mater.* **29**, 1–9 (2017).

68. Pu, K. Y. *et al.* Fluorescent single-molecular core-shell nanospheres of hyperbranched conjugated polyelectrolyte for live-cell imaging. *Chem. Mater.* **21**, 3816–3822 (2009).

69. Qiao, Y. *et al.* Extracellular oxygen sensors based on PtTFPP and four-arm block copolymers. *Appl. Sci.* **9**, (2019).

70. Li, K. *et al.* Generic strategy of preparing fluorescent conjugated-polymer-loaded poly(DL-lactide-co-Glycolide) nanoparticles for targeted cell imaging. *Adv. Funct. Mater.* **19**, 3535–3542 (2009).

71. Ahmad Khanbeigi, R. *et al.* Surface chemistry of photoluminescent F8BT conjugated polymer nanoparticles determines protein corona formation and internalization by phagocytic cells. *Biomacromolecules* **16**, 733–742 (2015).

72. Watters, R. J. *et al.* Chapter five - development and use of ceramide nanoliposomes in cancer. in *Nanomedicine* (ed. Düzgüneş, N. B. T.-M. in E.) vol. 508 89–108 (Academic Press, 2012).

73. Pochapski, D. J. *et al.* Zeta potential and colloidal stability predictions for inorganic nanoparticle dispersions: effects of experimental conditions and electrokinetic models on the interpretation of results. *Langmuir* **37**, 13379–13389 (2021).

74. Gao, Z. yan *et al.* Conjugated polymer nanoparticles based on carbazole for detecting ferric ion (III) with a large Stokes shift and high sensitivity and the application in cell imaging. *Dye. Pigment.* **168**, 68–76 (2019).

75. Fang, X. *et al.* Compact conjugated polymer fots with covalently incorporated metalloporphyrins for hypoxia bioimaging. *ChemBioChem* **20**, 521–525 (2019).

76. Kim, C. *et al.* Synthesis of conjugated polymer nanoparticles with core-shell structure for cell imaging and photodynamic cancer therapy. *Macromol. Res.* **25**, 572–577 (2017).

77. Bourke, S. *et al.* Silica passivated conjugated polymer nanoparticles for biological imaging applications. *Reporters, Markers, Dye. Nanoparticles, Mol. Probes Biomed. Appl. IX* **10079**, 100790A (2017).

78. Bourke, S. *et al.* Cellular imaging using emission-tuneable conjugated polymer nanoparticles. *RSC Adv.* **9**, 37971–37976 (2019).

79. Liu, L. *et al.* Polyfluorene nanoparticles coated with folate-functionalized triblock copolymer: effective agents for targeted cell imaging. *Macromol. Biosci.* **12**, 1384–1390 (2012).

80. Wang, Y. *et al.* Photothermal-responsive conjugated polymer nanoparticles for remote control of gene expression in living cells. *Adv. Mater.* **30**, 1–5 (2018).

81. Wang, S. *et al.* Polymerization-enhanced two-photon photosensitization for precise photodynamic therapy. *ACS Nano* **13**, 3095–3105 (2019).

82. Spano, F. C. & Silva, C. H- and J-aggregate behavior in polymeric semiconductors. *Annu. Rev. Phys. Chem.* **65**, 477–500 (2014).

83. Zhou, S. *et al.* A high brightness probe of polymer nanoparticles for biological imaging. *Spectrochim. Acta - Part A Mol. Biomol. Spectrosc.* **192**, 228–235 (2018).

84. Lu, X. *et al.* Single nanoparticles as versatile phototheranostics for tri-modal imaging-guided photothermal therapy. *Biomater. Sci.* **7**, 3609–3613 (2019).

85. Pu, K. *et al.* Phosphorylcholine-coated semiconducting polymer nanoparticles as rapid and efficient labeling agents for in vivo cell tracking. *Adv. Healthc. Mater.* **3**, 1292–1298 (2014).

86. Li, S. *et al.* Near-infrared (NIR)-absorbing conjugated polymer dots as highly effective photothermal materials for in vivo cancer therapy. *Chem. Mater.* **28**, 8669–8675 (2016).

87. Hong, G. *et al.* Ultrafast fluorescence imaging in vivo with conjugated polymer fluorophores in the second near-infrared window. *Nat. Commun.* **5**, 1–9 (2014).

88. Pu, K. *et al.* Diketopyrrolopyrrole-based semiconducting polymer nanoparticles for in vivo photoacoustic imaging. *Adv. Mater.* **27**, 5184–5190 (2015).

89. Li, D. D. *et al.* A Donor-acceptor conjugated polymer with alternating isoindigo derivative and bithiophene units for near-infrared modulated cancer thermo-chemotherapy. *ACS Appl. Mater. Interfaces* **8**, 19312–19320 (2016).

90. Lyu, Y. *et al.* Intraparticle molecular orbital engineering of semiconducting polymer nanoparticles as amplified theranostics for in vivo photoacoustic imaging and photothermal therapy. *ACS Nano* **10**, 4472–4481 (2016).

91. Feng, G. *et al.* Multifunctional conjugated polymer nanoparticles for image-guided photodynamic and photothermal therapy. *Small* **13**, 1–12 (2017).

92. Yuan, Y. *et al.* Conjugated-polyelectrolyte-based polyprodrug: Targeted and image-guided photodynamic and chemotherapy with on-demand drug release upon irradiation with a single light source. *Angew. Chemie - Int. Ed.* **53**, 7163–7168 (2014).

93. Liang, Z. *et al.* F127/conjugated polymers fluorescent micelles for trace detection of nitroaromatic explosives. *Dye. Pigment.* **125**, 367–374 (2016).

94. Wang, X. H. *et al.* Indocyanine green-platinum porphyrins integrated conjugated polymer hybrid nanoparticles for near-infrared-triggered photothermal and two-photon photodynamic therapy. *J. Mater. Chem. B* **5**, 1856–1862 (2017).

95. Hashizume, H. *et al.* Openings between defective endothelial cells explain tumor vessel leakiness. *Am. J. Pathol.* **156**, 1363–1380 (2000).

96. Hare, J. I. *et al.* Challenges and strategies in anti-cancer nanomedicine development: An industry perspective. *Adv. Drug Deliv. Rev.* **108**, 25–38 (2017).

97. Balasundaram, G. *et al.* Molecular photoacoustic imaging of breast cancer using an actively targeted conjugated polymer. *Int. J. Nanomedicine* **10**, 387–397 (2015).

98. Tian, Z. *et al.* Amplified energy transfer in conjugated polymer nanoparticle tags and

sensors. *Nanoscale* **2**, 1999–2011 (2010).

99. Win, K. Y. & Feng, S.-S. Effects of particle size and surface coating on cellular uptake of polymeric nanoparticles for oral delivery of anticancer drugs. *Biomaterials* **26**, 2713–2722 (2005).

100. Rampado, R. *et al.* Recent advances in understanding the protein corona of nanoparticles and in the formulation of "stealthy" nanomaterials. *Front. Bioeng. Biotechnol.* **8**, 1–19 (2020).

101. Guarnieri, D. *et al.* Effect of serum proteins on polystyrene nanoparticle uptake and intracellular trafficking in endothelial cells. *J. Nanoparticle Res.* **13**, 4295–4309 (2011).

102. Fröhlich, E. The role of surface charge in cellular uptake and cytotoxicity of medical nanoparticles. *Int. J. Nanomedicine* **7**, 5577–5591 (2012).

103. Augustine, R. *et al.* Cellular uptake and retention of nanoparticles: Insights on particle properties and interaction with cellular components. *Mater. Today Commun.* **25**, 101692 (2020).

104. Guo, B. *et al.* Biocompatible conjugated polymer nanoparticles for highly efficient photoacoustic imaging of orthotopic brain tumors in the second near-infrared window. *Mater. Horizons* **4**, 1151–1156 (2017).

105. Jiang, Y. *et al.* Broadband absorbing semiconducting polymer nanoparticles for photoacoustic imaging in second near-infrared window. *Nano Lett.* **17**, 4964–4969 (2017).

106. Wu, W. *et al.* Polymerization-enhanced photosensitization. *Chem* **4**, 1937–1951 (2018).

107. Moustaoui, H. *et al.* Shape and size effect on photothermal heat elevation of gold nanoparticles: absorption coefficient experimental measurement of spherical and urchin-shaped gold nanoparticles. *J. Phys. Chem. C* **123**, 17548–17554 (2019).

108. Kim, C. *et al.* Synthesis of conjugated polymer nanoparticles with core-shell structure for cell imaging and photodynamic cancer therapy. *Macromol. Res.* **25**, 572–577 (2017).

109. Zhang, D. *et al.* Lipid micelles packaged with semiconducting polymer dots as simultaneous MRI/photoacoustic imaging and photodynamic/photothermal dual-modal therapeutic agents for liver cancer. *J. Mater. Chem. B* **4**, 589–599 (2016).

110. Blanco, E. *et al.* Principles of nanoparticle design for overcoming biological barriers to drug delivery. *Nat. Biotechnol.* **33**, 941–951 (2015).

111. Pino, P. del *et al.* Protein corona formation around nanoparticles – from the past to the future. *Mater. Horizons* **1**, 301–313 (2014).

112. Lundqvist, M. *et al.* Nanoparticle size and surface properties determine the protein corona with possible implications for biological impacts. *Proc. Natl. Acad. Sci. U. S. A.* **105**, 14265–14270 (2008).

113. Alexis, F. *et al.* Factors affecting the clearance and biodistribution of polymeric nanoparticles. *Mol. Pharm.* **5**, 505–515 (2008).

Chapter 2 – Materials and methods

This chapter deals with the materials and methods that are common to most steps. In particular, this chapter starts by describing the synthesis and characterization of CPNs, since most of the work in this thesis involved these steps of CPNs fabrication, measurements of their properties, and evaluation of their potential for applications. The remainder of the chapter focuses on descriptions of several spectroscopic techniques and experimental methods used, including detailed experimental protocols where appropriate.

2.1 CPNs preparation and characterization

Two types of conjugated polymers were used in this work described in this thesis: PTB7 and PTB7-Th CPNs. Because the two types of CPs are intrinsically hydrophobic and require the use of amphiphilic copolymers to increase their water dispersibility and allow them to be used in biological. To enable aqueous dispersibility to our CPNs, two types of copolymers, F127 and PSMA, were used in this work. F127 is composed of a PEOx-PPOy-PEOz triblock structure where the PEO is hydrophilic, and the PPO is hydrophobic. This triblock structure self-assembles into micelles in an aqueous environment in which PPO encapsule the hydrophobic CPs to form a hydrophobic core, and the PEO forms a hydrophilic outer shell. The hydroxyl group from the PEO end can provide further modification. While PSMA is a copolymer composed of hydrophobic styrene and hydrophilic maleic anhydride monomeric units, the hydrophobic units encapsulate the hydrophobic CPs as a core into micelles and leave the maleic anhydride as an outer shell in an aqueous environment.

The PTB7 CPNs and PTB7-Th CPNs were prepared according to the nanoprecipitation method described by Wu et al,[1] as summarized in Scheme 1. (1) Both the CPs and copolymers were dissolved in water miscible solvent THF at a concentration of 1 mg/ml, THF was chosen here because both polymers dissolve well in it, and it can be evaporated out easily. (2) After mixing the CPs and copolymer solutions, they were added to de-ionized (DI) water with ultrasonication and vigorous stirring to form PTB7 CPNs or PTB7-Th CPNs. The rapid exposure to water drives the amphipathic copolymer into a micelle, with the hydrophobic blocks forming a core and the hydrophilic blocks flaring out into the solvent,[2] encapsulating CPs within this micelle. (3) Finally, the suspension was left to stir for an additional 72 hours to completely remove THF from CPNs and the new CPNs sample was topped up with DI water to make the final concentration of the PTB7 CPNs and PTB7-Th CPNs to be 100 μg/ml.

To purify the PTB7@F127 CPNs and get rid of loose F127 from the surface of CPNs, a millipore centrifugal filter (30 kDa) was used. The molecular weight of F127 is 12.6 kDa and

the molecular weight of PTB7 is 80-200 kDa, therefore loose strands of the F127 will easily pass through the filter, whilst CPN particles will remain above it. The purification process achieved by centrifugation at 7000 rpm for 20 minutes, repeated twice.

2.1.1 Fabrication protocol for PTB7@F127 CPNs.

The method below was used to make a 10 ml suspension of PTB7@F127 CPNs with a final concentration of 100 μg/ml.

1. The PTB7 powder was dissolved in THF to a concentration of 1 mg/ml, and F127 was dissolved in THF to a concentration of 100 mg/ml. These were the stock solutions for each polymer.

2. A mixture of 1 ml of PTB7 stock solution and 1 ml of F127 stock solution was prepared. The mixture was then added to 10 ml of DI water while being sonicated at the same time. A stirrer bar was added, and the suspension was left stirring for 3 days, then topped up with DI water to 10 ml.

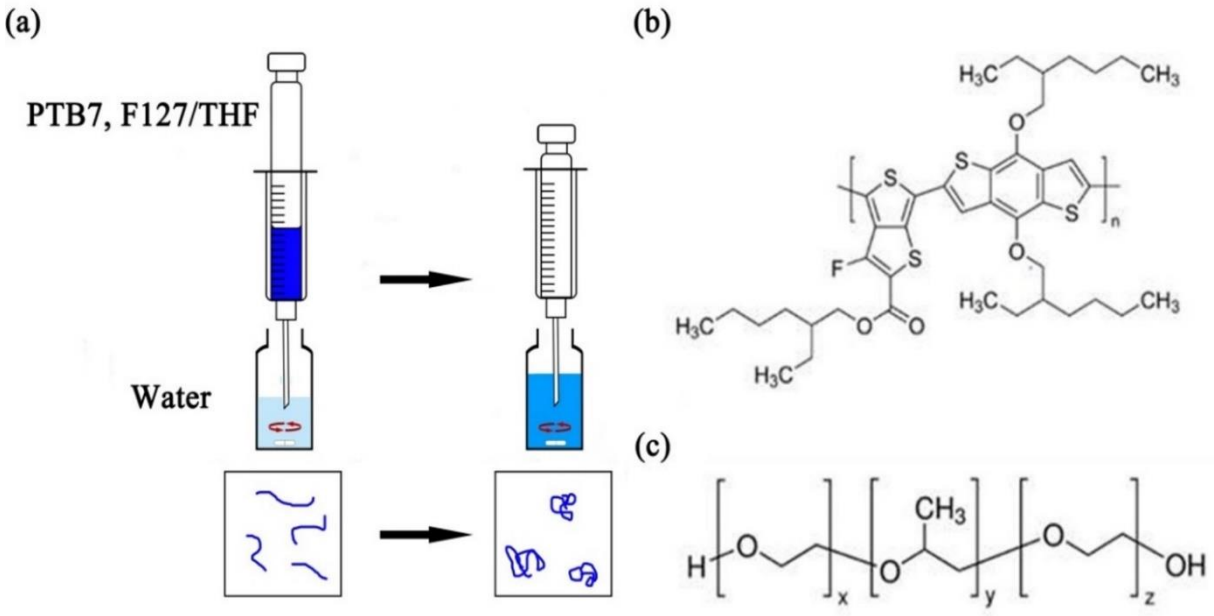

Figure 2.1 (a) Schematic of the Nanoprecipitation Method, (b) structure of PTB7, (c) structure of F127.

2.1.2 Initial characterisation of PTB7 CPNs samples

Preliminary characterisation of PTB7 CPNs samples involved determination of their absorption and PL peaks' positions, determination of the QY of their emission and their physical and hydrodynamic size.

2.2 Spectroscopic measurements

Various techniques were employed to investigate the CPNs' characteristics. For initial characterization, absorption and photoluminescence spectroscopies were the most crucial. In this section, the experimental procedures and equipment used are described.

2.2.1 Steady-state spectroscopic measurements

In the UV-vis spectroscopy, the concentration of sample components was determined using the Beer-Lambert Law:

$$A_\lambda = \varepsilon_\lambda \cdot C \cdot L \qquad (2.1)$$

where A_λ and ε_λ (M^{-1} cm^{-1}) are sample absorbance and extinction coefficient at wavelength λ, respectively, with the latter usually chosen to be the wavelength at the absorption peak. L is sample length in cm, corresponding to sample thickness for thin films and to the length of the cuvette cavity for liquids. C is the molar concentration of the sample in $M = mol\ L^{-1}$.

Shimadzu UV-2600 UV-visible spectrophotometer was used to record all absorption spectra. Samples being analysed were diluted until their absorption was around 0.15 to avoid re-absorption and optical filtering effects.

2.2.2 Photoluminescence spectroscopy

Photoluminescence (PL) measurements can be used to determine the photoluminescence quantum yield (PLQY, $\emptyset$_s) of CPNs, the other application is to investigate the emission spectrum and emission peak locations.

The PLQY of CPNs was measured under room temperature using the relative method. In this method the Q_f of CPNs is calculated by comparing its fluorescence intensity to a standard reference NIR dye according to the following formula:[3]

$$\emptyset_s = \emptyset_{ref} \times \frac{a_{ref}}{a_s} \times \frac{A_s}{A_{ref}} \times \left(\frac{n_s}{n_{ref}}\right)^2 \qquad (2.2)$$

Where $\emptyset_{ref}$ is the quantum yield of reference dye. a's refers to absorbance values at a particular excitation wavelength. A's stand for the integrated area under the emission curves and n is the refractive index of the medium. The PLQY of Atto700 dye in water solution ($\emptyset_{ref} = 0.25$) was used as the reference. Atto700 was selected as the reference dye because it absorbs and emits in the same range as PTB7@F127 CPNs (shown in Figure 2.2), allowing absorption and fluorescence measurements of both samples to be performed at the same experimental conditions.

Agilent Cary 60 spectrometer was used to record all emission spectra.

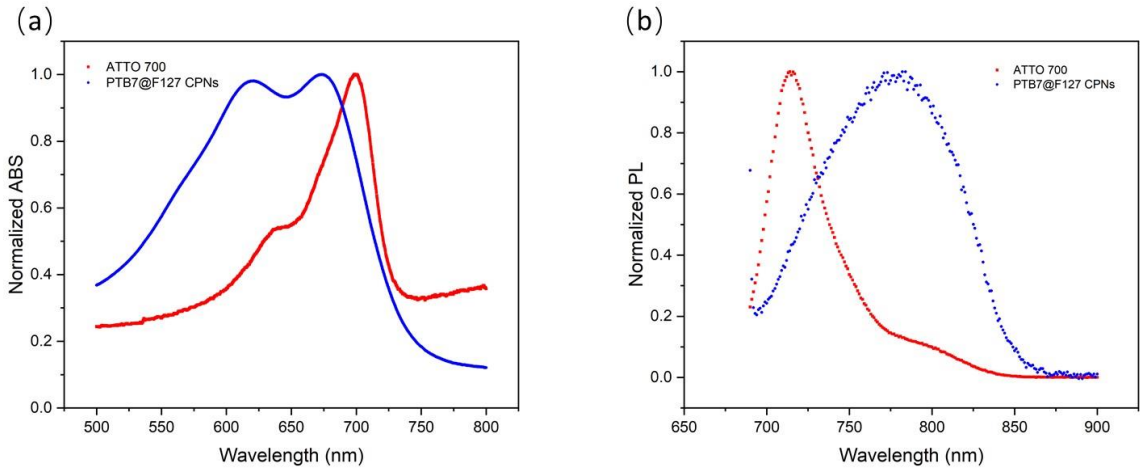

Figure 2.2 Steady-state (a) absorption and (b) emission spectra of Atto700 (red) and PTB7@F127 CPNs (blue).

2.3 Other techniques

2.3.1 ζ-potential and nanoparticle size measurements

The hydrodynamic size of NPs is a crucial metric for the characterisation of colloidal polymeric NPs. It influences the efficiency of cellular absorption and cytotoxicity. Their ζ-potentials is a crucial factor in determining the stability of NPs in aqueous solutions. As a result, ζ-potentials are crucial factors that need to be included in any investigations involving optimisation of the fabrication process or when modifying the surface of CPNs.

The DLS technique involves the temporal correlation of signal fluctuations induced by the motion of particles, with the signal resulting from particle-scattered light. The light dispersed by particles interferes constructively and destructively, resulting in the creation of a 2-D pattern of bright and dark patches at the detector.[4] As the particles move, the area of these patches increases and decreases, and it is these fluctuations that are time-correlated. Brownian motion is responsible for the movement of particles during these measurements. The larger the particles are, the slower they move; hence, the correlation between fluctuation patterns persists at longer time lags. In principle and using detailed analysis of the time lags at which fluctuations in pattern persist, it is therefore possible to obtain an estimate for the size of nanoparticle causing the fluctuations. In this work, however, this analysis was performed automatically during the measurement, by the instrument used (proprietary software), yielding statistical outputs and histograms directly. These outputs are subject to interpretation, however,

especially in cases where the measurements were “noisy”, *e.g.* due to the low concentration of particles.

ζ-potential measurements are performed using the same underlying principle, with the only difference being that an alternating voltage is applied across the liquid. Under such stimuli, the particles oscillate instead of undergoing Brownian motion. The oscillation frequency and the time a particle spends in the excitation volume can be extracted from the fluctuating patterns described above. The higher the ζ-potential, the faster the particles move, reducing the correlation at higher time lag intervals. In this case also, the analysis of correlation between fluctuating patterns as a function of lag times is performed by the proprietary software provided with the equipment, outputting the ζ-potential values of the particles directly.

Zeta potentials and hydrodynamic diameters of CPNs were measured using a ZetaSizer Nano ZS (Malvern Panalytical). Disposable polystyrene cuvettes (DTS0012) and Folded Capillary cells (DTS1070) were utilized for size and ζ-potential measurement, respectively. 2 ml of 5 μg/ml CPNs water dispersion was used and measurements were performed at 20°C; the duration of each measurement was determined automatically by the Malvern software. For each sample, three measurements with 10 repeats were performed, and the results were averaged.

2.3.2 Protocols followed in cell experiments

Cell staining with PTB7 CPNs:

1. Incubated Hela cells or HEK 293 cells, previously grown in a confocal dish (35 mm) to an appropriate density (0.3×10^6-0.5×10^6). To each cells sample, 2 mL incubation suspension was added, which was composed from 200 μL PTB7 CPNs stock suspension (100 μg/mL) and 1.8 mL pure DMEM. The cells samples were then placed and kept in a 37 ℃ cell culture incubator for 4 hours.
2. Upon the end of incubation period, the cultures were washed with a PBS solution three times.
3. Cells were fixed with 1 mL 2.6% paraformaldehyde (PFA) for 15 minutes at 37 ℃.
4. The cultures were washed with PBS solution three times, and then mounted using 5 μL Prolong Gold, whilst keeping the confocal dish covered with a round glass cover slip.

Cell staining with PTB7 CPNs, wheat germ agglutinin (WGA) and 4',6-diamidino-2-phenylindole (DAPI):

WGA was used to stain the cell membrane and DAPI was used to stain the nucleus.

1. Incubated Hela cells or HEK 293 cells, previously grown in a confocal dish (35 mm) to an appropriate density (0.3×10^6-0.5×10^6), each cells sample added 2 mL incubation suspension which include 200 μL of PTB7 CPNs stock suspension (100 μg/mL) and 1.8 mL of pure DMEM, put the cells samples in a 37 ℃ cell culture incubator for 4 hours.
2. Upon the end of incubation period, washed the cultures with PBS solution (pH=7.4) three times.
3. Fixed the cells with 1 mL 2.6% PFA for 15 minutes at 37℃.
4. Washed the cultures with PBS solution three times.
5. Stained with a 200 μL of 1:200 volume dilution (in PBS solution) of WGA for 10 minutes at room temperature.
6. Washed the cultures with PBS solution three times.
7. Permeabilised the cells with 100 μL perm buffer (1% BSA, 0.3% Triton X, HBSS, pH 7.5) for 10 minutes at room temperature.
8. Stained with 100 μL of 1:1000 volume dilution (in PBS solution) of DAPI for 30 min at room temperature.
9. Washed the cultures with PBS solution three times.
10. Fix cells with 1 mL 2.6% PFA for 15 minutes at 37℃.
11. Washed the cultures three times with PBS solution, mount with 5 μL Prolong Gold and cover dishes with a round glass cover slips.

Cell imaging with home-built fluorescence microscope and NIKON confocal microscope:

When using the home-built fluorescence microscope, samples were illuminated using a white light source (OSL-2, Thorlabs), filtered by a 650 ± 40 nm band-pass filter (Thorlabs). Fluorescence images, filtered by a 700 nm longpass filter (ThorLabs) were then captured using a 40× oil objective and recorded using an Orca Fusion camera (Hamamatsu). When using the NIKON confocal microscope, fluorescence images in the 663-738 nm collection window were captured with a 60× oil objective. For these measurements, samples were excited at 647 nm. In all cases, scanning parameters (such as excitation intensity and image resolution) were adjusted as necessary to obtain high-contrast images.

Error-Processing:

1. Standard Deviation:

Standard deviation value of DLS/ζ-potential for each run of measurements was obtained directly from the proprietary software of ZetaSizer NanoSeries instrument. In all measurements of these parameters, 3 experimental runs of 10 measurements each were performed and the standard deviation for each was obtained via the software. This data was then processed using the STDEV function in EXCEL to obtain the standard deviation for the whole set of measurements:[5]

$$\sigma = \sqrt{\frac{\sum(x-\bar{x})^2}{(n-1)}} \qquad (2.3)$$

Where x is the measured value and $\bar{x}$ is the mean value, n is the sample size.

2. SOG measurement errors:

When measuring SOG, the biggest source of error was the pipette sampling error, *i.e.* from the error in the volume that the pipette draws. The relative sampling errors of pipettes used for these measurements were obtained from specifications provided by the manufacturer (Gilson): for P20 pipette, the error is ±0.1 µL,[6] the error of P200 is ±0.8 µL,[7] the error of P1000 pipette is ±4 µL[6].

These errors were used to calculate the errors in the concentrations of various agents used in the SOSG/PLQY measurements and the resulting relative error in the fluorescence intensity measurements. The details of these calculations are specified below.

Stock SOSG solution

To make up the stock SOSG solution, 100 µg of SOSG was added to 33 µL of methanol. The methanol solution was drawn using the P200 pipette, resulting in the following error in SOSG concentration:

$$C = \frac{m}{V}$$

$$\frac{\Delta C}{C} = \frac{\Delta m}{m} + \frac{\Delta \mathrm{V}}{V} = \frac{\Delta \mathrm{V}}{V} = \frac{0.8}{33}$$

Diluted stock (fresh on the day)

To prepare the diluted stock of SOSG solution, to be used on the day of measurements, 2 µL of concentrated stock solution was added to 18 µL of water. (P20 pipette was used to measure out both substances.) The error in the SOSG concentration in the diluted stock was then calculated according to the following:

$$V_{tot} = V_{stock} + V_{water}$$

$$\Delta V_{tot} = \Delta V_{stock} + \Delta V_{water}$$

Final concentration:

$$C_{dil} = C_{stock} * \frac{V_{stock}}{V_{tot}}$$

$$\frac{\Delta C_{dil}}{C_{dil}} = \frac{\Delta C_{stock}}{C_{stock}} + \frac{\Delta V_{stock}}{V_{stock}} + \frac{\Delta V_{tot}}{V_{tot}} = \frac{\Delta C_{stock}}{C_{stock}} + \frac{\Delta V_{stock}}{V_{stock}} + \frac{\Delta V_{stock} + \Delta V_{water}}{V_{stock} + V_{water}}$$

$$= \frac{0.8}{33} + \frac{0.1}{2} + \frac{0.1 + 0.2}{20} = 0.089$$

SOSG measurements:

For SOSG only measurements (used as reference), samples were prepared by diluting 2 µL SOSG diluted stock solution in a solvent mixture, containing of 100 µL of DI water (labelled in equations below), 500 µL of D_2O and 400 µL of Tris buffer. For measurements of SOSG production by CPNs, the 100 µL of DI water was replaced by 100 µL of CPN suspensions (labelled CPN in equations below), but otherwise the composition of the samples was kept the same. The error in the concentration of SOSG for the two cases was:

$$\frac{\Delta C_{SOSG}}{C_{SOSG}} = \frac{\Delta C_{dil}}{C_{dil}} + \frac{\Delta V_{dil}}{V_{dil}} + \frac{\Delta V_{dil} + \Delta V_{wtr/CPN} + \Delta V_{Tris} + \Delta V_{D2O}}{V_{dil} + V_{water/CPN} + V_{Tris} + V_{D2O}}$$

$$= 0.089 + \frac{0.1}{2} + \frac{0.1 + 0.8 + 4 + 4}{2 + 100 + 400 + 500} = 0.148$$

The intensity of SOSG fluorescence measured during measurements must be proportional to its concentration in the sample, therefore the relative error in the measurements must equal the relative error in its concentration:$I_{PL} \propto C_{SOSG} = k * C_{SOSG}$

$$\frac{\boldsymbol{\Delta I}}{\boldsymbol{I}} = \frac{\boldsymbol{\Delta C}}{\boldsymbol{C}}$$

$$\Delta I_{PL} = \left(\frac{\Delta C}{C}\right) I_{PL} = 0.148 * I_{PL}$$

The intensity of normalized CPNs fluorescence is obtained by dividing the fluorescence intensity of CPNs mixed with SOSG by the fluorescence intensity of SOSG only.

$$I_{PL,norm} = \frac{I_{CPN+SOSG}}{I_{SOSG\ only}}$$

$$\frac{\Delta I_{PL,norm}}{I_{PL,norm}} = \frac{\Delta I_{CPN+SOSG}}{I_{CPN+SOSG}} + \frac{\Delta I_{SOSG\ only}}{I_{SOSG\ only}}$$

$$\Delta I_{PL,norm} = (0.148 + 0.148) * I_{PL,norm} = 0.296 * I_{PL,norm}$$

3. PLQY measurement errors:

In these measurements, fluorescence intensities and absorbances of several samples were measured and plotted against each other. A such, the biggest source of error in these

measurements was the accuracy and precision of the spectrometer used. The Shimadzu UV-2600 UV-visible spectrophotometer measures absorbance values to an accuracy of ±0.002 a.u.[8] For the Agilent Cary 60 spectrometer, the error depends on the settings used (*e.g.* gain and integration time) and as such it is not specified by the manufacturer. In this case, the error was instead obtained by first smoothing the emission curve using Origin 2020 (Savitsky-Golay). This was then used to then subtracted from the original raw data and used to calculate the root-mean-square error in the integrated fluorescence intensity of the sample.

For each set of samples, the integrated fluorescence of individual samples was plotted against their absorbances in Origin 2020, assigning the calculated errors as the respective errors for the two measurement types. The data was fitted to a linear fit in the same software, yielding a value and an error for the slope for the set. Once this procedure has been completed for both the reference and the sample sets, the error in $\emptyset_s$ was obtained using the following equations:

$$\emptyset_s = \emptyset_{ref} \frac{Slope_s}{Slope_{ref}}$$

$$\frac{\Delta\emptyset_s}{\emptyset_s} = \frac{Error\ in\ Slope_s}{Slope_s} + \frac{Error\ in\ Slope_{ref}}{Slope_{ref}}$$

$$\Delta\emptyset_s = \emptyset_s * \left(\frac{Error\ in\ Slope_s}{Slope_s} + \frac{Error\ in\ Slope_{ref}}{Slope_{ref}}\right)$$

2.4 References:

1. Wu, C. *et al.* Preparation and encapsulation of highly fluorescent conjugated polymer nanoparticles. *Langmuir* **22**, 2956–2960 (2006).

2. Harada, T. *et al.* Low-bandgap conjugated polymer dots for near-infrared fluorescence imaging. *ACS Appl. Nano Mater.* **1**, 4801–4808 (2018).

3. Maity, B. *et al.* Effect of nano-confinement on the photophysics of lumichrome. *Chem. Phys. Lett.* **565**, 108–115 (2013).

4. Malvern Instruments (2004) ZetaSizer NanoSeries: User Manual. http://www.nbtc.cornell.edu/facilities/downloads/Zetasizer Manual.pdf.

5. STDEV function. https://support.microsoft.com/en-us/office/stdev-f.

6. Pipetman Classic User's Guide. https://gb.gilson.com/pub/media/docs/PIPETMANCLASSIC_UG_LT801120-F.pdf.

7. Pipetman Guaranteed Performance and Accuracy. https://gb.gilson.com/pub/media/docs/PIPETMANM_BROC.pdf.

8. Instrument Database: Shimadzu Europe - UV-2600 - Spectrophotometer. https://speciation.net/Database/Instruments/Shimadzu-Europe/UV2600--Spectrophotometer-;i3076.

Chapter 3

The work demonstrated in this chapter was published in ACS NANO.
(DOI: 10.1021/acsnano.1c01257)

ACSNANO

www.acsnano.org

ARTICLE

Theranostic Near-Infrared-Active Conjugated Polymer Nanoparticles

Miao Zhao, Edward Leggett, Struan Bourke, Souzana Poursanidou, Sadie Carter-Searjeant, Steve Po, Marciano Palma do Carmo, Lea Ann Dailey, Philip Manning, Sean G. Ryan, Laura Urbano, Mark A. Green,* and Aliaksandra Rakovich*

Cite This: *ACS Nano* 2021, 15, 8790−8802

Read Online

ACCESS | Metrics & More | Article Recommendations | Supporting Information

ABSTRACT: **Conjugated polymer nanoparticles (CPNs) based on a common solar cell material (PTB7) have been prepared, and their potential in theranostic applications based on bioimaging and photosensitizing capabilities has been evaluated. The main absorption and emission bands of the prepared CPNs both fell within the NIR-I (650−950 nm) transparency window, allowing facile and efficient implementation of our CPNs as bioimaging agents, as demonstrated in this work for A549 human lung cancer cell cultures. The prepared CPN samples were also shown to produce reactive oxygen species (ROS) upon photoexcitation in the near-infrared or ultraviolet spectral regions, both in aqueous solutions and in HaCaT keratinocyte cell cultures. Importantly, we show that the photosensitizing ability of our CPNs was largely determined by the nature of the stabilizing shell: coating the CPNs with a Pluronic F-127 copolymer led to an improvement of photoinitiated ROS production, while using poly[styrene-*co*-maleic anhydride] instead completely quenched said process. This work therefore demonstrates that the photosensitizing capability of CPNs can be modulated *via* an appropriate selection of stabilizing material and highlights the significance of this parameter for the on-demand design of theranostic probes based on CPNs.**

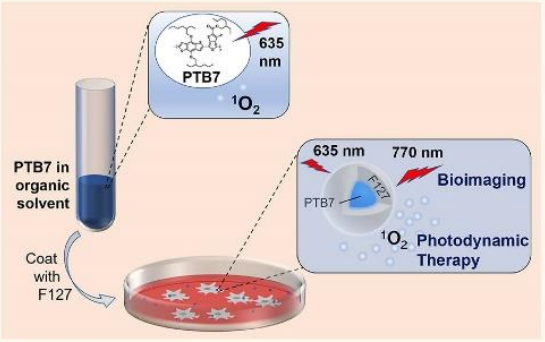

KEYWORDS: *conjugated polymer nanoparticles, theranostic probe, NIR-I, reactive oxygen species, photodynamic therapy*

Photodynamic therapy (PDT) is a treatment method that relies on a photoinduced generation of reactive oxygen species by a photosensitizer (PS). When applied to cancer therapy, PDT has many advantages compared to conventional cancer treatments such as chemotherapy, surgery, and radiation, which include minimal invasiveness or damage to healthy tissues, lack of drug resistance, and appropriateness to a broad spectrum of cancer targets.[1−3] It is highly desirable to develop biocompatible photosensitizers with excellent reactive oxygen species (ROS) generation ability and strong near-infrared (NIR) absorption, as NIR wavelengths experience less absorption and scattering in tissues,[4−6] leading to a deeper activation of the PDT. Nanomaterials are promising photosensitizers because of the advantageous properties that they offer. This includes the enhanced permeability and retention effect (EPR), which promotes nanomaterial accumulation in pathologically relevant areas.[7] However, many nanomaterials have intrinsic problems as photosensitizers: quantum dots (QDs) have excellent optical properties, but many are made from toxic heavy metals;[8] gold nanoparticles have better biocompatibility than QDs, but most absorb in the less favorable UV−vis region.[9]

In contrast, conjugated polymer nanoparticles (CPNs), which comprise large π-conjugated backbones and delocalized electronic structure, have attracted much attention because of their inherent photostability, high fluorescence brightness, visible or NIR emission, excellent biocompatibility, and compositions that are free from heavy metal ions.[10−15] As such, they present distinct advantages over existing dye systems and QDs as imaging agents, enabling effective imaging of numerous biological systems, with minimal toxicity.[16−18] However, CPNs have also been utilized as agents in PDT and photothermal therapy (PTT),[15,19] and, while in many such

Received: February 9, 2021
Accepted: May 7, 2021
Published: May 12, 2021

https://doi.org/10.1021/acsnano.1c01257
ACS Nano 2021, 15, 8790−8802

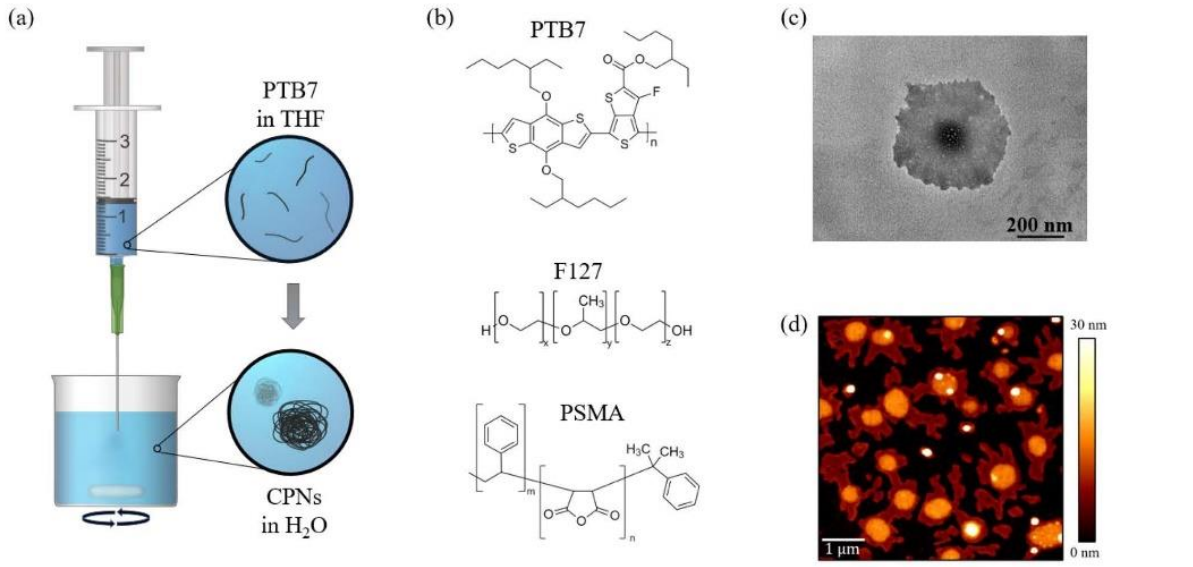

Figure 1. Fabrication of PTB7 CPNs using the nanoprecipitation method. Panel (a) summarizes the process used to prepare the nanoparticles of PTB7 conjugated polymer. To prepare coated PTB7 CPNs, Pluronic F-127 or PSMA was added to the PTB7 solution in THF, prior to injection into water. Panel (b) shows the chemical structures of PTB7, F127, and PSMA. Panels (c) and (d) show TEM and AFM images of PTB7@F127 CPNs dried on appropriate substrates, respectively. The process of drying the CPNs on a substrate results in flatter, larger-diameter particles, so the sizes apparent in the TEM and AFM images exceed those determined from DLS.

cases the PDT/PTT properties are endued through the addition of dopants,[20−22] examples exist where such PDT/PTT properties stem from the CPNs themselves.[21] Thus, the idea of CPNs as "safe" and "nontoxic" imaging agents can be at odds with their phototoxicity as PDT/PTT agents. However, this paradox also offers an opportunity to exploit CPNs for theranostic applications, combining their NIR imaging and photosensitization abilities for simultaneous detection and treatment of cancer.

PTB7 (poly({4,8-bis[(2-ethylhexyl)oxy]benzo[1,2-b:4,5-b′]dithiophene-2,6-diyl}{3-fluoro-2-[(2-ethylhexyl)carbonyl]-thieno[3,4-*b*]thiophenediyl})), whose structure is shown in Figure 1(b), is a standard conjugated polymer that has received much attention for solar energy devices because of its low bandgap, with related absorption and emission in the NIR spectral region.[23] However, it is known to produce ROS under photoexcitation, requiring mitigation strategies when it is utilized in solar energy devices, as it leads to degradation of thin films.[24] However, for theranostic purposes, its optical and photosensitization properties offer great advantages. Hereby, we report the development of three NIR-fluorescent CPN probes based on PTB7, which are capable of photosensitization of ROS upon excitation in the first biological window (NIR-I). This establishes them as a promising nanomaterial system for PDT-based theranostic applications.

RESULTS AND DISCUSSION

Fabrication and Initial Characterization of Conjugated Polymer Nanoparticles. Bare PTB7 CPNs were prepared using the reprecipitation method[25] (see Methods section), which is extremely facile and reliable and does not require the use of any additives or surfactants that need to be removed at the end, making it an easily scalable process. Furthermore, the reprecipitation method directly produces an aqueous dispersion of the CPNs, which is ideal for biological applications. Briefly (Figure 1(a)), the PTB7 conjugated polymer was first dissolved in tetrahydrofuran (THF), in which it has good solubility, and then injected rapidly into water, in which it has poor solubility, under sonication and vigorous stirring. It should be noted that most samples of bare PTB7 CPNs produced in this manner were unstable in aqueous solutions, precipitating within hours. This, however, could be easily overcome through the addition of an amphiphilic copolymer to the PTB7/THF solution, prior to injection into water. Upon injection, the rapid exposure to water drives the amphiphilic copolymer into a micelle, with the hydrophilic blocks exposed to the aqueous environment, while the hydrophobic blocks flare into the PTB7-containing core.[26]

Pluronic F-127 (F127) and poly[styrene-*co*-maleic anhydride] (PSMA), whose chemical structures are shown in Figure 1(b), are two copolymers often employed for such purposes and were used here to improve the solubility of our PTB7 CPNs in aqueous environments. To enable direct comparison of different CPNs and to minimize any changes of CPN properties arising as a result of different synthesis conditions, the same PTB7 polymer/copolymer ratios were used to prepare F127- and PSMA-coated CPNs.

PTB7 CPNs coated with F127 and PSMA, herein referred to as PTB7@F127 and PTB7@PSMA CPNs, had significantly improved stabilities in aqueous solutions, remaining stable as suspensions for more than 6 months (see the Supporting Information (SI) for a full discussion of sample stabilities under different conditions). The improved stability also allowed us to employ centrifugal ultrafiltration as a means of concentrating these CPN samples. Samples of high concentration are of great value to bioapplications, because it reduces the amount of solvent that is introduced into the biosystem, which can have a negative impact.

Briefly, the sample was placed on a membrane whose pore size (30 kDa) was large enough to pass individual strands of F127 (12.6 kDa) but too small to allow CPN particles through it. The sample was then centrifuged, which drew the solvent

https://doi.org/10.1021/acsnano.1c01257
ACS Nano 2021, 15, 8790−8802

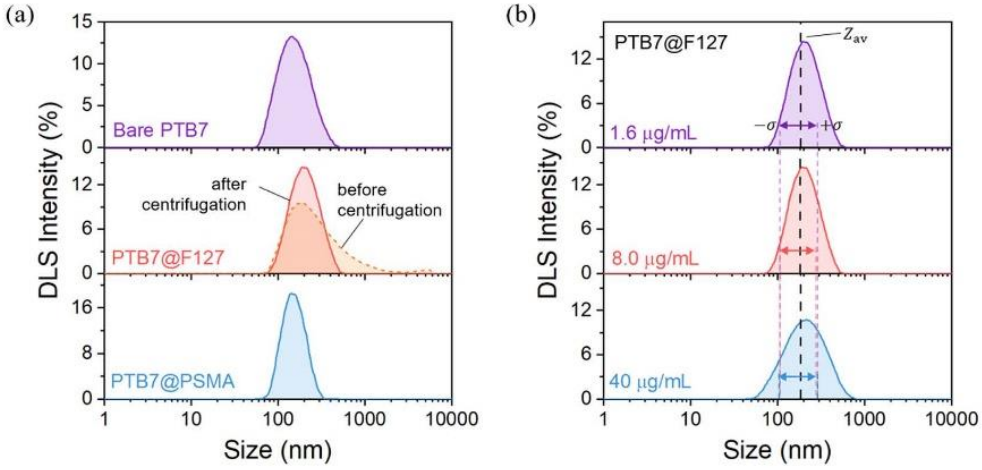

Figure 2. Hydrodynamic sizes of PTB7 CPNs. Results of DLS measurements of aqueous dispersions of (a) different PTB7 CPNs and (b) different concentrations of PTB7@F127 CPNs. In panel (a), the size of PTB7@F127 CPNs was measured before (dashed orange line) and after (solid red line) centrifugal ultrafiltration. In panel (b), the dashed black line indicates the average size (Z_{av}) of the CPNs across the three samples and the arrows indicate the range of size decreasing with a single standard deviation σ. Corresponding colored dashed lines run vertically across the panel for easier comparisons of the samples.

together with individual copolymer strands through the pores under the influence of the centrifugal force. In such a way, and to a certain extent, the sample above the membrane was gradually concentrated. We note that there existed an optimum combination of centrifugation speed and duration that produced the highest possible concentration of well-dispersed samples without a significant reduction in the yield of the preparation process (overcentrifugation of the sample caused the sample to adhere to the ultrafiltration membrane to an extent where it was no longer dispersible). In our case, the highest concentrations obtained for the coated samples was 420 μg/mL, whereas the highest concentration attained for the bare PTB7 CPNs was 90 μg/mL. Even at the highest concentrations, the CPN-containing dispersions were homogeneous and clear, with no observable aggregates.

The hydrodynamic size of the as-prepared and filtered CPNs was measured using dynamic light scattering (DLS). As expected, the size of the bare PTB7 CPNs was the smallest at a mean size of 140 nm, with a standard deviation of ~50 nm; the PTB7@PSMA CPNs were slightly larger at 150 ± 40 nm, while PTB7@F127 CPNs were the largest at 190 ± 60 nm (Figure 2(a)). The size of the coated CPN samples remained unvaried for a large range of sample concentrations (Figures 2(b) and S2.2 for PTB7@F127 and PTB7@PSMA data, respectively) with only a slight increase in sample polydispersity, which is a testament to their stability as colloidal dispersions.

The different sizes of the two coated CPN samples could be attributed to the different sizes of the copolymer chains (M_n(PSMA) ≈ 1900 Da, M_w(F127) ≈ 12 600 Da). Our hypothesis is that the size of the copolymer not only directly impacts the thickness of the coat[27] but also plays a role in the steric effects that determine the degree of intercollation of the copolymer chains into the PTB7 core and the packing of the PTB7 polymer chains inside the core. Thus, co-precipitation of PTB7 with the shorter PSMA copolymer yielded CPNs that were only slightly larger than the bare PTB7 CPNs, while the presence of the longer F127 copolymer during the co-precipitation process leads to bigger CPN sizes and a relatively loose packing of F127 copolymer in the coat (Figure S3.3). The latter fact was evidenced by the much larger size and polydispersity of the as-prepared PTB7@F127 CPN samples (220 ± 60 nm), compared to those that were filtered (see middle graph of Figure 2(a)). The centrifugal ultrafiltration process removed the loosely bound F127 from the surface of the CPNs, resulting in smaller CPN sizes described above. The looseness of the F127 coat was further evidenced by the atomic force microscopy images of the dried PTB7@F127 samples: in Figure 1(d), it is clear that the PTB7 core remains relatively intact upon drying, while the F127 coating layer is more fluid and spreads out around each CPN during the drying process (see the SI for a further discussion of F127 coat fluidity).

Both transmission electron microscopy (TEM) and atomic force microscopy (AFM) images (Figure 1(c) and (d), respectively) confirmed the expected core–shell structure of the CPNs co-precipitated with a copolymer. However, the heights and widths of the CPNs obtained from these images did not match those measured by DLS, yielding much larger widths (400–1000 nm) and smaller heights (10–30 nm). We attribute this to the capillary and centrifugal forces that the CPNs experience during the spin-coating and drying process, which deform them into "fried egg"-like shapes and yield the observed deviations in measured widths and heights. This hypothesis is supported by an observation that the mean volume of spherical CPNs, calculated using their average hydrodynamic diameter, $V_{DLS} \approx 3.1 \times 10^{-3}$ fL, is approximately the same as the mean obtained from the AFM data, $V_{AFM} \approx 4.7 \times 10^{-3}$ fL, especially in view of the possible deformation of particles under the forces they experience during sample preparation. Further details of these calculations can be found in the SI.

The sizes of the CPN particles produced in this work sit within the range identified by several studies as being optimum for accumulation in tumorous tissues (*in vivo*) by the enhanced permeability and retention effect.[28−30] Further specificity to tumorous tissues could be achieved relatively easily by modifying the reprecipitation mixture to include a copolymer coating material that has been prefunctionalized with targeting

https://doi.org/10.1021/acsnano.1c01257
ACS Nano 2021, 15, 8790−8802

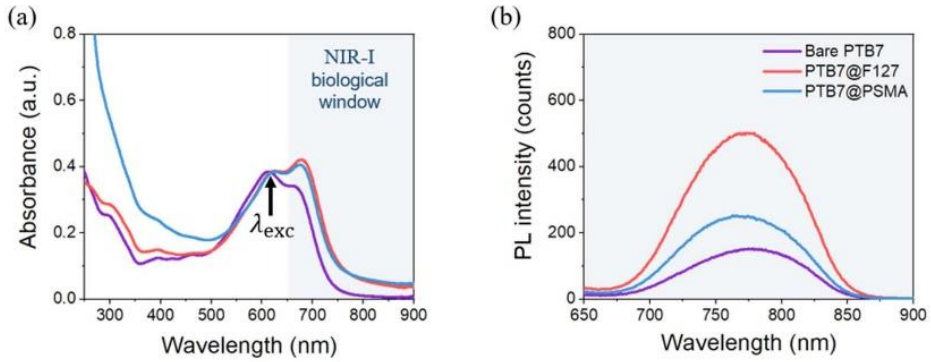

Figure 3. Optical properties of PTB7-based CPNs in aqueous solutions. Steady-state (a) absorption and (b) emission spectra of PTB7 (purple), PTB7@F127 (red), and PTB7@PSMA (blue) CPNs. The shaded region indicates the first (NIR-I) transparency region of biological tissues. The photoluminescence spectra shown in (b) were recorded using an excitation wavelength of 618 nm, as indicated by the arrow in panel (a), where all samples absorbed equally. The concentration of all samples was ~8 μg/mL.

entities or with functional groups that could be used for attachment of such entities post-reprecipitation of the CPNs. In a similar way, other modalities could also be endued onto the CPNs, while maintaining their native theranostic capability arising from the PTB7 core.

Optical Properties of PTB7 CPNs. The absorption spectra of all PTB7 CPNs (Figures 3a and S4.4a) showed the characteristic two-peak absorption in the 550−750 nm region, with absorption maxima at approximately 615 and 675 nm corresponding to the transitions between the ground state and the first two vibronic levels of the excited state of PTB7.[31] Deconvolution of these spectra into contributions corresponding to these two transitions (see the SI) showed that the two absorption peaks were slightly blue-shifted for the bare PTB7 CPNs compared to the coated samples, which we attribute to a shorter characteristic length of the conjugated segments in bare PTB7 CPNs originating from an increased contortion of the chains in these particles. Furthermore, the relative intensity of the two absorption peaks was much smaller for these CPNs, when compared to coated CPNs and the free PTB7 chains dissolved in THF (Table S4.1). The ratio of the peaks or, equivalently, the intensity of the lower-energy peak (at 675 nm) is known to be sensitive to aggregation in PTB7 chains, with increased interchain interactions causing a decrease in its intensity;[31,32] therefore, the observed decrease can be attributed to decreased interchain interactions. Most likely, this is due to an increased chain disorder which disturbed the $\pi-\pi$ stacking of the conjugated domains and therefore caused a reduction in interchain interactions.[31] In the coated samples, the presence of copolymers mitigated some of the steric hindrance owing to the bulky side chains of the PTB7 and allowed for tighter and better-ordered packing of the PTB7 chains; this promoted inter- and intrachain interactions and resulted in increased absorption by excitation into the lowest vibronic excited state.

The photoluminescence spectrum of all three CPN samples appeared to consist of a single, approximately Gaussian, peak in the 700−850 nm spectral region (Figure 3(b)). The average position of the fluorescence peaks (~1.55 eV) and the corresponding Stokes' shifts (~100 nm) were consistent with previously reported results for PTB7 films and solutions,[31,33] which attributed this peak to a de-excitation *via* emission from the lowest vibrational level of the excited state to the first vibrational level of the ground state. No emission corresponding to the de-excitation into the zeroth vibrational level (expected to appear at ~1.86 eV) was observed in our case, indicating that most of the observed emission is from densely packed and weakly interacting H-aggregates.[32]

A further careful examination of the PL spectra led to the conclusion that each PL peak consisted of two Gaussian contributions (Figure S4.7, Table S4.2), located at approximately 1.55 and 1.65 eV for all samples; the observed red- and blue-shifts between different samples were solely the result of different ratios of these contributions (Figure S4.7, Table S4.2). We note that the separation of these contributions (~0.1 eV) was half of the typically reported vibronic splitting of the ground state (~0.2 eV), for both PTB7 solutions and thin films.[31] In addition, in H-aggregated emission, de-excitation to the zeroth vibrational level is forbidden and is typically not observed unless a high degree of disorder is present, *e.g.*, in dilute PTB7 solutions where interchain interactions are minimized.[32] As the above discussion indicates, this exception does not apply to our densely packed nanoparticles of PTB7. Therefore, it is unlikely that the origin of dual-contribution emission has to do with the vibronic splitting of the ground state. Instead, we suspect that they correspond to emissions from two different excited state species or the existence of two "populations" of conjugation lengths in our CPNs. Further investigations are underway to elucidate the exact nature of the observations.

The PTB7@F127 CPNs had the strongest fluorescence; their fluorescence quantum yield (QY) was measured to be 1.3% using the relative method[34] with Atto700 dye used as a reference (see the SI for details). The QYs of the bare PTB7 CPNs and PTB7@PSMA CPNs (0.5% and 1.0%, respectively) were determined relative to PTB7@F127 CPNs (see the SI for details). These values were of the same order of magnitude as the QY of the PTB7 polymer in solid films (2%)[35] and when dissolved in THF (1.52%; see the SI), indicating that the packing of the PTB7 chains into CPNs did not have a major detrimental impact on the fluorescence properties of the PTB7 polymer. Furthermore, the increased QYs of the coated samples correlated with the improvement in the colloidal stability of these CPNs in aqueous solutions (see the SI for stability discussions) and the corresponding changes of their absorption and emission spectra. Therefore, we expect this to be due to the nature of the excitonic species that are formed in the individual CPN samples, as determined by intra- and

https://doi.org/10.1021/acsnano.1c01257
ACS Nano 2021, 15, 8790−8802

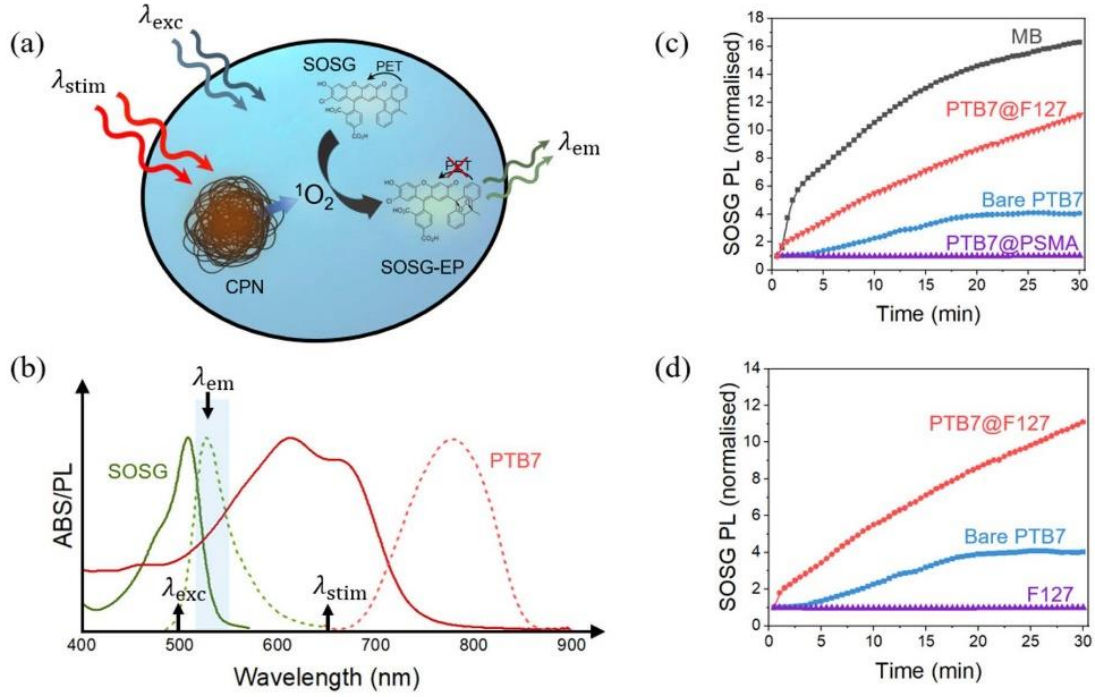

Figure 4. Measurements of singlet oxygen production by PTB7 CPNs using the SOSG chemical sensor. (a) The measurement scheme consisted of continuous stimulation of singlet oxygen production by the CPNs, conversion of SOSG into its fluorescent form, SOSG-EP, *via* a reaction with singlet oxygen, and a recording of SOSG-EP to evaluate the amount of singlet oxygen produced by the CPNs. The arrows in panel (b) indicate the relevant wavelengths used in the experiments, along with normalized absorption and emission spectra of SOSG and PTB7 CPNs. Panel (c) shows the temporal evolution of the SOSG-EP fluorescence signal for different types of CPNs and a reference photosensitizer (methylene blue, MB). Panel (d) compares singlet oxygen production by the PTB7@F127 CPNs, the bare PTB7 CPNs, and the F127 copolymer. For all measurements, samples had absorbances of ~0.5 at the stimulation wavelength (635 nm) prior to the addition of SOSG. This corresponded to CPN samples' concentrations of ~10 μg/mL and a concentration of 7.6 μM for the MB solution.

interchain interactions,[31] which are inevitably influenced by steric and other interactions between the chains of the PTB7 and F127/PSMA copolymers.

While the fluorescence QYs of our CPN samples were low (0.4−1.3%), in terms of their absolute values, these values are not atypical of many NIR emitters. Furthermore, even faint NIR-I fluorescence can be detected relatively efficiently because of the reduced autofluorescence contributions typically observed in this spectral range. More to the point, to function effectively as photosensitizers for PDT, our CPNs require an efficient intersystem crossing from the singlet excited state to the triplet excited state, a process that competes with direct de-excitation *via* emission and therefore necessarily favors a CPN with a low fluorescence QY. One should note, however, that the addition of the copolymer coating was shown to improve the fluorescence QY of the PTB7 CPNs, which is consistent with previous observations of coated CPNs made from different conjugated polymers.[19,36] Furthermore, this improvement did not come at the expense of an inhibition of ROS production, as discussed in the next sections.

It is important to highlight that the demonstrated optical properties of PTB7 CPNs are highly advantageous for bioimaging applications; they partially absorb and emit in the NIR spectral region, allowing *linear* excitation and collection of emission in the NIR-I biological transparency window. The large (~100 nm) Stokes' shifts between their absorption and emission bands allow for facile and efficient implementation into off-the-shelf imaging systems, requiring nothing more than a standard continuum lamp or laser and a judicious choice of filters. As such, the optical properties of the developed PTB7 CPNs allow facile bioimaging in the NIR-I biological transparency window, while at the same time overcoming the commonly reported drawbacks for NIR-I theranostic polymer nanoparticles, such as low photostability, rapid and irreversible photodegradation, and poor aqueous solubility (see the SI for stability evaluation of our CPNs).

Singlet Oxygen Production by CPNs. Singlet oxygen ($^1O_2$) is a highly energetic and reactive form of molecular oxygen that can be formed by triplet−triplet energy transfer between the triplet ground state of molecular oxygen and a triplet excited state of a photosensitizer.[37−39] The triplet excited state of PTB7 has been previously reported to be sufficiently energetic to generate singlet oxygen; in fact this process is widely acknowledged to cause degradation of thin PTB7 films.[24,40,41] However, and as suggested above, this property can be exploited for PDT applications.

Hence, the ability of our CPNs to produce singlet oxygen was evaluated using a chemical sensor—Singlet Oxygen Sensor Green—which turns from a nonfluorescent form (SOSG) into a highly fluorescent form (SOSG-EP) upon reaction with singlet oxygen (Figure 4(a)).[42] The production of singlet oxygen by the CPNs was continuously stimulated using a red CW laser (λ_{stim}=635 nm). After every 30 s of stimulation, the SOSG-EP fluorescence was recorded (λ_{exc}=500 nm). As shown in Figure 4(b), the SOSG did not absorb at the stimulation wavelength, and conversely, the CPNs do not

https://doi.org/10.1021/acsnano.1c01257
ACS Nano 2021, 15, 8790−8802

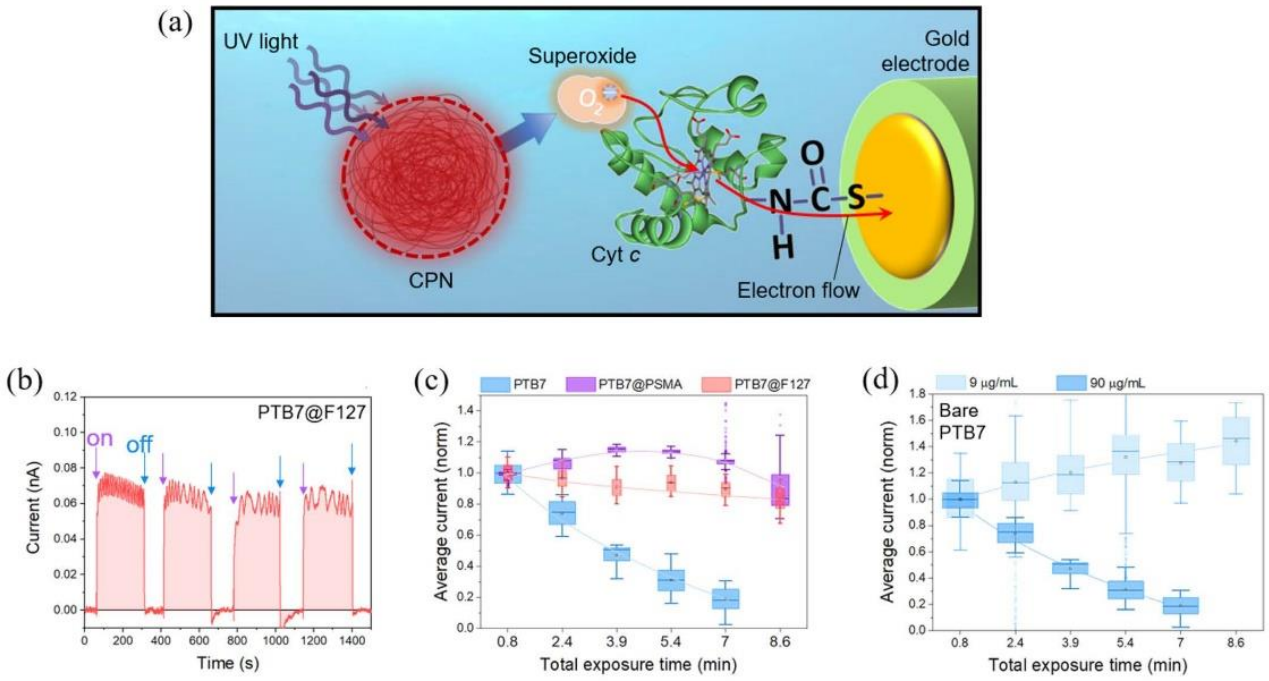

Figure 5. Superoxide production by CPNs in response to photostimulation at 365 nm. (a) Schematic showing the proposed mechanism of electrochemical superoxide detection by CPNs using a cytochrome *c*-functionalized gold electrode, poised at +100 mV. (b) Repeated photostimulation of a 40 μg/mL PTB7@F127 CPN sample at 365 nm produced reproducible current spikes. (c) Effect of PSMA and F127 coating on superoxide production by PTB7 CPN samples of high concentrations (90 μg/mL for bare PTB7 and 100 μg/mL for PTB7@PSMA and PTB7@F127 CPNs). (d) Effect of CPN concentration on superoxide production, demonstrated using the bare PTB7 CPN sample. Each data point in panels (c) and (d) represents an average of 80 s worth of data (1.2 min). During the photostimulation, the light source was consistently positioned at a distance of 10 mm away from the electrode/CPN solution.

fluoresce at wavelengths where SOSG-EP emits, thereby minimizing any crosstalk. In all cases, the concentration of the tested samples was adjusted so that they all absorbed equally at the stimulation wavelength (*i.e.*, at 635 nm). Control experiments involving evaluation of absorption spectra of CPN/SOSG mixtures postmeasurements were performed to confirm photochemical and structural stability of the CPNs during these measurements (see the "Photochemical stability of CPNs during singlet oxygen measurements" section in the SI).

We note that the excitation wavelength of 635 nm was chosen because of the compatibility of the 635 nm laser diode with the integrated spectrophotometer. In principle, any excitation wavelength in the 600−750 nm spectral range could be used instead, including those in the NIR spectral region, since the SOSG does not absorb there (Figure 4(b)).

Bare PTB7 CPNs produced singlet oxygen steadily over the 30 min measurement period (Figure 4(c)). Since the lifetime of the singlet oxygen in heavy water is on the order of tens of microseconds,[43,44] and the decay of SOSG-EP fluorescence occurred with a characteristic lifetime of ~18 min (see Section 5 of the SI), the observed trend represents a continuous generation of SOSG-EP throughout the measurement period. The plateau reached at approximately 20 min into the measurement thus represents a steady state characterized by equal rates of SOSG-EP production *via* the process described above and the decay of its fluorescence due to diffusion out of the excitation volume (see the discussion of ROS production under prolonged stimulation in the SI for further information).

Interestingly, the PTB7@F127 CPNs exhibited a marked improvement in singlet oxygen production: a 2-fold improvement was observed over a 30 min measurement period, as shown in Figure 4(c), and a 7.5-fold improvement was achieved over a 3 h period (data shown in Figure S5.2(c) in the SI). The F127 copolymer on its own produced no singlet oxygen (Figure 4(d)) and hence was not the source of the observed increase in the SOSG-EP fluorescence signal.

Production of singlet oxygen by the PTB7@F127 CPNs was stable, with no observable decreases in the signal during stimulation periods lasting up to 3 h (data in the SI). This was contrary to our control experiments with methylene blue (MB), which exhibited a steady decrease in the SOSG-EP signal after 30 min of initial increase (data in the SI). Most likely, this decrease can be attributed to MB undergoing gradual photodegradation during the prolonged stimulation.[45] In fact, despite the initially lower singlet oxygen yield of our PTB7@F127 CPNs (8.5% in ethanol and 32.4% in water) compared to that of MB (52% in ethanol and 50% in water), the CPNs perform better than MB when longer exposure times are considered (see the SI for further details of these measurements). This clearly demonstrates the advantage of CPNs over molecular photosensitizers for PDT applications, in which prolonged continuous exposures often result in photobleaching and an associated reduction in efficiencies.

It is important to note that the nature of the copolymer coats was critical in determining the performance of the PTB7 CPNs as singlet oxygen producers. While the addition of the F127 coat resulted in a 7.5-fold improvement of the singlet oxygen production compared to bare PTB7 CPNs, the

https://doi.org/10.1021/acsnano.1c01257
ACS Nano 2021, 15, 8790−8802

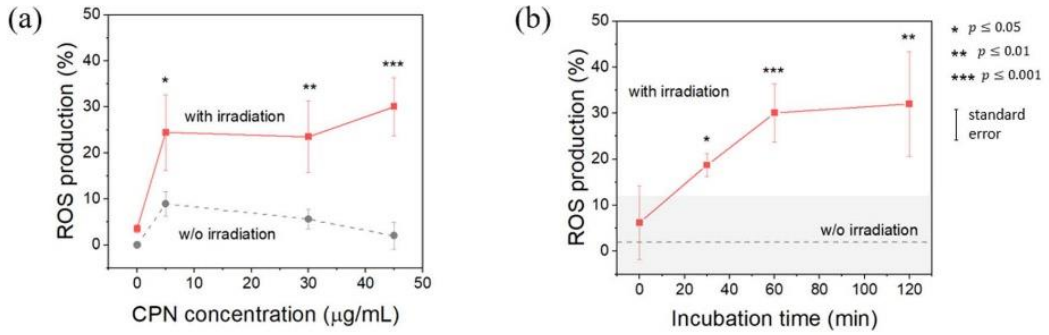

Figure 6. ***In vitro*** **ROS production by PTB7 CPNs in HaCaT cells incubated with PTB7@F127 CPN samples at concentrations up to 45 μg/mL (a). Cells were incubated with (red data points) and without NIR irradiation (gray data points) for 60 min prior to ROS measurement. The intracellular ROS production was also measured as a function of time following exposure to 45 μg/mL PTB7c@F127 CPNs (b). The dashed gray line and the height of the light gray box correspond respectively to the mean and standard deviation of ROS production for nonirradiated cells exposed to 45 μg/mL CPN samples. Each data point is an average of three repeats (n = 3). For all measurements, the NIR source used for irradiation of samples had a broad emission profile covering the 660−850 nm spectral range.**

addition of the PSMA coat completely quenched it! This observation cannot be explained by the different size/density/nature of the copolymer coats, all of which affect the diffusion of the molecular oxygen through the coat. This is because both F127 and PSMA are amphiphilic polymers that contain oxygen in their composition, and while F127 does form looser shells compared to PSMA, the PSMA shells are smaller than F127; therefore we expect the diffusion of molecular oxygen to be comparable for the two. Equally, the difference in singlet oxygen production cannot be attributed to any differences of the photophysical processes occurring within the core of the CPNs, *i.e.*, within the PTB7 polymer itself. The absorption, emission, and excitation spectra of the two coated CPN samples are very similar (see SI Figures S4.4 and S4.5 for normalized spectra that allow easier comparison); this suggests that the key photophysical processes occurring in the PTB7 cores are identical for the two CPN types. Therefore, the observed quenching of singlet oxygen production must originate at the interface of the CPN core and its copolymer coat, with PSMA completely quenching the triplet excited state of the PTB7 and the F127 facilitating the triplet−triplet energy transfer from PTB7 to molecular oxygen. This photoinitiated toxicity dependency on the capping agent highlights the significance of its role in determining the properties of the CPNs and explains why some CPNs are described as nontoxic[46−48] while others are reported to be PDT-active.[19,49] It is expected that further investigations into these aspects will allow on-demand modulation of phototoxic behavior of CPNs *via* an appropriate selection of its solubilizing shell.

Superoxide Production by CPNs. Photodynamic therapy does not always rely on the singlet oxygen production: other ROS can also be exploited. Therefore, we also investigate the possibility that our CPNs could produce another type of ROS—the superoxide radical of oxygen, O_2^-—which is also known to cause cell damage.[50,51] In this study, O_2^- production by CPNs was measured directly and in real time by using chronoamperometry.[52−54] This involved the use of a gold electrode to which cytochrome *c* was bound. The cytochrome *c* was reduced to its Fe^{2+} state by O_2^- produced by CPNs, before being reoxidized to its Fe^{3+} state at the electrode surface. This redox cycling led to a current that was proportional to the rate of O_2^- production, as shown in Figure 5(a).

Measurements showed that all three PTB7 CPN samples produced superoxide radicals upon illumination at 365 nm with a 6 W lamp (Figure 5). Note that the 365 nm wavelength was chosen, as it contributed minimally to the measured electrical currents; conversely, the use of light sources emitting in the red or NIR spectral regions, although superior for excitation of CPNs, was impractical in this case, as it caused direct photoexcitation of the gold electrode, resulting in measurements of overwhelmingly large currents that overshadowed those arising as a result of superoxide production by CPNs. Further control experiments involved using periodic illumination and addition of 100 μg/mL of superoxide specific scavenger superoxide dismutase (SOD). The modulation by periodic illumination (Figure 5(b)) and its quenching by SOD (Figure S6.1) confirmed that the current measured was superoxide radical specific and that it was, in all cases, photoinitiated (see the SI for further details). Unusually, at relatively high CPN concentrations of ∼100 μg/mL, the initial rate of superoxide production was comparable for all three samples (see the non-normalized data in the SI), indicating that it originates from the PTB7 core. However, on continued exposure to UV radiation (Figure 5(c)), the superoxide production by bare PTB7 CPNs decreased rapidly, indicating a potential degradation of the sample. In contrast, the coated CPN samples experienced only a moderate decrease in the superoxide production (<15%) over the ∼9 min irradiation period. This is significant because, at high concentrations, there is a high probability that the photogenerated superoxide radical will encounter and cause damage to another CPN, degrading the sample, whereas lower concentration reduces this risk, as seen for the bare PTB7 CPN sample of low concentration in Figure 5(d). Clearly, and importantly, the F127 and PSMA copolymer coats are sufficient to protect the PTB7 core from unfavorable photodegradation even at high sample concentrations, which maintains their ability to produce ROS such as superoxide radicals for longer periods of time. The protection offered by the copolymer coats against the ROS produced by the CPNs themselves, and the consequent longevity of the sample, is critical for the implementation of PTB7 CPNs as PDT-enabled probes *in vivo*.

In Vitro **ROS Production by PTB7 CPNs.** The optical, physical, and photochemical properties of our CPNs in aqueous dispersions, as described above, clearly demonstrate their potential as photosensitizers. To determine whether they would perform equally well in more complex, biologically relevant environments, we tested their feasibility as PDT

https://doi.org/10.1021/acsnano.1c01257
ACS Nano 2021, 15, 8790−8802

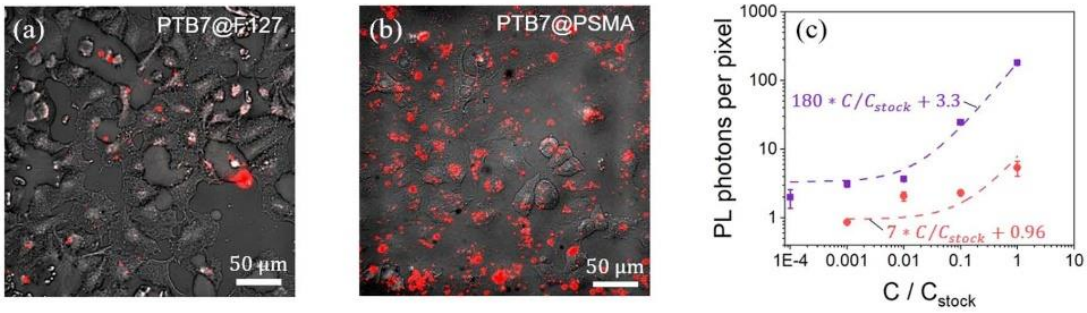

Figure 7. PTB7 CPNs as *in vitro*NIR fluorescence imaging probes. Human lung epithelial cells (A549) following incubation with (a) PTB7@F127 and (b) PTB7@PSMA CPNs at the concentration C_{stock} = 150 μg/mL, imaged using a 40× objective and RG715 filter (700−1000 nm). In both panels, the NIR fluorescent image (red) under 400−650 nm excitation is superimposed on a (grayscale) ambient-light image. (c) Number of detected fluorescence photons (average per pixel) arising from PTB7@PSMA (purple data) and PTB7@F127 CPNs (red data) imaged through a 10× objective, for different concentrations. Error bars are standard errors, based on measurements in eight subregions of the recorded image. The linear fit to the data (dashed lines) was obtained using OriginLab 2019b software and is shown as guidelines only.

agents by performing an intracellular ROS assay (see Methods for details).

The HaCaT cell line (immortalized human keratinocyte skin cells) was chosen for the purpose because PDT is particularly suited to the treatment of skin conditions. The full experimental details of the intracellular assay can be found in the Methods section. Briefly, the assay involved the use of a nonfluorescent sensor, 2′,7′-dichlorofluorescin diacetate (DCFDA), which is oxidized into a fluorescent form, 2′,7′-dichlorofluorescein (DCF), by hydroxyl, peroxyl, and other ROS. In this case, the ROS were produced by the CPNs following irradiations with a lamp whose emission spectrum covered the first biological transparency window (660−850 nm). The resulting fluorescence signals from DCF yielded a measure of ROS production by the CPNs, measured in % relative to *tert*-butyl hyperoxide (TBHP, positive control, 100% ROS production), and the medium only as a negative control (0% ROS production). As nonirradiated controls, cells dosed with the same concentrations were incubated under light exclusion for the same durations as the irradiation course, to ensure the same exposure conditions.

Results of the assay showed that nonirradiated samples incubated with CPNs produced a relatively small amount of ROS, and the differences in DCF signal of these samples and the negative control were not statistically significant ($p > 0.05$; Figure 6 and Figure S8.1). The presence of CPNs had a minimal detrimental effect on cell proliferation; this fact was confirmed by a viability assay, as discussed in Section 8 of the SI. Irradiated samples, however, showed a significant and dose-dependent increase in ROS production ($0.001 < p < 0.05$, as indicated by asterisks in Figure 6). Furthermore, for the highest concentration (45 μg/mL), there was a statistically distinguishable increase of DCF signal for incubation times of up to 60 min ($p < 0.05$ between 0/30 min and 30/60 min time points), after which the signal did not vary significantly ($p > 0.05$ for 60/120 min). These results confirm the ability of our CPNs to generate ROS under photoexcitation in biological environments and validate their photosensitizing abilities under NIR-I excitation.

PTB7 CPNs as NIR-I Imaging Agents. The existence of other modalities besides photosensitization, such as those allowing *in situ* imaging of tissues, is of particular interest for theranostic applications of nanoparticle-based agents because they allow delineation of treatment areas and therefore constitute a noninvasive diagnostic tool. In many cases, imaging modalities are achieved through addition of a dopant (*e.g.*, covalent conjugation of an MRI probe to the nanoparticle surface). However, PTB7 CPNs are inherently NIR fluorescent, thereby offering an in-built imaging modality. To demonstrate the potential of PTB7 CPNs for theranostic applications, we imaged the NIR fluorescence of our CPNs in A549 cell cultures. The uptake was assessed semiquantitatively based on the evaluation of the fraction of cells showing both internalization and stable external adherence after multiple washes. The experimental details are provided in the Methods section.

The recorded images confirmed that the CPNs were widely but nonuniformly distributed within the cells (Figure 7 and Figure S7.1 in the SI). Samples incubated with the bare PTB7 CPNs showed the weakest fluorescence signals (Figure S7.2), consistent with the lowest fluorescence QY of this sample. Of the two coated samples, PTB7@PSMA CPNs provided the strongest fluorescence signals, evaluated in terms of the photons recorded per pixel of NIR fluorescence image, despite having a lower fluorescence QY than PTB7@F127 CPNs (Figure S7.2); we attribute this to a more efficient internalization of the PTB7@PSMA CPNs by the A549 cells and note that a different trend could be observed for other cell lines.

Fluorescence images of cells incubated at lower concentrations of CPNs suggested a concentration-dependent nanoparticle uptake and fluorescence: for coated PTB7 CPNs, the average number of fluorescence photons scaled linearly with CPN concentration during incubation, as expected (Figure 7(c)). Ambient images of these samples confirmed that neither the reduced fluorescence signals for different capping agents (Figure 7(b)) nor lower CPN concentrations (Figure 7(c)) are due to variations of cell numbers and distributions, which were similar in all cases (Figure S7.3).

Therefore, the improvement of the fluorescence signals for PTB7@PSMA CPNs is again attributed to the higher affinity of PSMA to A549 cells, resulting in larger overall CPN numbers being retained on the sample post incubation and washing (Figure 7). This agrees with existing literature on PSMA, in that it is known to facilitate the penetration of the lipid bilayer of cell membranes, and the internalization and binding of drug-polymer conjugates with the hydrophobic milieu of the cell.[55−57] PTB7@F127 CPNs, on the other hand, demonstrated reduced cell uptake and internalization into the

https://doi.org/10.1021/acsnano.1c01257
ACS Nano 2021, 15, 8790−8802

A549 cells, as is expected for folate receptor-deficient cells.[58] We note, however, that this folate receptor-dependent uptake of the PTB7@F127 CPNs, along with well-established functionalization of these CPNs with appropriate ligands,[59,60] can be exploited to achieve tumor-type-specific uptake[61,62] and therefore a high degree of selectivity to tumorous tissues in theranostic applications. Nonetheless, these results perfectly demonstrate that the capping copolymers are crucial in determining the particle uptake profiles; therefore, a promising future direction is the control of CPN functionalization aimed at ligand-mediated targeting.

CONCLUSION

In this work, we have successfully prepared PTB7 CPNs, both bare and coated with F127 and PSMA copolymers. We demonstrated that the prepared CPNs have many advantageous properties for theranostic applications that consolidate bioimaging-based diagnostics and photodynamic therapy. The optical properties of PTB7 CPNs allow linear excitation and collection of emission in the NIR-I transparency window, making them a very good bioimaging agent; their sizes are optimum for accumulation in tumorous tissues *via* the EPR effect; and finally, they generate various ROS species upon photoexcitation, including singlet oxygen with quantum yields of up to 33% in water, highlighting their potential for PDT applications.

Furthermore, we demonstrated that selection of the capping material is crucial in determining the key properties of the CPNs. These not only include their fluorescence QY, their hydrodynamic size, and their cellular uptake, but also the nature and efficiency of ROS production. We show that, despite having similar optical and physical properties, and thus also similar chain packing and photophysics, the photosensitizing behavior of the F127- and PSMA-coated PTB7 CPNs was widely different: coating PTB7 CPNs with F127 copolymer led to an improvement of singlet oxygen production, while a similar process with the PSMA copolymer led to its complete quenching.

These results highlight the critical importance of the interplay between conjugated polymer and its capping agent, and the resulting photophysical and chemical properties of the conjugated polymer nanoparticles. They also explain why most conjugated polymer particles are biologically inert yet some can display photoinitiated toxicities that can be exploited for photodynamic therapy applications.

METHODS

Material. Poly({4,8-bis[(2-ethylhexyl)oxy]benzo[1,2-b:4,5-b′]-dithiophene-2,6-diyl}{3-fluoro-2-[(2-ethylhexyl)carbonyl]thieno[3,4-*b*]thiophenediyl}) (PTB7), Pluronic F-127 (F127), poly[styrene-*co*-maleic anhydride] (PSMA), tetrahydrofuran (THF), Methylene Blue (MB), Atto700 dye, and cytochrome c (from horses heart) were all purchased from Sigma-Aldrich. Singlet Oxygen Sensor Green (SOSG), deuterium oxide (D_2O), 3,3′-dithiobis(sulfosuccinimidyl propionate)) (DTSSP), and Tris Buffer were obtained from Thermo Fisher Scientific.

Preparation of PTB7 CPNs. To prepare PTB7 CPNs using the nanoprecipitation method described previously by Wu *et al.*, PTB7 powder was dissolved in THF at a concentration of 1 mg/mL, while the F127 (or PSMA) powder was dissolved in THF at a concentration of 100 mg/mL. The two solutions were sonicated until the powders were fully dissolved and then mixed in a 1:1 ratio. Two milliliters of this mixed solution was then added in a stepwise manner to 10 mL of deionized (DI) water, 200 μL at a time, under ultrasonication and vigorous stirring. The solution was then left to continuously stir for an additional 72 h in order to completely remove THF from CPNs *via* evaporation. Upon completion of this period, the sample was purified of any unbound or loosely bound copolymer by centrifugal ultrafiltration through a Millipore centrifugal filter (30 kDa, Sigma-Aldrich) at 7000 rpm for 20 min, repeated twice.

To prepare the bare PTB7 CPNs, the protocol was essentially the same, with the exclusion of addition of the F127/PSMA solution to the PTB7 solution and a reversal of the roles of the water and PTB7 solution; that is, instead of adding PTB7 to DI water, 10 mL of DI water was added to 1 mL of 1 mg/mL PTB7 solution in THF, in steps of 100 μL, under ultrasonication. The rest of the protocol remained the same.

Characterization of CPNs. Hydrodynamic diameters of CPNs in aqueous solutions were obtained using Malvern Zetasizer Nano ZS. Atomic force microscopy images were obtained using a Bruker Icon Dimension atomic force microscope. TEM imaging was performed on a JEOL 1400 transmission electron microscope, operated at 120 kV. UV−vis spectra were recorded using a Shimadzu UV-2600 spectrophotometer. Steady-state photoluminescence spectra were recorded using an Agilent Cary 60 spectrophotometer. Concentrations of samples, sizes of excitation and emission slits, and integration times were adjusted as necessary to obtain a reasonable signal. Full experimental protocols for all measurements can be found in the SI.

Singlet Oxygen Generation. Production of singlet oxygen by CPNs in aqueous solutions was monitored using a spectroscopic method, employing SOSG as a chemical sensor, according to the manufacturer's instructions. The test solution was prepared by diluting 100 μL of 100 μg/mL CPN solution in 400 μL of TRIS buffer and 500 μL of D_2O, in a 1400 μL microcuvette (Hellma). For comparison measurements, the concentration of the samples was further and finely adjusted by addition of minute amounts of D_2O, to ensure the same absorbance by all samples at the stimulation wavelength (635 nm). To this was added 0.2 μL of 5 mM SOSG probe in the dark just prior to the start of spectroscopic measurements. Singlet oxygen production by the CPNs was continuously stimulated using a 635 nm diode laser (ThorLabs, 4.5 mW) with an elliptical beam profile (4.5 mm × 1 mm), and SOSG fluorescence at 530 nm (λ_{exc} = 500 nm) was recorded at 30 s intervals, with each spectrum recorded over a 3 s period. MB was used as a positive control, employing the same protocol as above, but replacing the CPN solution with a 100 nM solution of MB instead.

The QY of singlet oxygen production by CPNs was measured using MB as a reference (Φ_{ref} = 0.52 in ethanol). Singlet oxygen production by MB was first recorded 5 min after the addition of the SOSG probe, for different concentrations of MB. These data were then used as a calibration curve to convert the SOSG fluorescence into yield of singlet oxygen for similar measurements involving a concentration series of CPN samples (full details in the SI).

Superoxide Radical Detection. Superoxide radicals photogenerated by the CPNs were detected using chronoamperometry. A MultiPalmSense4 low-noise potentiostat (Alvatek, Gloucestershire, UK) was used for the purpose, with a Ag/AgCl glass reference electrode (Clark Electrochemical Instruments Ltd., Reading, UK) and a 2 mm o.d. gold working electrode, encased in KEL-F plastic (Biotech Instruments Ltd., Kimpton, UK). Immediately prior to measurements, the working electrode was functionalized with cytochrome *c* using a protocol described previously by P. Manning *et al.*,[52] without modification. For measurements, the CPN stock solutions were diluted to the required concentrations with PBS. The working electrode was placed inside the solution, and the UV lamp was positioned in such a way as to illuminate the solution from the side. Currents were then recorded for a period of up to 30 min, with the potentiostat operating at +100 mV *versus* Ag/AgCl.

Cell Culture. A549 human lung epithelial and HaCaT human keratinocyte cell lines (European cell culture collection, ECACC, and U. Nottingham, respectively) were maintained in Roswell Park Memorial Institute RPMI-1649 with 10% v/v Fetal Bovine Serum (FBS) and supplemented with 100 IU/mL penicillin−100 μg/mL

https://doi.org/10.1021/acsnano.1c01257
ACS Nano 2021, 15, 8790−8802

streptomycin solution and 2 mM L-glutamine (Sigma-Aldrich, Dorset, UK). For experiments, 100 μL of cells at an optimal density of 5×10^5 cells/mL (HaCaT) or 5×10^4 cells/mL in complete cell culture medium were seeded onto bottom μclear black 96-well plates (Greiner Bio-One, Gloucester, UK) and incubated overnight.

ROS and Viability Assays with PTB7 CPNs. The DCFDA cellular ROS detection kit (Abcam, Cambridge, UK) was used to determine the ROS production induced by photoexcitation of CPNs, according to the manufacturer's instructions. Briefly, the cells were washed with 100 μL of 1× ROS assay buffer. The buffer was then replaced by 100 μL of DCFDA solution and incubated for 45 min in the dark and then replaced by PTB7@F127 CPN dilutions in RPMI medium (0−45 μg/mL). Without allowing time for internalization, NIR irradiation was applied with a light dose of 10 J/cm^2 at 660−850 nm using a Derma Red lamp (Care Lamps, UK) to excite the nanoparticles. Normalized fluorescence readings from the ROS-signaling DCF with an emission wavelength of 520−530 nm were taken at time intervals of 0, 30, 60, and 120 min upon incubation. Positive control wells for the ROS assay were supplemented with 100 μL of TBHP, and negative control wells contained untreated cells (n = 3). The result shows a significant increase in ROS production in the presence of even a very small amount of PTB7@F127 CPNs, while at higher CPN concentrations, the ROS production inevitably becomes dependent on the incubation time.

To better understand the cytotoxicity of PTB7@F127 CPNs, different concentrations of PTB7@F127 CPNs with different incubation times from 0 to 120 min were investigated. We used the PrestoBlue (PB) assay (Life Technologies, Carlsbad, USA), a commercially available, ready-to-use, water-soluble preparation. A HaCaT viability assay with PB reagent was performed according to the manufacturer's protocol. Briefly, HaCaT cells were seeded in a 96-well plate at a density of 1×10^4 cells per well. Prior to the assay, the growth medium was replaced by PTB7@F127 CPN dilutions in RPMI (Sigma-Aldrich, USA), 0−45 μg/mL. At the end of treatment, the cells were washed with PBS and incubated with PB reagent. The viability signaling PB (resorufin) fluorescence was read (Ex/Em 560 nm/590 nm) after 0, 60, and 120 min. The cell viability was expressed as a percentage relative to the untreated cells.

Near-Infrared Imaging. Cell cultures were prepared with CPN concentrations 1/10, 1/100, and 1/1000 of the stock solutions (90 μg/mL for bare PTB7 CPNs, 150 μg/mL for PTB7@PSMA CPNs, and 200 μg/mL for PTB7@F127 CPNs), by first replacing the A549 growth medium with CPN dilutions in complete culture cell medium (10 μL) and then incubating with cells for 7 h. Following incubation, cells were washed with warm phosphate-buffered saline (pH 7.0) and fixed with paraformaldehyde. Culture-containing plates were then imaged using an Olympus IX71 fluorescence microscope in transmission mode, imaging onto a 512 × 512 Hamamatsu 9100-23B electron-multiplying (EM-)CCD. All images were taken through a 3 mm Schott RG715 long-pass filter (715FCS; Knight Optical, Maidstone), which, together with the EM-CCD quantum efficiency, isolated the detection sensitivity to ∼700−1000 nm. Ambient and fluorescent images were obtained by varying the illumination spectrum from a 6 V, 30 W halogen lamp, which provides broadband illumination; ambient images utilized a 3 mm Schott RG665 long-pass filter (665FCS; Knight Optical), while fluorescent images were obtained through a 3 mm Schott BG39 short-pass filter paired with a 1 mm IR-cut short-pass filter (575FCS and 400FIC; Knight Optical) restricting the excitation wavelength range to ∼400−650 nm, crucially outside the ∼700−1000 nm bandpass of the imaging system. Fluorescent images required moderate EM sensitivity gain. (Note that the "ambient" illumination overlaps with the CPN excitation spectrum (Figure 3(a)) in the range ∼650−750 nm, but ambient images are used for orientation purposes only and are in any case dominated by the illumination spectrum.) The recorded raw images were minimally processed using ImageJ (Rasband 1997).

ASSOCIATED CONTENT

Supporting Information

The Supporting Information is available free of charge at https://pubs.acs.org/doi/10.1021/acsnano.1c01257.

Stabilities of bare and coated PTB7 CPNs under different ambient and physiological conditions; experimental details of size-characterization of PTB7 CPNs; discussion of F127 shell fluidity; calculation and comparison of PTB7 CPN volumes obtained from DLS and AFM data; experimental details of optical characterization of CPN samples; normalized optical spectra of all samples and their deconvolution into Gaussian components; further experimental details of measurements of singlet oxygen production by PTB7@F127 CPNs and related data; additional data for superoxide production by CPNs; additional data highlighting potential of PTB7 CPNs as NIR-I imaging agents; experimental details and additional data regrading *in vitro* ROS production by PTB7 CPNs (PDF)

AUTHOR INFORMATION

Corresponding Authors

Aliaksandra Rakovich − *Physics Department, King's College London, London WC2R 2LS, U.K.;* orcid.org/0000-0003-1056-5729; Email: aliaksandra.rakovic@kcl.ac.uk

Mark A. Green − *Physics Department, King's College London, London WC2R 2LS, U.K.;* orcid.org/0000-0001-7507-1274; Email: mark.a.green@kcl.ac.uk

Authors

Miao Zhao − *Physics Department, King's College London, London WC2R 2LS, U.K.;* orcid.org/0000-0001-6972-0872

Edward Leggett − *Physics Department, King's College London, London WC2R 2LS, U.K.;* orcid.org/0000-0003-0327-6857

Struan Bourke − *Physics Department, King's College London, London WC2R 2LS, U.K.;* orcid.org/0000-0003-1534-6736

Souzana Poursanidou − *Department of Clinical, Pharmaceutical and Biological Sciences, University of Hertfordshire, Hatfield, Hertfordshire AL10 9AB, U.K.*

Sadie Carter-Searjeant − *Physics Department, King's College London, London WC2R 2LS, U.K.;* orcid.org/0000-0003-4912-4779

Steve Po − *Physics Department, King's College London, London WC2R 2LS, U.K.;* orcid.org/0000-0002-1826-4966

Marciano Palma do Carmo − *Physics Department, King's College London, London WC2R 2LS, U.K.;* orcid.org/0000-0002-1022-3246

Lea Ann Dailey − *Department of Pharmaceutical Technology and Biopharmacy, University of Vienna, Vienna 1090, Austria;* orcid.org/0000-0001-8220-5701

Philip Manning − *Translational and Clinical Research Institute, Faculty of Medical Sciences, Newcastle University, Newcastle upon Tyne, Tyne and Wear NE2 4HH, U.K.;* orcid.org/0000-0001-6961-827X

Sean G. Ryan − *Department of Physics, Astronomy and Mathematics, University of Hertfordshire, Hatfield, Hertfordshire AL10 9AB, U.K.; Centre for Advanced*

https://doi.org/10.1021/acsnano.1c01257
ACS Nano 2021, 15, 8790−8802

Biomedical Imaging, University College London, London WC1E 6BT, U.K.; orcid.org/0000-0001-9069-5122

Laura Urbano − *Department of Clinical, Pharmaceutical and Biological Sciences, University of Hertfordshire, Hatfield, Hertfordshire AL10 9AB, U.K.;* orcid.org/0000-0001-8524-3359

Complete contact information is available at: https://pubs.acs.org/10.1021/acsnano.1c01257

Author Contributions

M.Z. contributed to all experimental work, with the exception of NIR imaging and intracellular ROS production measurements. E.L. and S.B. contributed to CPN fabrication. S.C.-S. and S.P. assisted with CPN characterization (TEM and AFM). S.P. and L.U. performed the intracellular ROS production measurements. L.U. and S.G.R. performed the NIR imaging of cell lines incubated with CPNs. A.R. and P.M. performed the superoxide measurements. M.Z., M.P.C., S.P., L.U., and A.R. performed data analysis. All authors contributed toward the writing of the manuscript. L.A.D., M.G., and A.R. are responsible for the conception of the project, its direction, and management of the team. All authors have approved the submitted version and have agreed to be personally accountable for their own contributions.

Notes

The authors declare no competing financial interest.

ACKNOWLEDGMENTS

A.R., S.P., and M.P.d.C. would like to acknowledge the financial support of the Royal Society (UF150542, RGF/EA/180118, RGF/R1/180068). M.Z. is sponsored by the China Scholarship Council (File No. 201806010011). The NIHR Newcastle Biomedical Research Centre (BRC) is a partnership between Newcastle Hospitals NHS Foundation Trust and Newcastle University, funded by the National Institute for Health Research (NIHR). P.M. is supported by the NIHR Newcastle Biomedical Research Centre (BRC). The views expressed are those of the author(s) and not necessarily those of the NIHR or the Department of Health and Social Care.

REFERENCES

(1) Dolmans, D. E. J. G. J.; Fukumura, D.; Jain, R. K. Photodynamic Therapy for Cancer. *Nat. Rev. Cancer* **2003**, *3* (5), 380−387.

(2) Agostinis, P.; Berg, K.; Cenge, K. A.; Foster, T. H.; Girotti, A. W.; Gollnick, S. O.; Hahn, S. M.; Hamblin, M. R.; Juzeniene, A.; Kessel, D.; Korbelik, M.; Moan, J.; Mroz, P.; Nowis, D.; Piette, J.; Wilson, B. C.; Golab, J. Photodynamic Therapy of Cancer: An Update. *Ca-Cancer J. Clin.* **2017**, *61* (April), 250−281. .

(3) Anand, S.; Ortel, B. J.; Pereira, S. P.; Hasan, T.; Maytin, E. V. Biomodulatory Approaches to Photodynamic Therapy for Solid Tumors. *Cancer Lett.* **2012**, *326* (1), 8−16.

(4) Tsai, M. F.; Chang, S. H. G.; Cheng, F. Y.; Shanmugam, V.; Cheng, Y. S.; Su, C. H.; Yeh, C. S. Au Nanorod Design as Light-Absorber in the First and Second Biological Near-Infrared Windows for *in Vivo* Photothermal Therapy. *ACS Nano* **2013**, *7* (6), 5330−5342.

(5) Cao, J.; Zhu, B.; Zheng, K.; He, S.; Meng, L.; Song, J.; Yang, H. Recent Progress in NIR-II Contrast Agent for Biological Imaging. *Front. Bioeng. Biotechnol.* **2020**, *7*, 1−21.

(6) Lane, L. A.; Xue, R.; Nie, S. Emergence of Two Near-Infrared Windows for *in Vivo* and Intraoperative SERS. *Curr. Opin. Chem. Biol.* **2018**, *45* (April), 95−103.

(7) Hashizume, H.; Baluk, P.; Morikawa, S.; McLean, J. W.; Thurston, G.; Roberge, S.; Jain, R. K.; McDonald, D. M. Openings between Defective Endothelial Cells Explain Tumor Vessel Leakiness. *Am. J. Pathol.* **2000**, *156* (4), 1363−1380.

(8) Hu, L.; Zhang, C.; Zeng, G.; Chen, G.; Wan, J.; Guo, Z.; Wu, H.; Yu, Z.; Zhou, Y.; Liu, J. Metal-Based Quantum Dots: Synthesis, Surface Modification, Transport and Fate in Aquatic Environments and Toxicity to Microorganisms. *RSC Adv.* **2016**, *6* (82), 78595−78610.

(9) Kim, H. S.; Lee, D. Y. Near-Infrared-Responsive Cancer Photothermal and Photodynamic Therapy Using Gold Nanoparticles. *Polymers (Basel, Switz.)* **2018**, *10* (9), 1−14.

(10) Pu, K. Y.; Liu, B. Optimizing the Cationic Conjugated Polymer-Sensitized Fluorescent Signal of Dye Labeled Oligonucleotide for Biosensor Applications. *Biosens. Bioelectron.* **2009**, *24* (5), 1067−1073.

(11) Kilin, V. N.; Anton, H.; Anton, N.; Steed, E.; Vermot, J.; Vandamme, T. F.; Mely, Y.; Klymchenko, A. S. Counterion-Enhanced Cyanine Dye Loading into Lipid Nano-Droplets for Single-Particle Tracking in Zebrafish. *Biomaterials* **2014**, *35* (18), 4950−4957.

(12) Duan, X.; Liu, L.; Feng, F.; Wang, S. Cationic Conjugated Polymers for Optical Detection of DNA Methylation, Lesions, and Single Nucleotide Polymorphisms. *Acc. Chem. Res.* **2010**, *43* (2), 260−270.

(13) Wu, C.; Chiu, D. T. Highly Fluorescent Semiconducting Polymer Dots for Biology and Medicine. *Angew. Chem., Int. Ed.* **2013**, *52* (11), 3086−3109.

(14) Zhu, C.; Liu, L.; Yang, Q.; Lv, F.; Wang, S. Water-Soluble Conjugated Polymers for Imaging, Diagnosis, and Therapy. *Chem. Rev.* **2012**, *112* (8), 4687−4735.

(15) Kuehne, A. J. C. Conjugated Polymer Nanoparticles toward *in Vivo* Theranostics − Focus on Targeting, Imaging, Therapy, and the Importance of Clearance. *Adv. Biosyst.* **2017**, *1* (11), 1700100.

(16) Li, K.; Liu, B. Polymer Encapsulated Conjugated Polymer Nanoparticles for Fluorescence Bioimaging. *J. Mater. Chem.* **2012**, *22* (4), 1257−1264.

(17) Abelha, T. F.; Dreiss, C. A.; Green, M. A.; Dailey, L. A.; Abelha, T. F. Conjugated Polymers as Nanoparticle Probes for Fluorescence and Photoacoustic Imaging. *J. Mater. Chem. B* **2020**, *8* (4), 592−606.

(18) Rohatgi, C. V.; Harada, T.; Need, E. F.; Krasowska, M.; Beattie, D. A.; Dickenson, G. D.; Smith, T. A.; Kee, T. W. Low-Bandgap Conjugated Polymer Dots for Near-Infrared Fluorescence Imaging. *ACS Appl. Nano Mater.* **2018**, *1* (9), 4801−4808.

(19) Feng, G.; Fang, Y.; Liu, J.; Geng, J.; Ding, D.; Liu, B. Multifunctional Conjugated Polymer Nanoparticles for Image-Guided Photodynamic and Photothermal Therapy. *Small* **2017**, *13* (3), 1−12.

(20) Yuan, H.; Wang, B.; Lv, F.; Liu, L.; Wang, S. Conjugated-Polymer-Based Energy-Transfer Systems for Antimicrobial and Anticancer Applications. *Adv. Mater.* **2014**, *26* (40), 6978−6982.

(21) Gesquiere, A. J.; Jasmin, K.; Topps, M.; Shroff, S.; Ortiz, A. M.; George, O.; Abdellatif, Y.; Ortiz Ortiz, A. M.; Abdellatif, Y. Conjugated Polymer Nanotherapeutics for Next Generation Photodynamic Therapy. *Med. Res. Arch.* **2018**, *6* (2), 23.

(22) Manandhar, S.; Sjöholm, E.; Bobacka, J.; Rosenholm, J. M.; Bansal, K. K. Polymer-Drug Conjugates as Nanotheranostic Agents. *J. Nanotheranostics* **2021**, *2* (1), 63−81.

(23) Wang, C.; Zhang, W.; Meng, X.; Bergqvist, J.; Liu, X.; Genene, Z.; Xu, X.; Yartsev, A.; Inganäs, O.; Ma, W.; Wang, E.; Fahlman, M. Ternary Organic Solar Cells with Minimum Voltage Losses. *Adv. Energy Mater.* **2017**, *7* (21), 1700390.

(24) Soon, Y. W.; Cho, H.; Low, J.; Bronstein, H.; McCullocha, I.; Durrant, J. R. Correlating Triplet Yield, Singlet Oxygen Generation and Photochemical Stability in Polymer/Fullerene Blend Films. *Chem. Commun.* **2013**, *49* (13), 1291−1293.

(25) Wu, C.; Szymanski, C.; McNeill, J. Preparation and Encapsulation of Highly Fluorescent Conjugated Polymer Nanoparticles. *Langmuir* **2006**, *22* (7), 2956−2960.

(26) Brown, W.; Schillén, K.; Almgren, M.; Hvidt, S.; Bahadur, P. Micelle and Gel Formation in a Poly(ethylene Oxide)/Poly(propylene Oxide)/ Poly(ethylene Oxide) Triblock Copolymer in Water Solution. Dynamic and Static Light Scattering and Oscillatory Shear Measurements. *J. Phys. Chem.* **1991**, *95* (4), 1850−1858.

(27) Abelha, T. F.; Neumann, P. R.; Holthof, J.; Dreiss, C. A.; Alexander, C.; Green, M.; Dailey, L. A. Low Molecular Weight PEG-PLGA Polymers Provide a Superior Matrix for Conjugated Polymer Nanoparticles in Terms of Physicochemical Properties, Biocompatibility and Optical/Photoacoustic Performance. *J. Mater. Chem. B* **2019**, *7* (33), 5115−5124.
(28) Hoshyar, N.; Gray, S.; Han, H.; Bao, G. The Effect of Nanoparticle Size on *in Vivo* Pharmacokinetics and Cellular Interaction. *Nanomedicine* **2016**, *11* (6), 673−692.
(29) Guo, X.; Wu, Z.; Li, W.; Wang, Z.; Li, Q.; Kong, F.; Zhang, H.; Zhu, X.; Du, Y. P.; Jin, Y.; Du, Y.; You, J. Appropriate Size of Magnetic Nanoparticles for Various Bioapplications in Cancer Diagnostics and Therapy. *ACS Appl. Mater. Interfaces* **2016**, *8* (5), 3092−3106.
(30) Nagayama, S.; Ogawara, K.-i.; Fukuoka, Y.; Higaki, K.; Kimura, T. Time-Dependent Changes in Opsonin Amount Associated on Nanoparticles Alter Their Hepatic Uptake Characteristics. *Int. J. Pharm.* **2007**, *342* (1−2), 215−221.
(31) Bencheikh, F.; Duché, D.; Ruiz, C. M.; Simon, J. J.; Escoubas, L. Study of Optical Properties and Molecular Aggregation of Conjugated Low Band Gap Copolymers: PTB7 and PTB7-Th. *J. Phys. Chem. C* **2015**, *119* (43), 24643−24648.
(32) Spano, F. C.; Silva, C. H- and J-Aggregate Behavior in Polymeric Semiconductors. *Annu. Rev. Phys. Chem.* **2014**, *65* (1), 477−500.
(33) Ito, M.; Palanisamy, K.; Kumar, A.; Murugesan, V. S.; Shin, P. K.; Tsuda, N.; Yamada, J.; Ochiai, S. Characterization of the Organic Thin Film Solar Cells with Active Layers of PTB7/PC71BM Prepared by Using Solvent Mixtures with Different Additives. *Int. J. Photoenergy* **2014**, *2014*, 8 .
(34) Demas, J. N.; Crosby, G. A. The Measurement of Photoluminescence Quantum Yields. A Review. *J. Phys. Chem.* **1971**, *75* (8), 991−1024.
(35) Hedley, G. J.; Ward, A. J.; Alekseev, A.; Howells, C. T.; Martins, E. R.; Serrano, L. A.; Cooke, G.; Ruseckas, A.; Samuel, I. D. W. Determining the Optimum Morphology in High-Performance Polymer-Fullerene Organic Photovoltaic Cells. *Nat. Commun.* **2013**, *4*, 2867.
(36) Crossley, D. L.; Urbano, L.; Neumann, R.; Bourke, S.; Jones, J.; Dailey, L. A.; Green, M.; Humphries, M. J.; King, S. M.; Turner, M. L.; Ingleson, M. J. Post-Polymerization C-H Borylation of Donor-Acceptor Materials Gives Highly Efficient Solid State Near-Infrared Emitters for Near-IR-OLEDs and Effective Biological Imaging. *ACS Appl. Mater. Interfaces* **2017**, *9* (34), 28243−28249.
(37) Wang, S.; Gao, R.; Zhou, F.; Selke, M. Nanomaterials and Singlet Oxygen Photosensitizers: Potential Applications in Photodynamic Therapy. *J. Mater. Chem.* **2004**, *14*, 487−493.
(38) Plaetzer, K.; Krammer, B.; Berlanda, J.; Berr, F.; Kiesslich, T. Photophysics and Photochemistry of Photodynamic Therapy: Fundamental Aspects. *Lasers Med. Sci.* **2009**, *24* (2), 259−268.
(39) Gorman, A. A.; Rodgers, M. A. J. Singlet Molecular Oxygen. *Chem. Soc. Rev.* **1981**, *10*, 205−231.
(40) Kim, S.; Rashid, M. A. M.; Ko, T.; Ahn, K.; Shin, Y.; Nah, S.; Kim, M. H.; Kim, B. S.; Kwak, K.; Cho, M. New Insights into the Photodegradation Mechanism of the PTB7-Th Film: Photooxidation of π-Conjugated Backbone upon Sunlight Illumination. *J. Phys. Chem. C* **2020**, *124* (5), 2762−2770.
(41) Salvador, M.; Gasparini, N.; Perea, J. D.; Paleti, S. H.; Distler, A.; Inasaridze, L. N.; Troshin, P. A.; Lüer, L.; Egelhaaf, H. J.; Brabec, C. Suppressing Photooxidation of Conjugated Polymers and Their Blends with Fullerenes through Nickel Chelates. *Energy Environ. Sci.* **2017**, *10* (9), 2005−2016.
(42) Lin, H.; Shen, Y.; Chen, D.; Lin, L.; Wilson, B. C.; Li, B.; Xie, S. Feasibility Study on Quantitative Measurements of Singlet Oxygen Generation Using Singlet Oxygen Sensor Green. *J. Fluoresc.* **2013**, *23* (1), 41−47.
(43) Matheson, I. B. C.; Lee, J.; King, A. D. The Lifetime of Singlet Oxygen ($1\Delta g$) in Heavy Water, a Revised Value. *Chem. Phys. Lett.* **1978**, *55* (1), 49−51.
(44) Lindig, B. A.; Rodgers, M. A. J.; Schaaplc, A. P. Determination of the Lifetime of Singlet Oxygen in D20 Using 9,10-Anthracenedipropionic Acid, a Water-Soluble Probe. *J. Am. Chem. Soc.* **1980**, *102* (17), 5590−5593.
(45) Sáenz-Trevizo, A.; Pizá-Ruiz, P.; Chávez-Flores, D.; Ogaz-Parada, J.; Amézaga-Madrid, P.; Vega-Ríos, A.; Miki-Yoshida, M. On the Discoloration of Methylene Blue by Visible Light. *J. Fluoresc.* **2019**, *29* (1), 15−25.
(46) Wei, Z.; Xue, F.; Xin, F.; Wu, M.; Wang, B.; Zhang, X.; Yang, S.; Guo, Z.; Liu, X. A Thieno-Isoindigo Derivative-Based Conjugated Polymer Nanoparticle for Photothermal Therapy in the NIR-II Bio-Window. *Nanoscale* **2020**, *12* (38), 19665−19672.
(47) Guo, B.; Sheng, Z.; Kenry; Hu, D.; Lin, X.; Xu, S.; Liu, C.; Zheng, H.; Liu, B. Biocompatible Conjugated Polymer Nanoparticles for Highly Efficient Photoacoustic Imaging of Orthotopic Brain Tumors in the Second Near-Infrared Window. *Mater. Horiz.* **2017**, *4* (6), 1151−1156.
(48) Calzoni, E.; Cesaretti, A.; Polchi, A.; Di Michele, A.; Tancini, B.; Emiliani, C. Biocompatible Polymer Nanoparticles for Drug Delivery Applications in Cancer and Neurodegenerative Disorder Therapies. *J. Funct. Biomater.* **2019**, *10* (1), 1−15.
(49) Meng, Z.; Hou, W.; Zhou, H.; Zhou, L.; Chen, H.; Wu, C. Therapeutic Considerations and Conjugated Polymer-Based Photosensitizers for Photodynamic Therapy. *Macromol. Rapid Commun.* **2018**, *39* (5), 1−15.
(50) Chen, Y.; Azad, M. B.; Gibson, S. B. Superoxide Is the Major Reactive Oxygen Species Regulating Autophagy. *Cell Death Differ.* **2009**, *16* (7), 1040−1052.
(51) Buccellato, L. J.; Tso, M.; Akinci, O. I.; Chandel, N. S.; Budinger, G. R. S. Reactive Oxygen Species Are Required for Hyperoxia-Induced Bax Activation and Cell Death in Alveolar Epithelial Cells. *J. Biol. Chem.* **2004**, *279* (8), 6753−6760.
(52) Manning, P.; McNeil, C. J.; Cooper, J. M.; Hillhouse, E. W. Direct, Real-Time Sensing of Free Radical Production by Activated Human Glioblastoma Cells. *Free Radical Biol. Med.* **1998**, *24* (97), 1304−1309.
(53) Manning, P.; Cookson, M. R.; McNeil, C. J.; Figlewicz, D.; Shaw, P. J. Superoxide-Induced Nitric Oxide Release from Cultured Glial Cells. *Brain Res.* **2001**, *911* (2), 203−210.
(54) Boulton, S. J.; Keane, P. C.; Morris, C. M.; McNeil, C. J.; Manning, P. Real-Time Monitoring of Superoxide Generation and Cytotoxicity in Neuroblastoma Mitochondria Induced by 1-Trichloromethyl- 1,2,3,4-Tetrahydro-Beta-Carboline. *Redox Rep.* **2012**, *17* (3), 108−114.
(55) Oda, T.; Maeda, H. Binding to and Internalization by Cultured Cells of Neocarzinostatin and Enhancement of Its Actions by Conjugation with Lipophilic Styrene-Maleic Acid Copolymer. *Cancer Res.* **1987**, *47* (12), 3206−3211.
(56) Guller, A. E.; Generalova, A. N.; Petersen, E. V.; Nechaev, A. V.; Trusova, I. A.; Landyshev, N. N.; Nadort, A.; Grebenik, E. A.; Deyev, S. M.; Shekhter, A. B.; Zvyagin, A. V. Cytotoxicity and Non-Specific Cellular Uptake of Bare and Surface-Modified Upconversion Nanoparticles in Human Skin Cells. *Nano Res.* **2015**, *8* (5), 1546−1562.
(57) Blanco, E.; Shen, H.; Ferrari, M. Principles of Nanoparticle Design for Overcoming Biological Barriers to Drug Delivery. *Nat. Biotechnol.* **2015**, *33* (9), 941−951.
(58) Chen, Y.; Zhang, W.; Huang, Y.; Gao, F.; Sha, X.; Lou, K.; Fang, X. The Therapeutic Effect of Methotrexate-Conjugated Pluronic-Based Polymeric Micelles on the Folate Receptor-Rich Tumors Treatment. *Int. J. Nanomed.* **2015**, *10*, 4043−4057.
(59) Pitto-Barry, A.; Barry, N. P. E. Pluronic® Block-Copolymers in Medicine: From Chemical and Biological Versatility to Rationalisation and Clinical Advances. *Polym. Chem.* **2014**, *5* (10), 3291−3297.
(60) Akash, M. S. H.; Rehman, K. Recent Progress in Biomedical Applications of Pluronic (PF127): Pharmaceutical Perspectives. *J. Controlled Release* **2015**, *209*, 120−138.
(61) Russo, A.; Pellosi, D. S.; Pagliara, V.; Milone, M. R.; Pucci, B.; Caetano, W.; Hioka, N.; Budillon, A.; Ungaro, F.; Russo, G.; Quaglia,

https://doi.org/10.1021/acsnano.1c01257
ACS Nano 2021, 15, 8790−8802

F. Biotin-Targeted Pluronic® P123/F127 Mixed Micelles Delivering Niclosamide: A Repositioning Strategy to Treat Drug-Resistant Lung Cancer Cells. *Int. J. Pharm.* **2016**, *511* (1), 127−139.
(62) Wang, H.; Zhang, F.; Wen, H.; Shi, W.; Huang, Q.; Huang, Y.; Xie, J.; Li, P.; Chen, J.; Qin, L.; Zhou, Y. Tumor- and Mitochondria-Targeted Nanoparticles Eradicate Drug Resistant Lung Cancer through Mitochondrial Pathway of Apoptosis. *J. Nanobiotechnol.* **2020**, *18* (1), 1−21.

https://doi.org/10.1021/acsnano.1c01257
ACS Nano 2021, 15, 8790−8802

Supplementary Information to

Theranostic Near Infrared-Active Conjugated Polymer Nanoparticles

Miao Zhao[1], Edward Leggett[1], Struan Bourke[1], Souzana Poursanidou[2], Sadie Carter-Searjeant[1], Steve Po[1], Marciano Palma do Carmo[1], Lea Ann Dailey[3], Philip Manning[4], Sean G. Ryan[5,6], Laura Urbano[2], Mark A. Green[1,], Aliaksandra Rakovich[1,*]*

1. King's College London, Physics Department, Strand Building, London, WC2R 2LS, UK.

2. University of Hertfordshire, Department of Clinical, Pharmaceutical and Biological Sciences, College Lane, Hatfield, Hertfordshire, AL10 9AB, UK.

3. University of Vienna, Department of Pharmaceutical Technology and Biopharmacy, Vienna, Wien 1090, Austria.

4. Newcastle University, Translational and Clinical Research Institute, Faculty of Medical Sciences, Newcastle upon Tyne, Tyne and Wear, NE2 4HH, UK.

5. University of Hertfordshire, Department of Physics, Astronomy and Mathematics, College Lane, Hatfield, Hertfordshire, AL10 9AB, UK.

6. University College London, Centre for Advanced Biomedical Imaging, Gower Street, London, WC1E 6BT, UK.

Contents

Stabilities of bare and coated PTB7 CPNs

Any application of the developed nanomaterials for photodynamic therapy would require storage for prolonged periods of time, utilization in physiological conditions and under prolonged excitations. Here we explore the stabilities of the prepared PTB7 CPN samples under such conditions.

Stability under physiological conditions (in vitro)

The stability of PTB7 CPN samples under physiological conditions was evaluated *in vitro* by monitoring the properties of the CPNs in solutions of different pH values and in the presence of Fetal Bovine Serum (FBS).

The stability of PTB7 samples in the presence of FBS was evaluated by monitoring their optical properties when dissolved in solutions of different FBS concentrations. Samples were excited at 620 nm, and the fluorescence spectra were recorded in the 640 – 900 nm spectral range. Results showed that the fluorescence intensity of the bare PTB7 and PTB7@F127 CPNs remained approximately the same across the investigated range of FBS concentrations (0-95 %v/v). For PTB7@PSMA CPNs sample, however, the fluorescence intensity increased sharply with increasing FBS concentrations, becoming stable at FBS concentrations higher than 50 %v/v (Figure S1.1a). For all samples and FBS

concentrations, the fluorescence peak fluctuated very little: a 4 nm and 6 nm shift was observed for PTB7@F127 CPNs and for PTB7@PSMA CPNs and bare PTB7 samples respectively (Figure S1.1b), all of which are much smaller than the full-width half-maximum of the peak (150-200 nm). Therefore, for PTB7@F127 CPNs and bare PTB7 samples, fluorescence appeared to be stable in the presence of different concentrations of FBS. For PTB7@PSMA CPN samples, the increase in the intensity of the fluorescence without major changes to the shape of the fluorescence bands indicates that the nature of the excitonic species responsible for the emission has not changed, but the interactions of the capping PSMA molecules with the core PTB7 chains is affected by the presence of the FBS. The result of these interactions seems to be reduced quenching of PTB7 fluorescence by the PSMA and a corresponding increase of the fluorescence intensity.

The different fluorescence behaviors of the three types of particles in FBS seem to suggest that the smaller PSMA copolymer molecules are affected the most by the presence of the FBS, implying possible changes to the physical packing of the polymer strands and/or organization of the copolymer molecules on the PTB7 core within the PTB7@PSMA CPNs, but not for the other two particles. Dynamic Light Scattering measurements were therefore performed to seek evidence for such reorganization. As can be seen in panels (c) and (d) of Figure S1.1, these data do support the hypothesis to some degree, as the largest changes in particle size were observed for the PTB7@PSMA CPNs. However, the hydrodynamic diameter of CPNs increased for all three samples at higher FBS concentrations: the average diameter of bare PTB7 CPNs increased from 211 nm to 370 nm, that of PTB7@F127 CPNs increased from 224 nm to 301 nm and that of the PTB7@PSMA CPNs increased from 164 to 410 nm. This corresponds to relative increases of 1.8, 2.5 and 1.4 in the average particle size of bare PTB7, PTB7@PSMA and PTB7@F127 CPNs. The DLS measurements presented here

clearly evidence the organization of polymer chains in the CPNs when in the presence of the FBS, but they do so for all three particles. It can be argued that the larger increase in particle size of the PTB7@PSMA CPNs is due to the stronger reorganization of the cap molecules, which would be in line with the observed changes in the fluorescence. However, further investigations into the photophysics of the PTB7 CPNs in FBS are required to make concrete conclusions in this regard.

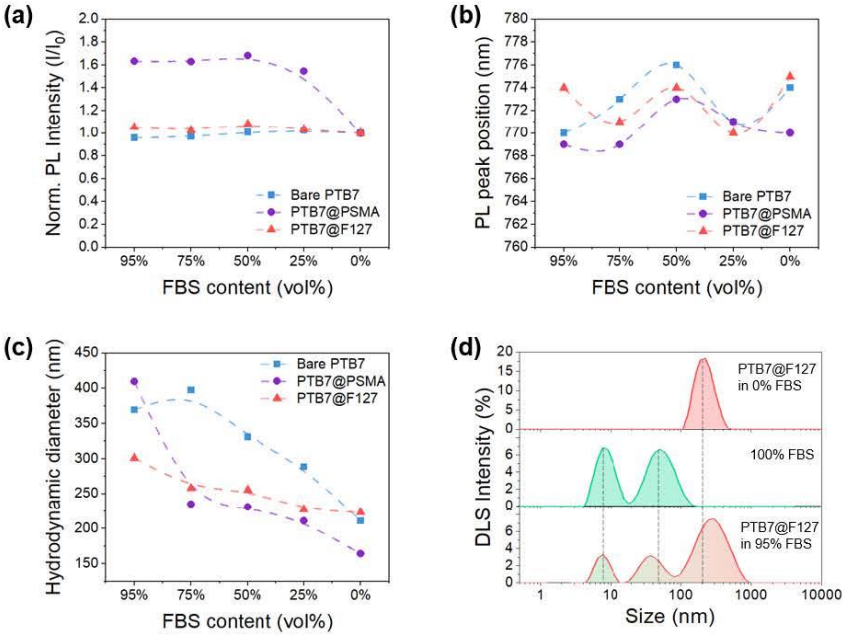

Figure S1.1. Fluorescence and size of PTB7 samples in presence of different concentrations of FBS. Both the intensity (a) and the position (b) of the fluorescence peak of all three PTB7 samples depended on the concentration of FBS. In panel (c), the size of all three PTB7 samples increased with increased concentration of FBS in solution and the size of PTB7@F127 is the mostly stable while the size of PTB7@PSMA CPNs increased the most obvious. In panel (d), the dashed violet line indicates the average size (Z_{av}) of the PTB7@F127 with 0% FBS in solution and the dashed olive line indicates the Z_{av} of pure FBS.

The performance of CPNs in solutions of different pHs was evaluated next. Results showed that all samples performed best at normal physiological conditions (pH 7.4), with highest fluorescence QYs recorded for all three samples in this pH region (Figure S1.2a). Equally, the fluorescence QY of all three samples decreased sharply, capping-dependent but by no more than 50%, for pH values corresponding to tumor pathology (pH 5-7).[1,2] Associated with this decrease was also a blue shift of the fluorescence peak of the order of 6 nm for all three samples (Figure S1.2b), but again this is minimal compared to the FWHM of the fluorescence peaks. Nonetheless, the pH-sensitive fluorescence intensity properties of our theranostic CPNs probes could be of significance for differentiation of healthy and tumorous tissues.

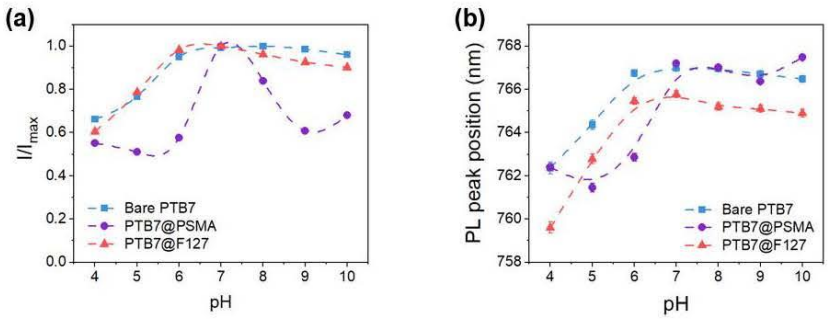

Figure S1.2. Fluorescence of PTB7 samples in solutions of different pH values. Both the intensity **(a)** and the position **(b)** of the fluorescence peak of all three PTB7 samples depended on the pH of the solution.

Dynamic light scattering measurements revealed that the hydrodynamic sizes of the bare PTB7 and PTB7@F127 CPNs remain approximately same across the investigated pH range (4-10, Figure S1.3a), and this was in line with the UV-vis measurements that showed minimal changes in the absorption spectra of these samples (Figure S1.3b and d). For PTB7@PSMA CPNs, however, notable

changes were observed both in the average hydrodynamic size of the CPNs and their absorption spectra (Figure S1.3a and c).

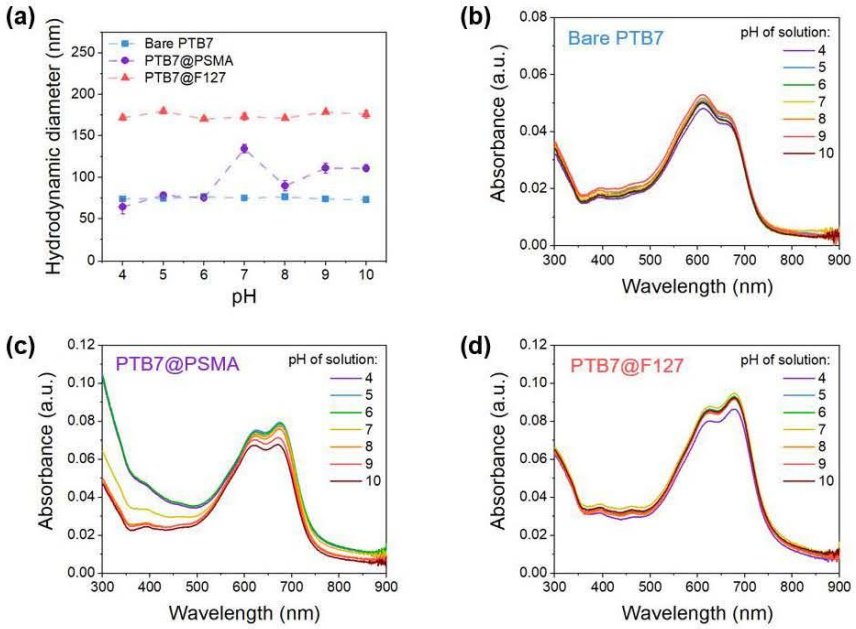

Figure S1.3. Absorption and size of PTB7 CPNs as a function of pH. (a) Average hydrodynamic diameter of bare PTB7 (blue), PTB7@PSMA CPNs (purple) and PTB7@F127 CPNs (pink) when dispersed in solutions of different pHs. Panels (b)-(d) show the pH dependency of the absorption spectra of (b) bare PTB7, (c) PTB7@PSMA CPNs and (d) PTB7@F127 CPNs.

The size of the particles decreased strongly when the pH of the solution was lowered (Figure S1.3a), with an associated increase in the absorption by these samples at the lower wavelength range (Figure S1.3c). In addition, above pH of 7.4, the relative intensities of the peaks corresponding to the two vibronic levels of the excited state of PTB7 polymer also changed, suggesting re-organization of the polymer in the CPNs. In general, it is reasonable that this would only occur for PTB7@PSMA CPNs as these particles have thin shells. For PTB7@F127 CPNs, the F127 copolymer is quite long and

therefore the energetic cost of restructuring is too high for it to occur. For base PTB7 CPNs, the relatively hydrophobic chains of PTB7 have already wrapped into the tightest core possible to minimize the surface energy; changing the pH of the solution does not change this energy significantly enough to cause a reorganization of the PTB7 chains. Therefore, for these two samples, the diameters remain approximately same under all pHs tested, while for PSMA coated CPNs, the reorganization of the PTB7 and copolymer chains led to changes in the CPNs diameter and changes of its absorbance.

Photostability of CPN samples

The photostability of the PTB7 CPN samples was investigated by monitoring the fluorescence signal under prolonged excitation. All PTB7 CPN samples showed some degree of photobleaching under continuous irradiation by the 635 nm CW laser, at 100μW power (Figure S1.4). However, for all of them, the photobleaching was relatively low: as shown in Figure S1.4, even after 2 hours of irradiation, the fluorescence intensity of PTB7 CPN samples decreased only by 25%. Therefore, the CPNs produced in this study demonstrate excellent photobleaching resistance and photochemical stable. This is critical for practical applications requiring long term imaging.

Even at higher excitation powers of 200 μW, the photobleaching of the CPN samples remained relatively low. A slightly stronger effect was observed for PTB7@F127 CPN samples (Figure S1.4d), while no change in the photobleaching behaviour was recorded for the PTB7@PSMA CPN samples (Figure S1.4c). These results seem to correlate with the different efficiencies of singlet oxygen production among the PTB7 CPN samples: the PTB7@F127 CPNs were the most efficient, exhibiting an approximately 7.5-fold improvement compared to bare PTB7 (see Figure 5.2(c)), while for PTB7@PSMA CPNs, the singlet oxygen production was completely quenched (Figure 4 of the main

text). This suggests that the singlet oxygen produced by the PTB7@F127 CPNs is somehow responsible for its increased photobleaching: at lower powers, the singlet oxygen production is negligible and PTB7@F127 CPNs behave in a similar way to the bare PTB7 and PTB7@PSMA CPNs; while at higher powers, the non-zero singlet oxygen production contributes to the temporal decrease of its fluorescence under continuous illumination. This property of PTB7@F127 CPNs could make it particularly suitable for biomedical applications as the outstanding resistance to photobleaching at lower power excitation laser can achieve long term imaging and at higher excitation powers, its photosensitization properties can be unlocked for photodynamic therapy.

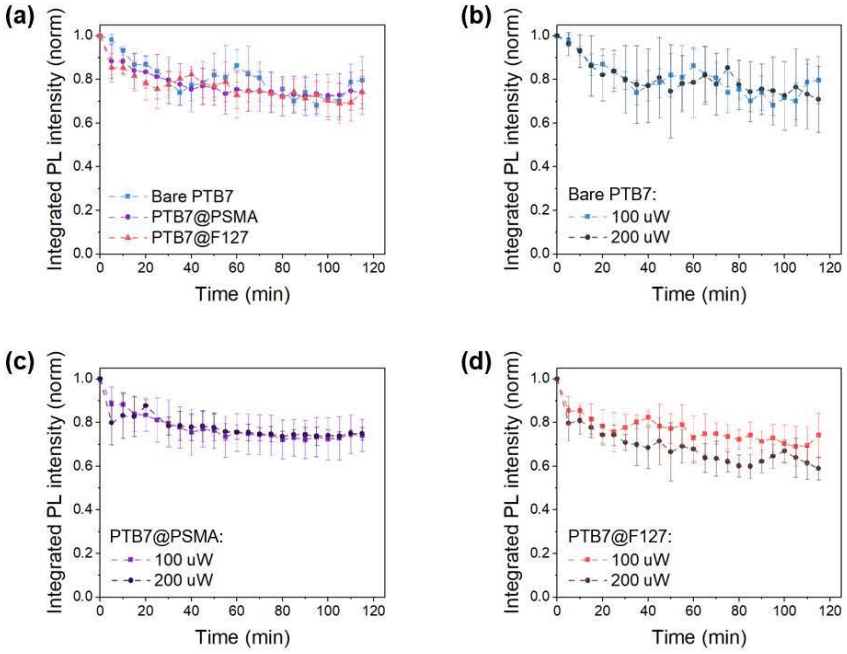

Figure S1.4. Photobleaching resistance of PTB7 CPNs under prolonged stimulation. Schematic illustration describing the slow fluorescence decrease of different type of **(a)** CPNs with 100 μW 635 nm laser stimulation for 2 hours and **(b)** bare PTB7 and **(c)** PTB7@PSMA CPNs and **(d)** PTB7@F127 CPNs are compared at 100 μW and 200 μW 635 nm laser stimulation for 2 hours.

It should be noted that the photobleaching of our PTB7@F127 CPNs was not permanent. Upon illumination at 200 μW for 25 mins, and subsequent removal of excitation, the fluorescence intensity of PTB7@F127 CPNs recovered to its original level (Figure S1.5). The reversible photobleaching suggests that no permanent changes occur to the PTB7 and F127 structures,[3] or their packing and that the cause of the photobleaching is transient in nature. In addition, the recovery time of ~2 hours allows for repeated treatment, if needed, since the half-time blood circulation for ~180 nm soft nanoparticles is expected to be on the order of 1 day.[4]

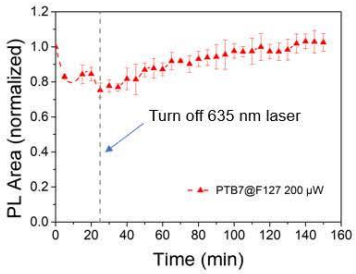

Figure S1.5. Fluorescence recovery after photobleaching of PTB7@F127 CPNs. The PTB7@F127 CPNs was photobleached for 25 mins using 200 μW of 635 nm laser. Fluorescence recovery was subsequently monitored by acquiring images every 5 mins (indicated by the dash line).

Temporal stability of CPN samples

The temporal stability of the synthesized PTB7 CPN samples was monitored for a period of 6 months and evaluated in the first instance by noting any changes in the size and optical properties of the CPNs. Figure S1.6 compares the hydrodynamic radii of the as-prepared CPN samples to the 6 month-old samples. The results show a significant change in the size of the bare PTB7 (approximately 50% reduction), but a reduced reduction in the size of the PTB7 CPNs coated with PSMA (~10%; statistically significant) and a minimal change in the hydrodynamic size of the PTB7@F127 CPNs

(~3% change *versus* 2% standard error). The reduction in the size of the bare PTB7 suggests some "unravelling" of the polymer chains and subsequent desorption from the surface, which is mitigated by the presence copolymer coatings.

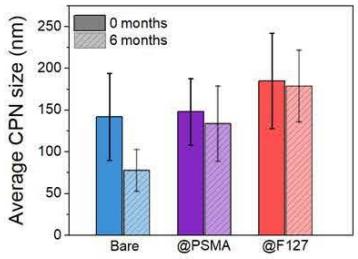

Figure S1.6. Changes to the hydrodynamic size of the CPNs upon sample aging. The average hydrodynamic size of the bare PTB7 (blue bars), PTB7@PSMA (purple bars) and PTB7@F127(red bars) CPNs are compared at different time points following their synthesis. The un-patterned darker filled bars correspond to the CPNs sizes immediately following the synthesis of the samples, while the lighter patterned bars correspond to the sizes of the CPNs following a 6 months storage in the dark at 4˚C. The error bars represent the standard deviation of particle sizes within each sample (and not the standard error in the average CPNs size for the sample).

Interestingly, very small changes were observed in the optical spectra of the three samples, especially in relation to the optical features corresponding to the excitation from the ground to the first excited state of the CPNs, *i.e.* the main absorption peaks with their 2-level vibronic structures and the emission peaks (Figure S1.7). This suggests that the overall structure of the PTB7 chains remains stable, with only a small level of reorganization over time. The organization of the chains necessarily results in the generation of different excitation species, resulting in slight shifts of the PL peaks, slight changes in the ratio of the absorbances of the two peaks (corresponding to transitions

into the different vibronic levels of the first excited state) and changes in the fluorescence QY of the samples. Regarding the latter, and despite minimal changes in other properties of the PTB7@F127 CPNs (Figure S1.9), fluorescence QY of this sample approximately halved over the 6-month monitoring period (0.6-0.8% for the 6-month-old sample, compared to 1.4% for the as-prepared sample, Figure S1.8). Hence, even minimal structural changes can lead to strong changes in the fluorescence properties of the CPNs particles.

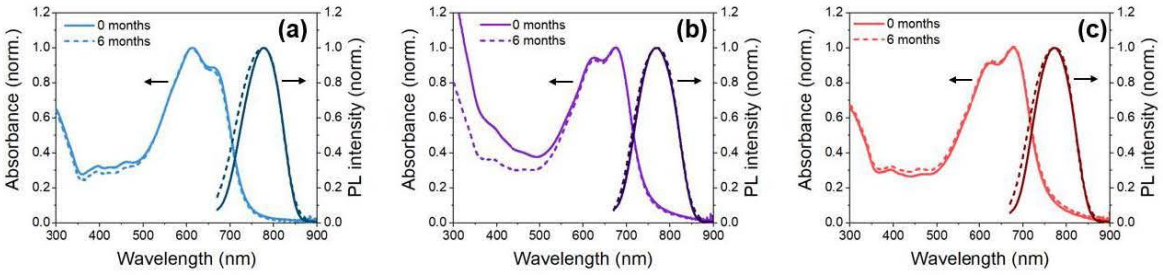

Figure S1.7. Changes in absorbance and fluorescence spectra of PTB7 CPNs upon aging. The absorbance (lighter colours) and fluorescence (darker colours) spectra of the **(a)** bare PTB7, **(b)** PTB7@PSMA CPNs and **(c)** PTB7@F127 CPNs are compared at 0 months (solid lines) and 6 months (dashed lines) after the synthesis of the sample.

Of interest is also the fact that the change in the optical properties and the fluorescence QY of the samples depended on how they were stored. The samples could either be stored as synthesized, and purified by centrifugation immediately prior to use ("a+c" = "aged + centrifuged"), or they can be purified by centrifugation immediately following synthesis and then stored ("c+a"). As can be seen from Figure S1.8, small but distinguishable changes in the optical properties of these samples were

observed, with either an increase or a decrease in the absorption at higher energies, and a varying degree of broadening of the emission peak (although in both cases it was small). In addition, the resulting fluorescence QY yields were also different for the two methods of storing the sample, with a slightly smaller reduction in the QY for the sample that was left unperturbed immediately after synthesis (0.76% for the "a+c" sample *versus* 0.58% for the "c+a" sample). It is unclear how the minute changes in the absorbance and emission peaks correlate with the large and differing reduction in the fluorescence QYs of these samples, and further investigation into the photophysics of the PTB7@F127 CPNs are required to elucidate the responsible mechanisms.

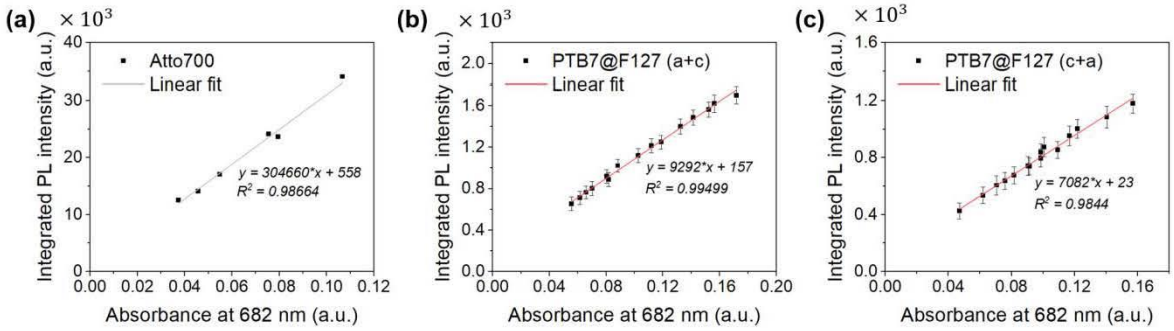

Figure S1.8. Determination of fluorescence quantum yield of 6-month-old PTB7@F127 CPNs. **(a)** Calibration of the absorbance by the sample at the excitation wavelength *vs* fluorescence signal measured from the fluorescence standard sample (Atto700; 25% QY). **(b)** and **(c)** show the dependence of fluorescence intensity *versus* absorbance at excitation wavelength for the PTB7@F127 sample, which was either **(b)** aged first and then purified by centrifugation (a+c), or **(c)** purified by centrifugation and then aged (c+a). The QYs of these two samples was then obtained by multiplying the QY of the standard (25%) and the corresponding ratio of the slopes obtained, yielding values of (0.76 ± 0.4)% and (0.58 ± 0.3)% for the (a+c) and (c+a) samples respectively. Full details of the method can be found in Section 4 below.

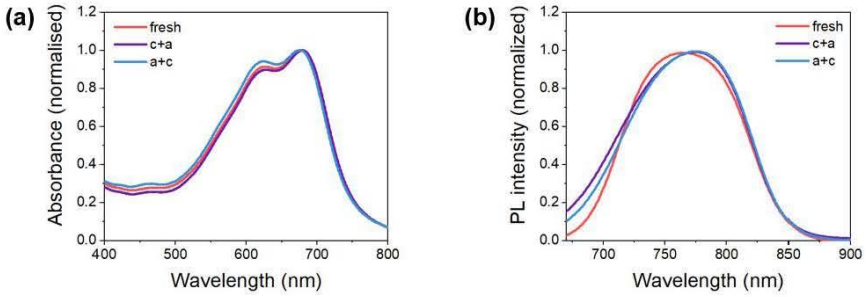

Figure S1.9. Changes to absorbance and fluorescence spectra of PTB7@F127 CPNs with aging. The **(a)** absorption and **(b)** fluorescence spectra of PTB7@F127 CPNs immediately after synthesis and purification *via* ultracentrifugation ("fresh"; red lines); 6 months after synthesis and purification *via* ultracentrifugation ("c+a", purple lines); and 6 months after synthesis, purified *via* ultracentrifugation immediately prior to measurement ("a+c", blue lines).

Characterization of PTB7 CPN sizes

The sizes (diameters) of the prepared CPN samples were characterized using three methods: dynamic light scattering (DLS), atomic force microscopy (AFM) and transmission electron microscopy (TEM).

The DLS method yielded the hydrodynamic diameters of the CPNs in aqueous solutions. Measurements were obtained using the Malvern Zerasizer NanoZS. For these measurements, samples were diluted to a final concentration of 5 μg/ml and 2 mL of this dilute CPN sample was then used in a dedicated disposable cuvette. Each DLS measurement consisted of 3 repeats of 10 runs, and the ZetaSizer software applied the model to output the size distribution data and averages directly from each measurement.

For AFM measurements, cover-slip substrates were first washed using Hellmanex III solution (Helma), according to manufacturer instructions, and then dried under N_2 flow. Onto this, 20 μL of

10 µg/ml CPNs solution was drop-casted and left to air-dry. Alternatively, 100 µL of this CPNs solution was spin-coated at 2000 rpm for 30 sec using Laurell WS-650HZB Spin Coater. The prepared CPNs-containing substrates were then imaged using the Bruker Icon Dimension Atomic Force Microscope.

For TEM measurements, 6 µL of 20 µg/ml CPNs solution was drop-casted onto a TEM grid (Fisher Scientific, 400 mesh carbon grids) and left to air-dry. Imaging was performed on a JEOL 1400 transmission electron microscope, operated at 120 kV.

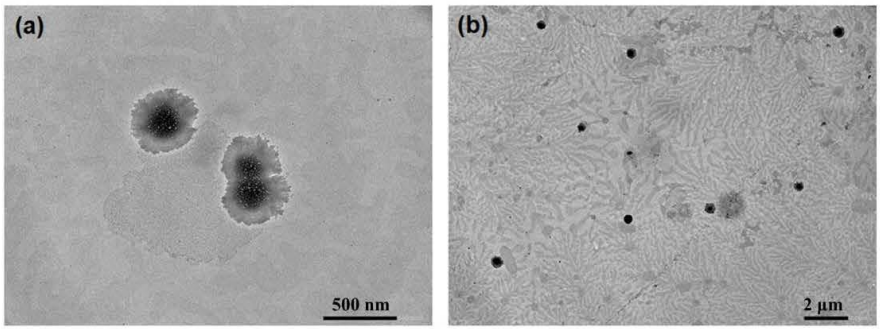

Figure S2.1. TEM images of PTB7@F127 CPNs in water at high (a) and low (b) magnification. **(a)** TEM image of PTB7@F127 CPNs at high magnification and **(b)** at low magnification. The fractal patterns that can be seen in (b) are formed by the excess F127 capping molecules present in the PTB7@F127 CPN solutions prior to purification by centrifugation.

Dispersion stability of PTB7@PSMA CPN solutions

The dispersion stability of PTB7@PSMA CPNs at different concentrations was evaluated using DLS measurements (Figure S2.2). Just like the PTB7@F127 CPN sample (described in the main text of the manuscript), the PTB7@PSMA CPNs shown an overall excellent dispersion stability over a wider range of concentrations, with a slightly increasing average size and polydispersity of the sample

at higher concentrations. However, the emerging contribution to DLS intensity at higher particle sizes for high sample concentrations, indicates that the PTB7@PSMA sample has a higher tendency to aggregate when compared to PTB6@F127 CPNs.

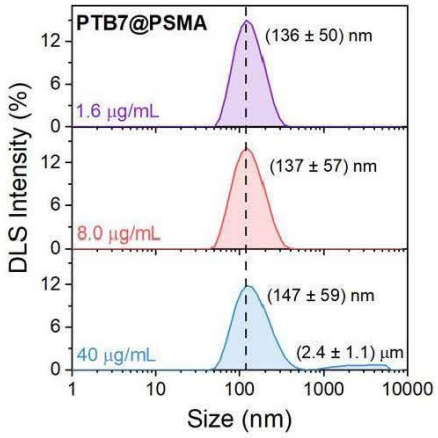

Figure S2.2. Hydrodynamic sizes of PTB7@PSMA CPN solutions of various concentrations. The concentrations of CPN samples are indicated in the bottom right corner of each panel, in colors corresponding to that of the plot data. The dashed line is included as a guideline only and represents the average size of the PTB7@PSMA CPNs for 1.6 µg/mL concentration. The numbers in brackets next to each peak indicate the average particle size for that peak and the corresponding standard deviation, as $(d_{av} \pm st.dev.)$.

A note on the fluidity of the F127 shell

We would like to note here that the F127 shell remains fluid even after removal of the loosely bound F127 strands from the surface of the CPNs by centrifugal ultrafiltration. This is clearly evidenced by the AFM and TEM images of the PTB7@F127 samples. Figure 1 of the main manuscript shows and AFM image of PTB7@F127 CPNs, in which the spread of F127 shell around

each PTB7 core can be easily distinguished. The spread of the fluid shell is caused by the evaporation and immersion forces experienced by the shell upon the drying of the sample. Preparation of samples for SEM/TEM imaging, which likewise involves the drying of the sample, caused similar effects although to a smaller degree, presumably because of different F127/substrate interactions. Nonetheless, the comparison of TEM images in Figure S2.1 shows a clear difference between the filtered and non-filtered samples: for filtered samples, particles have clearly distinct F127 shells, whereas the loosely-bound F127 in non-filtered samples separates from the CPN surface and forms a fractal pattern on the TEM grid.

Comparison of DLS and AFM volumes of PTB7 CPNs

The volumes of the PTB7@F127 CPNs were estimated both from the DLS and the AFM data. For the DLS data, it was assumed that the particles are spherical in shape when dispersed in aqueous solutions. Their volume can then be approximated by:

$$V_{DLS} = \frac{4}{3}\pi\left(\frac{d_{DLS}}{2}\right)^3$$

where d_{DLS} is the average diameter obtained from dynamic light scattering measurements (ZeraSizer, Malvern), which was determined to be 185 nm with a standard deviation of 57 nm. Substituting these values into above equation yields a value of 3.3×10^{-3} fL (with a standard deviation of 3.1×10^{-3} fL).

The shapes of the particles in the AFM images were clearly not spherical, hence a simple approximation was not possible. To determine the mean volume of particles from the AFM data, the AFM images were first corrected for the background and any contributions from impurities deposited on the surface (Figure S3.1(a)). The counting and segregation procedure described by

http://pythonvision.org/basic-tutorial/ was then used to delineate and count the number of CPNs particles in the AFM image (Figure S3.1(b)), and finally segregate the scanned area into regions occupied by each particle (Figure S3.1(c)) using bespoke python3.2 code.

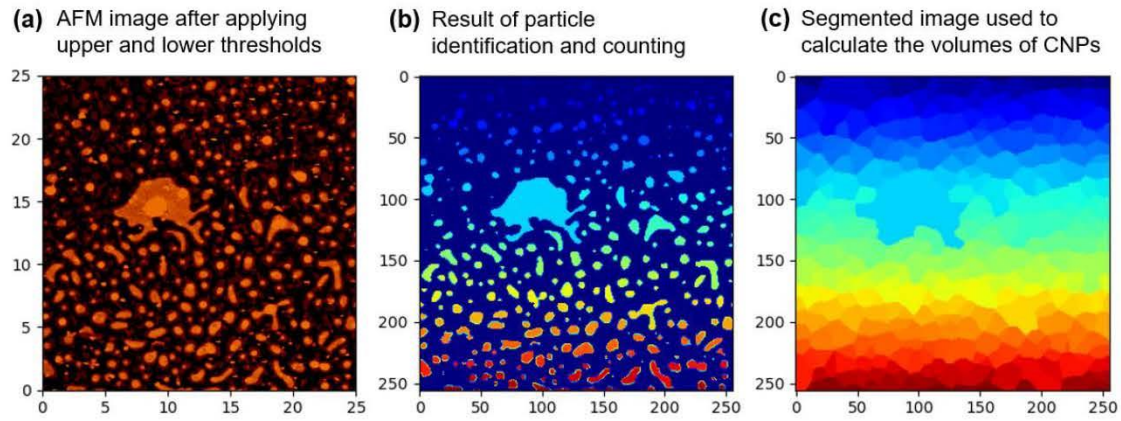

Figure S3.1. Results of particle counting and area segmentation. (a) The AFM image (25 x 25 μm^2) used to calculate V_{AFM}, after background correction and reduction of contributions from impurities deposited on the surface *via* an application of lower and upper thresholds. **(b)** Application of an intermediate threshold resulted in delineation of each particles' and identification of the total number of particles in the AFM image (328). The color in the image corresponds to the index of the particle on a jet colorscale, from 1 to 328. **(c)** Result from (b) was used to segment the area of the AFM image into smaller areas, corresponding to the regions occupied by each individual particle. The AFM height data from (a) was integrated over each of these areas to obtain the volume of each particle. The x and y scales of (b) and (c) are in pixels.

The height data at every pixel (h_i) in each of these regions was then integrated to yield an approximation for the volume of each particle, according to:

$$V_{particle} = \sum_{i=1}^{itot} h_i * \Delta x * \Delta y$$

here Δx and Δy were the x and y sizes of each pixel in nm, respectively. The results of these calculations are histogrammed in Figure S3.2. The mean and the standard deviation of the results were finally obtained using Microsoft Office Excel, yielding the average volume of $V_{AFM} = (4.7 \pm 0.2) \times 10^{-3}$ fL (with a standard deviation of 4.2×10^{-3} fL).

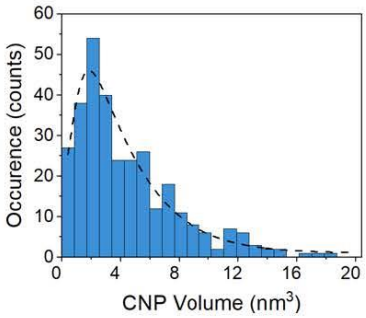

Figure S3.2. Histogram of PTB7@F127 CNP volumes obtained from AFM data. A total of 328 particles were identified by the delineation code, and the volume of each was calculated by summing the AFM height data over segmented areas of Figure S3.1(c).

The two volumes are of the same order of magnitude and are well within each other's standard deviations, but they do differ by ~23%. The discrepancy in the two values is most likely due to the deformation of the CPNs during the preparation of the AFM samples by spin-coating, and the much smaller sample size for the AFM data compared to the DLS measurements.

Comparison of AFM images of F127 and PSMA-coated PTB7 CPNs

Since the rigidity of the polymer can influence the sizes of the particles measured by DLS, it was important to confirm the relative sizes of the coated samples using other means. For this reason, we have imaged air-dried PTB7@F127 and PTB7@PSMA samples using Atomic Force Microscopy (Figure S3.3). The results confirmed that, on average, PTB7@PSMA CPNs are smaller than the F127 counterparts, with the majority of the difference coming from the size of the copolymer shell, *i.e.* the PTB7 core sizes were approximately the same for both samples.

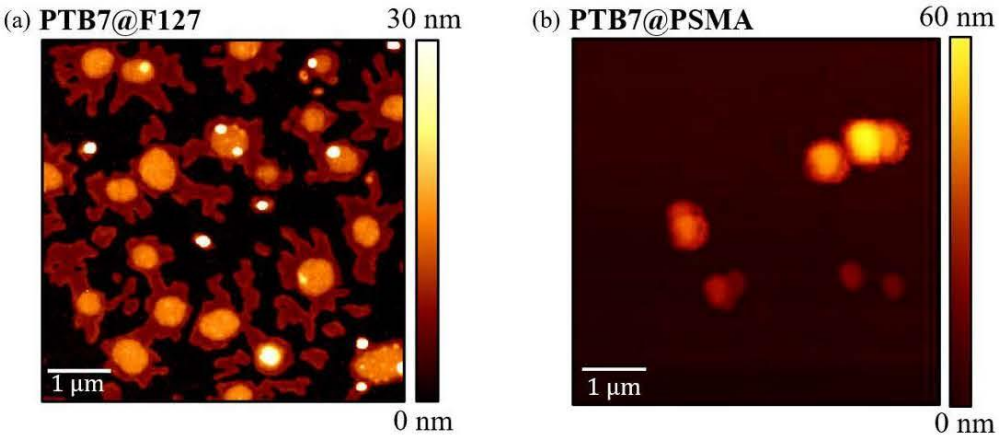

Figure S3.3. AFM images of coated PTB7 CPNs. AFM image of (a) PTB7@F127 CPNs and (b) PTB7@PSMA CPNs, air-dried on a microscope slide. The white line in each panel corresponds to 1 µm distance. The color bars show the corresponding AFM heights for the two scans.

Optical characterization of CPN samples

UV-vis and steady-state fluorescence measurements

The absorption spectra of ATTO700 and CPNs in water were measured at room temperature, in the 300-900nm spectral range using a UV-2600 spectrometer from Shimadzu. The emission spectra were

recorded in the 600-900 nm spectral range of using an Agilent Cary 60 spectrometer. For all measurements, 1 mL of test solution was placed inside the 1.4 mL fluorescence microcuvettes (Helma) of 1 cm path length.

Fluorescence quantum yield measurements

The fluorescence quantum yield (QY) of CPN samples was measured *via* the relative method, using an aqueous solution of the Atto700 dye as a reference ($QY_{\mathrm{ref}} = 0.25$). A concentration series of both the Atto700 and the PTB7@F127 CPNs were prepared by diluting the respective samples in DI water, to achieve samples with absorptions in the 0.1-0.2 and 0.1-0.35 ranges respectively for the two samples, at 682 nm. The fluorescence spectra of all samples were then recorded in the 700-900 nm spectral range, using 682 nm as the excitation wavelength, and keeping the excitation and emission slit widths constant at 5 nm. An estimated integrated fluorescence intensity (I_{PL}) was obtained from the data by first smoothing the raw data (see red curve in Figure S4.1c) and then calculating the integrated area under the smoothed curve according to:

$$I_{\mathrm{PL}} = \sum_{i=1}^{N} I_i$$

where i are the individual data points in the smoothed data and N is the total number of the data points. During these calculations, the wavelength step ($\Delta\lambda = 1$ nm) and the spectral range of integration (700-900 nm) were same for all sets of data. The error in the integrated fluorescence intensity (ΔI_{PL}) was also estimated by calculating the total root-mean-square deviation between the raw and smoothed data (Figure S4.1c):

$$\Delta I_{\mathrm{PL}} = \sum_{i=1}^{N} \sqrt{\left(I_i^{raw} - I_i^{smoothed}\right)^2}$$

This procedure was repeated for every sample in the dilution series, and then plotted against absorption at the excitation wavelength (Figure S4.1a and S4.1b). Straight line plots of $I = K * A(682\ nm) + B$ form were fitted to the Atto700 and PTB7@F127 sets of data (Origin 2019b) and the slopes (K) were then used to calculate the QY of the PTB7@F127 sample, according to:

$$QY_{\mathrm{PTB7@F127}} = \frac{K_{\mathrm{PTB7@F127}}}{K_{\mathrm{atto700}}} * QY_{\mathrm{atto700}}$$

where $K_{\mathrm{PTB7@F127}}$ and K_{atto700} are the slope of the line fits for the PTB7@F127 CPNs and Atto700 solutions, respectively. The error in the QY of the PTB7@F127 sample was obtained using:

$$\Delta QY_{\mathrm{PTB7@F127}} = QY_{\mathrm{PTB7@F127}} * \sqrt{\left(\frac{\Delta K_{\mathrm{PTB7@F127}}}{K_{\mathrm{PTB7@F127}}}\right)^2 + \left(\frac{\Delta K_{\mathrm{atto700}}}{K_{\mathrm{atto700}}}\right)^2}$$

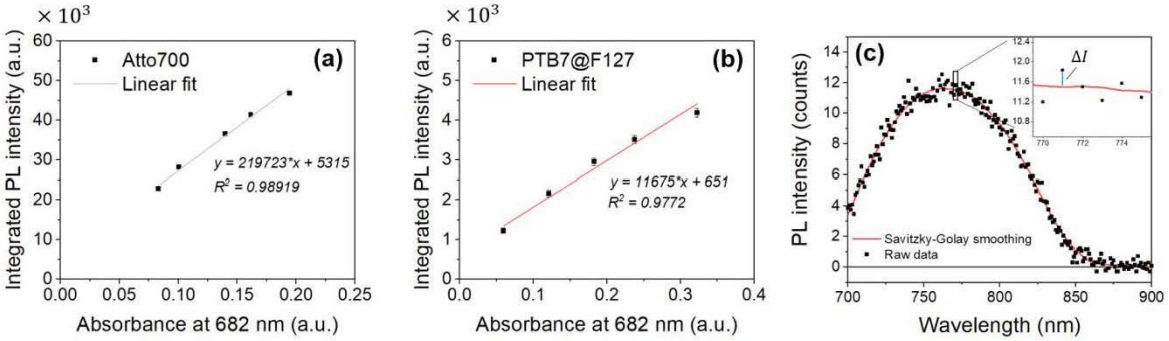

Figure S4.1. Determination of fluorescence quantum yield of PTB7@F127 CPNs. Figure shows integrated fluorescence intensities for **(a)** ATTO 700 and **(b)** PTB7@F127 CPNs of different concentrations, and therefore different absorbances at the excitation wavelength (682 nm). The grey and red lines are the corresponding linear fits to the data. Panel **(c)** illustrates the approach taken to calculate the error in the integrated fluorescence intensity of each sample. Each spectrum was first smoothed, and the absolute differences between the raw and smoothed data (ΔI_i) were summed to obtain the total error in the estimate of I_{PL}.

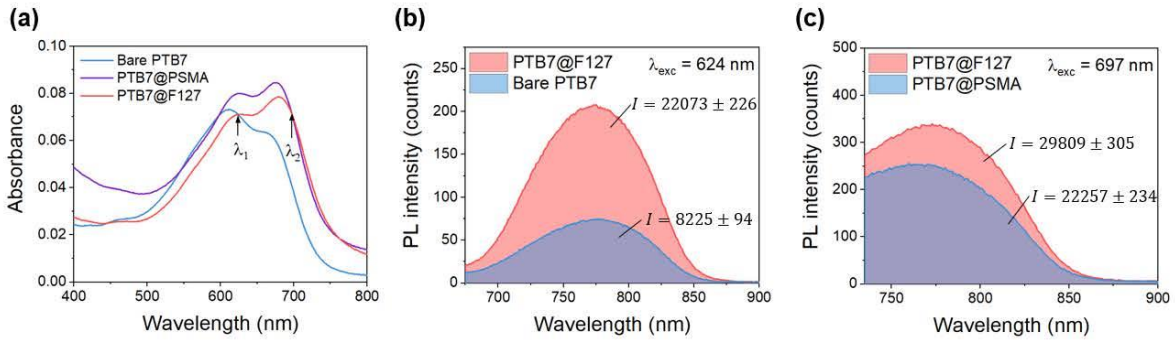

Figure S4.2. Determination of the fluorescence quantum yield (QY) of bare PTB7 and PTB7@PSMA CPNs. (a) The absorbance spectra of bare PTB7(blue), PTB7@PSMA CPNs (purple) and PTB7@F127 CPNs (pink) samples used for determination of fluorescence QYs of bare PTB7 and PTB7@PSMA CPNs. The excitation wavelengths to use in fluorescence measurements (λ_1 and λ_2) were chosen such that each sample of unknown wavelength had same absorbance as PTB7@F127 CPNs. **(b)** and **(c)** compare the fluorescence intensities of the PTB7@F127 CPNs with those of (b) bare PTB7 and (c) PTB7@PSMA sample. Also shown are the fluorescence intensities of each sample, integrated over the shown spectral range (I).

Using above method and a value of 25% for QY_{atto700}, the QY of PTB7@F127 CPNs was determined to be ~(1.33 ± 0.32)% which is within our expectation, with literature values of ~2% for thin PTB7 films.

The QYs of bare PTB7 and PTB7@PSMA samples were then obtained using a simplified relative method, with the PTB7@F127 sample acting as a reference. For these measurements, all samples were first diluted to have absorptions of less than 0.1 at the peak, and the excitation wavelengths were chosen such that the absorptions were the same for a single pair of samples, as illustrated in Figure S4.2a. The samples were then analyzed in pairwise fashion, using the same set of settings to record the fluorescence spectra of samples in each pair. For bare PTB7, the test and the reference

(PTB7@F127) samples were both excited at 624 nm, and the fluorescence spectra were recorded in the 670 – 900 nm spectral range (Figure S4.2b). For PTB7@PSMA CPNs, the test and the reference samples were excited at 697 nm and as a result their fluorescence spectra were recorded over a narrower range of 735 – 900 nm (Figure S4.3c). The integrated fluorescence intensities of these all samples were then calculated using the procedure described above (results shown in respective panels of Figure S4.2), and the fluorescence QY of the bare and PSMA-coated PTB7 CPNs were then calculated according to:

$$QY_{\text{sample}} = \frac{I_{\text{sample}}}{I_{\text{F127}}} * QY_{\text{F127}}$$

$$\Delta QY_{\text{sample}} = QY_{\text{sample}} \sqrt{\left(\frac{\Delta QY_{\text{F127}}}{QY_{\text{F127}}}\right)^2 + \left(\frac{\Delta I_{\text{sample}}}{I_{\text{sample}}}\right)^2 + \left(\frac{\Delta I_{\text{F127}}}{I_{\text{F127}}}\right)^2}$$

where I's are the integrated fluorescence intensities of the samples, and the subscripts "sample" and F127 refer respectively to CPN samples of unknown fluorescence QY and the PTB7@F127 sample. The fluorescence QYs of $(0.5 \pm 0.1)\%$ and $(1.0 \pm 0.2)\%$ were obtained for the bare PTB7 and PTB7@PSMA CPNs respectively.

A note on red-to-NIR absorption and CPN concentration

In several figures presented in the main text of the manuscript and in this supplementary file, the fluorescence spectra of CPN samples were measured at an excitation wavelength where the absorbances of the three CPN samples were equal, with the excitation wavelength selected within the main absorbing region falling between 500 and 800 nm. In this spectral region, neither the F127 nor the PSMA absorb and hence PTB7 is the main contributor to any extinction observed (Figure S4.3). Thus, a similarity of extinction in the red-NIR spectral region by different PTB7 CPNs, combined with their comparable sizes, implies a similarity of sample concentrations.

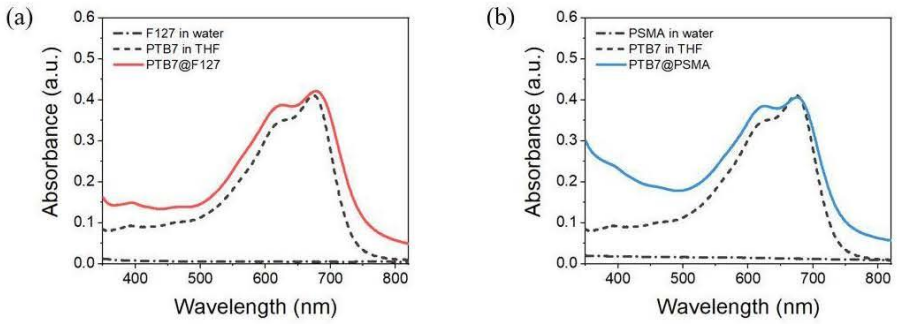

Figure S4.3. Extinction of F127 and PSMA copolymers in water. Figure compares the absorbances of (a) F127 and (b) PSMA copolymers in water to those of the correspondingly coated PTB7 CPNs. In both cases, the copolymer contributes negligibly to absorption of respective CPN samples in the 500-800 nm region.

Normalized optical spectra of all samples

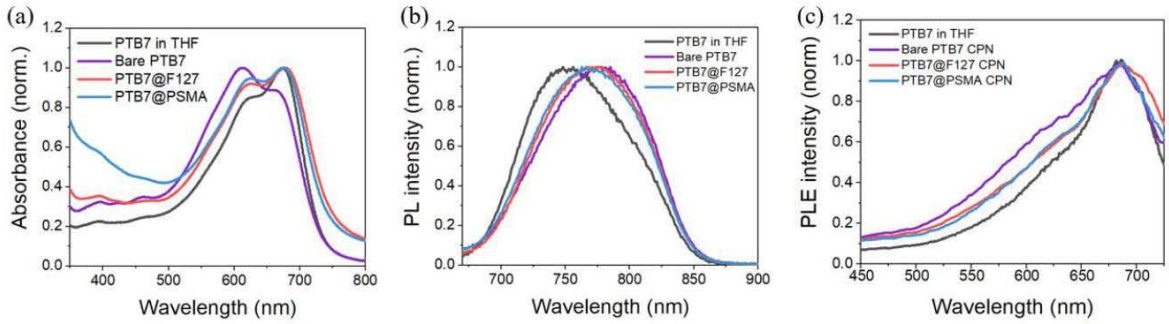

Figure S4.4. Normalised optical spectra of all CPN samples and that of a PTB7 solution. Panels (a), (b) and (c) compare, respectively, the normalized steady-state absorption, photoluminescence and photoluminescence excitation spectra of PTB7 polymer dissolved in THF (black lines), bare PTB7 CPNs (purple lines), PTB7@F127 CPNs (red lines) and PTB7@PSMA CPNs (blue lines). In panel (c), the emission wavelength for the PLE measurements was set to the peak photoluminescence wavelength for each corresponding sample.

Photoluminescence excitation spectra of all samples

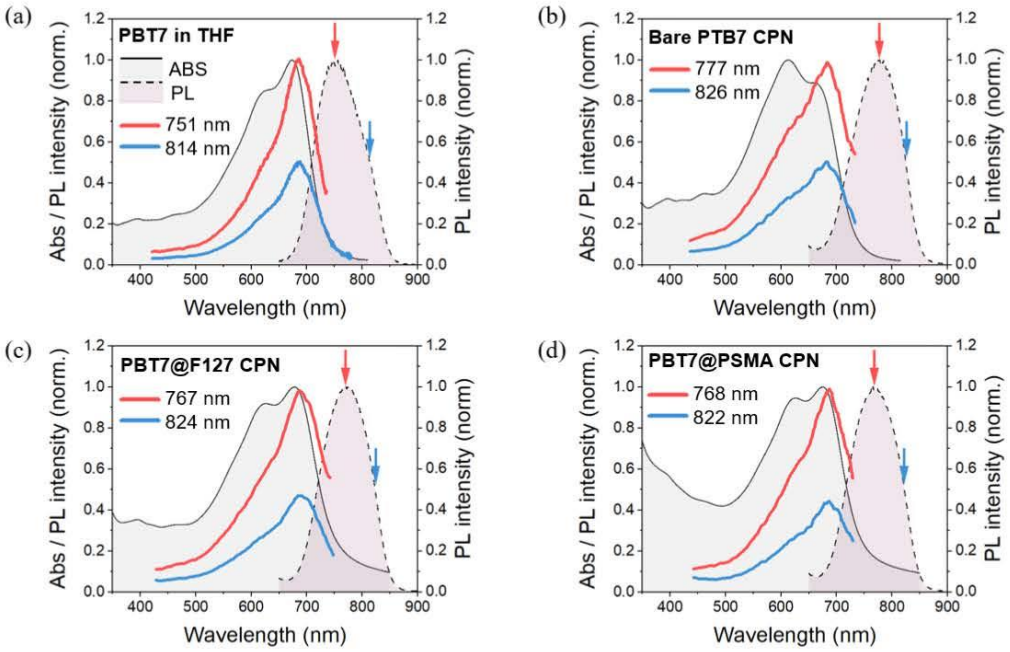

Figure S4.5. Absorbance, photoluminescence and photoluminescence excitation spectra of all samples. Panels (a), (b), (c) and (d) compare the absorbance (solid black line with gray shading), photoluminescence (dashed black line with pale grey/pink shading) and two photoluminescence excitation spectra (red and blue solid lines) for PTB7 solution in THF, bare PTB7 CPNs, PTB7@F127 CPNs and PTB7@PSMA CPNs, respectively. The colored arrows in each panel indicate the emission wavelength used to collect the respectively colored PLE spectrum. The emission wavelengths used are also indicated in the legend of each panel. For clarity, absorbance and photoluminescence spectra were normalized to 1 at peak wavelength. The PLE spectra were normalized to the values of normalized photoluminescence at the emission wavelengths used.

Deconvolution of optical spectra into components

Each of the normalized absorbance spectra in Figure S4.5(a) above was deconvolved into five Gaussian contributions (in energy scale) using the Multi Peak Fit analysis option of the Origin (2019b) software. The decision to use 5 components for the deconvolution of each spectrum was based on previous reports of similar procedures for PTB7 thin films and solutions,[5] but also on our inability to fit the curves successfully with a 4-Gaussian components model. The initial values for the positions of the peaks were approximated from the same reference. For each deconvolution, a fit with an R-square value of >0.999 was considered to produce a suitable quality of deconvolution. The results of the fitting procedure are shown in figure S4.6 below, and the extracted parameters of peaks 1 and 2 are summarized in Table S4.1. The errors quoted in the table are the direct results of the fitting procedure and are stated as outputted by Origin (2019b) software.

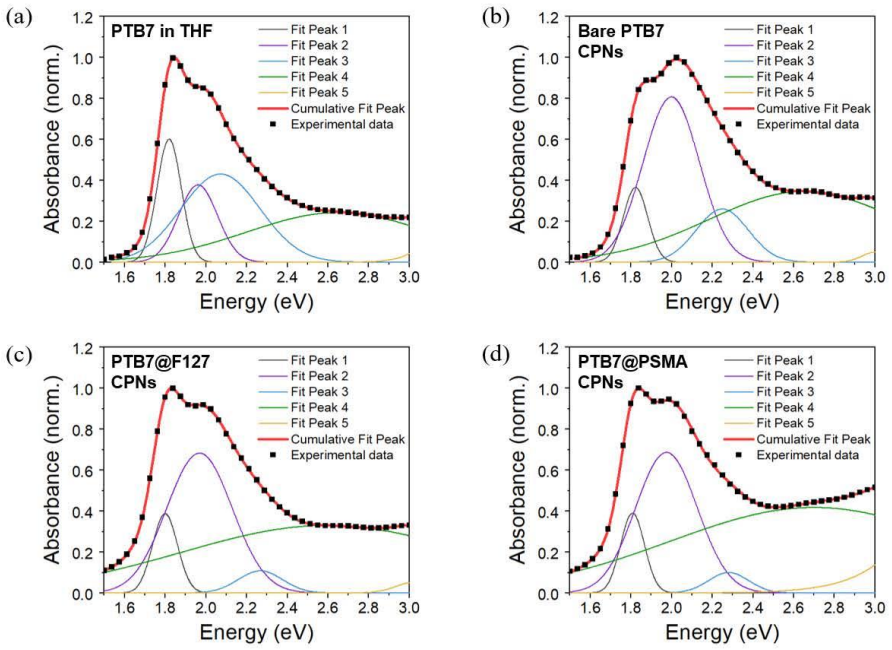

Figure S4.6. Deconvolution of absorbance spectra into Gaussian contributions. Panels (a)-(c) show, respectively, the results of the fitting procedure for PTB7 polymer dissolved in solution, bare

PTB7 CPNs, PTB7@F127 CPNs and PTB7@PSMA CPNs. For each case, the experimental data are shown as black scatter points, the Gaussian individual contributions are shown in solid colored lines and the sum of the contributions is shown in a thicker red solid line. The R-squared value for each fit was greater than 0.999.

A similar procedure was also applied to the normalized photoluminescence spectra of PTB7 polymer dissolved in THF and PTB7 CPNs dispersed in aqueous solutions. The results of these deconvolutions are shown in Figure S4.7 and Table S4.2.

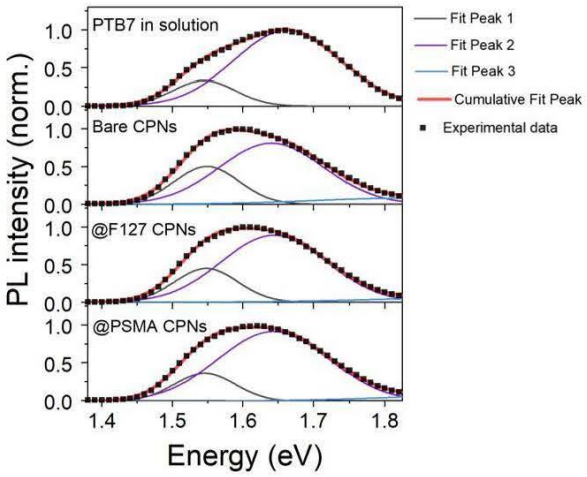

Figure S4.7. Deconvolution of photoluminescence spectra into Gaussian contributions. The results of the fitting procedure are shown (top-to-bottom) for PTB7 polymer dissolved in solution, bare PTB7 CPNs, PTB7@F127 CPNs and PTB7@PSMA CPNs. For each case, the experimental data are shown as black scatter points, the Gaussian individual contributions are shown in solid colored lines and the sum of the contributions is shown in a thicker red solid line. The R-squared value for each fit was greater than 0.99.

Table S4.1. Summary of results obtained from deconvolution of absorption spectra into contributions from different excitation processes.

Sample	E_{0-0} (eV)	w_{0-0} (eV)	E_{0-1} (eV)	w_{0-1} (eV)	A_{0-0} $/A_{0-1}$	R^2
PTB7 in THF	1.8200 ± 0.0001	0.1199 ± 0.0002	1.9618 ± 0.0006	0.193 ± 0.001	0.99 ± 0.02	0.99996
Bare PTB7	1.8231 ± 0.0002	0.1207 ± 0.0006	1.999 ± 0.001	0.277 ± 0.002	0.197 ± 0.005	0.99999
PTB7@F127	1.7998 ± 0.0001	0.1232 ± 0.003	1.9691 ± 0.0007	0.3231 ± 0.0008	0.216 ± 0.002	0.99910
PTB7@PSMA	1.8080 ± 0.0001	0.1178 ± 0.0004	1.9752 ± 0.0004	0.3047 ± 0.0006	0.220 ± 0.002	0.99983

E_{0-i} denote the peak energy of absorption contribution corresponding to an excitation from the ground state into the ith vibrational level of the excited state

w_{0-i} denote the width of the absorption peak, at half maximum, corresponding to an excitation from the ground state into the ith vibrational level of the excited state

A_{0-0}/A_{0-1} is the ratio of amplitudes of absorption peaks corresponding, respectively, to excitations from ground state into the 0th and 1st vibrational levels of the excited states

R^2 is the R-squared value for the multi-gaussian fit used to generate the data in the table

Table S4.2. Summary of results obtained from deconvolution of photoluminescence spectra into contributions from different de-excitation processes.

Sample	PL_{0-1} (eV)	w_{0-1} (eV)	PL_{0-0} (eV)	w_{0-0} (eV)	R^2
PTB7 in THF	1.545 ± 0.001	0.089 ± 0.002	1.663 ± 0.001	0.150 ± 0.001	0.99870
Bare PTB7	1.549 ± 0.002	0.092 ± 0.006	1.641 ± 0.007	0.15 ± 0.02	0.99827
PTB7@F127	1.548 ± 0.002	0.090 ± 0.004	1.644 ± 0.003	0.15 ± 0.01	0.99883
PTB7@PSMA	1.547 ± 0.001	0.089 ± 0.003	1.646 ± 0.003	0.15 ± 0.01	0.99890

PL_{0-i} denote the energy at peak of photoluminescence contribution corresponding to a de-excitation from the lowest excited state into the ith vibrational level of the ground state

w_{0-i} denote the width of the photoluminescence peak, at half maximum, corresponding to a de-excitation from the lowest excited state into the ith vibrational level of the ground state

R^2 is the R-squared value for the multi-gaussian fit used to generate the data in the table

Singlet oxygen production by PTB7@F127 CPNs.

General description of the method

The production of $^1O_2$ by the fabricated CPNs was measured using SOSG as a chemical sensor. SOSG is a non-fluorescent molecule that is converted into a fluorescent form, SOSG-EP, upon reaction with $^1O_2$. In our case, production of $^1O_2$ was continuously stimulated using a red laser ($\lambda_{stim} = 635$ nm), which was absorbed by the PTB7 CPNs but not the SOSG. With this stimulation uninterrupted, the amount of SOSG-EP in the solutions was tested every 30 seconds by recording the SOSG-EP fluorescence spectrum ($\lambda_{exc} = 500$ nm), over a period of 3 seconds (Figure S5.1). By continuing the stimulation of $^1O_2$ production and collection of SOSG-EP fluorescence, the amount of $^1O_2$ produced by our CPNs could be monitored over time.

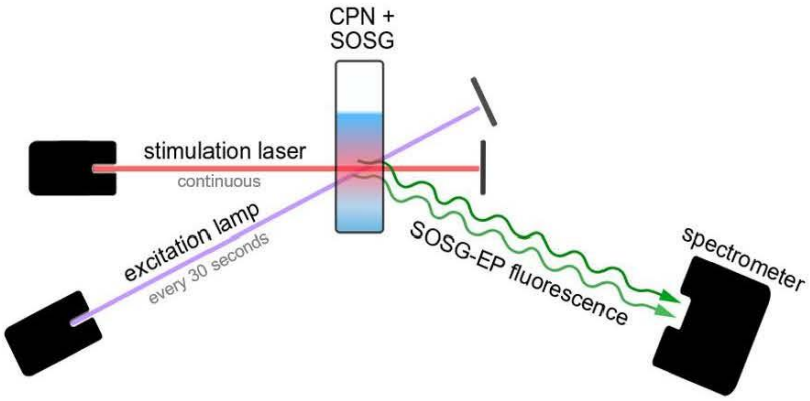

Figure S5.1. Set-up used for measurements of ROS production by the PTB7 CPNs. The CPN samples and SOSG were placed in a fluorescence cuvette. The production of $^1O_2$ was continuously stimulated by a red laser (635 nm, 4.5 mW, with an elliptical beam profile). The produced $^1O_2$ converted the non-fluorescent SOSG into its fluorescent form of SOSG-EP. The fluorescence from SOSG-EP was recorded every 30 seconds using a standard steady-state spectrometer ($\lambda_{exc} = 500$ nm).

The positive control involved the use of methylene blue (MB) instead of the CPNs in the test solution. The negative control was a sample to which no singlet oxygen producer was added (*i.e.* SOSG only in solution).

Singlet oxygen production by PTB7@F127 CPNs and MB under prolonged stimulation

In addition to experiments described in the main text of the paper, the production of $^1O_2$ by PTB7@F127 CPNs sample was also analyzed under prolonged stimulation conditions. The protocol for these experiments was identical to that found in the Methods section (and the same as the summary above), with the exception that the $^1O_2$ production was measured over a much longer stimulation period of 3 hours. For reference, the experiment was also repeated for our positive reference (MB dye). Figure S5.2(a) shows the results of these measurements, normalized to SOSG-EP fluorescence at the start of the measurements ($t = 0$). As can be seen from this graph, the ROS production by the PTB7@F127 CPNs increased continuously throughout the 3-hour measurement period. For MB, however, the SOSG-EP fluorescence decreased steadily after an initial 0.5 hour of increase, indicating a reduction in the rate of ROS production by this standard photosensitizer.

There exist several possibilities that may be responsible for the observed decrease of SOSG-EP signal. The first is that SOSG-EP reverts back to the non-fluorescent form (SOSG) or, even more likely, diffuses out of the excitation volume faster than the MB is producing singlet oxygen to drive the SOSG-to-SOSG-EP reaction. We tested whether this was a contributing factor by building up a substantial level of SOSG-EP signal and then turning off the stimulation laser, thereby prohibiting any further $^1O_2$ production by the photosensitizer.

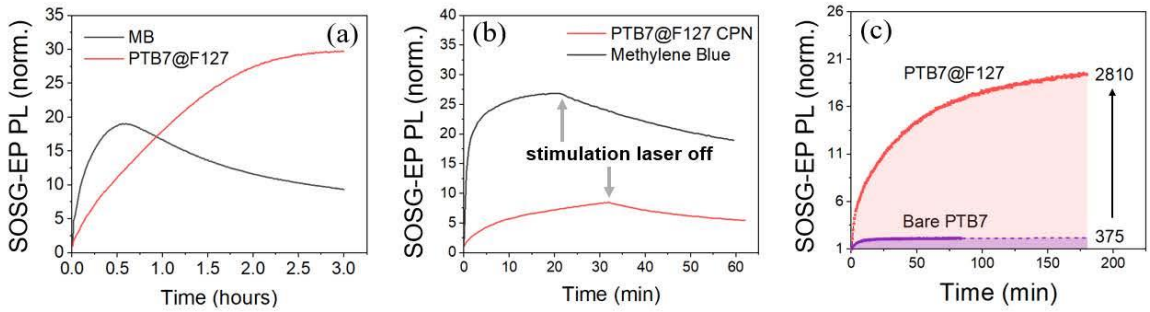

Figure S5.2. Singlet oxygen generation by PTB7@F127 CPNs under prolonged stimulation. Panel **(a)** shows the comparison of singlet oxygen production by the PTB7@F127 CPNs with the reference photosensitiser (methylene blue, MB) for a long stimulation period. In Panel **(b)**, the stimulation laser (635 nm) was turned off mid-way through the experiment, at times indicated by arrows in the graph. In the absence of stimulation, the fluorescence signal of SOSG decayed slowly over time. Panel **(c)** shows the evolution of the SOSG-EP PL signal for the bare PTB7 (purple) and PTB7@F127 (pink) samples of equal absorptions at the stimulation wavelength (635 nm). The numbers next to the data sets indicate the values of the SOSG-EP PL intensities for the two samples, integrated over a 3-hour period (shaded regions) with the bare PTB7 data extrapolated from 90 to 180 min. In the time period shown, the PTB7@F127 is estimated to have ~7.5-fold higher singlet oxygen generation efficiency compared to bare PTB7 sample.

As can be seen in Figure S5.2(b), the trends observed for Methylene Blue and PTB7@F127 CPNs were in this case similar, with a gradual decrease of SOSG-EP fluorescence over time, once the stimulation was removed. By fitting the SOSG-PL data post-stimulation with a mono-exponential function, the time constant for the SOSG-EP fluorescence decay was determined to be 18.3 ± 0.6 min. In the presence of stimulation (Figure S5.2a), the SOSG-EP fluorescence observed in the presence of MB was much slower, with an approximate time constant of 85.5 ± 1.1 min. However,

in this case, the production of $^1O_2$ was not inhibited, and therefore the continuous stimulation $^1O_2$ production by MB should have been much faster than the SOSG-EP fluorescence decay, and this was indeed the case at the beginning of the measurement (the first 30 minutes for MB) and for $^1O_2$ production by the PTB7@F127 CPNs, for which no decrease was observed at any point during the 3-hour measurement period.

A much more likely explanation is then that the observed decrease of SOSG-EP fluorescence after the 30 minutes is the result of reduced production of the $^1O_2$ by the MB after a prolonged excitation. The most likely cause is the degradation of the MB molecule through photobleaching and/or chemical destruction of the MB by the $^1O_2$ it itself produces.[6] In this regard, the performance of PTB7@F127 CPNs is notable since it seems to be stable against any such attacks. Continuous singlet oxygen production under prolonged excitation is critical for practical applications of the photosensitizers for PDT, and singlet oxygen-producing PTB7 CPNs developed in this work satisfy this requirement. This includes the bare PTB7 sample that was shown to have a continuously increasing generation of singlet oxygen over a 90-minute period, although at ~7.5-times smaller efficiency compared to the PTB7@F127 sample (see Figure S5.2c).

Measurements of singlet oxygen QY for PTB7 CPN samples

The QY for $^1O_2$ generation by CPNs was determined using a comparative method employing SOSG as the chemical fluorescence sensor for $^1O_2$. The process of converting SOSG to its fluorescence form SOSG-EP essentially constitutes a two-step reaction involving the singlet-oxygen producing sample (S) and the SOSG sensor molecule, with the first step requiring stimulation at frequency ν_1 (red laser in our case):

1) $h\nu_1 + \mathrm{S} \rightarrow {}^1\mathrm{O}_2$

2) ${}^1\mathrm{O}_2 + \mathrm{SOSG} \rightarrow \mathrm{SOSG\text{-}EP}$

The two reactions occur with respective efficiencies of η_{SO} for the singlet oxygen production by the sample and η_{EP} for the SOSG to SOSG-EP conversion, with η_{SO} being the limiting factor during the measurement since SOSG is present in excess. The fluorescence signal obtained from SOSG-EP is therefore dependent on both the absorbance A of the sample (at the stimulation wavelength) and its singlet oxygen yield η_{SO}. It can be shown that at low sample concentrations, the fluorescence signal is linearly proportional to both, namely that:

$$I_{PL} = K\eta_{SO}A$$

where K is a proportionality constant that incorporates all relevant experimental parameters that remain constant throughout the measurement, including the power of the stimulation lasers, the total time of the stimulation, the power of the excitation lamp, attenuation of fluorescence intensity by slits, efficiency of detector, extinction coefficient of SOSG *etc.* Therefore, a linear fit to I_{PL} *vs* A data will yield a slope that is proportional to the quantum yield of the singlet oxygen production by the sample.

Figure S5.3(b) shows the I_{PL} *vs* A data collected for MB in ethanol solution, in which it is known to have a singlet oxygen quantum yield of 52%. The SOSG fluorescence data were recorded after 5 minutes of continuous excitation with the 635 nm laser, as described earlier (Figure S5.3a). Using the value of the slope obtained from the linear fit to the I_{PL} *vs* A data (= 6993.3 ± 835.5) and η_{SO}= 0.52 yields a value of 13448.7 for our experimental constant K. Using this value for K, the singlet oxygen QY of other samples can now be measured, as long as the experimental conditions are kept the same. The red data points in Figure S5.3(b) show the results of the measurements for PTB7@F127

CPNs. The linear fit to the data yielded slope of 1136.1 ± 181.3, which implies that the singlet oxygen quantum yield of this sample in ethanol is 100%* 1136.1 / 13448.7 = (8.5 ± 1.7)%.

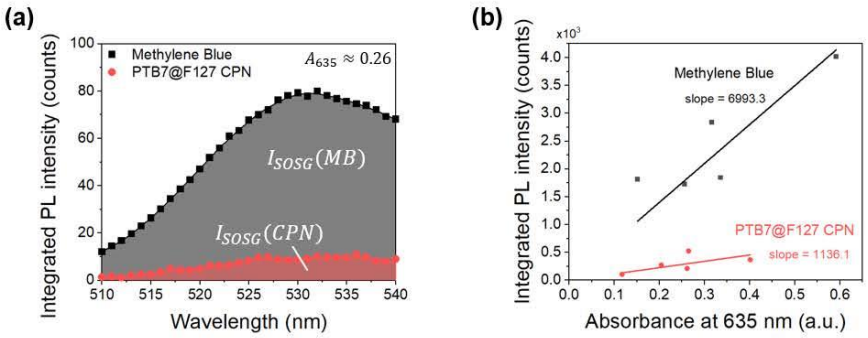

Figure S5.3. The singlet oxygen generation quantum yield (QY) of PTB7 @F127 in ethanol. (a) Fluorescence spectra of SOSG in the presence of Methylene Blue (black squares) and PTB7@F127 CPNs (red circles), for samples in ethanol with approximate absorbances of 0.26 at the stimulation wavelength of 635 nm. The integrated fluorescence intensity of SOSG was obtained by integrating the SOSG fluorescence over the shown spectral region (shaded areas). This was performed for solutions of different concentrations, yielding a plot of integrated SOSG fluorescence *versus* sample absorbance at 635 nm shown in panel (b). These data were fitted with linear fits; the slopes of these fits are indicated in (b) below sample names, and they were used to calculate the singlet oxygen QY of the PTB7@F127 CPNs.

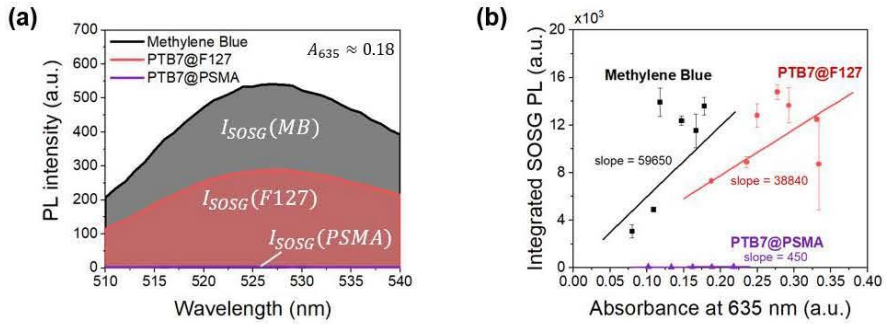

Figure S5.4. The singlet oxygen generation quantum yield (QY) of PTB7 @F127 and PTB7@PSMA in water. (a) Fluorescence spectra of SOSG in the presence of Methylene Blue (black line), PTB7@F127 CPNs (red line) and PTB7@PSMA CPNs (violet line), for samples in water with approximate absorbances of 0.18 at the stimulation wavelength of 635 nm. The integrated fluorescence intensity of SOSG was obtained by integrating the SOSG fluorescence over the shown spectral region (shaded areas). This was performed for solutions of different concentrations, yielding a plot of integrated SOSG fluorescence *versus* sample absorbance at 635 nm shown in panel (b). These data were fitted with linear fits; the slopes of these fits are indicated in (b) below sample names, and they were used to calculate the singlet oxygen QY of the PTB7@F127 CPNs and PTB7@PSMA CPNs.

The QY for $^1O_2$ generation by CPNs in water was determined using the same procedure, Figure S5.4(b) shows the I_{PL} *vs A* data collected for MB in water, in which it is known to have a singlet oxygen quantum yield of 52%. The SOSG fluorescence data were recorded after 5 minutes of continuous excitation with the 635 nm laser, as described earlier (Figure S5.4a). Using the value of the slope obtained from the linear fit to the I_{PL} *vs A* data (= 59650) and $\eta_{SO} = 0.52$ yields a value of 114711.5 for our experimental constant K. The red data points in Figure S5.4(b) show the results of

the measurements for PTB7@F127 CPNs and the violet data points show the results of PTB7@PSMA CPNs. The linear fit to the PTB7@F127 CPNs data yielded slope of 38840 ± 5500, which implies that the singlet oxygen quantum yield of this sample in water is 100%* 38840 ± 5500 / 114711.5 = (32.4 ± 4.8)%, while the PTB7@PSMA CPNs produced negligible amount of SO, with a QY of 0.38 ± 0.07%.

Photochemical stability of CPNs during Singlet Oxygen measurements

The polymeric backbones of conjugated polymers are highly susceptible to degradation in radical environments, often leading to poor photochemical stabilities of these polymers in the presence of highly reactive species such as singlet oxygen. To validate our results of singlet oxygen production measurements, it was important to exclude the possibility of any sample degradation during the measurements. To confirm this, the absorption spectra of the CPN/SOSG mixtures were recorded post- singlet oxygen production measurements. As can be seen in Figure S5.5(a) for bare PTB7 CPNs, the absorption spectra of these mixtures had clear signatures from both the PTB7 CPNs and the chemical sensor SOSG, allowing us to estimate contributions from both using a simple linear regression analysis.

Regression analysis was performed on the mixture absorption spectra, using pure CPN and SOSG spectra as basis for the linear regression ($A_{CPN}(\lambda)$ and $A_{SOSG}(\lambda)$ respectively). Regression analysis fitted the absorption spectra of the mixture to a linear combination of the two specified basis and a wavelength-independent background (A_{bgr}):

$$A_{CPN+SOSG}(\lambda) = A_{bgr} + k_{CPN} * A_{CPN}(\lambda) + k_{SOSG}A_{SOSG}(\lambda)$$

where A_{bgr} and contribution coefficients k_i were determined by the regression analysis. Figure 5.5(a) shows the result of the regression analysis ($A_{CPN+SOSG}(\lambda)$, dashed red line), as well as the calculated contributions from the CPNs and the SOSG ($k_i A_i$, purple and blue solid lines). In all cases, the result of the regression closely matched the as-measured absorption spectra of the CPN/SOSG mixture (R-squared values >0.999).

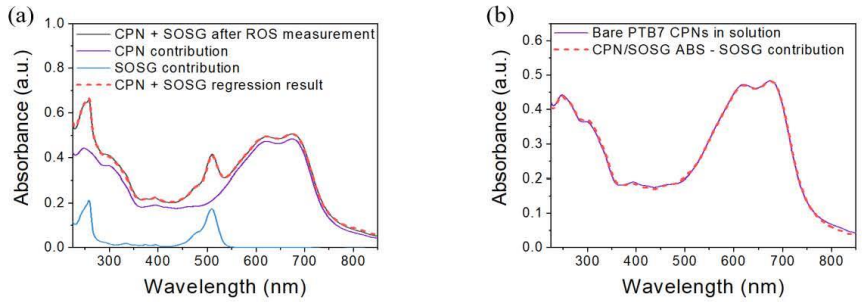

Figure S5.5. Photochemical stability of bare PTB7 CPNs in the presence of singlet oxygen. (a) Deconvolution of absorption spectrum of bare PTB7 CPN/SOSG mixture (black solid line) after 3 hours of continuous stimulation with 635 nm irradiation, into individual contributions from bare PTB7 CPNs (purple solid line) and SOSG (blue solid line) using regression analysis. The dashed red line shows the result of the deconvolution (R-squared value of 0.99927). Regression analysis was performed using the Multiple Linear Regression analysis functionality of Origin Pro 2018 software. **(b)** Comparison of PTB7 CPN contribution to the absorption spectrum of the CPN+SOSG mixture (red dashed line) to the absorption spectrum of bare PTB7 CPNs (purple solid line). The PTB7 contribution here is defined as the difference between the absorption of the CPN/SOSG mixture and the SOSG contribution, as determined by the regression analysis.

Using the outputs of the regression analysis, the CPN contribution to the CPN/SOSG mixture absorption can then be calculated *via* subtraction of the SOSG and background contributions:

$$A_{CPN}^{'}(\lambda) = A_{CPN+SOSG}(\lambda) - A_{bgr} - k_{SOSG}A_{SOSG}(\lambda)$$

This allowed us to compare this contribution to the original spectra of the CPN solutions (*i.e.* to compare $A_{CPN}^{'}(\lambda)$ to $k_{CPN} * A_{CPN}(\lambda)$). As shown in Figure S5.5(b) for bare PTB7 CPNs, the two spectra were nearly identical; furthermore, the CPN/SOSG solutions remained clear, homogenous and coloured throughout the singlet oxygen generation measurements. Since the absorption spectra of conjugated polymers is highly sensitive to their environment as well as chain packing, these results imply that no major chemical or structural changes occurred within the PTB7 CPNs as a result of 3-hour NIR stimulation and the resulting singlet oxygen production. That is, under the experimental conditions used, our PTB7 CPNs are resilient to photo-oxidative damage, most likely *via* efficient scavenging of the generated singlet oxygen by SOSG.

Superoxide production

Superoxide production by prepared PTB7 CPN samples was evaluated using the chronoamperometry method, as described in the main text of the paper. Prior to all measurements, the cell was tested on a known superoxide producer (xanthine oxide enzyme) to confirm that the electrode functioned as expected. Further control experiments were conducted to confirm 1) that the superoxide generation by the PTB7 CPNs was photoinitiated, and 2) that any changes in current measured by our cell were specific to superoxide production. To reaffirm photoinitiation, periodic irradiation with a UV source was used (Figure S6.1a): in all cases, the sizable increase in the measured current was observed when the light source was turned on (purple arrows in Figure S6.1) and a similar

decrease in the current followed when the light source was turned off (blue arrows). Note that for the PTB7 CPNs in the presence of the superoxide scavenger (superoxide dismutase, SOD), no such increase in the time-averaged current was observed (Figure S6.1a), although the amplitude and frequency of current oscillations did alter at the on/off time points. This, together with control experiments involving addition of SOD mid-way through the measurement, validates the specificity of our measurements to superoxide production by the CPNs.

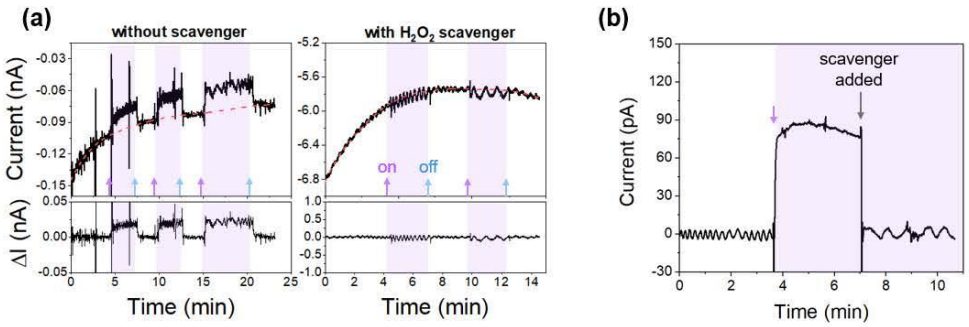

Figure S6.1. Superoxide production by PTB7 CPNs in the presence of H_2O_2 scavenger. (a) Chronoamperometry measurements on bare PTB7 CPNs in PBS, in the absence (left column) and presence (right column) of superoxide dismutase, under periodic UV irradiation. **(b)** Chronoamperometry measurements on PTB7@PSMA CPNs in PBS, under continuous UV irradiation, with the addition of superoxide dismutase at ~7 min, indicated by the grey arrow in the graph. In both panels, the UV lamp used to illuminate the cell was turned on at times indicated by purple arrows and turned off at time indicated by blue arrows, and the periods during which the UV lamp remained on are designated *via* purple shading.

According to these chronoamperometry measurements, all three types of fabricated CPNs produced approximately similar amounts of superoxide when used at high concentration of ~100 μg/mL. However, the capping of the PTB7 CPN played a crucial role in governing superoxide production by CPNs under continued illumination with UV radiation (Figure S6.2). The current dropped sharply for bare PTB7 CPNs, dropping to statistically insignificant levels within 7-10 minutes. On the other hand, chronoamperometric current remained high for both capped samples over the same period. These results are not in line with the photobleaching measurements described in Section 1, which showed approximately the same behavior for all three samples. Therefore, the superoxide itself is expected to be involved in the degradation process which leads to the decrease in the measured current, and the presence of the cap on the PTB7 CPNs affects the performance of the particle favourably.

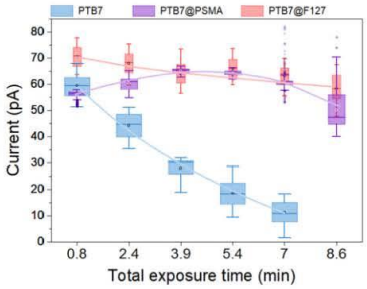

Figure S6.2. Superoxide production by different PTB7 CPN, as measured by chronoamperometry method. The effect of PSMA and F127 capping on superoxide production by PTB7 CPNs samples of high concentrations (90 for bare PTB7 and 100 μg/mL for PTB7@PSMA and PTB7@F127 CPNs). Non-normalized data.

PTB7 CPNs as NIR-I imaging agents

NIR images of 96-well plates containing fixed A549 cells previously incubated with CPNs were obtained using a customized microscopy system, as detailed in the Methods. By comparing the non-uniform distribution of cells under ambient illumination with the locations of the fluorescent CPNs, it is clear even at low magnification (10X and 20X objectives) that the CPNs trace the distribution of cells and not the zones of the well plate between cells (Figure S7.1). This co-localization is consistent with both fluorescent CPNs internalization and stable external adherence after multiple washes (see Methods).

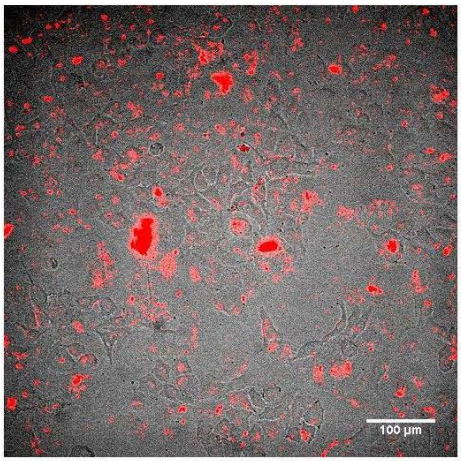

Figure S7.1. NIR fluorescence imaging of A549 cell line incubated with PTB7@PSMA. The fluorescence image (red) is superimposed on the ambient images (grey). Image taken with 20x objective.

Bare PTB7 CPNs as well as coated PTB7@PSMA and PTB7@F127 CPNs were incubated in duplicate wells within a 96-well plate, prior to being imaged. While the cell densities vary slightly from well to well, and from region to region in each well, they are broadly similar (Figure S7.2,

ambient images), but the fluorescence localizations are very different, showing a much larger number of fluorescence sources on the PTB7@PSMA samples than the other two. We ascribe this to an increased uptake of PTB7@PSMA compared to the other CPN formulations by the A549 cells. The fluorescence signal from the three CPN formulations is quantified in Figure S7.2(b).

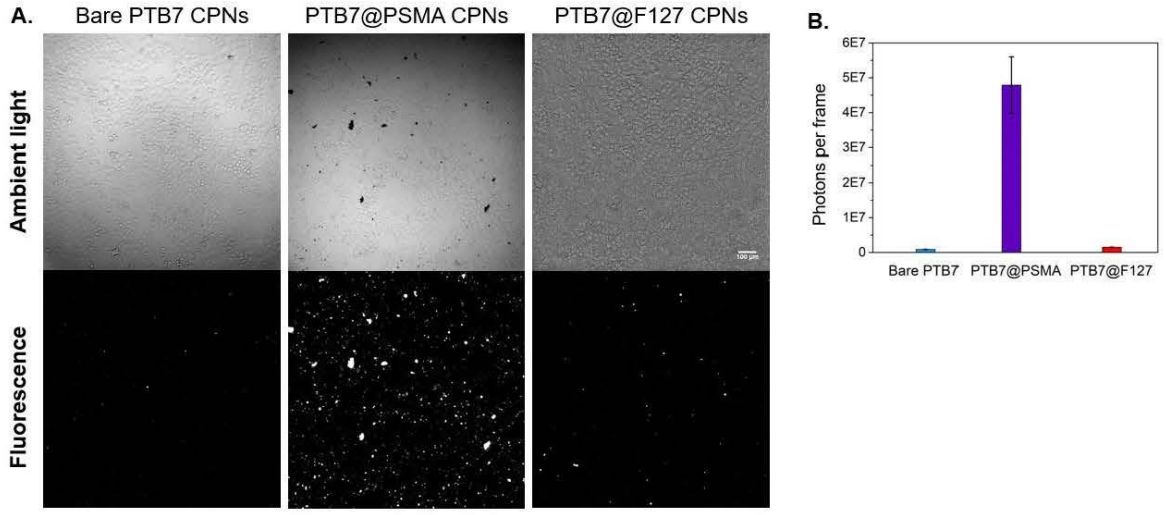

Figure S7.2. NIR fluorescence imaging of fixed A549 cells incubated with PTB7 CPNs. A. Figure shows ambient-light images (top row) and NIR fluorescence images (bottom row) for bare PTB7@F127 (left column), bare PTB7 (middle column) and PTB7@PSMA (right column). The illumination, camera settings and display greyscale were the same for all three fluorescent images, to ensure comparability. Images taken with 10x objective. **B.** Number of detected fluorescent photons (average per frame, above background) arising from cells incubated with stock concentrations of bare PTB7, PTB7@PSMA and PTB7@F127 CPNs, imaged through 10x objective. Error bars are standard errors, based on measurements in eight subregions across two samples.

At higher magnification (60x), the distribution of PSMA-capped CPNs within or on to the cells can be discerned (Figure S7.3). CPNs internalization is non-uniform, displaying both a low-level diffuse component consistent with local concentrations of CPNs or CPNs aggregates below the limit of resolution of the microscope. Additionally, a relatively small number of CPN aggregates are observable within the cells (consistent with vescicle mediated internalization) and non-colocalized with cells (consistent with non-internalized CPNs' un-soluble precipitates adhering to the bottom of the well).

Figure S7.3. NIR fluorescence imaging of fixed A549 cells previously incubated with PTB7@PSMA. Fluorescent image (red) superimposed on ambient-light image (greyscale), through a 60x objective, showing in detail the non-uniform distribution of CPNs in the cells.

Cell cultures were incubated with a range of CPN concentrations, at successive dilutions by a factor of ten. Images of the PTB7@PSMA cultures over two decades of concentration (Figure S7.4) show that despite similar densities of cells (ambient images), the fluorescence signals decrease with dilution, broadly as expected. The fluorescent signal from these three CPN concentrations, and from

a fourth incubated at 1/1000th of the initial value but for which the measured fluorescence value represents the sensitivity limit of our system, is quantified in (main text) Figure 7(c).

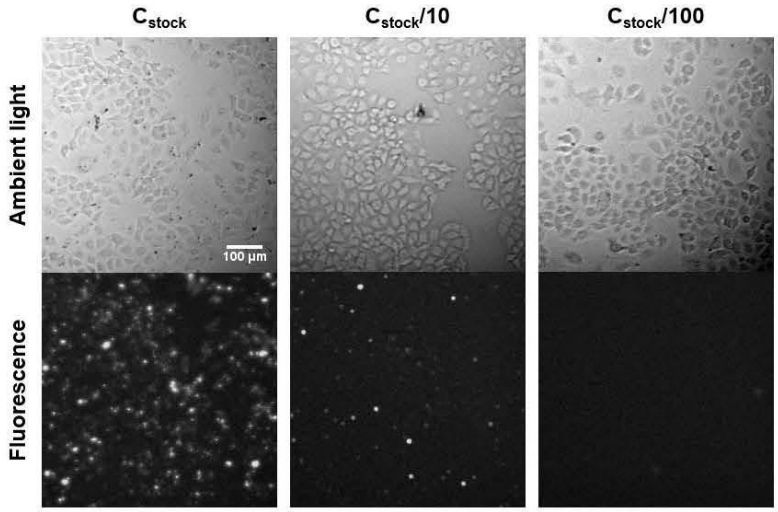

Figure S7.4. NIR imaging of fixed A549 cell line incubated with different concentrations of PTB7@PSMA CPNs. Ambient-light (top row) and fluorescence (bottom row) images for cells incubated with maximum concentration (left column), $1/10^{th}$ dilution (middle column) and $1/100^{th}$ dilution (right column) PTB7@PSMA. The illumination, camera settings and display greyscale were the same for all three fluorescent images, to ensure comparability. Images taken with 10x objective.

In vitro ROS production by PTB7 CPNs

The DCFDA cellular ROS detection kit (Abcam, Cambridge, UK) was used to determine the ROS production induced by photoexcitation of CPNs, according to the manufacturer's instructions. Briefly, the cells were washed with 100 µl of 1X ROS assay buffer. The buffer was then replaced by 100 µl of DCFDA solution and incubated for 45 minutes in the dark, and then replaced by PTB7@F127 CPNs dilutions in Roswell Park Memorial Institute medium (RPMI, 0-45 µg/mL).

Without allowing time for internalisation, NIR irradiation was applied with a light dose of 10 J/cm^2 at 660 - 850 nm using Derma Red Lamp (Care Lamps, Care Lamps, UK) to excite the nanoparticles. Normalised fluorescence readings from the ROS-signalling DCF with an emission wavelength of 520-530 nm were taken at time intervals of 0, 30, 60 and 120 minutes (Figure S8.1a) upon incubation. Details about repeats and Positive control wells for the ROS assay were supplemented with 100µL THBP and negative control wells contained untreated cells (n=3). The result shows a significant increase in ROS production even with small amount of PTB7@F127 CPNs and the ROS production ability shows incubation time dependent at a higher concentration of PTB7@F127 CPNs.

To better understand the cytotoxicity of PTB7@F127 CPNs, different concentrations of PTB7@F127 CPNs with different incubation times from 0-120 min were investigated using the PrestoBlue (PB) assay (Life Technologies, Carlsbad, USA) – a commercially available, ready-to-use and water-soluble preparation. A HaCaT viability assay with PB reagent was performed according to the manufacturer's protocol. HaCaT cells were seeded in a 96-well plate at a density of 1×10^4 cells per well. Prior to the assay, the growth medium was replaced by PTB7@F127 CPNs dilutions in RPMI (Sigma-Aldrich, USA), 0-45 µg/mL. Without allowing time for internalisation, NIR irradiation was applied with a light dose of 10 J/cm^2 at 660 - 850 nm using Derma Red Lamp (Care Lamps, Care Lamps, UK) to excite the nanoparticles. At the end of treatment, the cells were washed with PBS and incubated with PB reagent. The viability signalling PB (resorufin) fluorescence was read (Ex/Em 560 nm/590 nm) after 0, 60 and 120 minutes. The cell viability (Figure S8.1b) was expressed as a percentage relative to the untreated cells.

All groups screened in this study showed cytotoxicity with cell viability generally lower than 5%. The cell viability did not change over the observed time period, and cell viability was not significantly affected by the increase of PTB7@F127 CPNs concentration (greater than 95% viability).

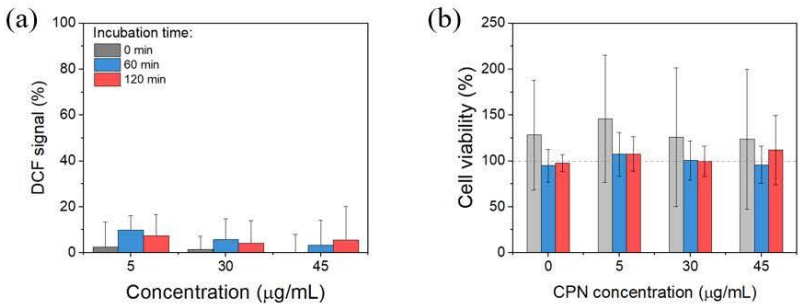

Figure S8.1. ***In vitro*** **ROS production by PTB7@F127 CPNs. (a)** DCF fluorescence signal and **(b)** cell viability of HaCaT cells incubated in the dark with different concentrations of PTB7 @F127 CPNs, for periods of 0 (grey), 60 (blue), and 120 (red) minutes.

References:

(1) Tian, G.; Sun, X.; Bai, J.; Dong, J.; Zhang, B.; Gao, Z.; Wu, J. Doxorubicin-Loaded Dual-Functional Hyaluronic Acid Nanoparticles: Preparation, Characterization and Antitumor Efficacy *in Vitro* and *in Vivo*. *Mol. Med. Rep.* **2019**, *19* (1), 133–142. https://doi.org/10.3892/mmr.2018.9687.

(2) Wang, X.; Geng, Z.; Cong, H.; Shen, Y.; Yu, B. Organic Semiconductors for Photothermal Therapy and Photoacoustic Imaging. *ChemBioChem* **2019**, *20* (13), 1628–1636. https://doi.org/10.1002/cbic.201800818.

(3) Bonnett, R.; Martinez, G. Photobleaching of Sensitisers Used in Photodynamic Therapy.

Tetrahedron **2001**, *57*, 9513–9547. https://doi.org/10.1002/chin.200211234.

(4) Liang, S.; Yang, X. Z.; Du, X. J.; Wang, H. X.; Li, H. J.; Liu, W. W.; Yao, Y. D.; Zhu, Y. H.; Ma, Y. C.; Wang, J.; Song, E. W. Optimizing the Size of Micellar Nanoparticles for Efficient SiRNA Delivery. *Adv. Funct. Mater.* **2015**, *25* (30), 4778–4787. https://doi.org/10.1002/adfm.201501548.

(5) Bencheikh, F.; Duché, D.; Ruiz, C. M.; Simon, J. J.; Escoubas, L. Study of Optical Properties and Molecular Aggregation of Conjugated Low Band Gap Copolymers: PTB7 and PTB7-Th. *J. Phys. Chem. C* **2015**, *119* (43), 24643–24648. https://doi.org/10.1021/acs.jpcc.5b07803.

(6) Nassar, S. J. M.; Wills, C.; Harriman, A. Inhibition of the Photobleaching of Methylene Blue by Association with Urea. *ChemPhotoChem* **2019**, *3* (10), 1042–1049. https://doi.org/10.1002/cptc.201900141.

3.1 Amendments and additions to the published text

In this section, some details of the published work are explained, expanded upon or amended.

Author contributions

M.Z. contributed to all experimental work, with the exception of NIR imaging and intracellular ROS production measurements. E.L. and S.B. contributed to CPN fabrication. S.C.-S. and S.P. assisted with CPN characterization (TEM and AFM). S.P. and L.U. performed the intracellular ROS production measurements. L.U. and S.G.R. performed the NIR imaging of cell lines incubated with CPNs. A.R. and P.M. performed the superoxide measurements. M.Z., M.P.C., S.P., L.U., and A.R. performed data analysis. All authors contributed toward the writing of the manuscript. L.A.D., M.G., and A.R. are responsible for the conception of the project, its direction, and management of the team. For the intellectual contribution to the original piece of work, I proposed suitable sample synthesis concentrations and experimental concentrations based on experimental needs, proposed a comparative volume approach to explain why the AFM and DLS/TEM diameters are different, proposed ideas to investigate the chemical and optical stability as good stability, as the current synthesis of highly stable CPNs offers significant advantages. Regarding stability studies, I designed specific experimental conditions that needed to be studied, such as different concentrations, size changes under different environmental PBS/FBS.

Corrections and additions

- Comparison of DLS and AFM volumes of PTB7 CPNs

In the manuscript, there was an error in the way standard deviation of the volume was propagated. The correct calculation is presented here.

Volume of particle can be calculated from its diameter:

$$V = \frac{4}{3}\pi\left(\frac{d}{2}\right)^3 = \frac{1}{6}\pi d^3$$

The diameter of the particle, d $(= 185\ nm)$, and its standard deviation, σ_d $(= 57\ nm)$, were obtained from DLS measurements. From this, the relative error in the standard deviation of particle volume is:

$$\frac{\sigma_V}{V} = \sqrt{\left(\frac{\sigma_d}{d}\right)^2 + \left(\frac{\sigma_d}{d}\right)^2 + \left(\frac{\sigma_d}{d}\right)^2} = \sqrt{3\left(\frac{\sigma_d}{d}\right)^2} = \sqrt{3}\,\frac{\sigma_d}{d} \sim 0.533$$

Therefore, the standard deviation in the volume of the particle should be:

$$\sigma_V = \left(\frac{\sigma_V}{V}\right) * V = 0.533 * (3.3 \times 10^{-3}\ fL) \approx 1.76 \times 10^{-3}\ fL$$

And not $3.1 \times 10^{-3}\ fL$ as stated in the text of the manuscript.

- Figures S1.1 and S1.2 were missing error bars. The updated versions of the graphs, which include errors of all measurements, are presented below.

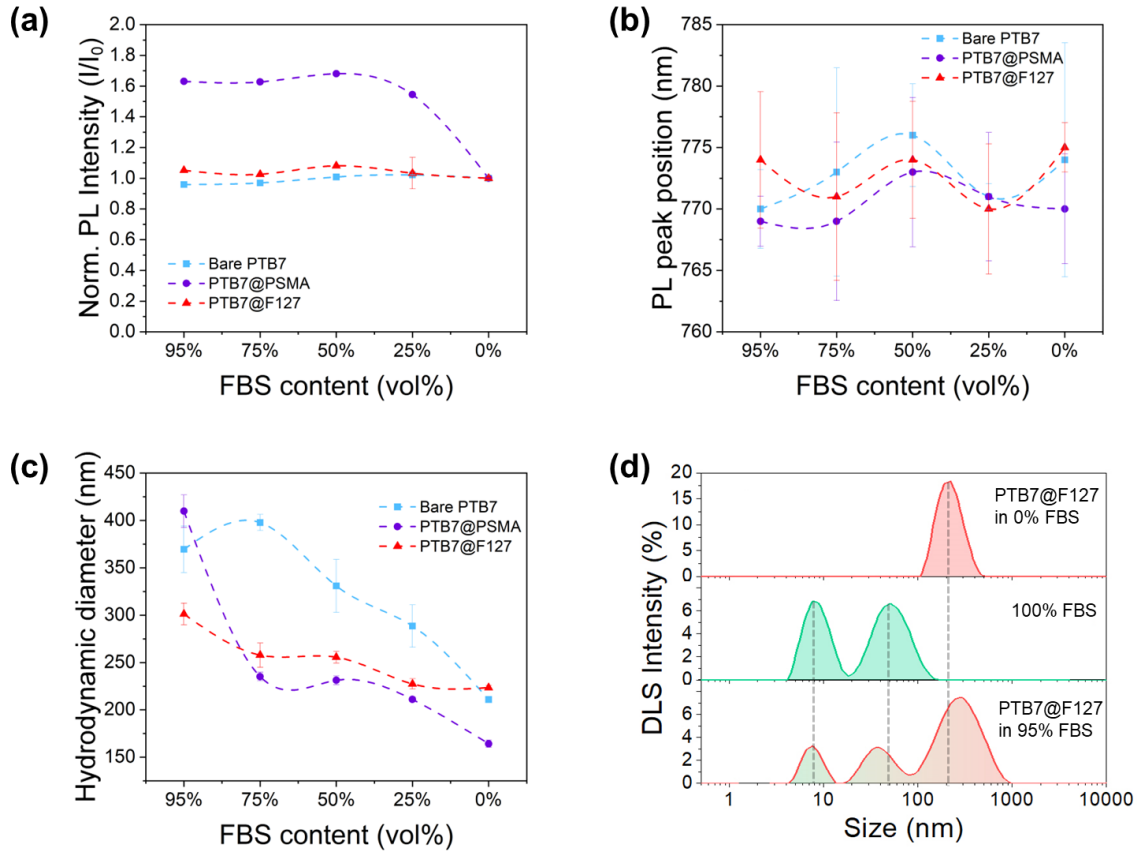

Figure S1.1. Fluorescence and size of PTB7 samples in presence of different concentrations of FBS. Both the intensity **(a)** and the position **(b)** of the fluorescence peak of all three PTB7 samples depended on the concentration of FBS. In panel **(c),** the size of all three PTB7 samples increased with increased concentration of FBS in suspension and the size of PTB7@F127 is the mostly stable while the size of PTB7@PSMA CPNs increased the most obvious. In panel (d), the dashed violet line indicates the average size (*Zav*) of the PTB7@F127 with 0% FBS in solution and the dashed olive line indicate the *Zav* of pure FBS.

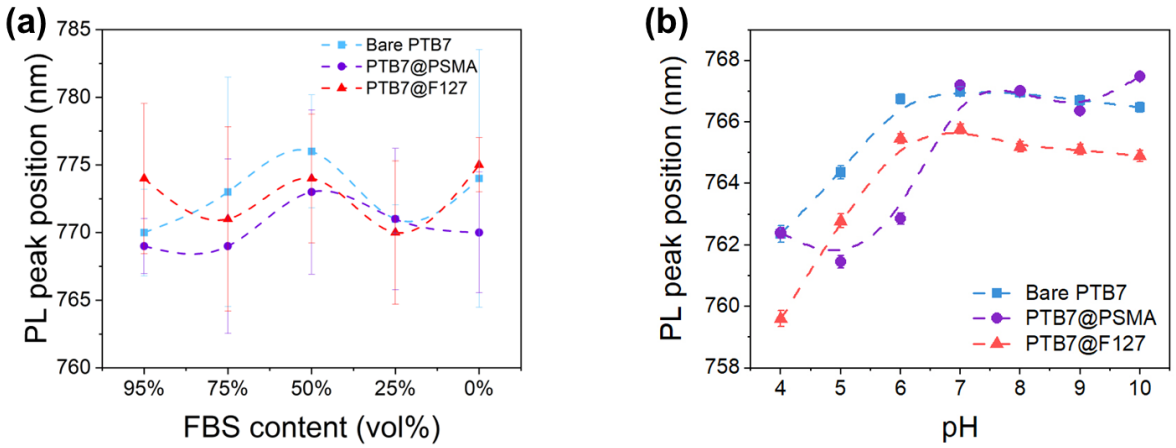

Figure S1.2. Fluorescence of PTB7 samples in suspensions of different pH values. Both the intensity **(a)** and the position **(b)** of the fluorescence peak of all three PTB7 samples depended on the pH of the suspension.

- In Figures S5.3 and S5.4, R^2 value of the fits were absent. Figures below show the same graphs with the R^2 values added:

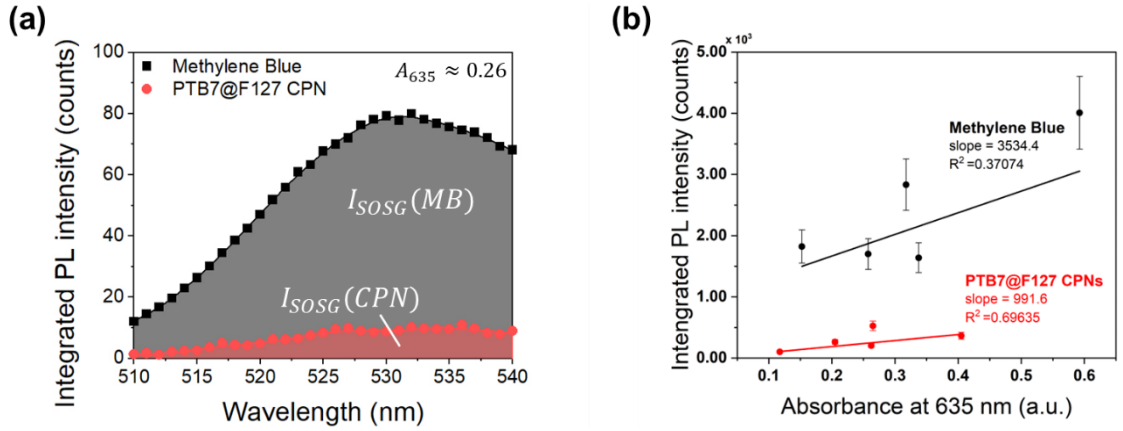

Figure S5.3. The $^1O_2$ generation quantum yield (QY) of PTB7 @F127 CPNs in ethanol. (a) Fluorescence spectra of SOSG in the presence of Methylene Blue (black squares) and PTB7@F127 CPNs (red circles), for samples in ethanol with approximate absorbances of 0.26 at the stimulation wavelength of 635 nm. The integrated fluorescence intensity of SOSG was obtained by integrating the SOSG fluorescence over the shown spectral region (shaded areas). This was performed for suspensions of different concentrations, yielding a plot of integrated SOSG fluorescence *versus* sample absorbance at 635 nm shown in panel (b). These data were fitted with linear fits; the slopes of these fits are indicated in (b) below sample names, and they were used to calculate the $^1O_2$ QY of the PTB7@F127 CPNs.

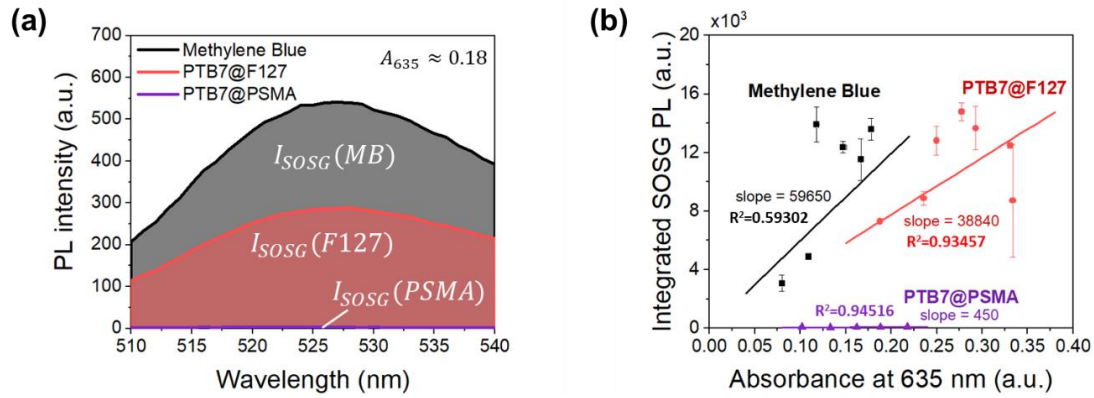

Figure S5.4. The $^1O_2$ generation QY of PTB7 @F127 and PTB7@PSMA in water. (a) Fluorescence spectra of SOSG in the presence of Methylene Blue (black line), PTB7@F127 CPNs (red line) and PTB7@PSMA CPNs (violet line), for samples in water with approximate absorbances of 0.18 at the stimulation wavelength of 635 nm. The integrated fluorescence intensity of SOSG was obtained by integrating the SOSG fluorescence over the shown spectral region (shaded areas). This was performed for suspensions of different concentrations, yielding a plot of integrated SOSG fluorescence *versus* sample absorbance at 635 nm shown in panel (b). These data were fitted with linear fits; the slopes of these fits are indicated in (b) below sample names, and they were used to calculate the $^1O_2$ QY of the PTB7@F127 CPNs and PTB7@PSMA CPNs.

- The scale bar of the figure S7.2 was not legible. Presented below is the same figure with updated caption text, which an added comment that specifies the size of the scale.

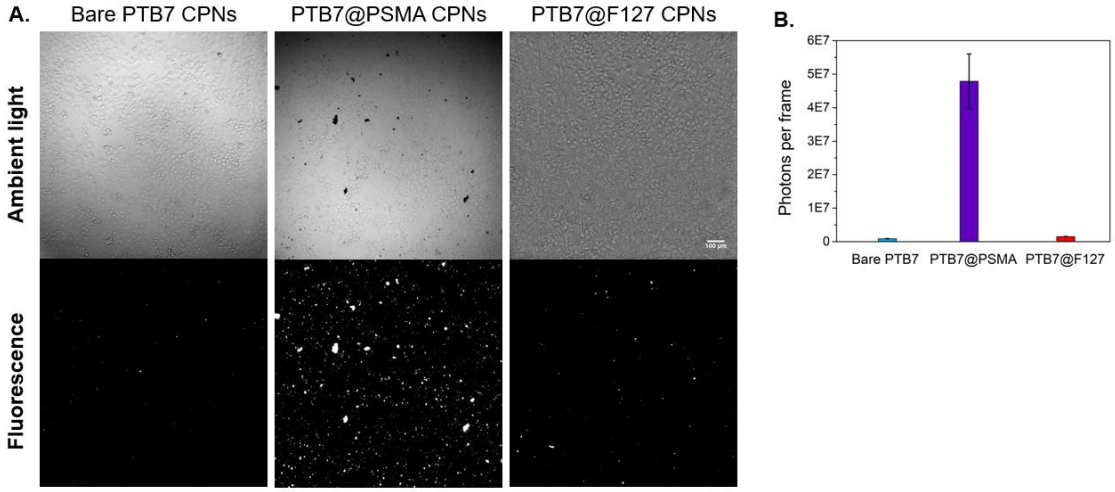

Figure S7.2. NIR fluorescence imaging of fixed A549 cells incubated with PTB7 CPNs. A. Figure shows ambient-light images (top row) and NIR fluorescence images (bottom row) for bare PTB7@F127 CPNs (left column), bare PTB7 CPNs (middle column) and PTB7@PSMA CPNs (right column). The illumination, camera settings and display greyscale were the same for all three fluorescent images, to ensure comparability. Images taken with 10× objective. Inserted scale bar represents 100 μm. **B.** Number of detected fluorescent photons (average per frame, above background) arising from cells incubated with stock concentrations of bare PTB7 CPNs, PTB7@PSMA CPNs and PTB7@F127 CPNs, imaged through 10× objective. Error bars are standard errors, based on measurements in eight subregions across two samples.

Chapter 4 - Optimization of PTB7@F127 CPNs

4.1 Introduction

In chapter 2, the nanoprecipitation method was described, which is the simplest method for the preparation of polymeric NPs.[1] Chapter 3 then described the development of CPNs-based NIR-I-active theranostic probes that can combine therapeutic and imaging actions together. The developed probes were shown to meet many of the criteria required for a theranostic probes, such as have good biocompatibility, excellent singlet oxygen generation, good fluorescence brightness, and strong near-infrared absorption allowing probe activation at larger penetration depths. The focus of this chapter is the optimization of the developed probes, using some of the above-mentioned criteria as feedback for the optimization. Specifically, the properties that are considered are the size of the CPNs, the optical spectrum, the fluorescence quantum yield, and the $^1O_2$ generation capacity.

The versatility of NPs largely depends on their physiochemical properties, with one of the most important properties being their size,[2] which is also an important factor to take into account when the CPNs are applied to the biological system.[3,4] As discussed in Chapter 1, the size should be appropriate for efficient cell adherent or cell uptake, and it should be suitable for EPR, which enables the accumulation of nanomaterials in the pathological areas.[5] Tumor tissues have irregular angiogenesis, which leads to impaired vessel structure and widespread fenestration of blood vessels.[6] When compared to healthy tissues, the leaky vasculature in a tumour makes it easy for NPs to get into the interstitium.[7] This extravasation of NPs is also considered to be a kind of passive targeting.[8] The surface to volume ratio of nanomaterials is determined by size, which can affect the uptake and biodistribution of nanomaterials and determine the effect of nanotherapeutics.[9] Guo and co-workers studied a series of monodispersed Fe_3O_4 NPs ranging in size from 60 to 310 nm to systematically investigate their biological behavior and application.[10] They found that small Fe_3O_4 NPs exhibited greater cellular internalization and showed higher bio-application efficacy *in vitro*. More applicable to our intended applications is that larger Fe_3O_4 NPs were shown to have enhanced accumulation in tumors, resulting in better tumor growth inhibition. They found that 120 nm may be the optimal nanoparticle diameter for bio-application *in vitro*, and even larger diameter NPs were needed for *in vivo* applications because NPs accumulation becomes predominantly important in most systems. Based on the above studies, the size of CPNs between 120 and 200 nm was chosen as the optimal range. Research has indicated that by adjusting the ratio of conjugated polymer to copolymer, the size of the CPNs can be varied between 40 and 500 nm.[11] This

strategy of changing the mass ratio of conjugated polymer to copolymer is applied in this chapter.

The other parameter that can be changed during the fabrication of the CPNs is the pH of the precipitating solution (organic phase, prior to CPNs formation) or indeed change of the pH of the precipitated suspension (aqueous phase, post CPNs formation). The pH of the solution prior to CPNs formation can affect the ionization state of the functional groups on the conjugated polymer,[12] thereby affecting the packing of the chains, and consequently the degree to which interchain interactions and aggregate formation affect the optical properties of the NPs.[13] On the other hand, previous research on the influence of pH on the encapsulation of hydrophobic drugs in F127 suggests that the pH of the aqueous solution can affect the quality of the F127 micelle, with lower pH values being associated with more compact micellar structures (Figure 4.1).[14] Therefore, the second optimization strategy to vary the pH of the nanoprecipitation mixture, either pre- or post-precipitation, through addition of acetic acid.

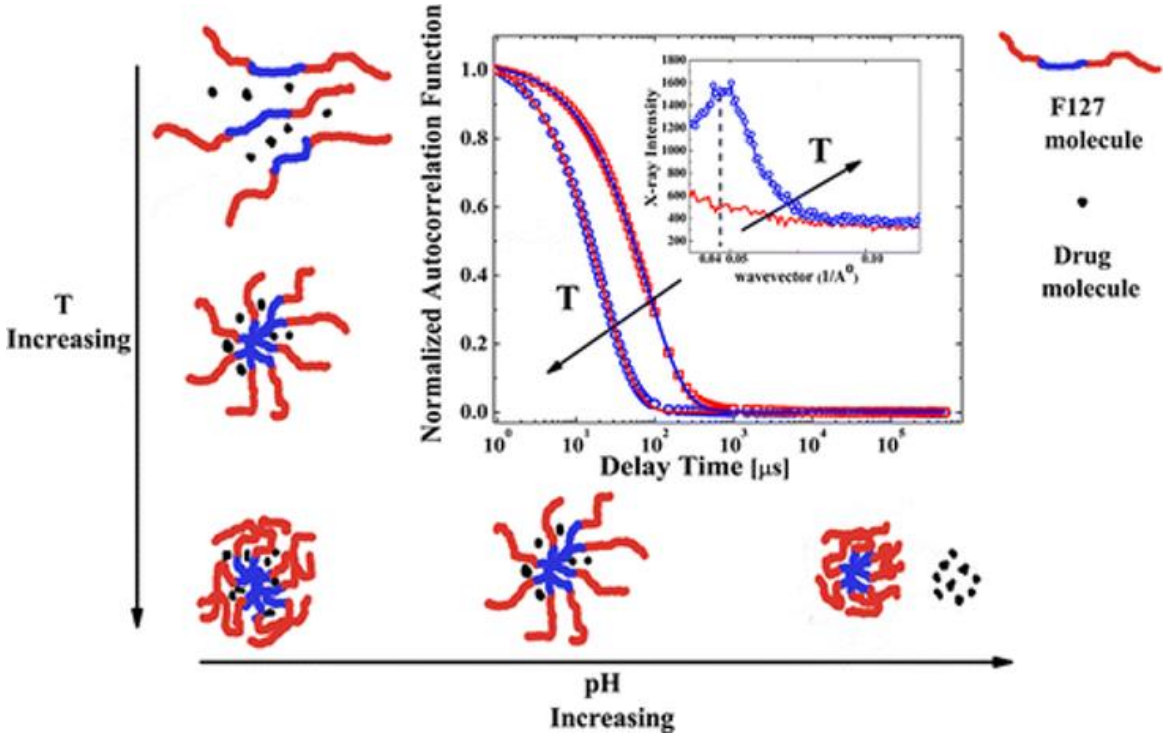

Figure 4.1 Effects of solution temperature and pH on the encapsulation of hydrophobic drugs in F127. (Copyright 2013 American Chemical Society)

4.2 Changing the mass ratio of PTB7 with F127

4.2.1 Sample preparation

In the work described in Chapter 3, PTB7 to F127 mass ratio used for the preparation of PTB7@F127 CPNs was 1:100. This mass ratio was selected somewhat arbitrarily, as this mass ratio tends to result in stable CPN formulations of many different compositions. Nonetheless, the focus of this chapter is the optimization of PTB7@F127 CPNs and, in view of the results of Chapter 3, is presents itself conveniently as the starting point for the optimization of CPs: copolymer mass ratio. I investigated two series of different mass ratios, starting from 1:10 to 1:1000 and 1:300 to 1:800. The specific dosages of PTB7 and F127 used during fabrication are shown in the following Tables 4.1 and 4.2 below.

Table 4.1. Fabrication of PTB7@F127 CPNs with different PTB7:F127 precursor mass ratios (1:10 to 1:1000).

PTB7@F127 CPNs samples	PTB7	F127	DI Water
PTB7@F127-1:10	0.25 mg	2.5 mg	2.5 mL
PTB7@F127-1:50	0.25 mg	12.5 mg	2.5 mL
PTB7@F127-1:100	0.25 mg	25 mg	2.5 mL
PTB7@F127-1:300	0.25 mg	75 mg	2.5 mL
PTB7@F127-1:1000	0.25 mg	250 mg	2.5 mL

Table 4.2. PTB7@F127 CPNs with different mass ratio (1:300 to 1:800)

PTB7@F127 CPNs samples	PTB7	F127	DI Water
PTB7@F127-1:300	0.25 mg	75 mg	2.5 mL
PTB7@F127-1:400	0.25 mg	100 mg	2.5 mL
PTB7@F127-1:500	0.25 mg	125 mg	2.5 mL
PTB7@F127-1:600	0.25 mg	150 mg	2.5 mL
PTB7@F127-1:700	0.25 mg	175 mg	2.5 mL
PTB7@F127-1:800	0.25 mg	200 mg	2.5 mL

Specifically, the fabrication protocol is as follows:

1. 20 mg PTB7 powder was dissolved in 20 mL THF to a concentration of 1 mg/mL, and 2 g F127 was dissolved in 20 ml THF to a concentration of 100 mg/mL. These were the stock solution of each polymer.

2. To make PTB7@F127 samples, 0.25 mL of PTB7 stock solution was first mixed with a small volume of F127 stock solution, and the mixture was then added into 2.5 mL DI water whilst being sonicated for 5 mins. The volume of the F172 stock used was such as to provide the masses stated in tables 4.1 and 4.2, *e.g.* 25 μL (=2.5 mg) for PTB7@F127-1:10 sample.

3. A stirrer bar was added and the suspension was left stirring for 3 days, then topped up with DI water to 2.5 ml. After THF fully evaporated, PTB7@F127 CPNs with specific mass ratio were obtained.

4.2.2 Size

The hydrodynamic size of the different as-prepared mass ratios of CPNs samples was measured using DLS. The results showed that the 1:10 mass ratio samples had a mean size of 249.4 nm, the 1:50 mass ratio samples were 176.9 nm, the 1:100 mass ratio samples were 181.1 nm, the 1:300 mass ratio samples were 170.9 nm, and the 1:1000 mass ratio samples were 365.1 nm (Figure 4.2(a)).

The result shows that the size is comparatively stable when the mass ratios increase from 1:10 to 1:300, and then the size increases remarkably when the mass ratio increases to 1:1000. So further investigation was conducted to focus on the mass ratios between 1:300 and 1:1000.

As shown in Figure 4.2(b), the results of DLS measurements show that the mean sizes for the 1:300, 1:400, 1:500, 1:600, 1:700 and 1:800 mass ratio samples were 152.0 nm, 195.2 nm, 199.9 nm, 167.2 nm, 188.8 nm, and 133.6 nm respectively. Therefore, the results show that the size of the CPNs oscillates for as the mass ratios are increased from 1:300 to 1:1000. Most likely, this is because the F127 is in large excess for any mass ratio above 1:500, thereby unable to form nice micelles, leading to less repeatability of the process.

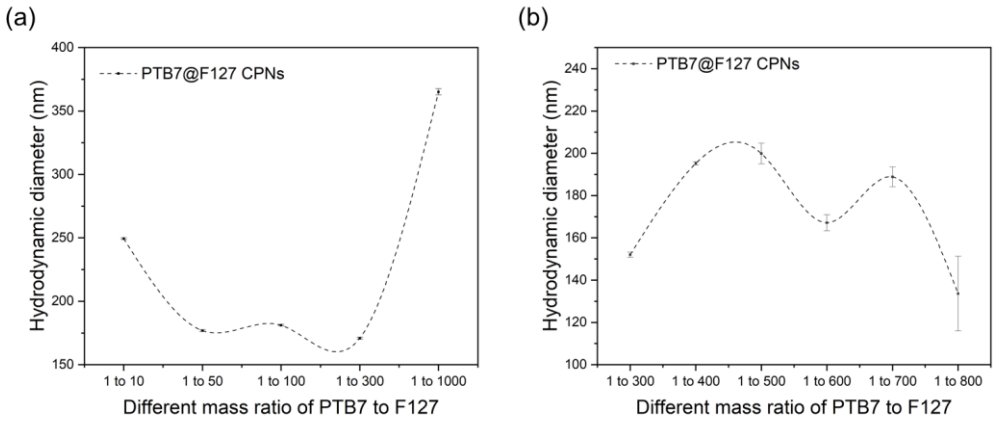

Figure 4.2 Hydrodynamic sizes of PTB7@F127 CPNs in different mass ratios. Comparison of DLS measurements of aqueous dispersions of CPNs formed using (a) PTB7 to F127 mass ratios ranging from 1:10 to 1:1000 and (b) PTB7 to F127 mass ratios varying from 1:300 to 1:800.

4.2.3 Optical spectrum

As can be seen from Figure 4.3, the absorption of 1:10 and 1:1000 samples differs from absorption of 1:50/1:100/1:300 samples, in that the mass ratio of amplitudes and the positions of the two absorption peaks corresponding to transitions into the 1st and 2nd excited levels are different for these two samples. The red shifts of the absorbance peaks for these two samples are typically associated with the large size of conjugated domains, whereas the mass ratio of the absorbance peaks is known to be sensitive to the interchain interactions (see Chapter 3). Both, however, are indicative of different organization of the conjugated polymer chains in these CPNs compared to those produced at other mass ratios.

Conversely, the absorptions of 1:300 to 1:800 samples vary little with PTB7:F127 mass ratio (Figure 4.4 (b)). The relative intensities of the peaks are more similar to each other, when compared to those of the 1:10 to 1:1000 samples, as are their positions, although subtle changes can be noticed. Specifically, the mass ratio of transition intensities into the first and second excited states (A_1/A_2) decreased at first with increasing PTB7:F127 mass ratio, upon which it displayed oscillatory behavior reminiscent of the already discussed DLS results, albeit with an opposite overall trend (Figure 4.2(b)).

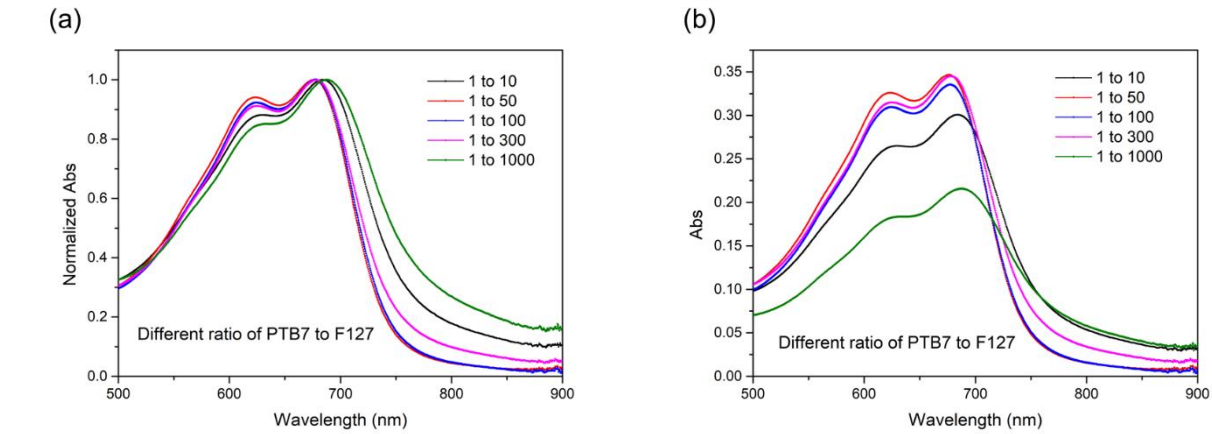

Figure 4.3 Steady-state absorption of PTB7@F127 CPNs in mass ratios from 1:10 to 1:1000 in aqueous suspensions. The absorption peak shown in (a) was normalized, and the absorption peak shown in (b) was the absolute absorption.

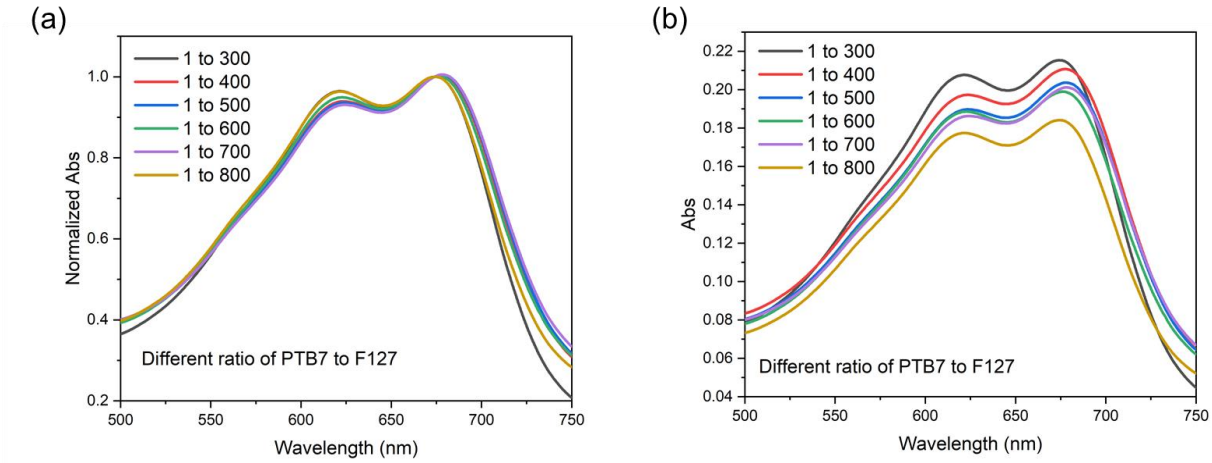

Figure 4.4 Steady-state absorption of PTB7@F127 CPNs in mass ratios from 1:300 to 1:800 in aqueous suspensions. The absorption spectra shown in (a) were normalized to highest value of sample absorption, and the absorption spectra shown in (b) are the non-normalized, as-measured results.

4.2.4 Singlet oxygen generation

The $^1O_2$ production by the CPNs produced at different PTB7:F127 mass ratios was evaluated next, using the same spectroscopic method as that described in Chapter 3. As one can see from Figure 4.5(a), the overall trend observed for the first series of samples is that of increasing $^1O_2$ production (4.4, 7.3, 8.8 and 10.17-fold increase in SOG signal over the measurement period for 1:10, 1:50, 1:100 and 1:300, respectively), with the exception of the last sample in the series (1:1000) for which the SOG production was reduced. For the series of samples with mass ratios varying from 1:300 to 1:800, the increase in $^1O_2$ production was recorded as 15.3, 9.4, 7.9, 10.7, 7.6, and 12.2 respectively (Figure 4.5(b)). That is, the observed trend is again one of

oscillations in values, consistent with observations of oscillation in the absorption and DLS experiments. In fact, like the trend observed in the A_1/A_2 ratio above, this oscillating trend is also opposite to the DLS results, and it becomes particularly obvious when SOG production and size results are compared side by side for both series (Figure 4.6). By comparing the trends across rows, one can conclude that the trends in the size of CPNs and $^1O_2$ production are in fact opposite. Therefore, under the same experimental conditions, the smaller size PTB7@F127 CPNs have better $^1O_2$ generation capacity. Combined with the similar trends in absorbance data, this phenomenon also indicates that all results are consistent with each other and that there is an intrinsic relationship between these three properties.

Considering all results (DLS, absorption, and $^1O_2$ generation), the mass ratio of 1:300 can be clearly identified as the best mass ratio for making PTB7@F127 CPNs. For this reason, samples of PTB7@F127 CPNs (1:300) were further characterized in terms of their fluorescence quantum yield, with a view to establish a baseline for the pH-based optimization.

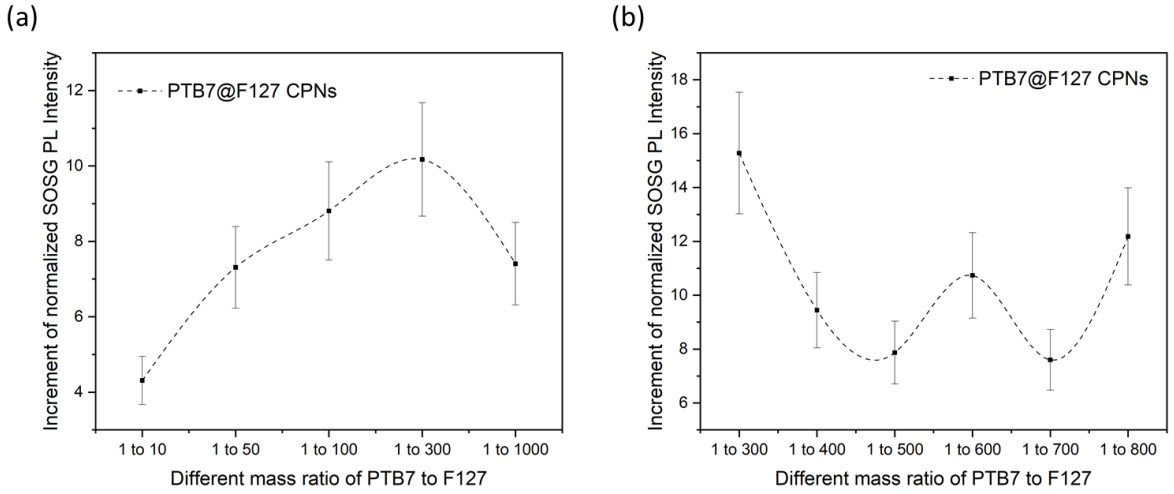

Figure 4.5 Measurement of $^1O_2$ production by different mass ratio of PTB7@F127 CPNs. Panel (a) compares $^1O_2$ production by the PTB7@F127 CPNs mass ratios from 1:10 to 1:1000. (b) Compares $^1O_2$ production by the PTB7@F127 CPNs mass ratios from 1:300 to 1:800. For all measurements, samples had absorbances of about 0.4 for 1:10 to 1:1000 samples and about 0.5 for 1:300 to 1:800 samples at the stimulation wavelength (635 nm) prior to the addition of SOSG. This corresponded to CPNs samples' concentrations of ~10 μg/mL and a concentration of 7.6 μM for MB solution. The illumination time is 30 mins.

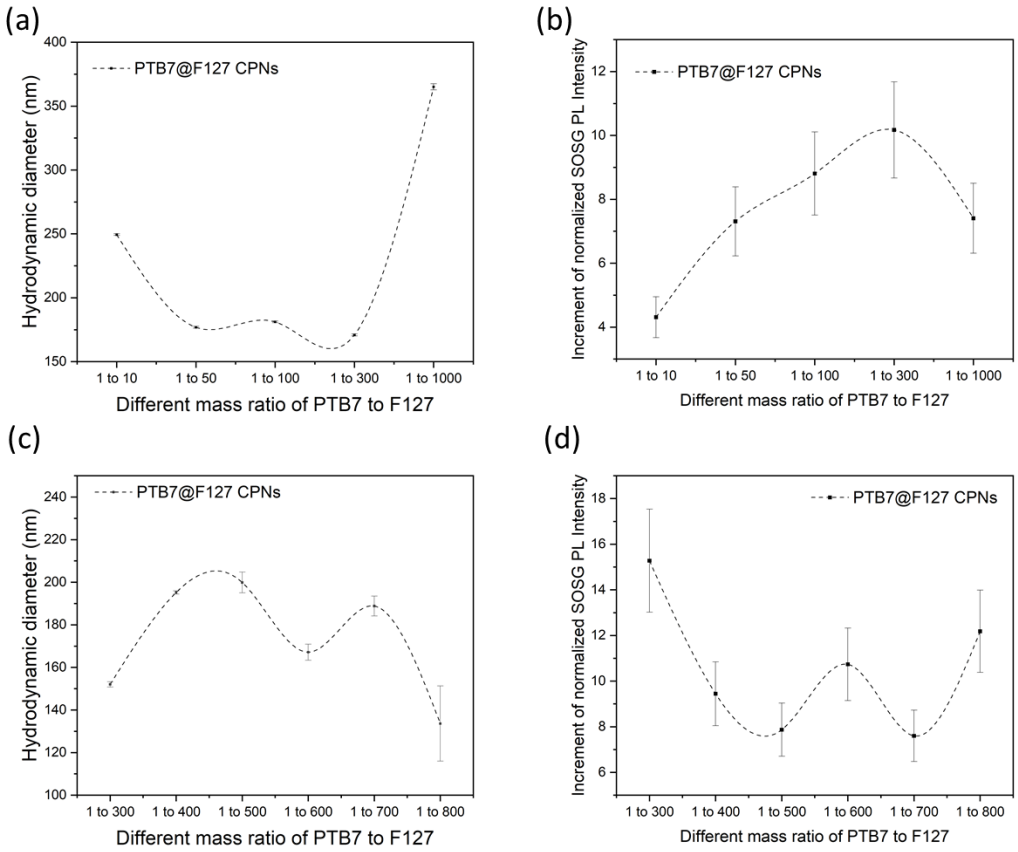

Figure 4.6 Hydrodynamic sizes and measurement of $^1O_2$ production by different mass ratio of PTB7@F127 CPNs. (a) and (b) Compares the oscillation trends of hydrodynamic sizes and $^1O_2$ production by the PTB7@F127 CPNs mass ratios from 1:10 to 1:1000. (c) and (d) Compares the oscillation trends of hydrodynamic sizes and $^1O_2$ production by the PTB7@F127 CPNs mass ratios from 1:300 to 1:800. (Indicate there is error bar (a))

Figure 4.7 shows the result of the measurement for an oppositely oscillating trend was observed between the measured hydrodynamic diameter of the particles in the set and their efficiency of SOSG production, highlighting the as yet not understood or reported anti-correlation between the two properties.

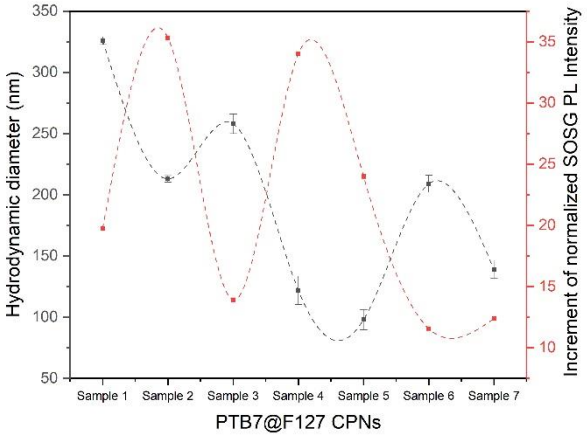

Figure 4.7 Hydrodynamic sizes and measurement of $^1O_2$ production by different size of PTB7@F127 CPNs.

4.2.5 Fluorescence quantum yield

The PLQY of PTB7@F127 CPNs (1:300) was measured using a simplified relative method. The PTB7@F127 (1:100) sample developed in Chapter 3 was used as a standard.

For the measurements, all samples were first diluted to have absorptions of less than 0.15 at the peak, and the excitation wavelength was chosen such that the absorptions were the same for a single pair of samples. The samples were then analyzed in a pairwise fashion, using the same set of settings to record the fluorescence spectra of samples in each pair. Specifically, both samples were excited at 680 nm, and the fluorescence spectra were recorded in the 700–900 nm spectral range. The fluorescence intensities under the peaks were then integrated and plotted versus sample absorbances, which were further fitted to linear relationships (shown in Figure 4.7). The slopes of the linear fits, combined with the known PLQY of the reference sample (Atto700, $\emptyset_{ref}$ =25%), were then used to calculate the PLQY of the test sample, as described in the chapter 2. In such a manner, the PLQY of (2.0 ± 0.053)% was obtained for the PTB7@F127 CPNs (1:300), which is 54% improvement over the previous formulation of PTB7@F127 CPNs.

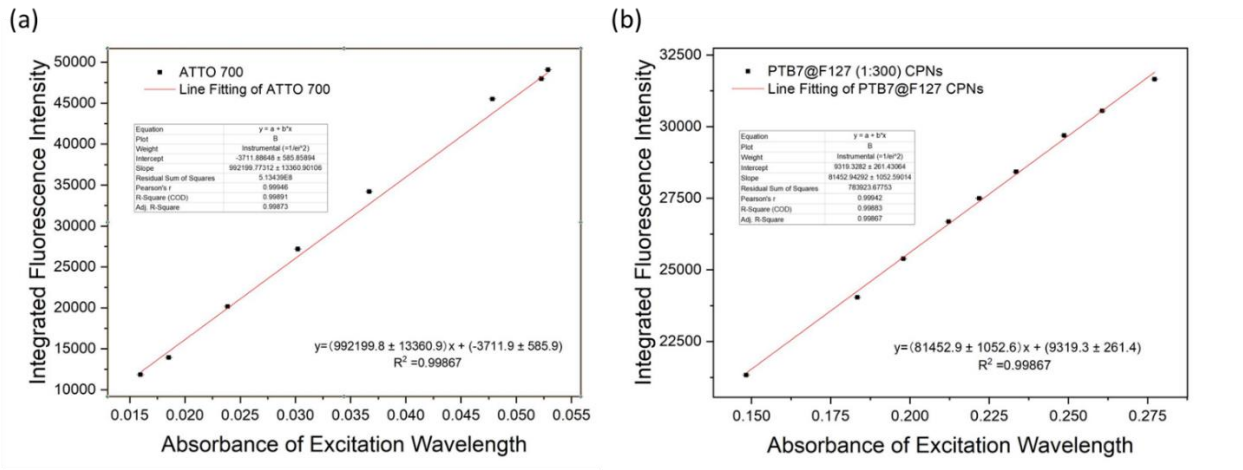

Figure 4.8 Comparation of PLQY of reference dye Atto700 with PTB7@F127 CPNs (1:300). (a) and (b) show the dependence of fluorescence intensity versus absorbance at excitation wavelength for the reference dye Atto700 and PTB7@F127 CPNs (1:300) sample respectively. The excitation wavelength was 680 nm for both samples. The error is too small to show. The errors in recorded fluorescence intensities and wavelengths are too small to be visible on the graph and were therefore omitted for clarity.

4.3 Change the pH of PTB7@F127 CPNs

4.3.1 Sample preparation

Having established the 1:300 PTB7:F127 mass ratio as the optimum mass ratio to produce PTB@F127 CPNs, further optimizations involving changing the pH of the precipitating mixtures was undertaken. Two different approaches for fabricating the PTB7@F127 CPNs at different pH have been explored.

The first approach was to investigate the influence of different pH conditions on the properties of CPNs, when the pH was changed after the PTB7@F127 CPNs were already formed. For these measurements, each sample was prepared to have 2.5 mL volume and to have a concentration of 0.1 mg/mL using a procedure that involved two steps:

A. The stock solutions of PTB7 and F127 in THF were prepared by dissolving PTB7 powder to a final concentration of 1 mg/mL and F127 powder to a concentration of 100 mg/ml.
B. 250 µL of PTB7 stock solution and 250 µL of F127 stock solution were mixed, and then added into 2.5 ml DI water. This yielded a sample of 3 mL, however, the 0.5 mL total volume of THF was gradually evaporated, resulting in the total final volume of the samples to be 2.5 mL. After the THF had been evaporated and the PTB7@F127

CPNs had been made, different amount of acetic acid was added accordingly to each sample, as summarized in Table 4.3.

Table 4.3. PTB7@F127 CPNs fabrication in different pH (adjust pH after forming CPNs)

PTB7@F127 CPNs samples	PTB7	F127	DI Water	Acetic Acid
PTB7@F127-1	0.25 mg	25 mg	2.5 mL	0 μL
PTB7@F127-2	0.25 mg	25 mg	2.5 mL	5 μL
PTB7@F127-3	0.25 mg	25 mg	2.5 mL	10 μL
PTB7@F127-4	0.25 mg	25 mg	2.5 mL	15 μL
PTB7@F127-5	0.25 mg	25 mg	2.5 mL	20 μL
PTB7@F127-6	0.25 mg	25 mg	2.5 mL	25 μL
PTB7@F127-7	0.25 mg	25 mg	2.5 mL	30 μL

The second approach was to investigate the influence of different pH environments during the formation of the PTB7@F127 CPNs by adjusting the pHs of the stock solutions before adding them into DI water. The total volume of each prepared sample was again kept to 2.5 mL, with a concentration of 0.1 mg/mL. The protocol for the preparation of these samples was:

A. The PTB7 powder was dissolved in THF to a concentration of 1 mg/mL and F127 was dissolved in THF to a concentration of 100 mg/mL. These were the stock solution of each polymer.
B. 250 μL of PTB7 stock solution and 250 μL of F127 stock solution were mixed together and different amounts of acetic acid were added accordingly to the mixture (as summarized in Table 4.4). This solution was then added to 2.5 mL DI water to from PTB7@F127 CPNs, following which 0.5 mL of THF present in the sample was evaporated.

Table 4.4. PTB7@F127 CPNs fabrication in different pHs (adjust pH before forming CPNs)

PTB7@F127 CPNs samples	PTB7	F127	Acetic Acid	DI Water
PTB7@F127-1	0.25 mg	25 mg	0 μL	2.5 mL
PTB7@F127-2	0.25 mg	25 mg	5 μL	2.5 mL
PTB7@F127-3	0.25 mg	25 mg	10 μL	2.5 mL
PTB7@F127-4	0.25 mg	25 mg	15 μL	2.5 mL
PTB7@F127-5	0.25 mg	25 mg	20 μL	2.5 mL
PTB7@F127-6	0.25 mg	25 mg	25 μL	2.5 mL
PTB7@F127-7	0.25 mg	25 mg	30 μL	2.5 mL

4.3.2 Size

DLS measurements of the two sets of samples described in previous section showed that once CPNs have already been formed, the pH of the environment does not influence the size of the CPNs greatly; in contrast, adjustment of the pHs of the stock PTB7 and F127 solutions in THF, prior to reprecipitation, strongly influenced both the hydrodynamic radius of the samples and the polydispersity of the samples (Figure 4.8). Interestingly, the trends in the DLS sizes of particles and polydispersity of samples were mirrored for both approaches, with samples characterized by particles of larger sizes consistently having larger polydispersities. One explanation of this effect could be that certain conditions are optimal for packing of chains within the CPNs, resulting in smaller particles and reduced variability in the chain packing from particle to particle, producing the observe mirrored trends. Regardless of this fact, however, it is clear that once CPNs are formed, they are relatively stable, with relatively small changes to their size depending on the pH of the environment. The changes observed in Figure 4.8(a) can easily be the result of the ionization of the end groups on F127, as well as its re-organization on the surface of the CPNs, especially in view of our observations of this shell being extremely fluid (see Chapter 3). On the other hand, the addition of the acid prior to CPNs formation has a very strong influence on the size and polydispersity of the formed particles, implying that it is the chain packing within the CPNs that is affected.

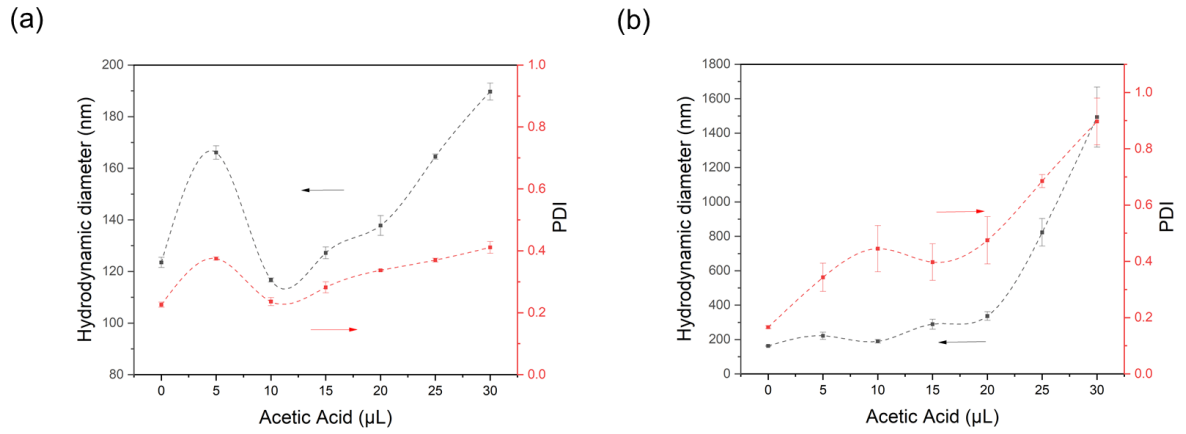

Figure 4.9 Hydrodynamic sizes of PTB7@F127 CPNs adding different amounts of acetic acid. Comparison of DLS measurements of aqueous dispersions of PTB7@F127 CPNs prepared under different pH conditions, when the pH of the solutions was adjusted (a) after and (b) before the reprecipitation of the CPNs. The pH was in each case adjusted by adding acetic acid to respective solutions. The dashed blue lines indicate the trend in the average size of the CPNs across each series of samples and the dashed red line indicates the corresponding trends in the polydispersity indices (PDI).

4.3.3 Optical spectrum

For the PTB7@F127 CPNs formed under neutral conditions, with subsequent addition of acetic acid (Figure 4.9 (a)), one can see that the absorption spectra of each sample is roughly the same amongst the set – little differences are observed, and those that are can be attributed to small changes in the amount of reagents used during the fabrication process. This result is in line with the above assumptions that only the F127 shell is affected by the change of the pH once NPs have formed, since no change in the PTB7 absorption peaks are observed here. In contrast, the absorption of PTB7@F127 CPNs formed in the presence of acetic acid (added prior to reprecipitation of CPNs, Figure 4.10 (a)) showed a clearly increasing scattering background (due to increased particle sizes) but also a clear change in the relative intensities of the absorption peaks and small shifts in their positions. Careful examination of the data showed that the A_1/A_2 ratio remained same for 0 to 10 µL acetic acid additions, but then decreased steadily with increasing amounts of acid added. These changes in absorbance at increasing acid amounts is consistent with the above DLS results (Figure 4.8), showing a somewhat oscillatory behavior for 0-10 µL acid volumes, followed by a steady increase in size thereafter.

Again, results seem to indicate that once formed in aqueous suspension, the pH has only a small influence on the performance of the PTB7@F127 CPNs. Therefore, the optimization

procedure should focus on the pH influence of performance by adding acid before forming CPNs in aqueous suspension.

Interestingly, for either of the approaches, the change in the pH caused no observable changes to the fluorescence spectra, be that its shape and or peak location (Figure 4.9 (b) and Figure 4.10 (b)). This is not altogether surprising, however, since emission from CPNs is more indicative of the nature of the lowest excited state, from which emission occurs, than the excitonic species that are initially excited, whose features we observe in the absorbance spectra and that are subject to change depending on the packing of the polymer chains. In the case of PTB7@F127 CPNs, the emission is H-aggregate like and these results indicate that this nature does not change upon any changes in the pH of the suspension, whether these changes were implemented prior or post re-precipitation of the CPNs.

One must note, however, that the spectra of these CPNs are markedly different to those presented in Chapter 3. This is not a result of different chain packing at different PTB7:F127 mass ratio nor the fabrication conditions used, but rather due to the different packing of the conjugated polymer due to its different molecular weight. In Chapter 3, PTB7 polymer of 80,000-200,000 Da was used (Sigma-Aldrich), whilst the work of investigating the influence of pH described here was performed using CPs of 78,852 Da molecular weight (Ossila, batch M216). Although different batch of sample was used in this investigation, the same batch of sample was same for all investigations described in this section. The purpose of this was to investigate the effect of fabrication pH on the optical properties of the resulting PTB7@F127 CPNs and to provide guidance for optimizing their fabrication. The results obtained here are specific to the batch of polymer precursor used - the fabrication protocol should be optimized for each new batch of sample.

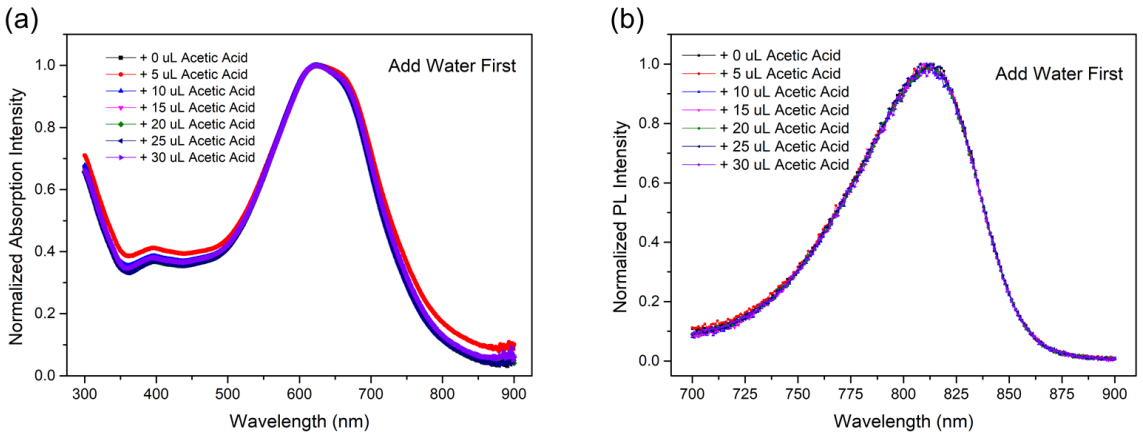

Figure 4.10 Optical spectrum of PTB7@F127 CPNs adding acetic acid after forming CPNs in aqueous suspensions. Steady-state normalized (a) absorption and (b) fluorescence spectra of PTB7@F127 CPNs after adding different amount of acetic acid, post CPNs formation.

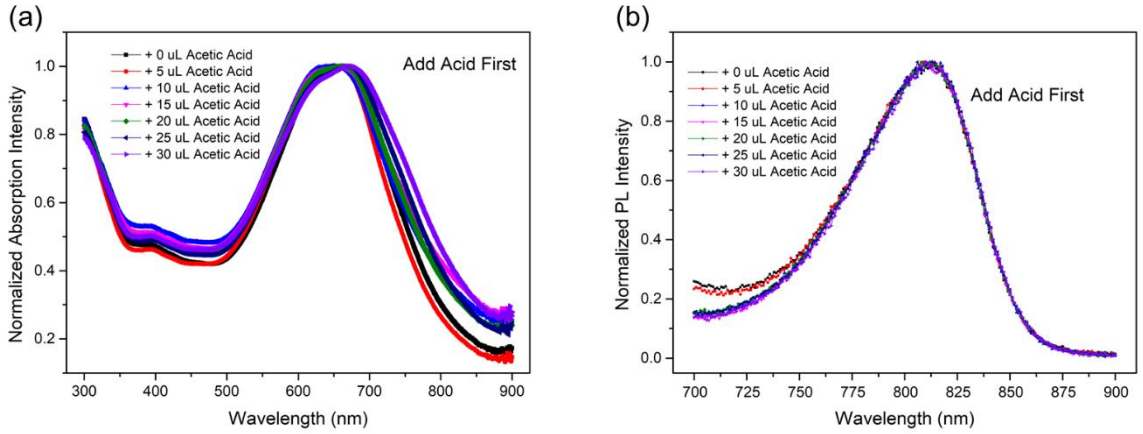

Figure 4.11 Optical spectrum of PTB7@F127 CPNs adding acetic acid before forming CPNs in aqueous suspensions. Steady-state normalized (a) absorption and (b) fluorescence spectra of PTB7@F127 CPNs, with different amounts of acetic acid added prior to CPNs formation.

4.3.4 Fluorescence quantum yield

As previously mentioned, the PLQY of PTB7@F127 CPNs prepared without any addition of acetic acid during the fabrication procedure was measured to be 1.3% on the same mass ratio of 1:100. Here, the PLQY of PTB7@F127 CPNs prepared at different amounts of added acetic acid were compared with each other, and the highest PLQY was normalized to be 1.

The results showed that, for the case where pH is varied after the CPNs fabrication, an increased amount of acid results in a trend characterized by initial increase and a subsequent decrease of the PLQY. The greatest PLQY is obtained by adding 15 μL of acetic acid.

For the alternate approach of acid addition prior to CPNs precipitation, the PLQY varies very little initially (with 4% of each other, which is approximately equal to the changes one obtains for different CPNs preparations – multiples of these measurements were not performed due to the time required to obtain each data point). It is clear, however, that the PLQY then drops very quickly for this case also, suggesting that adding of large amounts of acid is detrimental to the fluorescence emission of the CPNs, whether the pH of the environment was change before or after CPNs formation.

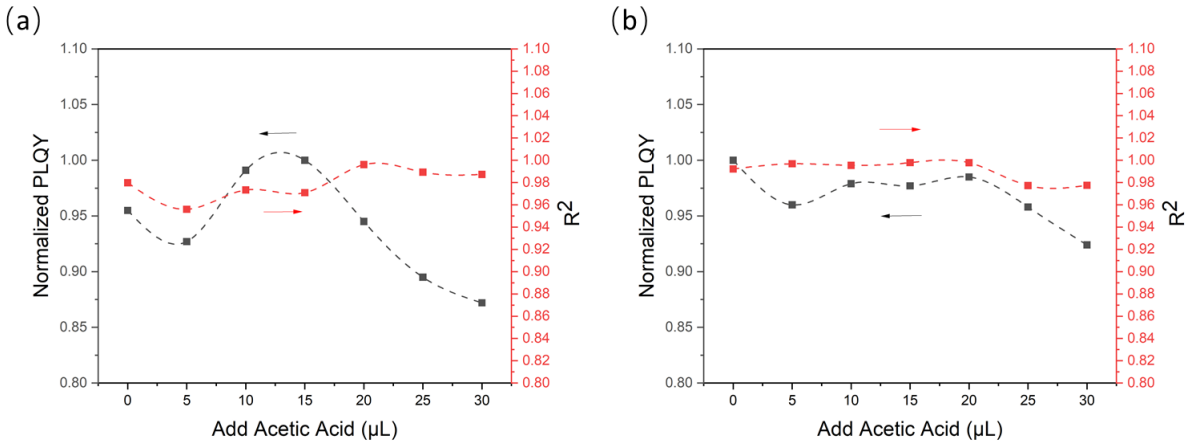

Figure 4.12 Comparation of PLQY of PTB7@F127 CPNs adding different amounts of acetic acid. Normalized PLQY of (a) PTB7@F127 add into water first, then add Acetic acid to adjust pH; (b) PTB7@F127 add Acetic acid to adjust pH first, then add into water.

4.3.5 Singlet oxygen generation

In addition to the experiments described previously, the production of $^1O_2$ by PTB7@F127 CPNs samples with different pH were analyzed under prolonged stimulation conditions, where the $^1O_2$ production by CPNs samples was measured for 1 hour, and the increase in SOSG PL intensity was recorded. Based on the above results of little variation in CPN properties via addition of acetic acid after the fabrication, these $^1O_2$ measurements were limited to the samples prepared according to the second approach (addition of acid pre-reprecipitation).

Figure 4.12 shows the results of these measurements. As can be seen from this graph, the ROS production by the PTB7@F127 CPNs increased continuously and dramatically by adding 5 μL to 10 μL acetic acid, which increased to 3 times compared to the original sample (no acid added). Thereafter, the singlet oxygen generation decreased rapidly at increasing acetic acid amounts, and by adding 20 μL of acid added into the system, the SOG production became

negligible. This measurement shows that adding 10 µL of acetic acid into the system has the optimal singlet oxygen generation capability. Combined with the results of previous experiments, adding 10 µL of acetic acid to a 2.5 mL (100 µg/mL) system during fabrication was determined to be the optimal synthesis procedure, maximizing CPNs PLQY and SOSG production whilst producing CPNs of sizes appropriate to biomedical applications.

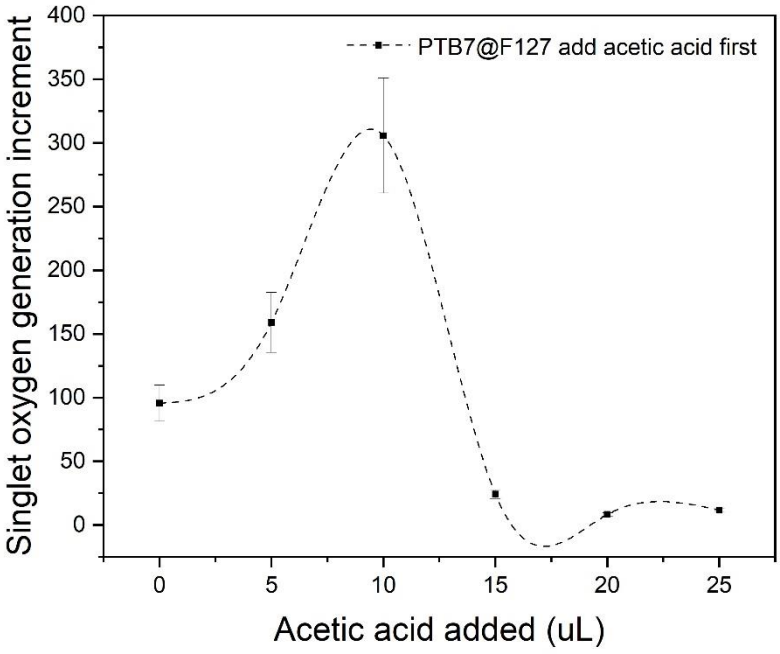

Figure 4.13 Comparison of $^1O_2$ generation by PTB7@F127 CPNs at increasing amount of acetic acid added during CPNs formation. The acid was added prior to CPNs formation. The SOG data shown here are the final intensity obtained for SOSG fluorescence after 1 hour irradiation of sample.

Repeated experiments (shown in Figure 4.14) confirmed that addition of 10 µL of acetic acid (blue line) to 2.5 mL (100 µg/mL) of precursor suspension during fabrication was the optimal synthesis procedure.

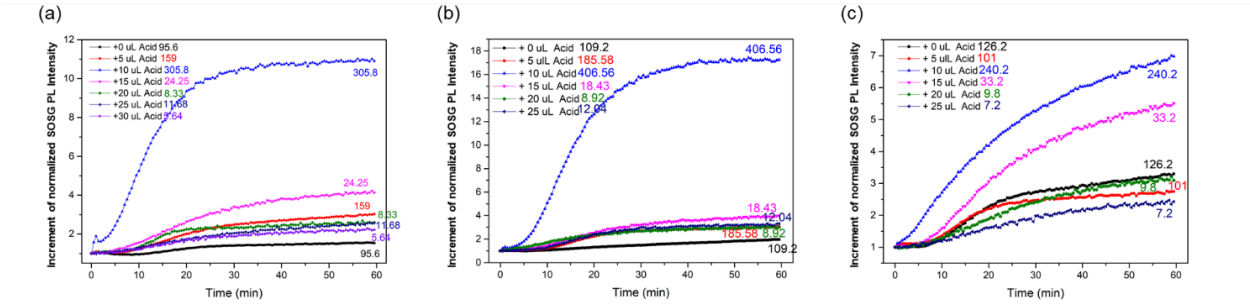

Figure 4.14 Repeated experiments of $^1O_2$ production by PTB7@F127 CPNs adding different amount of acetic acid. For all measurements, samples had absorbances of ~0.5 at the stimulation wavelength (635 nm) prior to the addition of SOSG. This corresponded to CPNs samples' concentrations of ~10 μg/mL.

4.4 PTB7-Th CPNs

In view of the results of this chapter so far, and especially those relating to the effect that the modification of pH conditions has on the properties of the resulting CPNs, it is clear that the steric interactions of the side chains (*e.g.* due to increased charges on them) do indeed affect the packing of the polymer chains and consequently the properties of the CPNs. There is, however, an alternate route to affect the steric interactions between the sidechains of the CPs and therefore the packing of the conjugated domains within the CPNs, and that is to modify the side chains structurally. In the case of PTB7, different versions of the copolymer powder are available commercially, facilitating investigations along this direction. In this section, this route to control the packing of the conjugated domains is tested by replacing the PTB7 conjugated polymer by a variant that includes within its structure two bulkier side chains – the PTB7-Th conjugated polymer (structure shown in Figure 4.15). The molecular weight of PTB7-Th is larger than 145,000 Da (purchased from Sigma-Aldrich). The PTB7-Th CPNs were fabricated using the same protocol as that used for PTB7 CPNs, only replacing the CPs powder. The fabricated PTB7-Th CPNs were then evaluated in terms of their optical properties and $^1O_2$ generation capability.

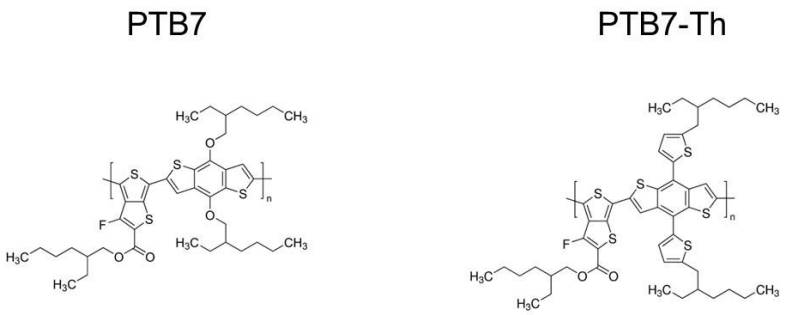

Figure 4.15 Comparison of chemical structures of PTB7 and PTB7-Th conjugated polymers. Figure adapted from website of Sigma-Aldrich.[6,7]

4.4.1 Optical properties of PTB7-Th CPNs

The absorption spectra of PTB7-Th@F127 CPNs showed a characteristic two-peak absorption like that of PTB7@F127 CPNs, but with a red shift of ~30 nm (panel (a) of Figure 4.16). The changes to the photoluminescence spectra were even more pronounced (panel (b) of Figure 4.16), not only displaying a shift of ~10 nm in the position of the main peak, but also changing its overall shape owing to a different ratio of contributions resulting from transitions to different vibronic levels of the ground states (described in Chapter 3). Noting that the emission spectra of PTB7-Th@F127 CPNs and PTB7@F127 CPNs were both obtained from samples of same concentration and absorption at the excitation wavelength used for PL measurements, the larger PL intensity of PTB7-Th CPNs observed in Figure 4.16 suggests an improved brightness for the PTB7-Th CPNs probes. However, this was not conclusive since different excitation wavelengths were used for these measurements. Therefore, further tests were performed to confirm this fact, by doing comparative measurements of the PLQYs of the two samples.

4.4.2 Fluorescence quantum yield of PTB7-Th CPNs

The PLQY of PTB7-Th@F127 CPNs (1:300) was measured using a simplified relative method, with the PTB7@F127 CPNs (1:300) sample acting as a reference. The protocol for the PLQY measurements was same as previously described in this chapter (*e.g.* in section 4.2.5) and the results of the measurements are shown in Figure 4.17. From these measurements, the PLQY of the PTB7-Th@F127 CPNs (1:300) was calculated to be (5.41 ± 0.23)%, which is distinctly larger than the best PLQY obtained for PTB7@F127 CPNs that is (2.0 ± 0.053)%, suggesting that aggregate formation does indeed play a large role in determining the optical properties of PTB7 CPNs.

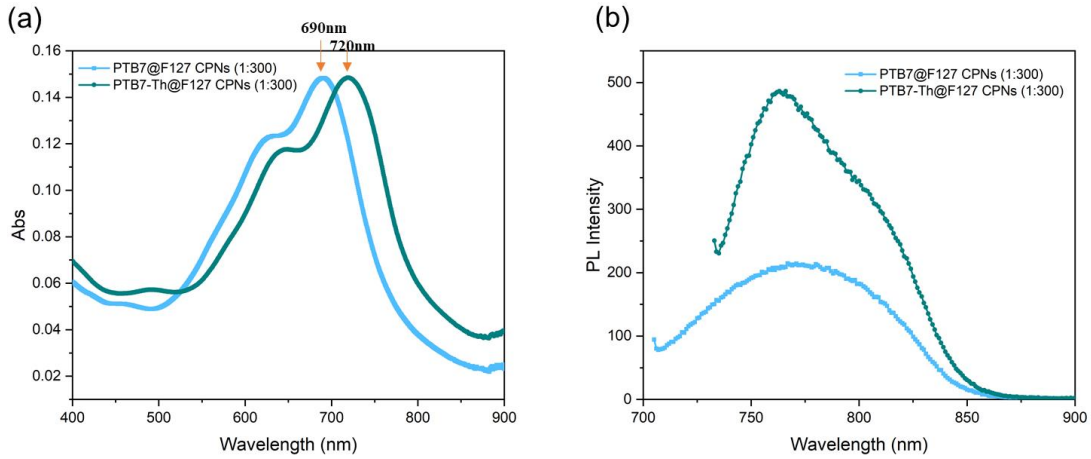

Figure 4.16 Optical properties of PTB7@F127 CPNs (1:300) and PTB7-Th@F127 CPNs (1:300). (a) Steady-state absorption and (b) emission spectra of PTB7@F127 CPNs (1:300) in blue line and PTB7-Th@F127 CPNs (1:300) in green line. The photoluminescence spectra shown in (b) was recorded using excitation wavelength of 690 nm for PTB7@F127 CPNs (1:300) and 720 nm for PTB7-Th@F127 CPNs (1:300), as indicated by the red arrow in panel (a), where both samples absorbed equally. The concentration of both samples was ~3 µg/mL.

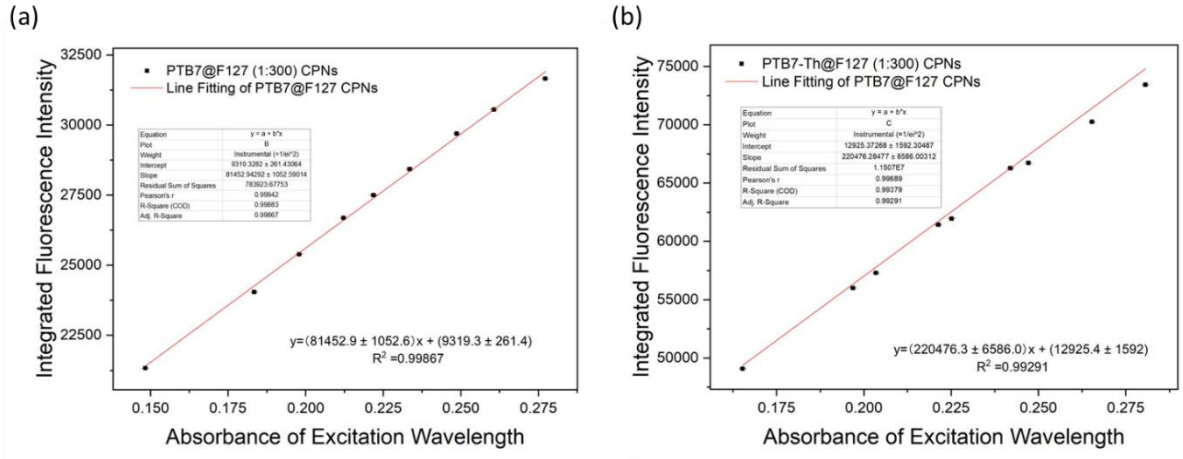

Figure 4.17 Measurements of PLQY of PTB7@F127 CPNs (1:300) and PTB7-Th@F127 CPNs (1:300). (a) and (b) show the dependence of fluorescence intensity versus absorbance at excitation wavelength for (a) the PTB7@F127 CPNs (1:300) sample and (b) PTB7-Th@F127 CPNs (1:300) sample. The excitation wavelength was 680 nm for both samples. Note that errors in measurements (fluorescence intensity and absorbance) were too small to be visible on the scales used in these graphs.

4.4.3 Singlet oxygen generation by PTB7-Th CPNs

The production of $^1O_2$ by PTB7-Th@F127 CPNs was compared to that of PTB7@F127 CPNs, using dispersions having same absorptions at 635 nm. Figure 4.18 demonstrates that the signal

of $^1O_2$ production in PTB7@F127 CPNs increased 11.1-fold after 45 minutes of illumination, which consistent with earlier research. For PTB7-Th@F127 CPNs, the signal increased 13.6-fold and was confirmed by a repeated measurement yielding an increase of 12.8-fold, which are consistent with one another. These results indicate that PTB7-Th@F127 CPNs have a similar capacity for $^1O_2$ generation as do PTB7@F127 CPNs. As such, they equally hold great potential for development as NIR-active theranostic probes.

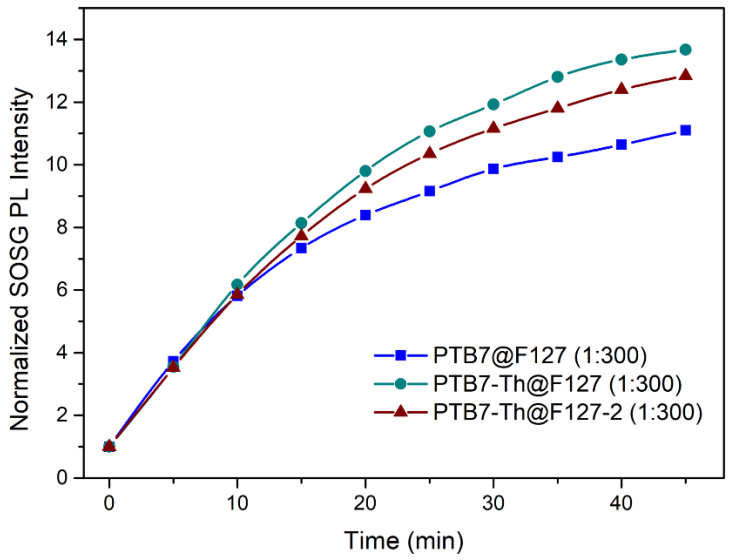

Figure 4.18 Comparison of $^1O_2$ production by PTB7@F127 CPNs (1:300) and PTB7-Th@F127 (1:300) CPNs. For all measurements, samples had absorbances of ~0.5 at the stimulation wavelength (635 nm) prior to the addition of SOSG. This corresponded to CPNs samples' concentrations of ~10 μg/mL.

4.5 Discussion

The observed effect of changes in size at different ratios is not yet fully understood and requires further investigation. One possibility is that the ratio determines the relative strengths of interactions between components, resulting in formation of different types of particles in a manner that is similar to what has been previously observed for SiO_2 core and poly (butyl acrylate) (PBA) shell NPs. In this reported system, when the concentration of PBA was lower than the lower critical value, aggregated micelles with multiple SiO_2 cores are formed. Whilst if the concentration of PBA was higher than the upper critical value, isolated PBA micelles without SiO_2 core appear in the system. Core–shell particles with a single SiO_2 core could only be obtained when the concentration of PBA was in between of these two critical values.[17] In

our case, similarly, PTB7@F127 CPNs with optimal amount of PTB7 core were obtained at the mass ratio of 1:300. For much lower mass ratios and much higher mass ratios, particles with poor optical and photosensitizing performance were obtained.

In view of previous report of the rupture of F127 micelles at high pH values, it is likely that observed effects can be attributed to strong changes in oxygen diffusion to/from PTB7 core and ionization of the PTB7 polymer that can come in contact with acetic acid once F127 micelle has ruptured[14]. In essence, the pH affects the way in which F127 encapsulates and/or protects PTB7 conjugated polymer from outside influences. This provides a promising new direction for examining the impact of copolymers on the photodynamic properties of conjugated polymers.

Another reason that makes it worthwhile to investigate the influence of pH on $^1O_2$ generation capability is that some of the tumors present a slightly acidic microenvironment, changing the way NPs interact with the tumors tissues. Exploiting this fact, Wang and co-workers found that by decreasing the pH slightly from 7.4 to 6.8, the negatively charged surface of their CPNs converted to a positively charged naked surface, which obviously enhanced cell internalization and consequently increased in vitro PDT efficacy.[18] Thus, CPNs that can produce $^1O_2$ efficiently in slightly acidic environments, such as those found in some tumorous tissues, can have notable advantages for *in vivo* applications.

The chemical structure of PTB7 and PTB7-Th polymers are extremely similar, but the electron acceptor unit-benzodithiophene, differs because 2-ethylhexyl-thiophenyl is added to the PTB7 benzodithiophene unit to create the PTB7-Th molecule. Similar superior photoelectric properties of PTB7-Th was observed in Jain and co-workers' research that compared the photovoltaic performance of PTB7:PC71BM and PTB7-Th:PC71BM thin films, and found that the 2-ethylhexyl-thiophenyl unit added to PTB7 resulted in reduced interfacial disorder between the donor and acceptor units and better bulk molecular packing, resulting in much improved photovoltaic performance of PTB7-Th:PC71BM thin films.[19]

4.6 Conclusions

This study was aimed to optimize the fabrication of PTB7@F127 CPNs by investigating the effects of varying mass ratios of core material PTB7 to shell material F127, as well as the effects of pH during the CPNs' synthesis. This investigation offers hints for improving the overall performance of CPNs during fabrication. It also shows how the packaging of the shell polymer changes the size and optical properties of the DLS.

Specifically, the effect of optimization was investigated in terms of DLS size, spectral properties, and $^1O_2$ production. By comparing PTB7 and F127 at mass ratios from 1:10 to 1:1000, 1:300 mass ratio was found to be optimal. At this mass ratio, the size of the DLS was approximately 180-190 nm, which is suitable for biological applications. The $^1O_2$ production was improved by a factor of 1.2 compared to the previously used 1:100 PTB7:F127 mass ratio, and the PLQY improved from 1.3% to 2.0%.

By studying the effect of varying pH on the properties of CPNs it was determined that, once water-dispersible CPNs have been formed, the pH had little influence on their size and even smaller impact on their other properties. This observation is consistent with Chapter 1's conclusion that CPs solubilized by F127 can exhibit excellent stability over a broad pH range,[20] which is typical of a nonionic surfactant.[14]

Contrary, variations in pH were found to have a noteworthy impact on the structure and properties of water-dispersible CPNs, if the change was implemented prior to CPNs formation. In this investigation of optimizing the fabrication procedure by adjusting the pH, acetic acid was chosen to be added into the system before the transfer the CPs into the aqueous phase. By comparing the addition of 0-30 μL of acetic acid to a 2.5 mL (100 μg/mL) system, we found that the best results were achieved by adding 10 μL. In this study, both the DLS size and the relative intensities of the higher-energy peaks to lower-energy absorption peaks showed similar oscillatory trends. Of note, however, is that the production of singlet oxygen was strongly affected by additions of acetic acid during the fabrication procedure. With the addition of 10 μL of acid, the production of singlet oxygen was improved three-fold, when compared to production of singlet oxygen by sample prepared in the absence of any acetic acid. At increasing concentration of acetic acid, however, the $^1O_2$ generation decreased quickly, decreasing to zero at the total volume of 20 μL of acetic acid added; at this point, the ability of the CPNs to produce $^1O_2$ was almost completely lost.

The PTB7-Th study demonstrates that this PTB7 variant exhibited superior optical qualities and a comparable ability to generate $^1O_2$, providing a foundation for the future development of new theranostic CPNs.

4.7 References

1. Salatin, S. *et al.* Development of a nanoprecipitation method for the entrapment of a very water soluble drug into Eudragit RL nanoparticles. *Res. Pharm. Sci.* **12**, 1–14 (2017).

2. Grey, J. K. *et al.* Size-dependent spectroscopic properties of conjugated polymer nanoparticles. *J. Phys. Chem. B* **110**, 25568–25572 (2006).

3. Abelha, T. F. *et al.* Conjugated polymers as nanoparticle probes for fluorescence and photoacoustic imaging. *J. Mater. Chem. B* **8**, 592–606 (2020).

4. Augustine, R. *et al.* Cellular uptake and retention of nanoparticles: Insights on particle properties and interaction with cellular components. *Mater. Today Commun.* **25**, 101692 (2020).

5. Shi, Y. *et al.* The EPR effect and beyond: Strategies to improve tumor targeting and cancer nanomedicine treatment efficacy. *Theranostics* vol. 10 7921–7924 (2020).

6. Jain, R. K. & Stylianopoulos, T. Delivering nanomedicine to solid tumors. *Nat. Rev. Clin. Oncol.* **7**, 653–664 (2010).

7. Wu, J. The enhanced permeability and retention (EPR) effect: The significance of the concept and methods to enhance its application. *J. Pers. Med.* **11**, (2021).

8. Martinelli, C. *et al.* Nanostructured carriers as innovative tools for cancer diagnosis and therapy. *APL Bioeng.* **3**, 11502 (2019).

9. Hoshyar, N. *et al.* The effect of nanoparticle size on in vivo pharmacokinetics and cellular interaction. *Nanomedicine* **11**, 673–692 (2016).

10. Guo, X. *et al.* Appropriate size of magnetic nanoparticles for various bioapplications in cancer diagnostics and therapy. *ACS Appl. Mater. Interfaces* **8**, 3092–3106 (2016).

11. Braeken, Y. *et al.* Conjugated polymer nanoparticles for bioimaging. *Materials (Basel).* **10**, 1–23 (2017).

12. Nita, L. E. *et al.* Effect of pH and temperature upon self-assembling process between poly(aspartic acid) and Pluronic F127. *Colloids Surfaces B Biointerfaces* **119**, 47–54 (2014).

13. Spano, F. C. & Silva, C. H- and J-aggregate behavior in polymeric semiconductors. *Annu. Rev. Phys. Chem.* **65**, 477–500 (2014).

14. Basak, R. & Bandyopadhyay, R. Encapsulation of hydrophobic drugs in pluronic F127 micelles: Effects of drug hydrophobicity, solution temperature, and pH. *Langmuir* **29**, 4350–4356 (2013).

15. PTB7. https://www.sigmaaldrich.com/GB/en/product/aldrich.

16. PTB7-Th. https://www.sigmaaldrich.com/GB/en/product/aldrich.

17. Ren, X.-M. et al. Accurately controlling the shell thickness in the core–shell microspheres with single silica core and poly (butyl acrylate) rubber shell via emulsion polymerization. *Colloid Polym. Sci.* 296, 575–584 (2018).

18. Wang, C. *et al.* Imaging-guided pH-sensitive photodynamic therapy using charge reversible upconversion nanoparticles under near-infrared light. *Adv. Funct. Mater.* **23**, 3077–3086 (2013).

19. Jain, N. *et al.* Interfacial disorder in efficient polymer solar cells: the impact of donor molecular structure and solvent additives. *J. Mater. Chem. A* **5**, 24749–24757 (2017).

20. Wang, S. et al. Encapsulation of MEH-PPV:PCBM hybrids in the cores of block copolymer micellar assemblies: Photoinduced electron transfer in a nanoscale donor-acceptor system. *Langmuir* **32**, 329–337 (2016).

Chapter 5 – Functionalization of PTB7@F127 CPNs with FA

Fluorescence techniques have become an important platform for cellular imaging, enabling the understanding of the function and mechanism of target biological species, which in turn provide crucial information for early cancer diagnosis and treatment.[1] Therefore, the development of theranostic probes possessing good biocompatibility, bright fluorescence and ability for bioconjugation is particularly important. CPNs have emerged as a promising new class of fluorescent bioimaging probes with high fluorescence, excellent photostability, and low cytotoxicity.[2] To date, CPNs have been extensively utilized for non-specific and targeted cellular imaging, as discussed in Chapter 1.[3,4] The work described in Chapter 3 has shown that the non-specific binding of PTB7@F127 CPNs to cells is weak, so in order to realise the application of PTB7@F127 CPNs in biological systems, this chapter explores the tumour-targeted functionalisation of PTB7@F127 CPNs and its performance after functionalisation.

5.1 Introduction

5.1.1 CPNs as theranostic probes

In addition to the diagnostic role, originating from the imaging signal, the CPNs are also involved in minimally invasive therapeutic techniques such as PDT[5] and PTT[6] to achieve theranostic application. For the PTT technique, the CPNs absorb light and convert it into thermal energy to destroy cancer cells and CPNs with strong NIR absorption and high heat conversion efficiency have the potential to become the next generation of PTT agents.[7] Because PDT and PTT hold great promise for non-invasive cancer treatment, and CPNs-based image-guided therapy is an emerging and highly active area of research.[8]

5.1.2 Pluronics as a functional copolymer

The extensive usage of amphiphilic block copolymers in nanomedicine arises not only from their valuable basic features in resolving drug transport issues, but also from their potential inherent biological activity. The family of ABA (A = hydrophilic block poly(ethylene oxide) (PEO) and B = hydrophobic block poly(propylene oxide) (PPO))triblock copolymers currently commercially available as Pluronic® has a pool of over 50 amphiphilic varieties.[9] By altering the molar mass ratio between the PEO and PPO blocks (from 1:9 to 8:2), the physical and chemical characteristics of Pluronic® copolymers may be carefully controlled, which directly alters the *in vivo* characteristics and interactions with cells and cell membranes, and offers great promise for the construction of novel nanomedicines and biomaterials.[10] The ability of Pluronic® block copolymers to provide steric stabilisation of isotropic liquid crystalline

particles may be of potential interest for the development of new drug delivery systems.[11] Specifically, maintaining the stability and integrity of these NPs over time is necessary for their storage and use, and the PEO-PPO-PEO triblock copolymer provides a steric barrier against the aggregation of non-lamellar lyotropic liquid crystalline particles.[12] Among these, F127 has been shown to be the most well-known liquid crystal stabiliser.[13] Polymeric micelles with a core-shell structure, which are usually generated by the self-assembly of amphiphilic polymers, are attracting a growing amount of interest.[14] The core-shell configuration is essential for enhancing drug stability and drug solubility, as well as providing an extended circulation time in the body and accumulation in tumorous tissues through the EPR effect.[15]

The majority of clinically proven therapeutic and imaging NPs target cancer cells passively,[16] either through the EPR effect or *via* non-specific binding; CPNs are no exception to this rule. However, since active targeting can reduce side effects and improve efficacy of the probe,[17] great improvements can be made by functionalising CPNs with targeting agents. The structural diversity of Pluronic® copolymers and their comparatively simple chemical structure of these ABA copolymers make them well suited for chemical modification and functionalization of NPs, specifically for tumour-targeted modifications. For instance, Zhang and co-workers have developed a load delivery system based on functional F127 for solasodine which has excellent bioactive inhibition against fungi, viruses, and tumours.[18] Solasodine, which has been identified as having anti-oxidant, anti-tumor, and anti-infection properties, can be isolated from the Solanum sisymbriifolium fruits.[19] However, solasodine has poor water solubility, and it plays a similar role to PTB7 when forming solasodine-loaded micelles with functional F127. By chemically conjugating FA and fluorescein isothiocyanate (FITC) with F127, the technique was able to simultaneously target and image cancer cells (Figure 5.1). This study also indirectly demonstrates the feasibility of using functional PTB7@F127 CPNs for targeted bioapplications.

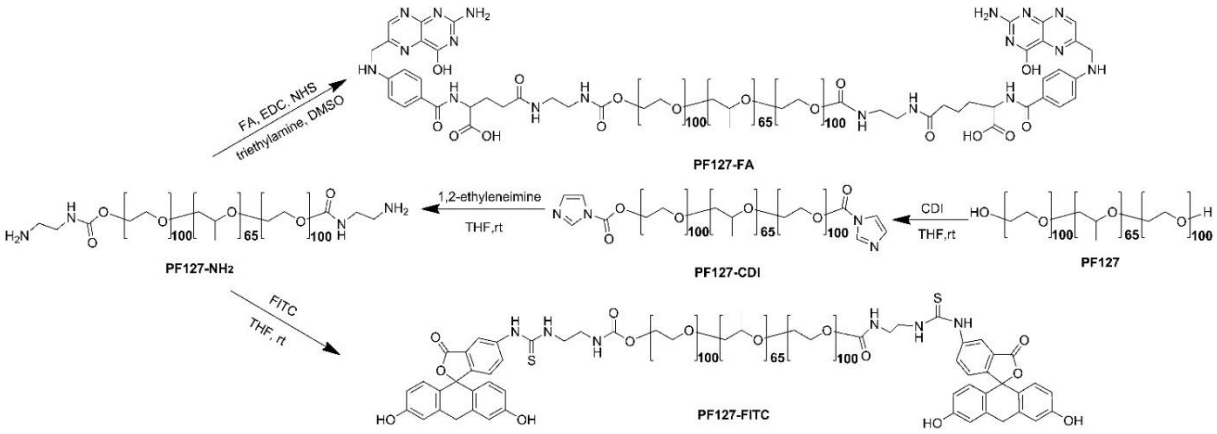

Figure 5.1 Schematic illustration of the synthesis of PF127-CDI, PF127-NH2, PF127-FA and PF127-FITC.[18] (With permission from Taylor & Francis)

5.1.3 Folic acid as a functional ligand

FA, an important vitamin created in the 1940s for the treatment of anaemia, is converted to functional, naturally occurring metabolites by dihydrofolate reductase and may thus be used as a dietary supplement for folates.[20] It has low molecular weight (441.1g/mol) and binds selectively to folate receptor (FR) which is overexpressed in many human tumours. Targeting of the folate receptor has been shown to be an effective method to mediate drug uptake efficiency,[21] FR is overexpressed in a range of human malignancies, including breast, ovarian, renal, and lung cancers. In fact, it is regarded to be a tumour-specific target platform because of its compatibility with intravenous drug administration.[22] The tumor targeting ligand FA was used to improve the targeting efficiency of therapy in mice by injecting it into the tail vein.[23] This approach allowed for increased localization of the therapeutic agent to the tumor site, resulting in enhanced efficacy of the therapy. Such targeted approaches overcome the disadvantages of conventional cancer treatments such as surgery, chemotherapy, and radiotherapy due to their non-targeted distribution throughout the body. The active targeting techniques can increase the intracellular concentration of therapeutic medicines in cancer cells while protecting normal cells from harmful effects.[17] Consequently, the cancer selectivity of FA and FA conjugates might be seen as a viable strategy for NPs-based tailored delivery of anticancer medicinal drugs during cancer diagnostics and therapy (Figure 5.2).[24]

FA has been exploited extensively in the function of lipid-, metal-, and nonmetal-based NPs for active cancer diagnostics and therapy, as discussed in detail in a recently-published review.[25] Li and co-workers conjugated FA to an amphiphilic alternating copolymer in order to establish a new active tumour-targeting drug delivery platform.[26] They have shown that the

functionalised polymeric template is pH-responsive, generating amphiphilic nanostructures at pH 7, allowing for the encapsulation of hydrophobic medicines. Moreover, the structure is stable only at neutral pH and collapses in acidic tumour microenvironments, releasing medicines from its core. As previously discussed, FA-modified F127 has also been studied as a drug delivery platform targeting tumours.[18]

5.2 Modification protocol of F127-FA

The following fabrication protocol was used for modifying F127 to F127-FA:

1. 437.9 mg (1.0 mmol) of FA was dissolved in 15 mL of dried DMSO and added to a one-necked flask.
2. 176.6 mg (1.1 mmol) of CDI was added into the above flask, and the reaction mixture was stirred for one day at room temperature, in the dark.
3. 3.1 g (0.25 mmol) of F127, which had been previously freeze-dried overnight in a vacuum, was added to the above solution (-50˚C, 0.137 mbar, LTE Scientific Ltd. freeze-dryer equipped with Edwards pump).
4. The reaction was allowed to proceed in the dark for 1 day, at room temperature.
5. The reaction mixture was then transferred into a dialysis tube (Spectra, Millipore, MWCO 1000) and dialyzed for 3 days against DI water, which was changed every 3–6 hours. The resulting F127-FA product was freeze-dried and stored in a dry box until use (24 hours, -50˚C, 0.137 mbar, LTE Scientific Ltd. Freeze-dryer equipped with Edwards pump).

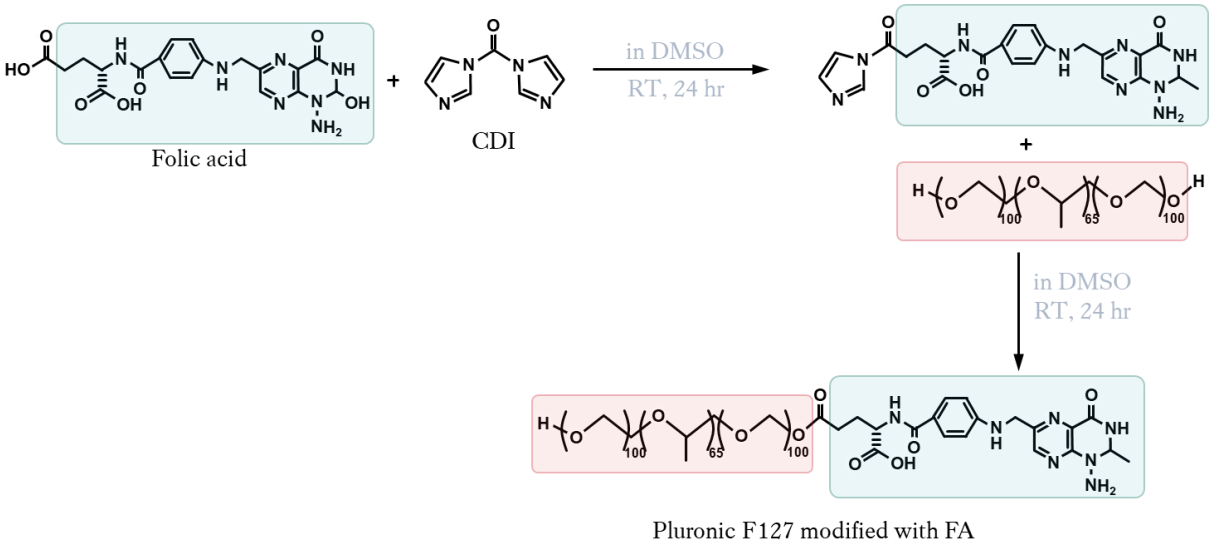

Figure 5.2 Schematic illustration of the synthesis of FA-functionalized F127.

5.2.1 Characterization after folic acid modification

The protocol for the functionalization of F127 with FA stated in the previous section was based on a protocol published by Lin *et al.*[27] Following this protocol, a sample of F127-FA was produced, and then analysed *via* absorption spectrophotometry. As can be seen from Figure 5.3, prepared sample exhibited a very similar absorption spectrum to that provided in the reference, in that both spectra had absorption peaks located at 215 nm, 285 nm, and 360 nm (here, the comparison is made between the spectrum in the inset of panel (a), which is reference result, and that shown in panel (b) which is my experiment result). These experimental results confirmed that FA was successfully added onto F127.

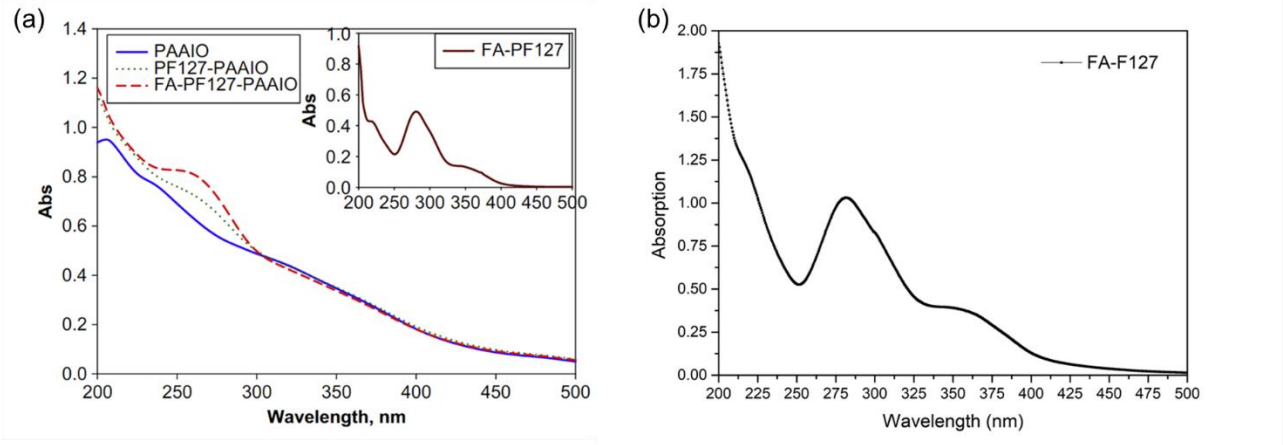

Figure 5.3 Comparison of absorption spectra of F127-FA products produced in this work to that reported by Lin *et al.*[27] Panel (a) shows steady-state absorption of products produced by Lin *et al.*[27] The inset show shows the absorption spectrum of F127 after modification with FA, in aqueous solutions. (b) Steady-state absorption of F127-FA produced in this work.

In order to confirm that the observed spectrum indeed corresponded to F127 modified with FA and not from FA or F127 themselves, further investigations were performed. Specifically, absorption spectra of FA, F127 and F127 after modification with FA were measured in aqueous solutions. The results revealed that F127 did not have any obvious absorption peaks in the 275 nm to 500 nm spectral range, and the spectrum of FA was clearly distinct from that of F127 modified with FA: both the relative intensities and the positions of the two absorption peaks were different. With regards to the latter, the lower energy peak is located at 293 nm and the higher-energy peak is located at 360 nm for FA. But for F127 modified with FA, the corresponding peaks were blue-shifted, and appeared at 283 nm and 354 nm, respectively (Figure 5.4)

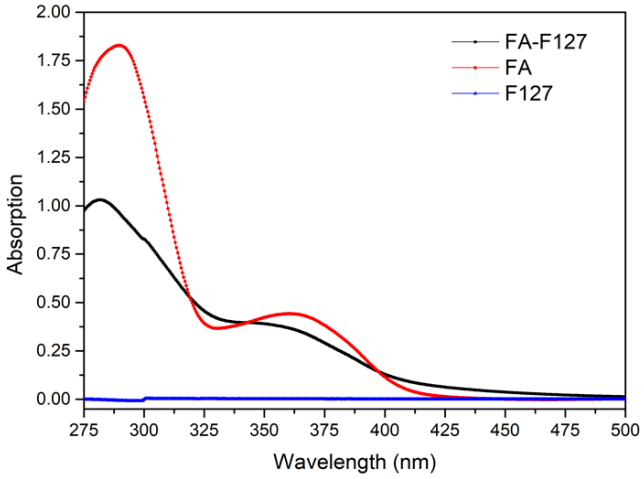

Figure 5.4 Steady-state absorption of FA (data shown in red), F127 (blue) and F127 after modification with FA (black), in aqueous solutions.

5.2.2 Fabrication of folic acid-functionalized PTB7@F127 CPNs

The above results confirm successful modification of F127 with FA. Therefore, attempts were then made to fabrication PTB7@F127-FA CPNs *via* nanoprecipitation method. However, when freeze-dried F127-FA powder (Figure 5.5(a)) was used in place of F127 during the protocol, the fabrication failed: upon injection of PTB7/F127-FA mixture (in THF) into DI water, the entire reaction system became cloudy and eventually precipitated (Figure 5.5(b)). My hypothesis is that the F127 successfully acts as a surfactant resulting in increased water dispersibility of PTB7 due to the hydrophilicity of the hydroxyl groups found on its ends. However, the modification of F127 with FA at the above-mentioned hydroxyl groups, decreases the amphiphilicity of F127. An alternate approach of modifying already-formed PTB7@F127 CPNs with FA was therefore attempted instead, even though there are no previous reports of successful outcomes for such a procedure.

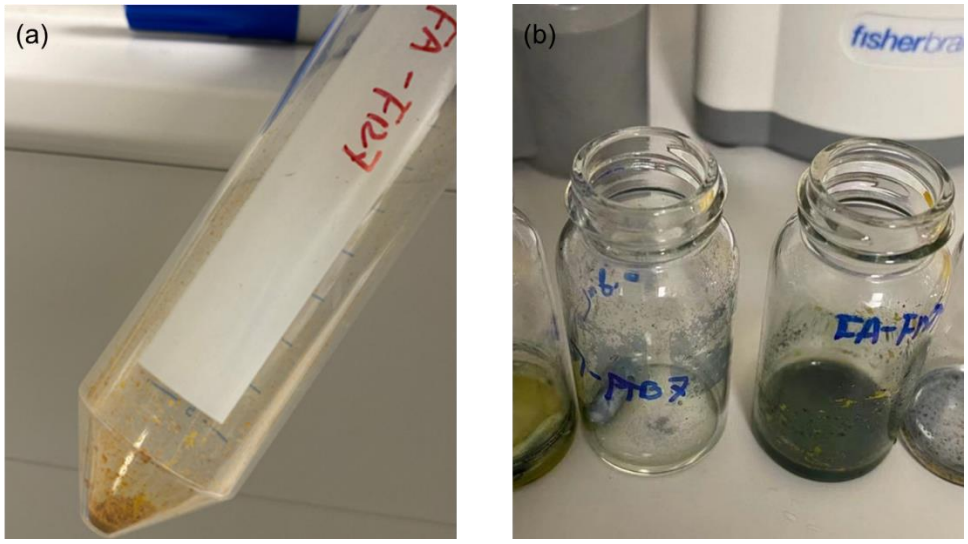

Figure 5.5 Fabrication of PTB7@F127-FA CPNs. (a) Freeze-dried F127-FA powder used in the nanoprecipitation method to form CPNs. **(b)** Result of the nanoprecipitation reaction when using F127-FA powder instead of F127 during the nanoprecipitation of CPNs. Nanoprecipitation reactions are very prone to failure; these failed results are provided here to act as a reference for other synthesizers**.**

In order to proceed with the alternate approach, the fabrication protocol for modification of PTB7@F127 with FA needed adjustment.

The developed protocol for fabrication of PTB7@F127-FA involved the following steps:

1. 437.9 mg (1.0 mmol) of FA was dissolved in 15 mL of dried DMSO and added to a one-necked flask.
2. 176.6 mg (1.1 mmol) of CDI was added into the above flask, and the reaction mixture was stirred for one day at room temperature, in the dark.
3. 3.1 g (containing 0.25 mmol F127) of PTB7@F127 CPNs which had been previously freeze-dried overnight in a vacuum, was added to the above solution.
4. The reaction was allowed to proceed in the dark for 1 day, at room temperature.
5. The reaction mixture was then transferred into a dialysis tube (Spectra, Millipore, MWCO 1000) and dialyzed for 3 days against DI water, which was changed every 3–6 hours.
6. The resulting PTB7@F127-FA product was freeze-dried and stored in a dry box until use.

The amount of PTB7@F127 CPNs used was such that the number of F127 moles contained in the CPNs was same as in the original reaction, accounting for the fact that the weight of F127 is 100 times that of PTB7 in PTB7@F127 CPNs (this work was performed on the non-optimized 1:100 PTB7:F127 ratio CPN samples). The rest of the protocol remained unchanged.

One should note, however, that the optimum ratio of FA to F127 in this synthesis is expected to be lower than the one used here. This is due to unavailability of some of the hydroxyl groups of F127 to the FA modification, once F127 has formed a micelle around the PTB7 core in the PTB7@F127 CPNs. Performing the reaction at higher than necessary FA-to-F127 ratio is likely to cause an excess of FA in solution post-fabrication, which can impact the pH of the system. To avoid any detrimental effects from excess FA, the fabricated samples were purified by ultracentrifugation post-fabrication.

Fabrication of PTB7@F127-FA CPNs using the above stated conditions resulted in a clear and homogeneous blue green suspension (Figure 5.6), indicative of a successful formation of CPNs that were colloidally stable.

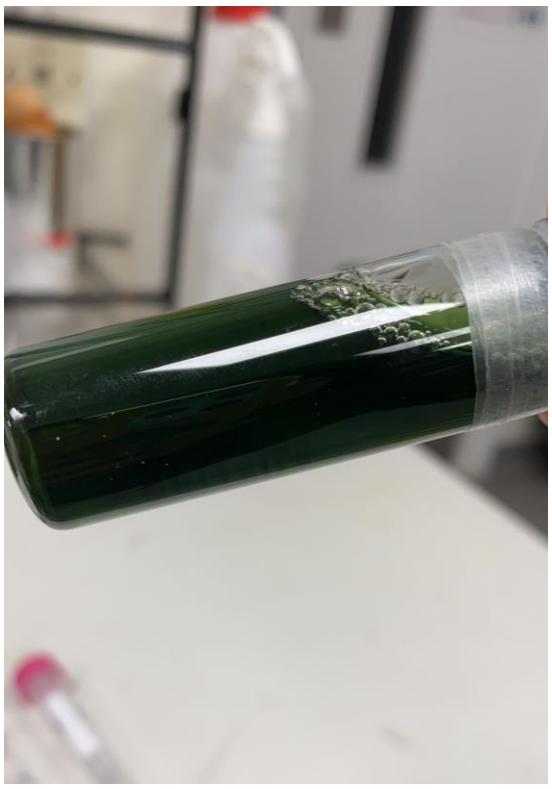

Figure 5.6 Homogeneous and clarified PTB7@F127-FA CPNs suspension synthesized by the modified method. The optimized synthesis method can produce a clear suspension, providing a reference for obtaining highly water-dispersible CPNs by modifying similar functional group onto CPNs.

5.2.3 Steady-state absorption of PTB7@F127-FA CPNs

To confirm that the sample obtained is PTB7@F127-FA CPNs, the steady state absorptions of FA, PTB7@F127 CPNs, and PTB7@F127-FA CPNs before and after centrifugation were

investigated. From the results (Figure 5.7) show that absorptions of PTB7@F127-FA CPNs samples before and after centrifugation remained features originating from the PTB7 absorption (peaks at 640 nm and 680 nm), but now also contained features characteristic of FA absorption (peaks at 280 nm and 350 nm). This confirmed successful modification of PTB7@F127 CPNs with FA, to yield PTB7@F127-FA CPNs.

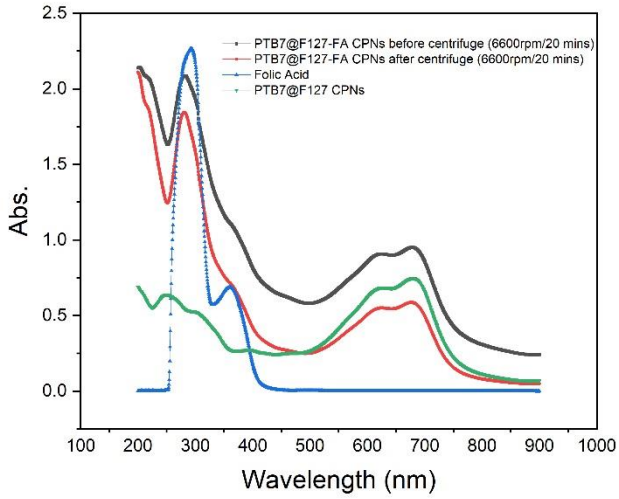

Figure 5.7 Confirmation of FA modification of PTB7@F127 CPNs. Steady-state absorption of FA (blue data points/line), PTB7@F127 CPNs sample (green) and PTB7@F127-FA CPNs before (black) and after (red) centrifugation. All measurements were performed on aqueous suspensions of specified samples.

5.2.4 Size of PTB7@F127 CPNs after modified with folic acid

The hydrodynamic diameters of the PTB7@F127-FA CPNs compared to PTB7@F127 CPNs in aqueous suspensions were investigated for different sample concentrations, ranging from 0.495 μg/mL to 9.5 μg/mL (see Figure 5.8). The results indicate that the sizes of both CPNs samples remained relatively stable across the range of tested concentrations, especially in view of only one major size population being observed in each of the measurements and contributions from background (*e.g.* scattering from solvent molecules) at low concentrations affecting the results of the measurements. Importantly, there is a clear and consistent difference in the sizes of PTB7@F127 CPNs and PTB7@F127-FA CPNs, which remains steady at approximately 30 nm across the tested range of concentrations. The increasement therefore, must be a result of attachment of FA to the outer surface of PTB7@F127 CPNs. Finally, I would like to note that the size of the PTB7@F127-FA CPNs produced here still sits within

the range defined as optimum for accumulation of NPs in tumorous tissues (*in vivo*) by the aforementioned EPR effect.[28, 29]

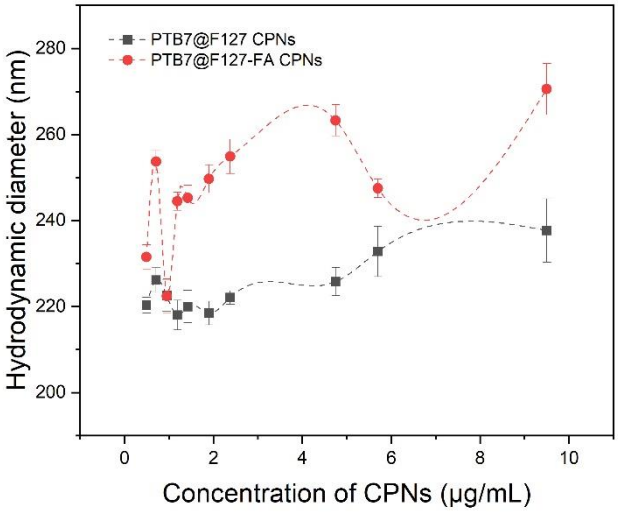

Figure 5.8 Hydrodynamic sizes of PTB7@F127 CPNs before (blue data) and after (orange data) modification with FA. All measurements were performed on aqueous dispersions of CPNs.

5.3 Singlet oxygen generation after folic acid modification

The motivation for modifying PTB7@F127 CPNs with FA was to increase the tumour cell targeting affinity of CPNs, when used as theranostic probes. In previous sections, such modification has been proposed, tested and successfully verified, and the size of the resulting CPNs was characterized. However, and as discussed extensively in Chapter 1, modifications of CPNs' copolymer shell can impact other CPNs properties, such as their optical properties, photosensitizing ability and cell affinity. The next few sections therefore focus on evaluating the impact that FA-modification of PTB7@F127 CPNs had on their function as theranostic probes, starting with photosensitization evaluation presented in this section.

As shown in Figure 5.9, both PTB7@F127 and PTB7@F127-Fa CPNs produced $^1O_2$ steadily over the 60 minutes measurement period, however the total $^1O_2$ production yield for FA-modified CPNs at the end of the 60 minutes was half that of the PTB7@F127 CPNs. Therefore, whilst modification of PTB7@F127 CPNs with FA can indeed improve the tumour cell affinity of the CPNs, it does so at the expense of its photosensitizing capability. It is important to note, however, that the overall performance of the probe is determined by the interplay of both of these facts. Given a substantial increase in the cellular affinity of PTB7@F127 CPNs following the modification of FA, the sacrifice of $^1O_2$ generation capacity can in fact be acceptable. In

addition, through subsequent optimisation of the synthesis, similar to the one performed for PTB7@F127 CPNs in Chapter 4, it is hoped that the ability of FA-modified CPNs to produce $^1O_2$ can be enhanced whilst also ensuring tumour targeting capability. Of particular importance here is the notable effect pH of the environment had on the ability of CPNs to produce $^1O_2$, as described in Chapter 4. This suggest that adjusting the pH of the FA-modified system by decreasing the proportion of FA could in principle improve the CPNs' ability to produce $^1O_2$.

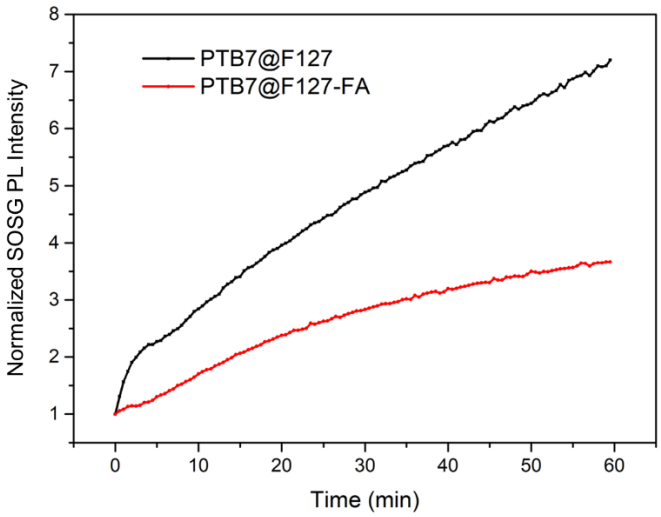

Figure 5.9 Comparation of $^1O_2$ production by PTB7@F127 and PTB7@F127-FA CPNs. For all measurements, samples had absorbances of ~0.5 at the stimulation wavelength (635 nm) prior to the addition of SOSG. This corresponded to CPNs samples' concentrations of 8 μg/mL.

The $^1O_2$ production capability of PTB7@F127-FA CPNs at different concentrations was further evaluated and compared to that of PTB7@F127 CPNs, for irradiations lasting 60 minutes. As can be seen from Figure 5.10, and as expected, the $^1O_2$ production by either of the samples was determined to be dose-dependent: more $^1O_2$ was generated by samples of higher concentrations. However, the trend observed was non-linear for both CPNs samples (see panel (b) of Figure 5.10), which could be reflective of the binding events required for the SOSG probe to be converted to its fluorescent form (to note here are the dashed lines in the panel, which are fits to the data using one of the typical biochemical models describing binding events, Hill equation). Alternatively, this could be an indication of saturation behaviour, be that optical (*e.g.* optical filtering effects) or chemical (*e.g.* less molecular oxygen being available per total nanoparticle surface). Further analysis and experimental investigations are required to determine the exact nature of the observed effect, but the dose-dependency of the $^1O_2$

production is indisputable. Therefore, the higher probe accumulation enabled by the FA functionalization should, in fact, result in sufficient photosensitizing performance of the PTB7@F127-FA CPNs despite a reduction in their $^1O_2$ production yield. Conversely, at low concentrations, such as those that may be attained from any non-specific attachment of the probe to healthy cells, the FA-modified CPNs produced much smaller amounts of $^1O_2$. Therefore, one would expect a substantial reduction in any damage to healthy cells for the modified probes, when compared to the non-modified versions.

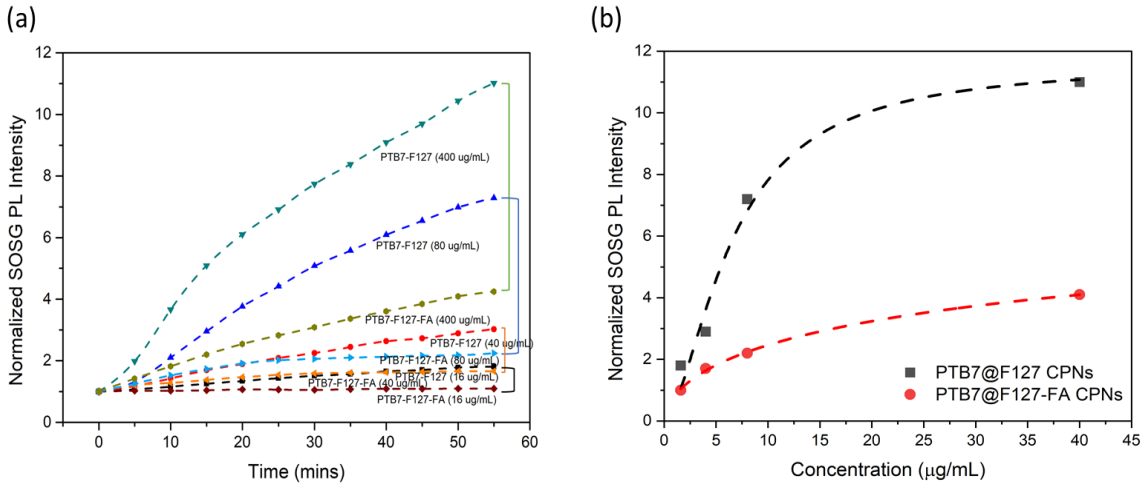

Figure 5.10 Comparison of $^1O_2$ production by PTB7@F127 and PTB7@F127-FA CPNs samples of different concentrations. (a) Time-dependent evolution of $^1O_2$ by samples, as measured by intensity of SOSG fluorescence. The labels in the graph indicate the stock concentrations of the samples used for the measurements. Each sample was diluted by a factor of 10 prior to measurements, yielding working sample concentrations of 40 μg/mL,8 μg/mL,4 μg/mL and 1.6 μg/mL. For all measurements, samples had the same absorbances at the stimulation wavelength (635 nm) for each concentration group, prior to the addition of SOSG. (b) Maximum SOSG signal at the end point of the experiment.

5.3.1 Fluorescence quantum yield of PTB7@F127-FA in aqueous suspension

The PLQY of PTB7@F127-FA CPNs was measured using a simplified relative method, with the PTB7@F127 CPNs sample acting as a reference. For these measurements, all samples were first diluted to have absorptions of less than 0.15 at the peak, and the excitation wavelength was chosen such that the absorptions were the same for a single pair of samples.

The samples were then analysed in pairwise fashion, using the same set of settings to record the fluorescence spectra of samples in each pair. Specifically, all samples were excited at 680 nm, and the fluorescence spectra were recorded in the 700–900 nm spectral range. The

integrated fluorescence intensities of these samples were then calculated using the procedure described previously, plotted against sample absorbances, and fitted to a linear function (Figure 5.11). The slopes of the fits were then used to calculate the PLQY of the PTB7@F127-FA CPNs samples, as before, yielding a value of (0.95 ± 0.06)% for PTB7@F127-FA CPNs. Therefore, the fluorescence QY of the CPNs slightly decreased upon FA-modification of their surface (~30% reduction). As in the case of $^1O_2$ production, however, this decrease is expected to be partially offset by the improved cell affinity of the probes enabled by FA targeting.

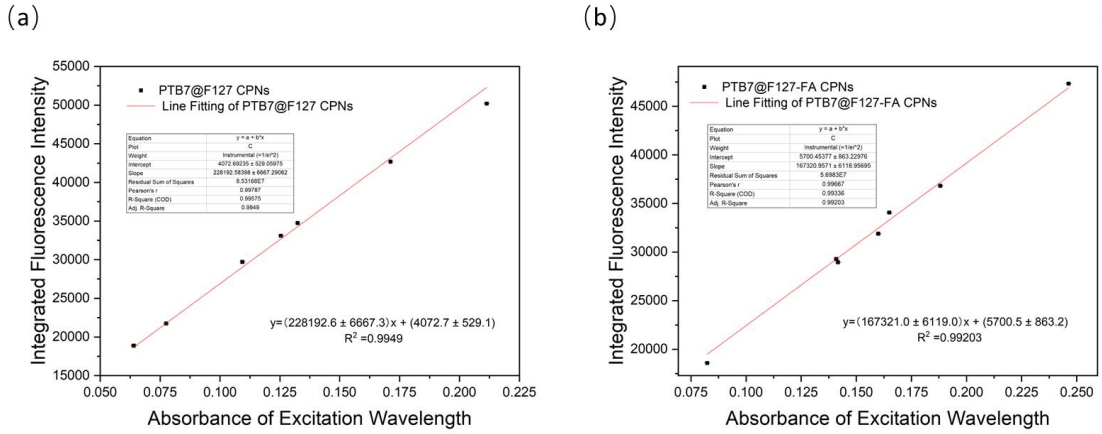

Figure 5.11 PLQY measurements of PTB7@F127-FA CPNs. Panels (a) and (b) show the dependence of fluorescence intensity versus absorbance at excitation wavelength for the PTB7@F127 CPNs sample and PTB7@F127-FA CPNs sample separately. The excitation wavelength used was 680 nm for both samples. In both cases, data were fitted to a linear function: resulting functions and R^2 values are stated above each fit. The slopes of the fit were then used to calculate the PLQY of the PTB7@F127-FA CPNs. Note that errors in measurements (fluorescence intensity and absorbance) were too small to be visible on the scales used in these graphs.

5.3.2 ζ-potential of PTB7@F127-FA CPNs

As discussed previously, the ζ-potential value is an excellent quantitative measure of the charge-induced colloidal stability. Therefore, ζ-potential of the PTB7@F127 CPNs were measured before and after FA modification, on samples of 10 μg/mL concentration. Results of these measurements, shown in Figure 5.12, reveal that functionalization of CPNs with FA resulted in a decrease of the ζ-potential, from (-23.1 ± 5.39) mV to (-27.9 ± 6.89) mV. This decrease in ζ-potential is consistent with previous observations of functionalization of F127 with FA, as reported by N. Suthiwangcharoen *et al.*, who report a decrease of the ζ-potential of F127 from -8.7 mV to approximately -10 mV upon functionalization with FA (Figure

5.12(c)).[30] As such, this result provides further conclusion of the CPNs functionalization with FA, and points towards improved colloidal stability of the probes.

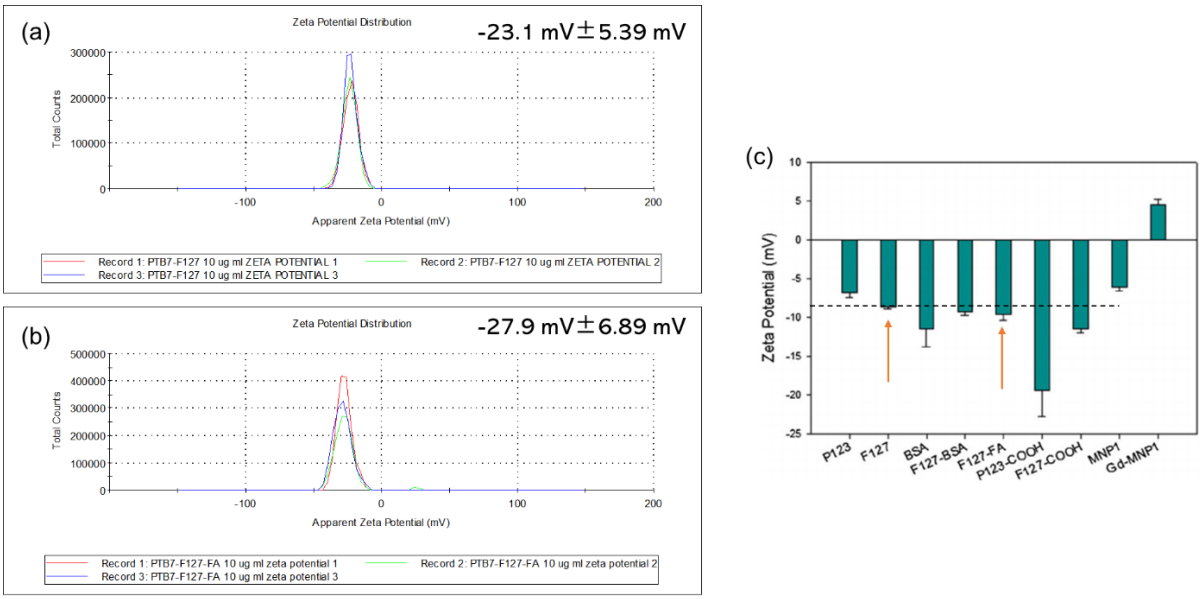

Figure 5.12 ζ-potential of PTB7@F127 CPNs and PTB7@F127-FA CPNs. (a) and (b) show the results of the ζ-potential measurements for PTB7@F127 CPNs and PTB7@F127-FA CPNs, respectively. Measurements were performed on samples dispersed in aqueous suspension at a concentration of 10 μg/ml. (c) shows the ζ-potential values of different ligands and polymer materials, including those of unmodified F127 and that of F127 copolymer modified with FA in PBS solution at pH 7.4 (indicated by arrows). Reproduced from reference[30] with permissions.

5.4 Targeted cell imaging

Tumour cell targeting ability of the prepared PTB7@F127-FA in cellular imaging was assessed using both a home-built fluorescence microscope and a number of confocal microscopes available at the NIKON imaging centre of KCL. In these experiments, FR-positive HeLa cells were incubated in culture medium with suspensions of PTB7@F127 CPNs and PTB7@F127-FA CPNs at a concentration of 10 μg/mL for 4 hours. HeLa cells did not exhibit any autofluorescence under the experimental conditions used.

In the preliminary experiments performed using a home-built set-up, shown in Figure 5.13, cells incubated with PTB7@F127 CPNs were found to exhibit almost no fluorescence, in contrast to cells incubated with PTB7@F127-FA CPNs, for which a strong fluorescence was observed. Furthermore, the red fluorescence from the sample incubated with PTB7@F127-FA CPNs suspensions overlap with the positions of the HeLa cells, indicating that PTB7@F127-FA CPNs are specifically binding to them by targeting FR. This demonstrates that FA promotes

the cellular uptake of PTB7@F127-FA CPNs due to the over-expressed folate receptors on Hela cells.

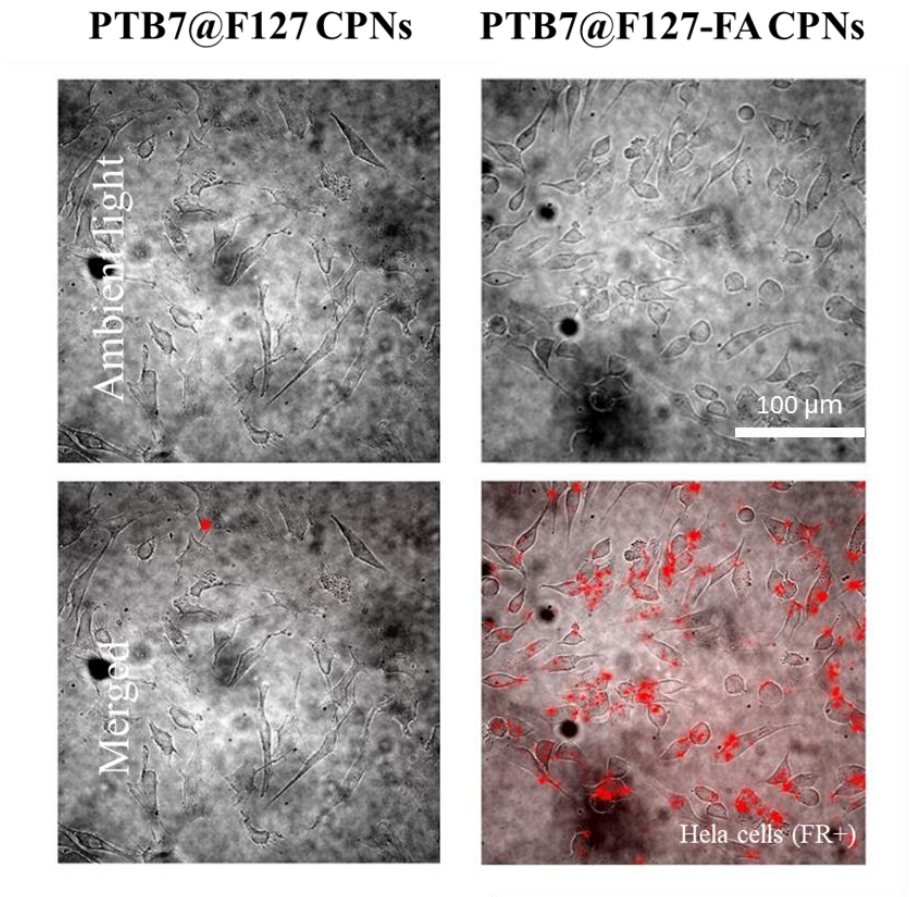

Figure 5.13 Demonstration of targeting ability of PTB7@F127-FA CPNs. Figure shows bright-field (top row, labelled "Ambient") and images of bright-field merged with fluorescence signal (bottom row, labelled "merged") of fixed HeLa cells (FR+) after 4 h incubation with PTB7@F127 CPNs (left column) and PTB7@F127-FA CPNs (right column) suspensions at 10 µg/mL. Images were obtained using white light produced by an LED lamp, filtered through a 650 ± 40 nm band pass filter. Fluorescence images were obtained by filtering the reflected signals with a long pass filter with a 700 nm onset. Images were captured with 40× oil objective, using exposure time of 1000 ms and later merged together with bright-field images in matlab, Scale bar is 100 µm.

To investigate whether FA can enhance the tumour cell-selective binding of PTB7@F127-FA CPNs, FR-negative HEK 293 cells were used as a low folate receptor control. In this experiment, HeLa and HEK 293 cells were incubated with 10 µg/mL PTB7@F127-FA CPNs suspensions for 4 h. As depicted in Figure 5.14, fluorescence from the PTB7@F127-FA CPNs is predominantly concentrated in the HeLa cells region, whereas in the HEK 293 cell sample, fluorescence from the PTB7@F127-FA CPNs is dispersed throughout the entire background. This indicates that the cellular affinity of PTB7@F127-FA CPNs by HEK 293 cells is lower

than that by HeLa cells, confirming the tumour cell targeting ability of PTB7@F127-FA CPNs. Additional Z-stack cell imaging is required to confirm whether PTB7@F127-FA CPNs entered the cells or have attached to the cells' membranes. In either case, one would expect a substantial increase in the efficacy of the photodynamic treatment due to the observed enhanced cellular affinity of our CPNs, as cell death can also be cause by ROS-induced disruption of the cell membrane.[31]

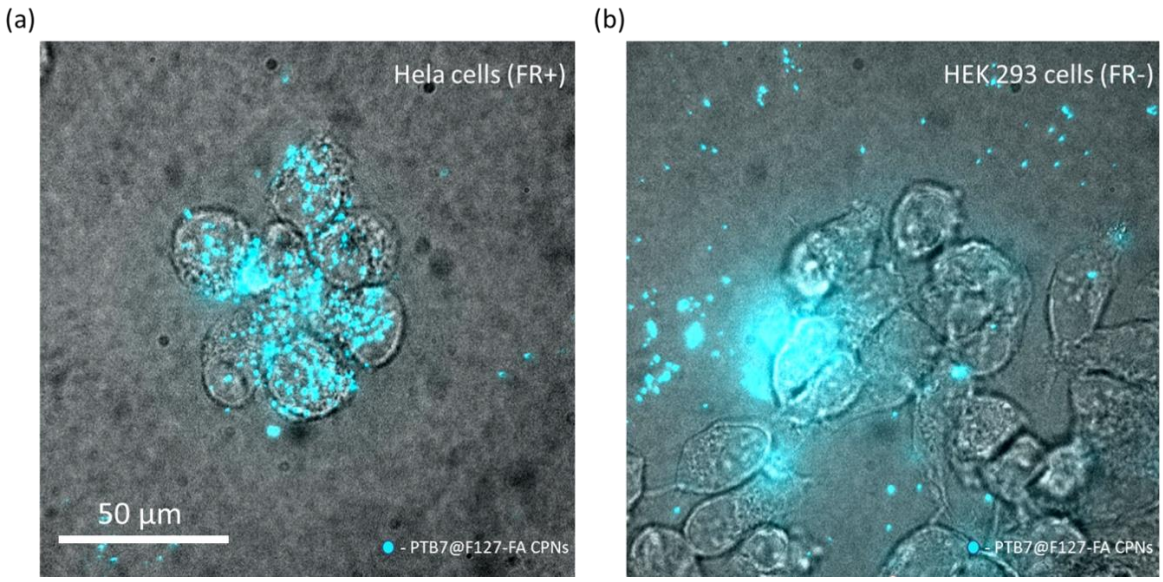

Figure 5.14 Comparison of cellular uptake of PTB7@F127-FA CPNs by FR+ and FR- expressing cell lines. Figure shows bright-field images (grey scale) merged with fluorescence confocal images (blue) of fixed (a) HeLa cells (FR+) and (b) HEK 293 cells (FR-) after 4 h incubation with 10 µg/mL suspensions of PTB7@F127-FA CPNs. Excitation wavelength used for recording fluorescence images was 647 nm. Fluorescence signals were collected in the 663-738 nm using a custom-made filter. Images were captured with 60× oil objective, using an exposure time of 100 ms. Scale bar is 50 µm. (Note: these images were recorded with the assistance of Dr. Katelyn Spillane)

5.5 Discussion

On a final note, the alternate method described here for FA-modification of F127 on CPNs surfaces represents an interesting first report of overcoming incompatibility of a copolymer with the nanoprecipitation process. It suggests that, in cases where such incompatibility exists, CPNs could be first formed with a more hydrophilic version of the desired copolymer and, upon successful formation of the CPNs, their surfaces could then be partially modified to the desired version of the copolymer. In such a way, the CPNs design strategy presented here could

be extended to the fabrication of other CPNs, where the target stabilizing shell may not have sufficient amphiphilicity to be used during the nanoprecipitation procedure.

It should be noted that functionalization of F127 with FA has been achieved previously in targeted drug-delivery applications (*e.g.* for delivery of DOX inside an F127 micelle). In these cases, however, the common approach is to use thin-film hydration method, in which F127-FA is first synthesised, and then dissolved with the material to be encapsulated/delivered. The mixture is then left to evaporate the solvent, to obtain a uniform thin layer which is then hydrated by DI water or buffer solution.[18,32,33] This thin-film hydration method, however, is much more complicated when compared to the direct nanoprecipitation method I used in this chapter. Furthermore, the bilayer F127 encapsulating shell formed via the thin film hydration method could be detrimental to the physicochemical properties of CPNs, such as the photodynamic properties of PTB7, since the inner interface inside such micelles fail to provide the beneficial organic environment for the conjugated polymer.

5.6 Conclusions

In this chapter, the modification of PTB7@F127 CPNs with FA is attempted as means of solving the previously encountered problem of poor cell affinity of PTB7@F127 CPNs, whilst simultaneously achieving specific target recognition of developed probes to FR, which is over-expressed by HeLa cells. FA modification is a common strategy for improving the tumour targeting ability of nanomaterials, as FR is over expressed by most tumour cells, thus ensuring the modified NPs can be applied in a wide range of tumour-targeting applications.

The conventional method of modifying F127 with FA was found to destroy the amphiphilic nature of F127, thus making subsequent nanoprecipitation with PTB7 difficult. A modified method, whereby CPNs were first synthesized and then FA was directly attached to their surface, resulted in a clear CPNs suspension with good water dispersibility. The attachment of FA to the CPNs surface was confirmed using a number of techniques. Firstly, the steady state absorption of PTB7@F127-FA CPNs possessed the characteristic features of PTB7 and FA absorptions. Secondly, the DLS size of PTB7@F127 CPNs was found to increase by ~30 nm upon modification with FA. Finally, a corresponding decrease in the ζ-potential values (-22.9 mV to -28.8 mV) was also observed upon modifications. Both the DLS sizes and ζ-potential values were shown to be appropriate for bio-applications of PTB7@F127-FA CPNs.

Further characterization of the FA-modified CPNs led to the conclusion that $^1O_2$ generation decreased to half of its original level. Concurrently, the PLQY also decreased slightly from 1.3% to 1.01% upon modification. Both decreases, however, are mitigated by the strongly improved

cell adhesion of FA-modified probes, as demonstrated for FR-expressing cells. Overall, the results of this chapter confirm the potential of PTB7@F127-FA CPNs as probes for tumour-targeted diagnostic therapy. To the best of my knowledge, this is the first report of functionalization of F127 with FA being used to achieve selective tumour targeting with CPNs.

5.7 References

1. Kondepati, V. R. *et al.* Recent applications of near-infrared spectroscopy in cancer diagnosis and therapy. *Anal. Bioanal. Chem.* **390**, 125–139 (2008).

2. Pu, K. & Liu, B. Fluorescent conjugated polyelectrolytes for bioimaging. *Adv. Funct. Mater.* **21**, 3408–3423 (2011).

3. Feng, G. *et al.* Multifunctional conjugated polymer nanoparticles for image-guided photodynamic and photothermal therapy. *Small* **13**, 1–12 (2017).

4. Feng, L. *et al.* Preparation and biofunctionalization of multicolor conjugated polymer nanoparticles for imaging and detection of tumor cells. *Adv. Mater.* **26**, 3926–3930 (2014).

5. Agostinis, P. *et al.* Photodynamic therapy of cancer: an update. *CA. Cancer J. Clin.* **61**, 250–281 (2011).

6. Yang, K. *et al.* Graphene in mice: ultrahigh in vivo tumor uptake and efficient photothermal therapy. *Nano Lett.* **10**, 3318–3323 (2010).

7. Geng, J. *et al.* Biocompatible conjugated polymer nanoparticles for efficient photothermal tumor therapy. *Small* **11**, 1603–1610 (2015).

8. Feng, G. *et al.* Conjugated polymer microparticles for selective cancer cell image-guided photothermal therapy. *J. Mater. Chem. B* **3**, 1135–1141 (2015).

9. http://worldaccount.basf.com/wa/NAFTA/Catalog/Chemicals.

10. Pitto-Barry, A. & Barry, N. P. E. Pluronic® block-copolymers in medicine: From chemical and biological versatility to rationalisation and clinical advances. *Polym. Chem.* **5**, 3291–3297 (2014).

11. Cervin, C. *et al.* A combined in vitro and in vivo study on the interactions between somatostatin and lipid-based liquid crystalline drug carriers and bilayers. *Eur. J. Pharm. Sci.* (2009).

12. Chong, J. Y. T. *et al.* Steric stabilisation of self-assembled cubic lyotropic liquid crystalline nanoparticles: high throughput evaluation of triblock polyethylene oxide-polypropylene oxide-polyethylene oxide copolymers. *Soft Matter* **7**, 4768–4777 (2011).

13. Yaghmur, A. & Glatter, O. Characterization and potential applications of nanostructured aqueous dispersions. *Adv. Colloid Interface Sci.* **147**–**148**, 333–342 (2009).

14. Tominaga, Y. *et al.* Flower micelle of amphiphilic random copolymers in aqueous media. *J. Phys. Chem. B* **114**, 11403–11408 (2010).

15. Keereweer, S. *et al.* Targeting integrins and enhanced permeability and retention (EPR) effect for optical imaging of oral cancer. *J. Surg. Oncol.* **105**, 714–718 (2012).

16. Barry, N. P. E. & Sadler, P. J. Challenges for metals in medicine: how nanotechnology may help to shape the future. *ACS Nano* **7**, 5654–5659 (2013).

17. Hirsjarvi, S. *et al.* Passive and active tumour targeting with nanocarriers. *Curr. Drug Discov. Technol.* **8**, (2011).

18. Zhang, D. *et al.* A functional drug delivery platform for targeting and imaging cancer cells based on Pluronic F127. *J. Biomater. Sci. Polym. Ed.* **26**, 468–482 (2015).

19. Fan, Y. *et al.* Solasodine, isolated from solanum sisymbriifolium fruits, has a potent anti-tumor activity against pancreatic cancer. *Drug Des. Devel. Ther.* **15**, 1509–1519 (2021).

20. Hoffbrand, A. V & Weir, D. G. The history of folic acid. *Br. J. Haematol.* **113**, 579–589 (2001).

21. Costantino *et al.* Colloidal systems for CNS drug delivery. *Prog. Brain Res.* (2009).

22. Zhong, S. *et al.* Folic acid functionalized reduction-responsive magnetic chitosan nanocapsules for targeted delivery and triggered release of drugs. *Carbohydr. Polym.* **168**, 282–289 (2017).

23. Wang, J. *et al.* PEGylated-folic acid–modified black phosphorus quantum dots as near-infrared agents for dual-modality imaging-guided selective cancer cell destruction. *Nanophotonics* **9**, 2425–2435 (2020).

24. Narmani, A. *et al.* Imaging, biodistribution and in vitro study of smart (99m)Tc-PAMAM G4 dendrimer as novel nano-complex. *Colloids Surf. B. Biointerfaces* **159**, 232–240 (2017).

25. Narmani, A. *et al.* Folic acid functionalized nanoparticles as pharmaceutical carriers in drug delivery systems. *Drug Dev. Res.* **80**, 404–424 (2019).

26. Li, X. *et al.* Folic acid-conjugated amphiphilic alternating copolymer as a new active tumor targeting drug delivery platform. *Drug Des. Devel. Ther.* **10**, 4101–4110 (2016).

27. Lin, J. J. *et al.* Folic acid-Pluronic F127 magnetic nanoparticle clusters for combined targeting, diagnosis, and therapy applications. *Biomaterials* **30**, 5114–5124 (2009).

28. Kang, H. *et al.* Size-Dependent EPR effect of polymeric nanoparticles on tumor targeting. *Adv. Healthc. Mater.* **9**, e1901223 (2020).

29. Liechty, W. B. & Peppas, N. A. Expert opinion: Responsive polymer nanoparticles in cancer therapy. *Eur. J. Pharm. Biopharm.* **80**, 241–246 (2012).

30. Suthiwangcharoen, N. & Nagarajan, R. Controlled design and construction of multifunctional nanoparticles by molecular self-assembly. *Rsc Adv.* **4**, 10076–10089 (2014).

31. Kwiatkowski, S. *et al.* Photodynamic therapy – mechanisms, photosensitizers and combinations. *Biomed. Pharmacother.* **106**, 1098–1107 (2018).

32. Li, Z. *et al.* Novel folated pluronic F127 modified liposomes for delivery of curcumin: preparation, release, and cytotoxicity. *J. Microencapsul.* **37**, 220–229 (2020).

33. Zhang, W. *et al.* Multifunctional Pluronic P123/F127 mixed polymeric micelles loaded with paclitaxel for the treatment of multidrug resistant tumors. *Biomaterials* **32**, 2894–2906 (2011).

Chapter 6 – Conclusions

Due to their nanoscale size and large surface area, NPs possess unique physical and chemical characteristics. Among these, CPs are very appealing because they are easy to synthesize, easy to modify on the surface, and have good biocompatibility. Designing and using CPNs to address medical and health-related challenges, such as drug delivery, bioimaging, and biotherapeutics, continues to attract growing interest. In this work, a non-water-soluble low-bandgap conjugated polymer PTB7 was used for the first time to develop water-dispersible theranostic NIR-active CPNs probes. Approaches to improve the performance of the probes were further investigated, including changes to fabrication procedures and structure of the CPNs probes, as well as modification of their surfaces, resulting in probes with improved PLQY, $^1O_2$ production and tumour-specific targeting ability.

The ratio of CPs to copolymer and the acidity of the reaction mixture pre-reprecipitation were determined to strongly influence the brightness and photosensitization ability of the CPNs, although not to a degree that the addition of bulky side chains modified these properties. The observed changes were attributed to differences in polymer chain packing within the CPNs, affecting interchain interactions and aggregate formation within the system. In addition, $^1O_2$ generation was shown to be sensitive to the pH of the environment in which the CPNs probes are employed, with slight acidity contributing to a notable increase in its production. This promotes the future application of PTB7-based CPNs probes in the typically mildly acidic tumour microenvironments.

The functionalization of the CPNs surface was shown to be equally important for probes' theranostic potential, as it influenced the affinity of the CPNs to cells. After all, a probe with low cellular affinity to a specific tumour cell will not accumulate in corresponding tumorous tissues passively, thereby rendering all of its other properties irrelevant. The initially developed PTB7@F127 CPNs probes did, in fact, possess such a low affinity, when tested on A549 cancerous cells. However, as the work in this thesis demonstrates, the low affinity of probes can be exploited when combined through further modification of the probes with targeting elements. In such a way, the probe is endowed with specificity to the target tumorous tissues whilst maintaining its low affinity to other cells, such as those found in healthy tissues. In this work, the attachment of FA to the surfaces of PTB7@F127 CPNs endowed these probes with specificity to any FR-expressing tumours.

During investigations described in this thesis, it became clear that the choice of the copolymer used to solubilise CPNs is critical in determining some of the CPNs properties – a fact that is

rarely explored in the literature. To mitigate this gap in knowledge, and to guide my own research, a detailed review of the existing literature was made to highlight some of the common trends and observations revealing any relations between the two. The key conclusion of this literature review is that selection of the copolymer dictates many of the CPNs' properties, including their size, dispersibility, colloidal stability, cell adhesion and biocompatibility, to name a few. Crucially, and in relation to the theranostic potential of CPNs probes, their photosensitization properties can be modulated *via* an appropriate selection of the solubilising copolymer, with some facilitating the production of ROS such as $^1O_2$ and others fully quenching it. These conclusions were partly based on my own investigations of the properties of PTB7 CPNs probes, which demonstrated that PSMA copolymer fully quenches the production of $^1O_2$ of these CPNs under NIR irradiation but does not stop superoxide production under UV excitation. In contrast, the use of the F127 copolymer led to an improvement of ROS production of PTB7, regardless of ROS type or wavelength of irradiation. As such, the various trends in the influence of copolymer selection on CPNs properties work identified in the thesis embody a valuable set of criteria for the design of CPNs-based probes for bio-applications.

In terms of future directions, several aspects have been identified in this thesis that warrant further investigations. Firstly, the origin of the observed quenching ability of PSMA for $^1O_2$ generation remains unclear. Further detailed studies are required to confirm that this effect is general to other CPNs that incorporate ROS-producing CPs. Equally, the mechanism of this effect should also be investigated from a structural perspective, using molecular dynamics calculations similar to those reported recently for F8BT CPNs[1] to elucidate what effect of interchain percolation caused by copolymer has on the properties of core CPs. Photophysical studies (*e.g.* transient absorption spectroscopy) should be performed in parallel, to confirm what photoexcited species form in the CPs and whether there are any differences in the photophysics of CPNs shelled with PSMA *versus* non-quenching copolymers such as PLGA or F127.

Secondly, the targeted specificity of PTB7@F127-FA CPNs towards tumour cells can be greatly improved by FA modification, but it reduces the ability of PTB7@F127-FA CPNs to generate $^1O_2$. Therefore, further optimization of PTB7@F127-FA CPNs synthesis is warranted, with the goal of maintaining targeting specificity whilst maximizing $^1O_2$ production. One potential strategy is to reduce the amount of FA used for the modification. Currently, FA is modified on PTB7@F127 CPNs at a 1:1 molar ratio with F127, which may impact the packing of F127 and subsequently decrease $^1O_2$ generation by PTB7@F127-FA CPNs. By reducing the amount of FA used for modification, the detrimental effect of FA on F127 packing could be

minimized, potentially leading to improved $^1O_2$ production by PTB7@F127-FA CPNs. Additionally, characterization techniques such as TEM, SEM, AFM and DLS together with ζ-potential measurement can be used to investigate the impact of FA modification on the structural and physicochemical properties of PTB7@F127-FA CPNs. This understanding could facilitate the optimization of fabrication conditions to maintain the structural integrity of PTB7@F127-FA CPNs while enhancing its $^1O_2$ generation capability. The careful design and optimization of PTB7@F127-FA CPNs make them promising candidates for PDT application. Finally, the size of nanomaterials plays a critical role in determining their physical and chemical properties. The relationship between the size of PTB7@F127 CPNs and its optical performance deserves further investigation. Preliminary experimental results presented in this thesis indicate an anticorrelation trend between the size of PTB7@F127 CPNs and its $^1O_2$ generation capability, as well as improved PLQYs for smaller PTB7@F127 CPNs. As the size of the NPs changes, the increased contortions of the CPs chains can cause shift in the energy levels of the electrons, resulting in changes in the bandgap, which affects the absorption and emission properties. This size-dependent bandgap energy can be studied by calculating the singlet and triplet excited states to probe the differences between CPNs of different sizes. Understanding the relationship between the size of CPNs and the singlet-triplet intersystem crossing process that determines $^1O_2$ generation is crucial for tailoring their optical properties for specific applications, such as optoelectronics, photonics, and nanomedicine.

6.1 References

1. Ziolek, R. M. *et al.* Conformational heterogeneity and interchain percolation revealed in an amorphous conjugated polymer. *ACS Nano* **16**, 14432–14442 (2022).